ICRR ANNUAL REPORT 2024



INSTITUTE

FOR

COSMIC RAY RESEARCH

THE UNIVERSITY OF TOKYO

ANNUAL REPORT
(APRIL 2024 – MARCH 2025)



Editorial Board

ASANO, Katsuaki

SAKAMOTO, Eri

TAKENAGA, Yumiko

NAKAMURA, Makio

UMEYAMA, Ikumi

©Institute for Cosmic Ray Research, The University of Tokyo

5-1-5, Kashiwanoha, Kashiwa, Chiba 277-8582, Japan

Telephone: (81) 4-7136-3102
Facsimile: (81) 4-7136-3115
WWW URL: http://www.icrr.u-tokyo.ac.jp/

TABLE OF CONTENTS

Preface

Research Divisions 1

Neutrino and Astroparticle Division 2
High Energy Cosmic Ray Division 29
Astrophysics and Gravity Division 66

Observatories and a Research Center 82

Norikura Observatory 83
Akeno Observatory 90
Kamioka Observatory 94
KAGRA Observatory 95
Research Center for Cosmic Neutrinos 96
High Energy Astrophysics Facility in Canarias 97

Appendix A. ICRR Workshops and Ceremonies 99

Appendix B. ICRR Seminars 101

Appendix C. List of Publications 101

(a) Papers Published in Journals
(b) Conference Papers

Appendix D. Doctoral Theses 116

Appendix E. Public Relations 116

(a) ICRR News
(b) Public Lectures
(c) Visitors

Appendix F. Inter-University Research Activities 123

Appendix G. List of Committee Members 129

(a) Board of Councillors
(b) Advisory Committee
(c) Inter-University Research Advisory Committee

Appendix H. List of Personnel 130

PREFACE

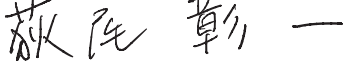
This report summarizes the scientific activities of the Institute for Cosmic Ray Research (ICRR) of The University of Tokyo in the Japanese FY (JFY) 2024.

ICRR is an inter-university research institute for studies of cosmic rays. The headquarters of ICRR is located in Kashiwa, Chiba prefecture, Japan. In order to promote various cosmic-ray-related studies efficiently, ICRR has three research divisions; Neutrino and Astroparticle division, High Energy Cosmic Ray division, and Astrophysics and Gravity division. ICRR have four observatories in Japan; Kamioka Observatory and KAGRA Observatory (Kamioka underground, Gifu prefecture), Norikura Observatory (2770 meters above sea level, Mt. Norikura, Gifu prefecture), and Akeno Observatory (Yamanashi prefecture), together with 1 research center; Research Center for Cosmic Neutrinos (Kashiwa, Chiba prefecture). In addition, there are three major experimental facilities outside of Japan. They are located in Utah in USA, Yangbajing in Tibet, China and the La Palma island in Spain.

Many researchers from various Japanese institutions as well as those from overseas are involved in the research programs of ICRR. It should be noted that most of the scientific outputs from ICRR are the results of the collaborative efforts by many researchers from various institutions. In order to produce outstanding results, it is very important to carry out an experiment by an international collaboration composed of top-level researchers all over the world. Hence, all of the experimental collaborations that ICRR is involved are international ones. With these activities, ICRR has been selected as one of the institutions of the "International Joint Usage/Research Center" program by Ministry of Education, Culture, Sports, Science and Technology -Japan (MEXT) in November 2018.

Thanks to the generous support from many individuals, including donations through the Hida City hometown tax program, we have been able to further enhance and advance our research activities, as well as support the development of young researchers. We would like to take this opportunity to express our sincere gratitude.

We hope that this report is useful for the understanding of the current research activities of ICRR. Finally, we appreciate the strong support of our colleagues in this research field, The University of Tokyo and MEXT. They are indispensable for the continuing, and exciting scientific outcome of ICRR.



Shoichi Ogio,

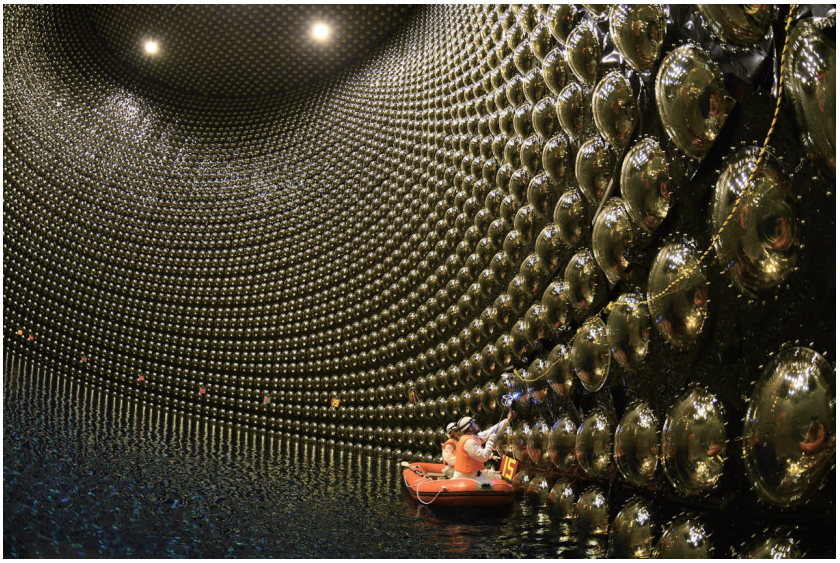
Director,

Institute for Cosmic Ray Research,

The University of Tokyo



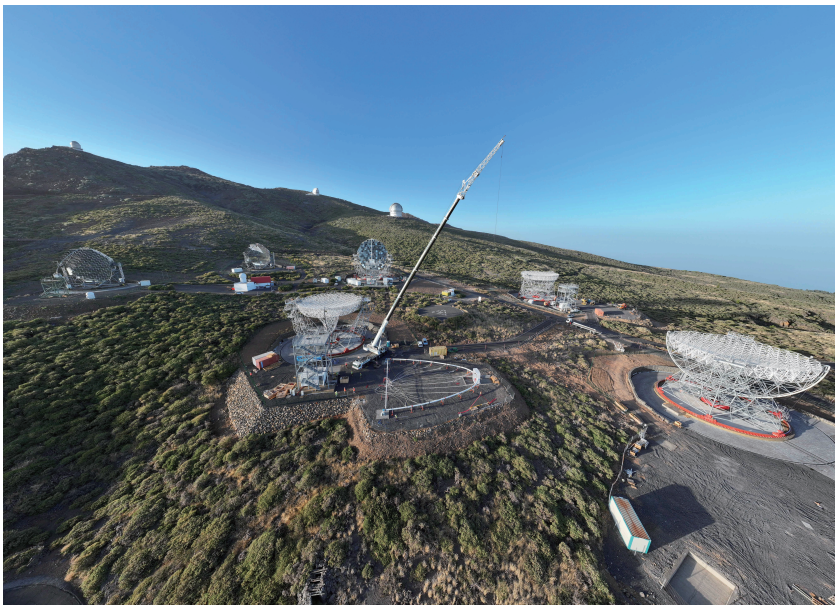
The ICRR building at Kashiwa, Chiba, Japan.



The Super-Kamiokande detector (the photo was taken during refurbishment work in 2018).



Excavation of cylindrical section of the Hyper-Kamiokande (20m depth by the end of March 2024).

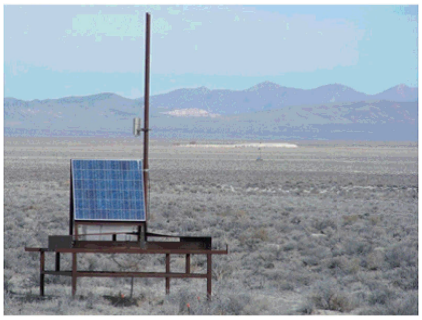


Three Large Sized Telescopes under construction at the northern site of CTAO on the Canary Island of La Palma. (August 2024)

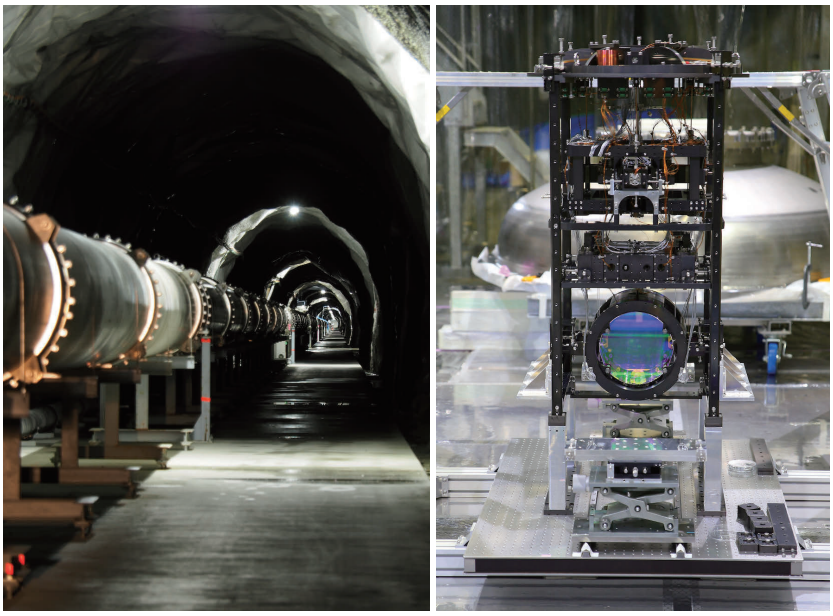


The construction of ALPAQUITA air shower array completed in 2023 and began to operate before the full scale ALPACA experiment at Chakartaya Plateau in Bolivia.





Air fluorescence telescopes (left) and a scintillator surface detector (right) of the Telescope Array experiment in Utah, USA to explore the origin of extremely high energy cosmic rays.

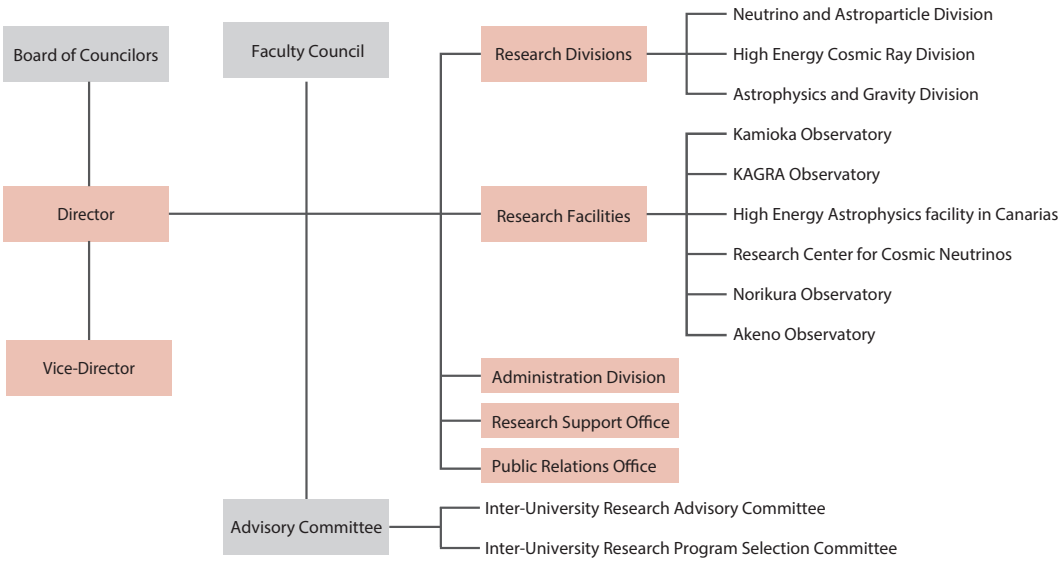


KAGRA's (left) 3km-long arm tunnel and (right) a sapphire mirror installed in a cryogenic suspension system.



Public lecture co-organized by ICRR and the Institute for the Physics and Mathematics of the Universe (Kavli IPMU).

Organization



Number of Staff Members (As of May 1, 2024)

	Scientific Staff	Technical Staff	Research Fellows	Administrators and Secretaries	Total
Neutrino and Astroparticle Div.	24	6	3	18	51
High Energy Cosmic Ray Div.	18	12	8	5	43
Astrophysics and Gravity Div.	19	12	7	10	48
Administration	0	0	0	18	18
Total	61	30	18	51	160

FY 2017-2024 Budget

	2017	2018	2019	2020	2021	2022	2023	2024
Personnel expenses	779 000	823 000	872 000	898 000	898 000	1 048 000	1 068 000	1 146 000
Non-personnel expenses	1 514 000	1 729 000	1 611 000	1 173 000	2 078 000	1 990 000	1 974 000	2 083 000
Total	2 293 000	2 552 000	2 483 000	2 071 000	2 976 000	3 038 000	3 042 000	3 229 000

(in 1 000 yen)

RESEARCH DIVISIONS

Neutrino and Astroparticle Division

Overview
Super-Kamiokande
T2K Experiment
XENON Experiment
Hyper-Kamiokande

High Energy Cosmic Ray Division

Overview
Cherenkov Cosmic Gamma-Ray Group
TA: Telescope Array Experiment
Tibet ASγ Experiment
ALPACA Project
High Energy Astrophysics Group

Astrophysics and Gravity Division

Overview
Gravitational Wave Group
Observational Cosmology Group
Theory Group

NEUTRINO AND ASTROPARTICLE DIVISION

Overview

This division aims to study particle physics with a primary interest in physics of neutrinos and proton decay, and astroparticle physics with the use of underground experimental facilities.

The Super-Kamiokande (SK) detector is a 50 kton water Cherenkov detector using 11,129 50 cm-diameter photomultipliers (PMTs) for its inner detector and 1,885 20 cm-diameter PMTs for its outer detector. The data taking of SK started in April 1996, and the 20th anniversary was celebrated in 2016. The neutrino oscillations in atmospheric neutrinos were discovered in 1998 and thereby it was demonstrated that neutrinos have a finite mass. In 2001, the accurate measurements of the ^{8}B solar neutrino flux by SK and SNO discovered that neutrino oscillations are the solution to the solar neutrino problem beyond doubt. These findings became the research achievement for which the Nobel Prize in Physics was awarded in 2015. After the epoch-making discoveries, precise measurements of atmospheric neutrinos and solar neutrinos have been performed, and they unraveled various phenomena of neutrino oscillations. The evidence of tau neutrino appearance in atmospheric neutrinos was confirmed in 2013, the atmospheric neutrino anomaly has been finally concluded. The indication of day-night asymmetry of the solar neutrino flux, which is expected from the matter effect of neutrino oscillations, was reported in 2014. At present, the most interesting subjects in those observations are the determination of neutrino mass hierarchy using atmospheric neutrinos and the consistency check of solar(ν_e) and reactor($\bar{\nu}_e$) oscillations.

A high-intensity neutrino beam experiment using the J-PARC accelerator (T2K) was started in 2009. The T2K experiment uses the SK detector as the far detector. Search for leptonic *CP* violation and the high precision measurement of oscillation parameters are the main physics subjects in T2K. An indication of electron neutrino appearance was found in June 2011, and later, the electron appearance was established with greatly improved significance. Since 2014, anti-neutrino beam data have also been taken in order to search for *CP* violation. T2K later reported the exclusion of the conservation of *CP* symmetry in neutrino oscillations at more than 95% CL.

The search for nucleon decay is another important subject at SK because it gives a direct evidence for the Grand Unified Theories (GUTs). SK gives the current best limit, which strongly constrains various GUT models.

If a supernova happens in our galaxy, thousands of neutrino interactions are expected at SK, and they will reveal the detailed mechanism of the supernova explosion. SK is the only detector in the world that can identify the direction of the supernova neutrinos. So, SK has been operated almost all the time with a small dead time, and if a supernova is observed at SK, we will send burst information to astronomers as soon as it is detected. In addition, SK aims to observe supernova relic neutrinos, which are accumulated supernova burst neutrinos from the beginning of the universe. For this purpose, it is planned to add 0.1% of gadolinium into the Super-K tank (called SK-Gd project) in order to tag neutrons for $\bar{\nu}_e$ detection. A feasibility study for the SK-Gd project is being performed using a 200-ton tank which mimics the Super-K detector. Refurbishment of the Super-K tank and upgrade of the water circulation system were conducted in 2018, 0.01% gadolinium was dissolved in the detector water in the summer of 2020, and further additions in the summer of 2022 achieved 0.03% gadolinium concentration.

Another activity of the Neutrino and Astroparticle division is a multi-purpose experiment using liquid xenon, aiming at the detection of cold dark matter, neutrino absolute mass using neutrinoless double beta decay, and low-energy solar neutrinos. An 800 kg liquid xenon detector, XMASS-I, was constructed in an experimental hall near the SK site. Data taking continued for more than five years and was completed in February 2019. This activity was strengthened by participating in the XENONnT experiment in 2017 at an overseas site. Searches for dark matter interactions and rare phenomena in liquid xenon are being conducted there.

The Hyper-Kamiokande (Hyper-K or HK) experiment is proposed as a joint project of the University of Tokyo and KEK by combining a next-generation underground water Cherenkov detector and upgraded J-PARC neutrino beam. The Hyper-K detector is an order of magnitude larger in detector fiducial mass than Super-K and has discovery potential of leptonic *CP* violation and proton decays. The project officially started by receiving its first Japanese funding at the beginning of 2020. Its construction schedule includes 5 years of cavern excavation, 2 years of instrumentation, and data taking commencement in 2028. In parallel, the J-PARC beam delivered to the detector will be upgraded from 0.5 to 1.3 MW over the same time period.

SUPER-KAMIOKANDE

[Spokesperson : Masayuki Nakahata / Hiroyuki Sekiya
(Kamioka Observatory, ICRR, The University of Tokyo)]

Atmospheric neutrinos

Atmospheric neutrinos are produced from the decays of secondary particles produced in the collision of primary cosmic rays with nuclei in the atmosphere. Atmospheric neutrinos have several remarkable features:

- The flavor ratio, $(\nu_\mu + \bar{\nu}_\mu)/(\nu_e + \bar{\nu}_e)$ is 2 (> 2 for above few GeV)
- Zenith angle distribution is up/down symmetry above a few GeV.

These features are realized without neutrino oscillations and provide a useful constraint in the study of these neutrinos. Super-Kamiokande has been observing atmospheric neutrinos since 1996 and has accordingly made several important measurements with them, including the discovery of neutrino oscillations [1].

Starting in the summer of 2020, SK was operated with a 0.01% concentration of Gd dissolved into the detector water. This period of the detector, SK6, lasted until 2022, when the concentration was increased to 0.03%, marking the start of the SK7 period. Figure 1 shows the atmospheric neutrino data taken with Gd-loaded water in SK7 in comparison to data taken from SK6. There is no large change in the detector's ability to observe atmospheric neutrinos, and the SK7 data are judged to be of similarly high quality as those in previous Gd-loaded and pure-water periods. In November 2023, a failure of the detector's geomagnetic field compensation coils resulted in a roughly six-month period of reduced atmospheric collection efficiency. Though data collection continued, the simulation development is ongoing to produce a reliable model for analyzing these data. Since the summer of 2024, additional compensation coils have been deployed in the detector and atmospheric neutrino data taking has returned to its full efficiency.

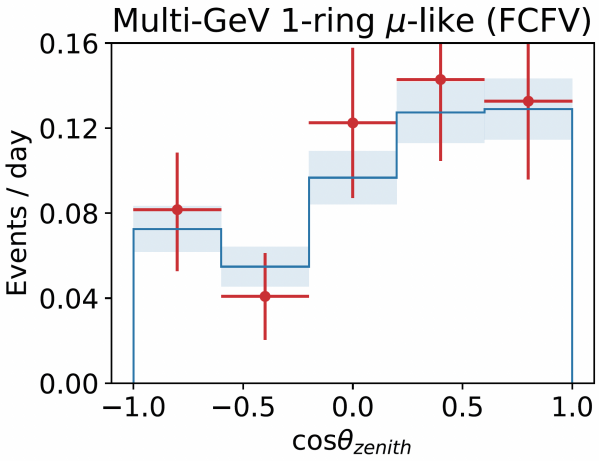


Fig. 1. Comparison of the atmospheric neutrino event rate in SK6 and SK7 for the multi-GeV μ-like sample.

Three flavor oscillations and the neutrino mass hierarchy

The SK atmospheric neutrino data are described at leading order by two-flavor $\nu_\mu \rightarrow \nu_\tau$ oscillations with maximal mixing (θ_{23}=π/4). However, sub-leading contributions via $\nu_\mu \rightarrow \nu_e$ oscillations induced by the mixing angle θ_{13} as well as the "solar" mixing parameters ($\Delta m^2_{12}, \theta_{12}$) provide the ability to probe currently unknown aspects of the standard neutrino oscillation paradigm, such as the existence of leptonic *CP* violation and the neutrino mass ordering (hierarchy). Understanding these open questions may bring important insight into larger questions, such as the origin and evolution of today's matter-dominated universe.

Several sub-leading oscillation effects are expected to appear in atmospheric neutrinos:

- Resonant enhancement of $\nu_\mu \rightarrow \nu_e$ oscillations due to matter along the neutrino path is expected to occur at energies between 2 and 10 GeV. This will manifest as an excess of upward-going electron-like events (e-like) in the atmospheric sample.
- This enhancement exists for either ν_e or $\bar{\nu}_e$ depending on the mass hierarchy. Therefore, the mass hierarchy can be probed by understanding the relative amount of neutrino and antineutrino interactions in the detector.
- The combination of the solar oscillation parameters and the octant of $\sin^2\theta_{23}$ may enhance or suppress the event rate and, to some extent, alter the spectral shape of Sub-GeV electron-like data due to the $\nu_\mu \leftrightarrow \nu_e$ oscillations they induce.
- The standard oscillation paradigm includes a *CP*-violating factor, δ_{cp}, which is expected to induce several sub-dominant oscillation effects in many of the SK atmospheric neutrino samples, even if CP is conserved.

Super-Kamiokande has studied the effects of these oscillations on atmospheric neutrino data separated into fully-contained (FC) events, partially-contained (PC) events, and upward-going muon (UPMU) topologies. Fully-contained events are characterized by a primary interaction vertex that is located inside the fiducial volume of the detector and whose visible particles stop within the inner detector. On the other hand, though the primary vertex position of PC events is within the fiducial volume, they are characterized by having at least one charged particle escaping the inner detector and depositing light in the outer detector. In most cases, the escaping particle is a muon. Upward-going muons originate from high-energy muon-neutrino interactions in the rock surrounding the detector. Since all other particles are lost to interactions in the rock, only the muon is penetrating enough to reach the detector and be identified. The FC sample is separated into electron-like and muon-like (μ-like) subsamples by applying a particle identification algorithm to the most energetic Cherenkov ring of each event. Since PC and upward-going events are predominantly produced by muon neutrinos, no particle identification is applied. Though SK cannot distinguish on an event-by-event basis between neutrino and antineutrino interactions, statistical separation of multi-GeV electron-like subsamples is performed to improve sensitivity to the mass hierarchy. A likelihood method designed to enhance the kinematic differences between neutrino and antineutrino interactions is applied to separate events into ν_e-like and $\bar{\nu}_e$-like subsamples.

Since the start of SK4, SK has had the ability to identify neutrons, albeit with a limited efficiency of 25%. In 2020, atmospheric neutrino events from this data set were separated into neutrino-like and antineutrino-like samples, taking advantage of the fact that the former are expected to produce fewer neutrons on average than the latter. Further, a novel event selection based on a boosted decision tree was introduced to improve the classification of multi-ring events in all

data periods. Using these new event selections, all SK data until the end of the SK5 period (2020) were analyzed to update the analysis presented in [3]. In addition, the fiducial volume used in the current analysis has been expanded by 20%. With these improvements, the analysis found a preference for the normal mass ordering (NO) of between 78% and 96.7% over the range of oscillation parameter values allowed at the 90% confidence level. The preference at the best fit of the analysis is 92.3%. Further, the updated analysis shows no strong preference for the octant of $\sin^2\theta_{23}$ and has a weak preference for a non-zero CP-violating phase. These results have now been published in Ref. [4].

Improved resolution on L/E

For atmospheric neutrinos the dominant oscillation mode, $\nu_\mu \leftrightarrow \nu_\tau$, can be approximated by two-flavor oscillations parameterized by a single mixing angle and a single mass splitting, Δm^2_{32}. The latter produces oscillations with a single frequency for a fixed ratio of pathlength, L, to energy,E:

$$P(\nu_\mu \to \nu_\tau) \propto \sin^2\left(\frac{1.27\Delta m^2 L}{E}\right). \quad (1)$$

While the disappearance of upward-going muon events in the Super-K data is attributed to oscillations into nearly unseen ν_τ events according to this formula, alternative models predict a disappearance but with a different dependence on the neutrino kinematic variables. To test the oscillatory features of the predicted PMNS probability and to improve constraints on Δm^2_{32}, an alternative oscillation analysis with event samples selected and binned in L/E has been prepared.

The analysis uses the event samples from the main oscillation analysis, but additionally, events are selected from the FC single-ring, FC multi-ring, PC Stopping, and PC Through-going data based on their resolution on the L/E ratio. This analysis updates a previous SK result from 2004 [5] with a four-times-larger data set and a new method that selects events with both high- and low-resolution on L/E. In order to maximize sensitivity and minimize statistical uncertainties, the separation into high-resolution subsamples is done as a function of the reconstructed L/E value. Figure 3 shows these high-resolution data compared to the L/E prediction assuming two-flavor PMNS oscillations and for a neutrino decay model. The data agree well with the former, rejecting the latter at 6σ. When the analysis is run with both high- and low-resolution data, including PMNS oscillations with all three active neutrino flavors, a tighter constraint on Δm^2_{32} is achieved as is shown in Figure 4. Though largely consistent with the standard analysis in the mixing variables, this L/E analysis slightly prefers the inverted mass ordering by 1.5 units of $\Delta\chi^2$.

Bibliography

[1] Y. Fukuda *et al.* [Super-Kamiokande Collaboration], Phys. Rev. Lett. **81**, 1562 (1998).

[2] R. Wendell *et al.* [Super-Kamiokande Collaboration], Phys. Rev. D **81**, 092004 (2010).

[3] K. Abe *et al.* [Super-Kamiokande Collaboration], Phys. Rev. D **97**, no. 7, 072001 (2018).

[4] T. Wester *et al.* [Super-Kamiokande], Phys. Rev. D **109**, 072014 (2024).

[5] M. Ishitsuka *et al.* [Super-Kamiokande], Phys. Rev. Lett. **93**, 101801 (2004).

Cosmic-ray muons

Introduction

Cosmic-ray muons predominantly come from the decay of mesons produced in hadronic showers that follow from the interaction between primary cosmic rays and nuclei in the atmosphere. Accordingly, these muons carry essential information on pion and kaon production in the hadronic interaction.

The charge ratio, which is defined as the ratio of the number of positive particles to negative particles, is an important observable to constrain the flavor ratio of atmospheric neutrinos. The kaon charge ratio is larger than that of pions because positive kaons are produced in association with lambda particles in air showers, and this results in a higher production rate than that of negative kaons. The contribution of kaon decays to muon production increases at high $E_\mu \cos\theta_{\mathrm{Zenith}}$, and this results in the rise of muon charge ratio above the TeV region [1, 2].

In addition to the muon charge ratio, the polarization of cosmic-ray muons is also an important observable to constrain the contribution from kaon decays. The muon produced in the two-body decay of a meson is completely polarized in the direction of motion of the muon in the rest frame of the meson [3]. The polarization of muons from kaon decays in the laboratory frame is therefore much larger than that from pion decays because the polarization reflects the rest mass of the parent meson [4]. Hence, a measurement of the magnitude of muon polarization constrains the relative contribution from kaons and pions to the muon flux.

Cosmic-ray muons must penetrate the mountain to reach the SK detector, selecting a typical momentum of 0.9 TeV at sea level. Although the detector cannot distinguish the charge of the penetrating cosmic-ray muons, the muon charge ratio can be statistically determined by measuring the decay time of stopping muons, since negative muons tend to have a shorter decay time due to the formation of muonic atoms with oxygen in the water. Furthermore, the angular distribution between the parent muon and the decay electron gives the magnitude of the muon polarization.

Results

By combining the results from three different SK phases (SK-IV, SK-V, and SK-VI), we determined the charge ratio and the polarization as $R = 1.32 \pm 0.02$ (stat.+syst.), and $P_0^\mu = 0.52 \pm 0.02$ (stat.+syst.), respectively.

The muon charge ratio has been experimentally measured by several methods in the energy region of GeV to tens of TeV. Figure 5 shows the comparison with the experimental results from other detectors. The muon charge ratio measured by the SK detector is consistent with that by the Kamiokande-II detector, which was located at almost the same depth in the same mountain, within their uncertainties. The result from the SK detector is consistent with the prediction from the Honda flux model while it deviates by 1.9σ from the πK model at

Table 1. Best fit oscillation parameters obtained by the three-flavor oscillation analysis. Fits are conducted for both the normal (NH) and inverted (IH) hierarchy assumptions The fit was performed assuming $\sin^2\theta_{13}$=0.0218, which is taken from the PDG.

Fit	Hierarchy	$\sin^2\theta_{23}$	$\lvert\Delta m^2_{32,31}\rvert$ [$\times 10^{-3}$ eV^2]	δ_{CP}	$\sin^2\theta_{13}$	$\delta\chi^2$ (IO-NO)
SK only	NH	0.45	2.40	-1.89	0.020	–
	IH	0.48	2.40	-1.89	0.010	5.23
SK, θ_{13} constrained	NH	0.45	2.40	1.75	–	–
	IH	0.45	2.40	-1.75	–	5.69

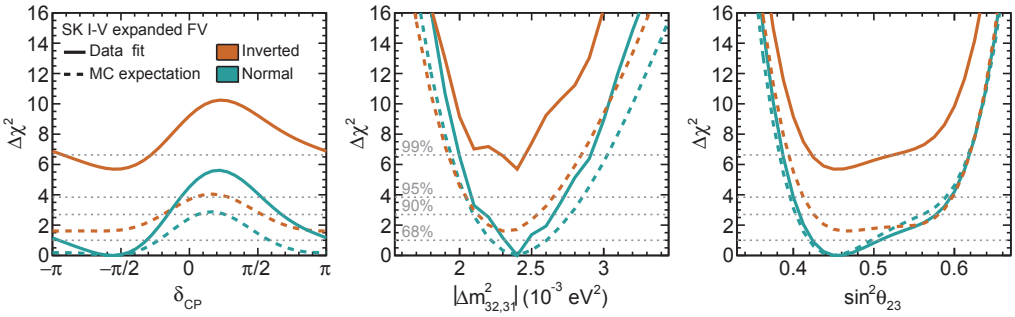


Fig. 2. Measured $\Delta\chi^2$ distributions for the $\Delta m^2_{23,31}$, $\sin^2\theta_{23}$, and δ_{cp} oscillation parameters for the Super-K only fit with $\sin^2\theta_{13}$ constrained to the value preferred by reactor measurements.

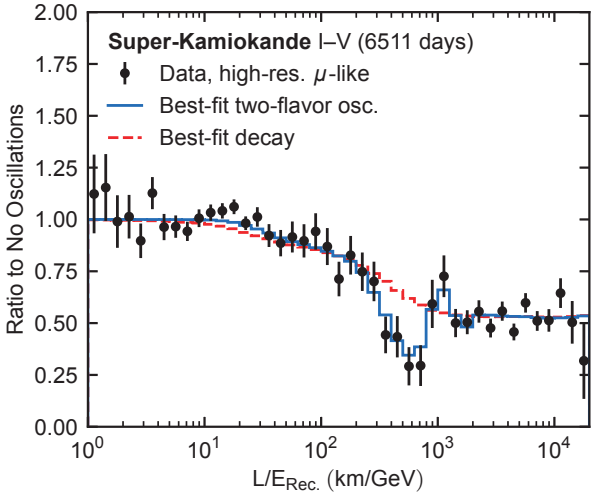


Fig. 3. Reconstructed L/E distribution for high-resolution data and MC showing good agreement with standard PMNs oscillations and a rejection of the neutrino decay hypothesis.

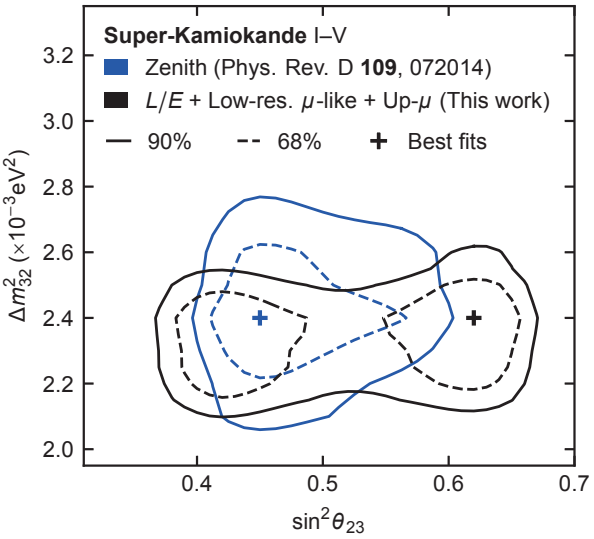


Fig. 4. Comparison of the atmospheric mixing plane for the standard zenith angle analysis compared to the analysis, including high-resolution L/E bins.

$E_\mu \cos\theta_{\text{Zenith}} = 0.7^{+0.3}_{-0.2}$ TeV. This tension between the measured charge ratio and the πK model should lead to further improvement of atmospheric neutrino simulations.

The muon polarization has been experimentally measured at various locations. It has been mostly measured below 15 GeV/c by experiments that measured the decay asymmetry of muons in a magnetic metal absorber on the ground. Those experiments measured the muon polarization in the energy region where pion decay is the dominant process. On the other hand, the SK detector, as well as the Kamiokande-II detector [5], uniquely measured the polarization of cosmic-ray muons with momentum around 1.0 TeV/c at sea level because of their shared underground location. Such a higher energy measurement of muon polarization can evaluate the contribution from kaon decays. Figure 6 shows the comparison of the polarization of cosmic-ray muons with different momenta.

The muon polarization measured by the SK detector deviates by 1.5σ from the expectation simulated by the Honda flux model [6] as shown in Fig. 6. This measurement com-

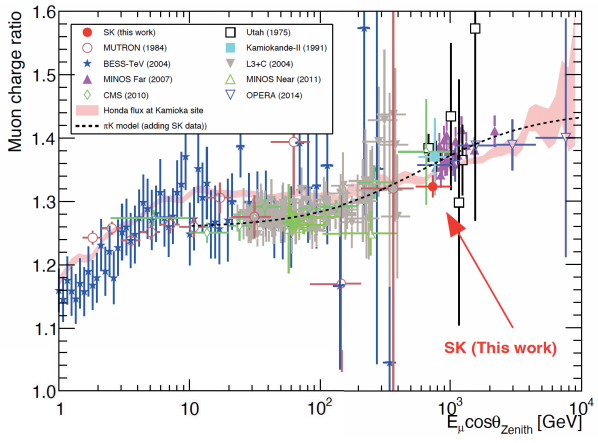


Fig. 5. The muon charge ratio measured by the experiments together with the expectations from simulation models. The red-filled circle shows the SK data, and other symbols with different colors show the experimental data measured by other groups.

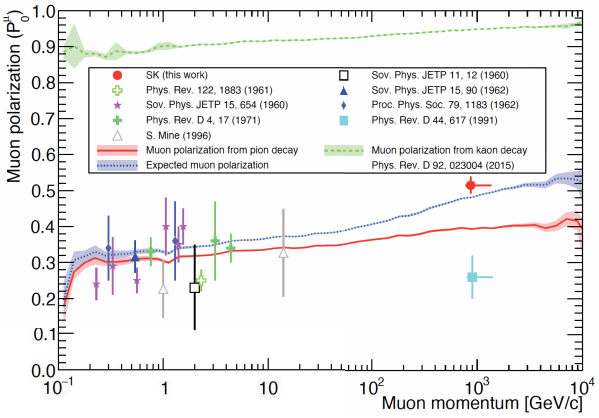


Fig. 6. The experimental data of the polarization of the cosmic-ray muon at the production site as a function of the muon momentum. The red-filled circle shows the SK data, and other symbols with different colors show the experimental data measured by other groups.

pletely excludes a "pure-pion scenario" based on the Honda flux model with a significance of 5.1–5.2σ level at the energy near 1 TeV/c.

As for prospects, the measurement result of charge ratio constrains the ratio of atmospheric neutrinos to anti-neutrinos ($\nu/\bar{\nu}$), and the measurement of muon polarization also constrains the energy spectrum of atmospheric neutrinos in neutrino flux simulation models. These measurements can therefore contribute to a more precise determination of neutrino oscillation parameters.

Bibliography

[1] T.K. Gaisser, Astropart. Phys. **35**, 801 (2012).

[2] P.A. Schreiner, J. Reichenbacher, and M.C. Goodman, Astropart. Phys. **32**, 61 (2009),

[3] P. Lipari, Astropart. Phys. **1**, 195 (1993).

[4] S. Hayakawa, Theory, Phys. Rev. **108**, 1533 (1957).

[5] M. Yamada et al. Phys. Rev. D **44**, 617 (1991).

[6] M. Honda, M. Sajjad Athar, T. Kajita, K. Kasahara, and S. Midorikawa, Phys. Rev. D **92**, 023004 (2015).

Solar Neutrinos

Introduction

Solar neutrinos constitute by far the largest component of the neutrino flux on the Earth among those produced from natural sources. Most of solar neutrinos are produced by proton-proton fusion, $p+p \rightarrow d+e^{+}+\nu_e$, and its subsequent fusion reactions (pp-chain)[1]. They are categorized into the *pp*, *pep*, ^{7}Be, ^{8}B and *hep* neutrinos. Among these, Super-Kamiokande is sensitive to ^{8}B and *hep* neutrinos, which have relatively higher energy that extends up to ∼20 MeV.

Past observations of solar neutrino flux by Super-Kamiokande (SK) [1] and the Sudbury Neutrino Observatory (SNO) [2] led to the discovery of solar neutrino flavor conversion. Our current interest in solar neutrino measurements with the SK detector [3] is to make a precision test of the neutrino flavor conversion through the Mikheyev-Smirnov-Wolfenstein (MSW) effect [4, 5]. The MSW effect leads to a resonant conversion of the solar neutrinos within the Sun and results in an about 30% level of the survival probability above ∼5 MeV. The survival probability of lower-energy neutrinos is described by the vacuum oscillation probability of ∼ 50%, and the transition region between the two lies in a few MeV region. This transition from the matter-dominant oscillation to the vacuum-dominant oscillation is often called the "upturn" of the solar neutrino spectrum. Current experimental data is not enough to directly demonstrate this "upturn" because of the experimental sensitivity as well as the statistics.

SK aims to directly test the "Spectrum up-turn" by precisely measuring the energy spectrum of ^{8}B solar neutrino in this transition region. This measurement is important not only to test the MSW effect but also to test several alternative theoretical models, such as sterile neutrinos [6, 7], mass-varying neutrinos [8], non-standard interactions [9, 10], and so on.

The matter effect can also be tested with the matter in the interior of the Earth. Electron flavor neutrinos are regenerated due to the matter effect of the Earth, making the neutrino flux at night larger than that during the day by about a few % level depending on the neutrino oscillation parameters.

In this article, we report results of solar neutrino measurements using the data taken through the end of the fourth SK data taking phase (SK-IV) in May 2018. These results are published in 2024 [11] with an analysis method improved from our previous publication with 1670 days data [12]. The total livetime used for this analysis is 5,805 days, with 2970 days from the SK-IV phase. In addition to the standard neutrino oscillation analysis, we briefly report the status of solar neutrino observation in the SK detector after loading the Gadolinium [13].

Analysis

For precisely measuring the energy spectrum of recoil electrons, the energy scale should be reduced, and the removal

*[1] with a subdominant (∼1%) contribution from the CNO cycle

of background events is essential. For that purpose, the detector simulation was improved with more accurate modeling of the PMT timing response and the non-uniformity of the water quality. For example, the energy reconstruction method was improved with a correction for the PMT gain drift and with a new correction of the energy scale non-uniformity. The correction for the gain drift was first introduced in 2017 and then refined in this analysis with an improved correction for the dark noise contribution. Furthermore, the correction for the PMT angular response was improved with a more realistic simulation of the PMT response and arrangement. By introducing those improvements, the standard variation of the energy scale variation was reduced to $\pm 0.5\%$, which is three times smaller than that previously estimated. For further reduction of background events, we newly developed algorithms locating muon-induced hadronic showers, both by improving the reconstruction of the energy deposited along the muon track, and by identifying neutrons using a recently implemented low-energy trigger [14]. New spallation cuts based on these algorithms allow for a reduction of the deadtime of the solar neutrino analysis by a factor of two, allowing a gain of the equivalent of one year of exposure at SK-IV. Moreover, the profiles of the neutron clouds produced in muon-induced hadronic showers are well reproduced by the spallation simulation, motivating its use to develop spallation reduction algorithms for future analyses. By applying this cut to the data sample, the signal efficiency improved about 12% while keeping the removal efficiency of muon spallation events about 90% [14].

^{8}B solar neutrino flux measurement

The SK detector observes solar neutrinos via elastic scatterings with electrons in pure water. The direction of a recoiled electron is highly correlated with the direction of the incident neutrino. Figure 7 shows the distribution of $\cos\theta_{\rm Sun}$ for solar neutrino candidates observed during the SK-IV phase. With the 2970 days of data in SK-IV, more than 60,000 events are observed over the background.

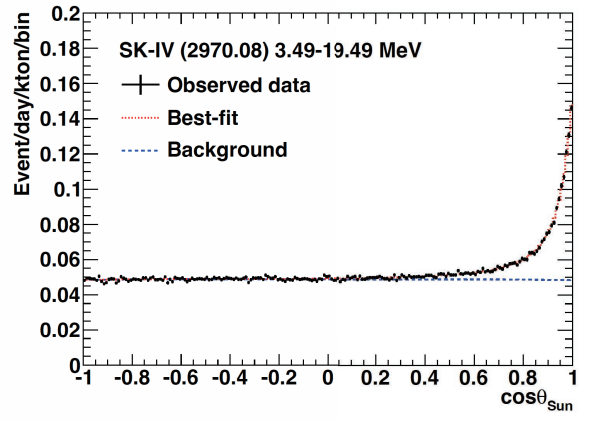


Fig. 7. The solar angle distribution in SK-IV. The horizontal axis shows the cosine of the solar angle $\cos\theta_{\rm Sun}$ and the vertical axis shows the number of observed events. The black points show the observed data, and the gray (light gray) histogram shows the best–fit (background) shape.

Adding the solar neutrino events observed in other phases, the total number of solar neutrino events is more than 100,000. Based on this data, the ^{8}B solar neutrino flux is determined to be $(2.34 \pm 0.04) \times 10^6$ /cm^2/sec assuming a pure electron neutrino flavor content. The ratio between the SK result and the SNO NC current flux (5.25×10^6 /cm^2/sec) [15] is found to be 0.445 ± 0.008. Figure 8 shows the ^{8}B solar neutrino flux measured by solar neutrino experiments, such as SK, SNO, Borexino, KamLAND, and SNO+. A comparison between different interaction channels is a clear demonstration of the existence of non-electron neutrino components in ^{8}B solar neutrinos.

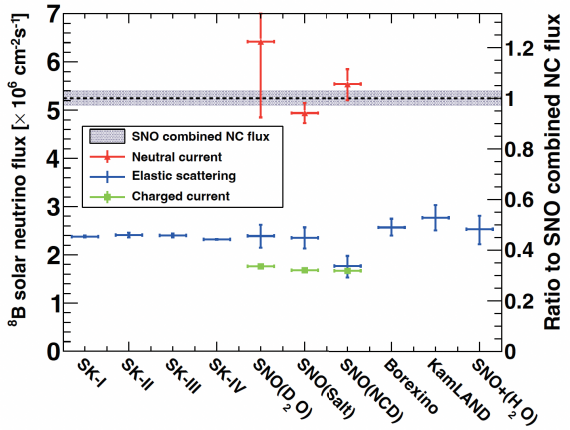


Fig. 8. Comparison of ^{8}B solar neutrino flux among solar neutrino experiments. The measured fluxes of other experiments are obtained from the three phases of SNO, Borexino, KamLAND, and SNO+ (pure water). The left (right) vertical axis shows the measured flux without neutrino oscillation (the ratio of the measured flux to the SNO's neutral current flux.

The solar activity cycle is the 11 years periodic change of sunspots, releasing the magnetic flux at the surface of the Sun. The number of Sunspots strongly correlated with the solar activity cycle. The solar neutrino data set, which is used for this analysis, spans more than 21 years and covers about two solar activity cycles. Figure 9 shows the SK yearly flux measured throughout the different phases of SK together with the corresponding sunspot number (Source: WDC–SILSO, Royal Observatory of Belgium, Brussels [16]). The χ^2 between observed data and no time dependence hypothesis is calculated with the total experimental uncertainties as $\chi^2/N_{\rm d.o.f} = 19.94/22$, where $N_{\rm d.o.f}$ is the number of freedom of this analysis. This calculation result corresponds to a probability of 58.9%. The SK solar rate measurements are fully consistent with a constant solar neutrino flux emitted by the Sun.

Using the 22-year data, we have also evaluated the annual modulation of solar neutrino flux due to the elliptic orbit of the Earth around the Sun. In this study, we determined the upper limit of the amplitude of the ^{8}B solar neutrino flux and the Kepler constants, such as eccentricity (ε) and perihelion shift ($\delta t_{\rm period}$). Table 2 summarizes the analysis results together with those from other experiments. The upper limit of the amplitude is the strongest constraint among the solar neutrino experiments.

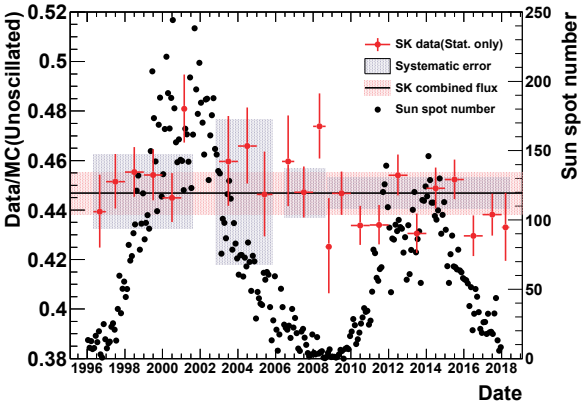


Fig. 9. The ratio of ^{8}B solar neutrino flux in SK over the SNO's NC current flux from 1996 to 2018. The red points show the yearly flux measured by SK (statistical uncertainty only), the gray bands show the systematic uncertainties for each SK phase, and the black-horizontal line shows the combined measured flux with the uncertainty drawn as the red horizontal band. The back circles show the sunspot number provided from [16].

Table 2. Comparison of time variation study results from SK [17], SNO [18], and Borexino [19] experiments.

	Amplitude [%]	Eccentricity ε [%]	Perihelion shift $\delta t_{\rm period}$ [day]
SK (^{8}B)	5.2	1.53 ± 0.35	-1.5 ± 13.5
SNO (^{8}B)	10.5	1.43 ± 0.86	–
Borexino (^{7}Be)	–	1.84 ± 0.32	7 ± 20

Energy spectrum analysis

An analysis of the solar neutrino energy spectrum was performed using all the data from SK-I to SK-IV [1, 20, 21, 12, 11]. The data quality for SK-IV was significantly improved by installing the new front-end electronics for SK-IV [22], upgrading the water circulation system, and developing the upgraded calibration methods [23].

Owing to these upgrades, SK has achieved the lowest background (induced by radioisotopes in pure water, especially ^{214}Bi) among all the SK phases [11]. The energy threshold in SK-IV has been lowered to 3.49 MeV in recoil electron kinetic energy (SK-I: 4.49 MeV, SK-III: 3.99 MeV) and this enabled SK to measure the solar neutrino energy spectrum with higher sensitivity. In addition, in May 2015, the trigger threshold was changed from 34 observed PMT signals within 200 nsec to 31 hits [24, 25]. Because of this lower threshold, the detection efficiency between 3.49 MeV and 3.99 MeV was improved from ∼86% to ∼100%. This improvement led to further reduction of the statistical uncertainty below 4.99 MeV in SK-IV.

Figure 10 shows the energy spectra obtained from SK-I, -II, -III, and -IV, overlaid with the predictions assuming the current oscillation parameters described in the next section. Because of long operation, low threshold of data acquisition, and the reduced systematic uncertainties for the spectrum measurement, the SK-IV energy spectrum data is statistically precise as demonstrated in Fig. 10.

Figure 11 shows the combined energy spectrum from SK-I to SK-IV with the predictions. Note that all SK phases are combined without regard to energy resolution or systematic uncertainties, but those uncertainties are taken into account in the χ^2 calculation between the data and the prediction. Comparing χ^2 between the spectrum data and the predictions, the energy spectrum of SK is consistent within $\sim 1.2\sigma$ with the MSW up-turn prediction. By adding the energy spectrum from the SNO experiment, a distorted spectrum is favored by $\sim 2.1\sigma$.

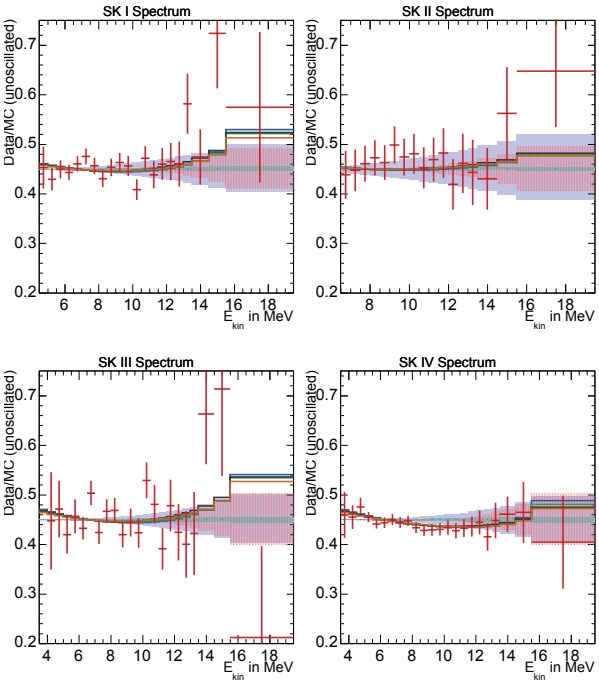


Fig. 10. SK-I, -II, -III, and -IV recoil electron spectra divided by the un-oscillated expectation. The green (blue) thick line represents the best-fit to SK data using the oscillation parameters from the fit to SK and SNO (with KamLAND) data. The thick (thin) lines are distorted (not distorted) by adjusting the energy scale, resolution, and neutrino spectrum within uncertainties.

Day-night asymmetry

The day-night asymmetry of the solar neutrino flux for the full SK-IV data set was extracted with the same method described in Ref. [26]. Here, the day-night asymmetry is defined as,

$$A_{D/N} = \frac{\Phi_{\rm day} - \Phi_{\rm night}}{0.5(\Phi_{\rm day} + \Phi_{\rm night})},$$

where $\Phi_{\rm day(night)}$ is the observed solar neutrino flux during day (night). In the analysis, we additionally fit the amplitude of the expected zenith angle variation to the observed data, which depends on the operation time of the SK detector. Figure 12 shows the comparison of the measured day-night flux asymmetry among four SK phases. The combined result is $A_{\rm D/N} = (2.86 \pm 0.85\,({\rm stat.}) \pm 0.32\,({\rm syst.}))\%$, where this value differs by 3.2σ level from zero. This result demonstrates the existence of Earth matter effects on solar neutrino oscillation.

The asymmetry parameter depends on the expected zenith angle variation shapes and, therefore, on the oscillation pa-

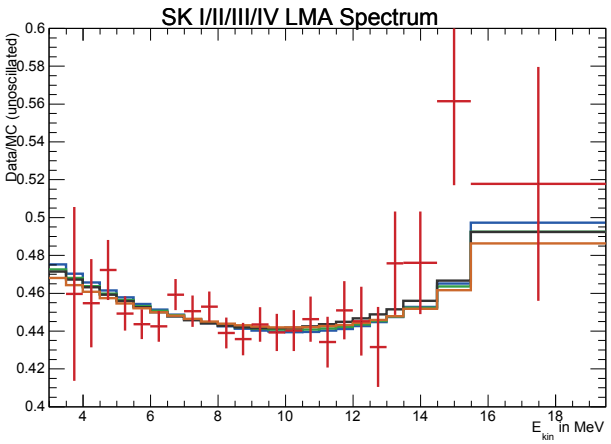


Fig. 11. The energy spectrum combining SK-I through SK-IV as a function of the recoil electron energy. The red points show the ratio of the data to the expected flux using an unoscillated ^{8}B solar neutrino spectrum. The definition of curves is the same as that in Figure 10.

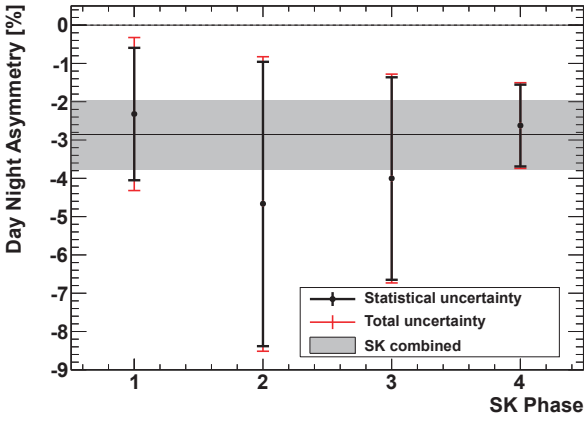


Fig. 12. Day/night asymmetries from amplitude fits by the four different SK phases. The black thick (red thin) bar shows the statistical (total) uncertainty, and the gray band shows the combined value.

rameters. The dependence on the mixing angle is negligible. Figure 13 shows the result of a day-night asymmetry amplitude fit as a function of Δm^2_{21} using the SK combined data from SK-I to SK-IV. In particular, at the solar+KamLAND best-fit value of $\Delta m^2_{21} = 7.5\times10^{-5}$ eV^2, the combined SK day/night amplitude fit corresponds to a slightly smaller asymmetry of $A_{\rm D/N} = (2.74\pm0.83\,({\rm stat.})\pm0.32\,({\rm syst.}))\%$, where an asymmetry of -1.7% is expected.

Oscillation parameter extraction

The oscillation parameters were extracted using the results from the solar neutrino measurements by radiochemical experiments (Homestake, SAGE, and GALLEX/GNO), and water Cherenkov experiments (SK and SNO) [15], and the liquid scintillator experiment (Borexino), as well as the reactor antineutrino measurement by KamLAND [27, 28]. Figure 14 shows the allowed parameter region from the SK+SNO data, all solar neutrino experiments, and the KamLAND data. SK significantly contributes to the measurement of the solar angle θ_{12}. From the SK+SNO data, the mixing angle is

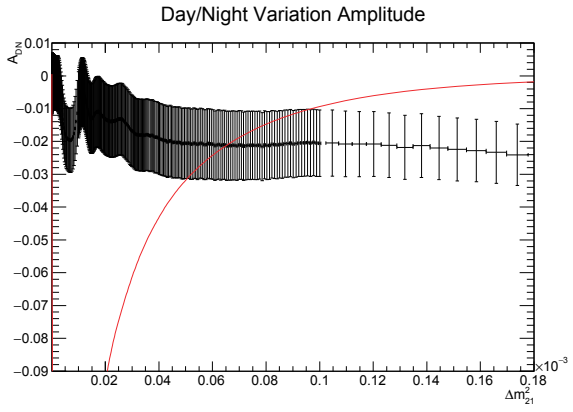


Fig. 13. SK-IV day/night amplitude fit dependence on Δm^2_{21}. The black line (gray band) shows the best-fit value of day/night asymmetry (its uncertainty). The red solid curve shows the expected day/night asymmetry. The green solid (blue dashed) box shows the 1σ range allowed by solar experiments (solar experiments and KamLAND).

determined to be $\sin^2\theta_{12} = 0.305\pm0.014$ and the mass difference is determined to be $\Delta m^2_{21} = 6.10^{+1.26}_{-0.86}\times10^{-5}$ eV^2 as shown in Fig. 14. The SK+SNO fit results favors a lower Δm^2_{21} value compared to the KamLAND best fit value of $\Delta m^2_{21} = 7.54^{+0.19}_{-0.18}\times10^{-5}$ eV^2. Currently, the SK+SNO data disfavors the KamLAND best-fit value at $\sim1.5\sigma$, while it was $\sim2\sigma$ in the previous analysis. Adding the KamLAND result, the oscillation parameters are determined to be $\sin^2\theta_{12} = 0.307\pm0.012$ and $\Delta m^2_{21} = 7.50^{+0.19}_{-0.18}\times10^{-5}$ eV^2.

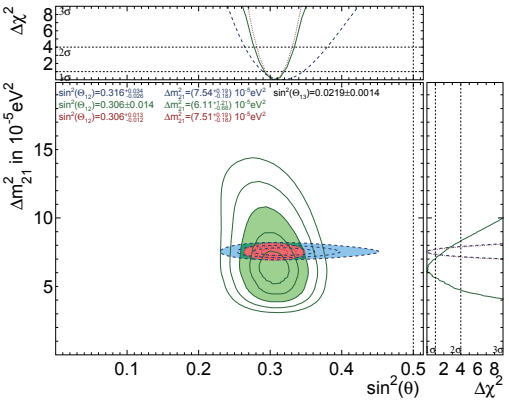


Fig. 14. The allowed contours for Δm^2_{21} vs. $\sin^2\theta_{12}$ from SK and SNO (green dashed line) and the all solar neutrino data (green solid line). The allowed contour from KamLAND is also shown in blue. The combined allowed region is shown in red.

Solar neutrino observation after Gd-loading

Gadolinium was loaded into the Super-Kamiokande's pure water [13] to enhance the detector's sensitivity to supernova relic neutrinos by tagging neutrons originating from the inverse beta decay of electron anti-neutrino interactions. The

first Gd loading was conducted in July 2020, and the second was done in June 2022.

In order to validate the detector performance, calibration data were taken after loading Gadolinium and compared with the results in the pure water phase. For example, Figure 15 shows the reconstructed electron kinetic energy with the DT calibration device [29] before and after the Gd loading. The differences of the peak position and resolution between SK-V (pure water) and SK-VI (Gd concentration 0.011%) are less than $\pm 1\%$. Hence, the detector's energy scale is enough to continue to observe the solar neutrinos in the MeV region.

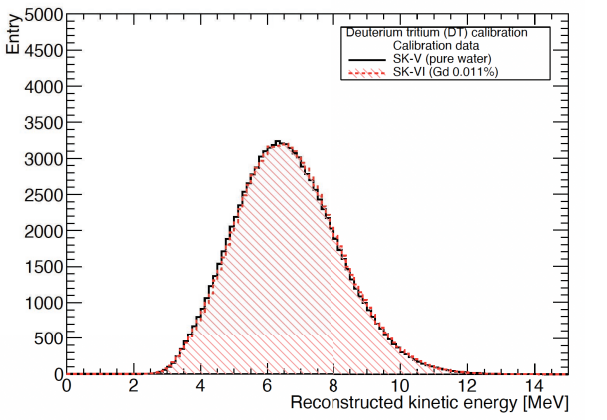


Fig. 15. The comparison of energy distribution between SK-V (pure water) and SK-VI (Gd concentration 0.011%). The calibration data were taken at the center position of the SK detector.

Figure 16 shows the typical distributions of $\cos\theta_{\rm Sun}$ before and after the Gd-loading. The peak of solar neutrinos around $\cos\theta_{\rm Sun} = 1$ is clearly observed even though we added the Gd into pure water. Figure 16 also demonstrates that no additional background exists in the energy range above 6.49 MeV even after the second Gd-loading. The background events below that level are under investigation since the detection efficiency for such events is different from that evaluated in the pure water phase mentioned in the previous section. Based on the DT calibration and $\cos\theta_{\rm Sun}$ distribution, the SK detector can continue to conduct the solar neutrino observation using Gd-loaded water.

Summary and outlook

In summary, Super-Kamiokande has precisely measured the ^{8}B solar neutrino flux, its time variation, and recoil electron spectrum. Using 5,805 days of data, more than 100,000 solar neutrino interactions were extracted over the background. No significant correlation between the observed solar neutrino flux and the sunspot number was found with more than 21 years of continuous observation of the solar neutrino flux. We have also set a strong constraint on the amplitude of the annual modulation of the solar neutrino flux due to the elliptic orbit of the Earth around the Sun.

The measured energy spectrum of ^{8}B solar neutrino is consistent within $\sim 1\sigma$ with the MSW upturn with both the solar best-fit parameters and the KamLAND best-fit parameters. The previously existed $\sim 2\sigma$ tension between the solar and KamLAND best fit Δm^2_{21} values was reduced to $\sim 1.5\sigma$ in

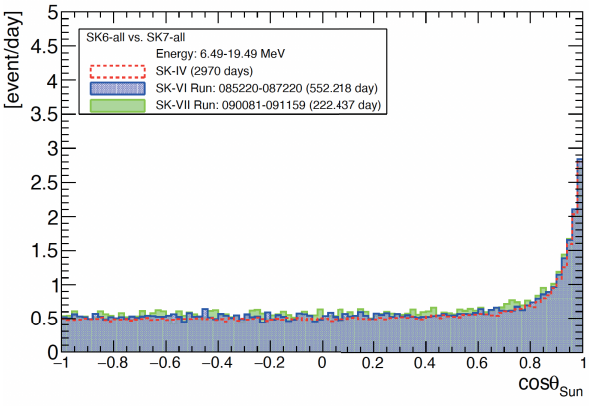


Fig. 16. The comparison of the cosine theta distribution between 6.49 and 19.49 MeV before and after the Gd-loading. The phases of SK-IV (red) were operated by filling pure water, while SK-VI (blue) and SK-VII (light green) were operated by adding Gd into the detector's pure water. Even after dissolving additional Gd in the second Gd-loading, the background rate is unchanged because of the development of ultra-low radio-purity Gd powder.

this analysis. Combining the solar neutrino oscillation analyses by SK, SNO, and KamLAND, the oscillation parameters are determined as $\Delta m^2_{21} = 7.50^{+0.19}_{-0.18} \times 10^{-5}$ eV^2 and $\sin^2\theta_{12} = 0.307 \pm 0.012$.

The Super-Kamiokande detector was recently upgraded by dissolving Gadolinium (Gd), and started a new phase of observation as SK-Gd. In order not to cause significant harm to the solar neutrino observation, ultra-pure $Gd_2(SO_4)_3$ powder with extremely low radio-impurity was newly developed and dissolved into the SK detector. Furthermore, the calibration data after the Gd-loading has been taken Enhanced neutron detection capability with Gd can be used to further reduce the cosmic-ray spallation backgrounds. We aim to further improve our solar neutrino measurements with additional data and analysis improvements in the SK-Gd era.

Bibliography

[1] J. Hosaka *et al.*, Phys. Rev. D **73**, 112001 (2006).

[2] Q.R. Ahmad *et al.*, Phys. Rev. Lett. **87**, 071301 (2001).

[3] Y. Fukuda *et al.*, Nucl. Instrum. Meth. A **501**, 418 (2003).

[4] S.P. Mikheyev and A. Y. Smirnov, Sov. Jour. Nucl. Phys. **42**, 913 (1985).

[5] L. Wolfenstein, Phys. Rev. D **17**, 2369 (1978).

[6] P.C. de Holanda and Y. Smirnov, Phys. Rev. D **69**, 113002 (2004).

[7] P.C. de Holanda and Y. Smirnov, Phys. Rev. D **83**, 113011 (2011).

[8] V. Barger *et al.*, Phys. Rev. Lett. **95**, 211802 (2005).

[9] A. Friedland *et al.*, Phys. Rev. B **594**, 347 (2004).

[10] O.G. Miranda *et al.*, J. High Energy Phys. **10** 008 (2006)

[11] K. Abe *et al.*, Phys. Rev. D **109**, 092001 (2024).

[12] K. Abe *et al.*, Phys. Rev. D **94**, 052010 (2016).

[13] K. Abe *et al.*, Nucl. Instrum. Meth. A **1027**, 166248 (2022).

[14] S. Locke *et al.*, Phys. Rev. D **110**, 032003 (2024).

[15] B. Aharmin *et al.*, Phys. Rev. C **88**, 025501 (2013).

[16] WDC-SILSO, Royal Observatory of Belgium, Brussels. http://www.sidc.be/silso/datafiles

[17] K. Abe *et al.*, Phys. Rev. Lett. **132**, 241803 (2024).

[18] B. Aharmim *et al.*, Phys. Rev. D **72**, 052010 (2005).

[19] S. Appel *et al.*, Astropart. Phys. **145**, 102778 (2023).

[20] J.P. Cravens *et al.*, Phys. Rev. D **78**, 032002 (2008).

[21] K. Abe *et al.*, Phys. Rev. D **83**, 052010 (2011).

[22] H. Nishino *et al.*, Nucl. Instrum. Meth. A **610**, 710 (2009).

[23] K. Abe *et al.*, Nucl. Instrum. Meth. A **737**, 253 (2014).

[24] S. Yamada *et al.*, IEEE Trans. Nucl. Sci. **57**, 428 (2010).

[25] Y. Nakano, PhD thesis, The Univ. of Tokyo (2016).

[26] A. Renshaw *et al.*, Phys. Rev. Lett. **112**, 091805 (2014).

[27] S. Abe *et al.*, Phys. Rev. Lett. **100**, 221803 (2008).

[28] A. Gando *et al.*, Phys. Rev. D **88**, 033001 (2013).

[29] E. Blaufuss *et al.*, Nucl. Instrum. Meth. A **458**. 636 (2001).

Searches for nucleon decays

Among many physics models beyond the Standard Model (SM) of particle physics, Grand Unified Theories (GUTs) are promising models that can explain several features of the SM, including the quantized hypercharge. One of the remarkable predictions of the GUTs is the decay of protons or bound neutrons, which are stable particles in the SM. Super-Kamiokande is the most sensitive experiment for these phenomena and has been looking for them since its beginning in 1996.

However, the minimal SU(5)-based grand unification was ruled out by a search for the proton decay, $p \to e^+\pi^0$, at Super-Kamiokande [1]. This SU(5) model was also rejected by the fact that there is no precise agreement of the three gauge coupling constants at the GUT scale by extrapolating from precise measurements of these constants at LEP [2]. To avoid these experimental constraints, it is needed to lift the GUT scale and make the proton's lifetime longer than the experimental limit by introducing extra fields predicted by models beyond the SM (BSM), such as supersymmetry (SUSY). This addition of the extra degrees of freedom above the electroweak scale, which are not experimentally identified, will also modify the renormalization group equations of the three coupling constants and allow these constants to meet at the GUT scale.

Since no hints for the BSM have been obtained in any experiments yet, it is particularly important to search for various nucleon decay modes to catch as wide a range of modifications to the SM as possible. In this context, Super-Kamiokande officially released four analyses this year, $n \to \bar{\nu}K^0$, $p \to \bar{\nu}\pi^+$, $p \to \mu^+X$, and $ppp \to e^+\pi^+\pi^+$, which will be briefly reviewed in this article.

In the first three analyses, we try to select the target nucleon decay signals from the data while rejecting the background events, mostly the atmospheric neutrinos, as much as possible, by making use of the features of events that the Super-Kamiokande detector provides for this discrimination. These features include the momenta of charged particles, which are roughly proportional to the amount of Cherenkov light. The total momentum or the total invariant mass is also a powerful variable because the signals are decays of protons (938.3 MeV/c^2) or neutrons (939.5 MeV/c^2) almost at rest while the backgrounds are caused by neutrinos flying from the outside of the detector and giving momenta to the events[2]. In addition, the detector can indicate the particle identification, the existence of electrons from decaying muons or pions, and the existence of neutrons kicked out of the nuclei. In the $ppp \to e^+\pi^+\pi^+$ analysis, a machine learning technique is employed, and the signal-background separation is automatically conducted.

Search for $n \to \bar{\nu}K^0$ decay

Supersymmetric GUTs predict proton decay $p \to \bar{\nu}K^+$ and neutron decay $n \to \bar{\nu}K^0$ as dominant decay modes [3, 4, 5]. This proton decay mode is considered an important mode and has been searched for extensively. Whereas a search for this neutron decay mode has been conducted by using 92 kton·years of data from SK-I [6], corresponding to 22% of the pure water SK data available today. This year, the analysis has been updated with an improvement in the pion momentum reconstruction, as well as utilizing 401 kton·years of the pure water SK data. Moreover, the signal extraction method has been improved by employing a spectral fitting instead of just applying a cut-based analysis, which was used in the previous research. The analysis defines two signal selection categories targeting signals involving $K^0 \to 2\pi^0$ and $K^0 \to \pi^+\pi^-$ decays, respectively. Fig. 17 shows comparisons of the data and simulated spectra of the reconstructed K^0 mass, with which the spectral fitting was performed. The figure shows no significant excess over the prediction of atmospheric neutrino events. Therefore, the lower limit on the partial lifetime for the $n \to \bar{\nu}K^0$ decay is set as 7.8×10^{32} years. This result improves the limit by a factor of 6 from the previous research by SK.

[*2] Since these three signals involve invisible particles such as a neutrino and an X particle, the total invariant mass and momentum are not directly used. However, this underlying difference between the signals and the backgrounds affects how they are seen in the detector.

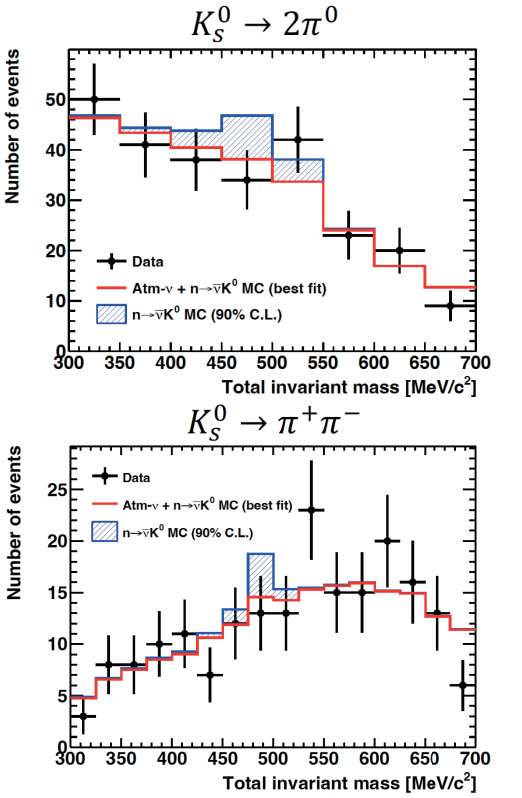


Fig. 17. Post-fit reconstructed K^0 invariant mass distributions for the $K^0 \to 2\pi^0$ (top) and $K^0 \to \pi^+\pi^-$ (bottom) selections. The black points, the red histogram, and the blue hatched histogram show the data, the best-fit background predictions, and the signal distributions allowed at a 90% confidence level. The data from SK-I to SK-V are combined.

Search for $p \to \bar{\nu}\pi^+$ decay

As mentioned in the previous paragraph, SUSY GUTs often predict the nucleon decays involving a kaon such as $p \to \bar{\nu}K^+$ and $n \to \bar{\nu}K^0$. However, depending on the top-quark-related elements of the Cabbibo-Kabayashi-Maskawa matrix, this decay mode can be suppressed due to the destructive interference between the transitions involving the supersymmetric partners of the top and charm quarks [3, 4]. In such cases, neutron decay modes involving a pion can become dominant. The $p \to \bar{\nu}\pi^+$ decay has been searched for using all the pure water SK data, following the $n \to \bar{\nu}\pi^0$ analysis officialized last year. The analysis increases the effective detector volume by adding events 1-2 meters away from the inner detector wall to the conventional detector region, which extends the exposure to 484.9 kton·years. In addition to increasing the amount of data, various improvements in the analysis method are employed, as well as revising the simulation of the pions traveling in the nuclei after the neutron decay. Separate analysis categories are defined for events with zero or one tagged Michel electron. The distributions of the simulation and the data after applying the event selections are shown in Fig. 18, and they suggest a good agreement between the data and the background prediction. The signal is tested by fitting the momentum spectrum in this figure, constraining the large contribution from the background events at the same time. The obtained lower limit on the lifetime is 3.9×10^{32} years at 90% confidence level, which is comparable with the previous search at SK [7]. The limit was not much improved because of the reduced survival probability of the pions inside oxygen nuclei in the revised simulation.

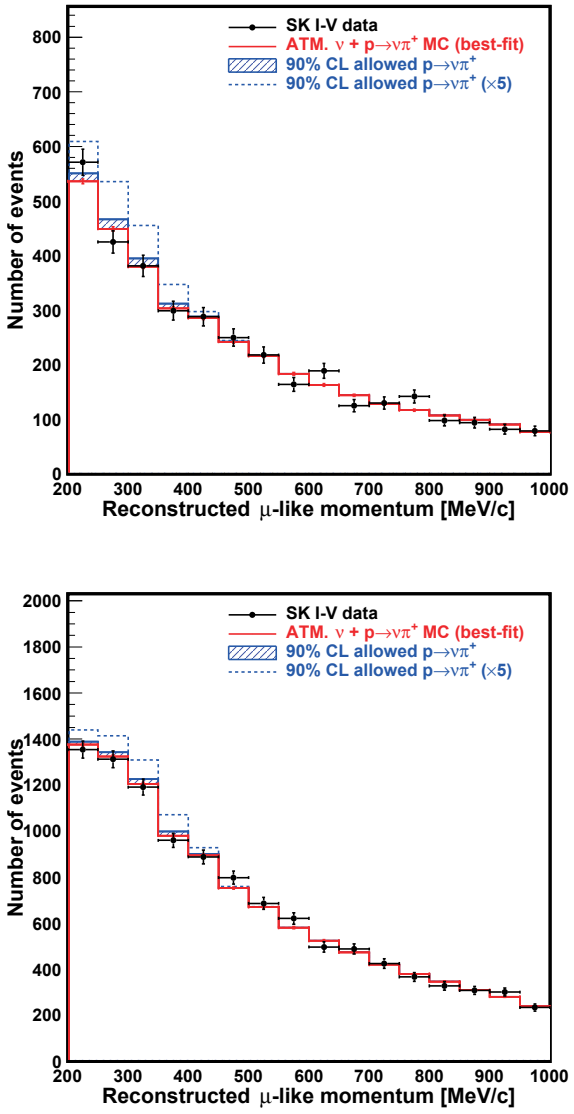


Fig. 18. Post-fit reconstructed π^+ (μ-like) momentum distributions in the analysis categories with 0 (top) or 1 (bottom) Michel electron. The data from SK-I to SK-V are combined. The black points, the red histogram, and the blue hatched histogram show the data, the best-fit background prediction, and the signal prediction at its lifetime limit (90% C.L.), respectively. The blue dashed curve shows the same allowed signal spectra with a scale factor of 5.

Search for $p \to \mu^+ X$ decay

The single muon events are studied to search for the $p \to \mu^+ X$ decay, where X is a massless, invisible particle. In this year, the analysis was extended to include the entire pure water SK periods, which corresponds to 401.1 kton·year. After applying all the event selection cuts, we searched for a bump in the single muon momentum spectra as shown in Fig. 19. The data is fairly consistent with the background-only distri-

butions. Similar to the $p \to \bar{\nu}\pi^+$ analysis, a spectral fitting was applied to test the signal. This results in a lower limit on the partial lifetime of 6.1×10^{33} years at 90% confidence level. The performance of the search is much improved from the previous research [8] mainly due to the increased amount of data.

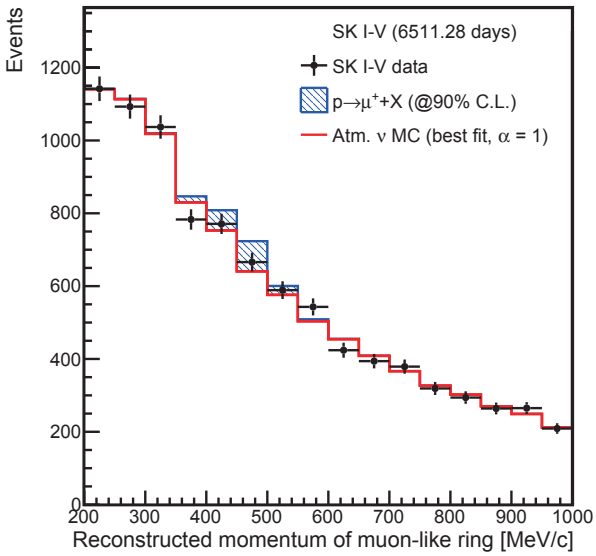


Fig. 19. Post-fit data MC distribution in the $p \to \mu^+ X$ analysis after all the selections are applied. The data from SK-I to SK-V are included. The red histogram and the black points show the simulated atmospheric neutrino background and the data, respectively. The blue histogram shows the signal contribution at its lower lifetime limit in addition to the background.

Search for $ppp \to e^+\pi^+\pi^+$ decay

A search for triproton decay is motivated by a new physics scenario different from conventional Grand Unified Theories. The energy scale where the quantum gravitational effects become significant is lowered from the Planck scale, $M_{\rm Pl} \sim 10^{19}$ GeV, to a few TeV due to possible large extra dimensions [9]. This low-scale BSM will induce baryon-number and lepton-number-violating processes, such as proton decay, at a rate ruled out by experiments. However, the authors of the theoretical paper argue that a Z_6 discrete symmetry in the SM with the small neutrino masses suppresses processes violating the baryon number by one and two. The Z_6 symmetry allows $\Delta B = 3$ processes, making trinucleon decays dominant processes.

In the analysis, a technique based on a convolutional neural network (CNN) is employed for the first time in nucleon decay searches in SK. This method directly takes the hit information from the detector, interpreting it as an image. The CNN is trained to separate signal events from the atmospheric neutrino backgrounds by using simulated events for those processes. A cut value for the CNN output score is optimized by maximizing a figure of merit computed with the simulated event samples, and we obtained 6.12 for this cut value. The analysis performance is improved with a 2.5 times better signal detection efficiency and a halved background rate compared with a reference analysis based on the conventional Cherenkov ring fitting.

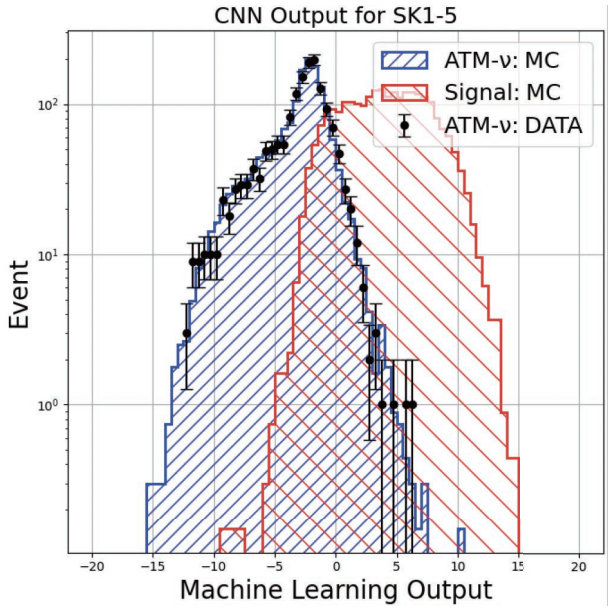


Fig. 20. CNN output distribution optimized for the $ppp \to e^+\pi^+\pi^+$ analysis, where larger values indicate that the events are more like a signal. The data from SK-I to SK-V are included. The black points, the blue and red histograms show the data, the background, and signal prediction, respectively. The cut value is 6.12, and only one data event remains after this cut.

Summary and prospects

The obtained limits on the lifetime for the four decay modes discussed above are summarized in Tab. 3 as well as their lower limit on the lifetime. In addition to these searches, other studies are ongoing targeting various nucleon decay modes. These studies include $n \to \bar{\nu}\eta^0$, $n \to e^- K^+$, $pp \to e^+\tau^+$, $n \to \ell^+\ell^-\bar{\nu}$, and $p \to e^+\pi^+\pi^-$. They are all aiming to finalize within a few years.

The current analysis efforts concentrate on the pure water, i.e. pre-gadolinium loading, phases. Enhanced analyses that make use of neutrons captured on the gadolinium are unseen yet, and these are anticipated in the future.

Bibliography

[1] A. Takenaka *et al.*, Super-Kamiokande Collaboration, Phys. Rev. D **102**, 112011 (2020)

[2] U. Amaldi *et al.*, Phys. Lett. B **260** 447, (1991)

[3] J. Hisano, *et al.*, Nucl. Phys. B **402** (1993) 46

[4] H. S. Goh, *et al.*, Phys. Lett. B **587** (2004) 105

[5] S. Antusch, *et al.*, J. High Energy Phys. **06** 022 (2022)

[6] K. Kobayashi, *et al.*, Super-Kamiokande Collaboration, Phys. Rev. D **72**, 052007 (2005)

[7] K. Abe, *et al.*, Super-Kamiokande Collaboration, Phys. Rev. Lett. **113** 121802 (2014)

Table 3. Summary of the lifetime limit obtained by the nucleon decay searches at Super-Kamiokande in 2024-2025. The $\times$ mark for the $ppp \to e^+\pi^+\pi^+$ analysis is because the limit is not computed for this decay.

Decay mode	Method	Lifetime limit (90% C.L.)
$n \to \bar{\nu}K^0$	Spectral fitting	$> 7.8 \times 10^{32}$ yrs
$p \to \bar{\nu}\pi^+$	Spectral fitting	$> 3.9 \times 10^{32}$ yrs
$p \to \mu^+X$	Spectral fitting	$> 6.1 \times 10^{33}$ yrs
$ppp \to e^+\pi^+\pi^+$	CNN	$\times$



Fig. 21. In the LAB-E cavern, the 200-ton tank (a) with currently 240 photo-multipliers installed, the Gd pre-mixing and pre-treatment 15-ton tank (b), the selective filtration system (d), Gd removal resins (c) for test, and a device to measure the water transparency (e) have been installed.

[8] V. Takhistov, *et al.*, Super-Kamiokande Collaboration, Phys. Rev. Lett. **115** 121803 (2015)

[9] K. S. Babu, *et al.*, Phys. Lett. B **570** (2003) 32-38

EGADS: From R&D for the gadolinium project to standalone Supernova monitor

As mentioned above, although at SK a few SRN events a year are expected, SRNs have not been detected yet because of the large backgrounds that constrain our search. The observation of SRNs in general or neutrinos from distant supernovae in particular would give us some information about the universe, for example, the core collapse rate from SRNs, and about the neutrino itself, too, for example, its lifetime. The main signal from SRN is expected to be the inverse beta decay reaction ($\bar{\nu}_e + p \to e^+ + n$), in which a positron and a neutron are produced; the delayed coincidence between the positron interaction and the neutron capture should allow for reducing the background affecting this analysis.

Before Gd loading in 2020, the SK detector had a poor neutron detection efficiency. It was then proposed to add 0.2% of gadolinium (Gd) sulfate by mass into SK in order to achieve a high neutron detection efficiency. Since Gd has a neutron capture cross section of 49.000 barns (about 5 orders of magnitude larger than that of protons) and emits a gamma cascade of 8 MeV, neutrons could be easily detected at SK (in space, vertices within tens of cm, and in time, with the neutron capture delayed about 30 μsec).

EGADS (Evaluating Gadolinium's Action on Detector Systems) project was funded in 2009. The main motivation of EGADS was to show that by adding Gd, SK will be able to detect anti-neutrinos using the delayed coincidence technique, while keeping all its capabilities in the other analyses, like solar and atmospheric neutrinos. Since then, a new hall near the SK detector has been excavated and a 200-ton tank with its ancillary equipment has been installed, see Fig.21, to mimic the conditions at SK. The selective water filtration system filters out water impurities while keeping the Gd in the water.

EGADS has been renamed as Employing Gadolinium to Autonomously Detect Supernovas after the installation of the new QBee electronics in 2017, following the Super-Kamiokande collaboration approval of the SK Gd loading.

Water system operations

From January 2010 to July 2011, we circulated pure water through the 200-ton tank and proved that our water system is stable and achieves a high water quality. In 2013, from February 6th to April 20th, the 200-ton tank was step-wise loaded with Gd sulfate until the final 0.2% concentration was reached. Two values are monitored at three different depths: the Cerenkov light left after travelling 15 m (LL15) in water and the Gd concentration. Both values confirmed that we can achieve and maintain a good water quality and that Gd sulfate homogeneously and quickly dissolves in the 200-ton tank.

In summer 2013, we installed 240 photo-multipliers, and the data taking started from September without Gd and with a DAQ based on old SK ATM modules. In April 2015, the target concentration of 0.2% $Gd_2(SO_4)_3$ was achieved. Figure 22 shows the time variation of LL15. The blue band in the figure shows typical values for SK-III and SK-IV. As shown in the figure, the transparency of 0.2% $Gd_2(SO_4)_3$ water is within the SK range. In addition to the good water transparency, no Gd loss has been detected since the EGADS detector reached the final concentration until it was emptied again after about 2 years and 5 months, in October 2017.

Detailed studies have evaluated the impact on current analyses at SK. These studies show that current analyses will be basically unharmed after adding Gd in SK, and all other tests and studies conducted have shown no showstoppers. As a consequence, the SK collaboration decided in spring 2015 to approve the SuperK-Gd project. The results of these analyses were published in [1].

In order to test the Gd-loading in SK, the detector was refilled with pure water in November 2017, and loaded with 0.02% $Gd_2(SO_4)_3$ at the end of March 2018. This loading was performed using only the pre-treatment and the fast recirculation systems, with one pass, similar to what is expected for SK 0.02% loading.

Since then, different configurations of the water system

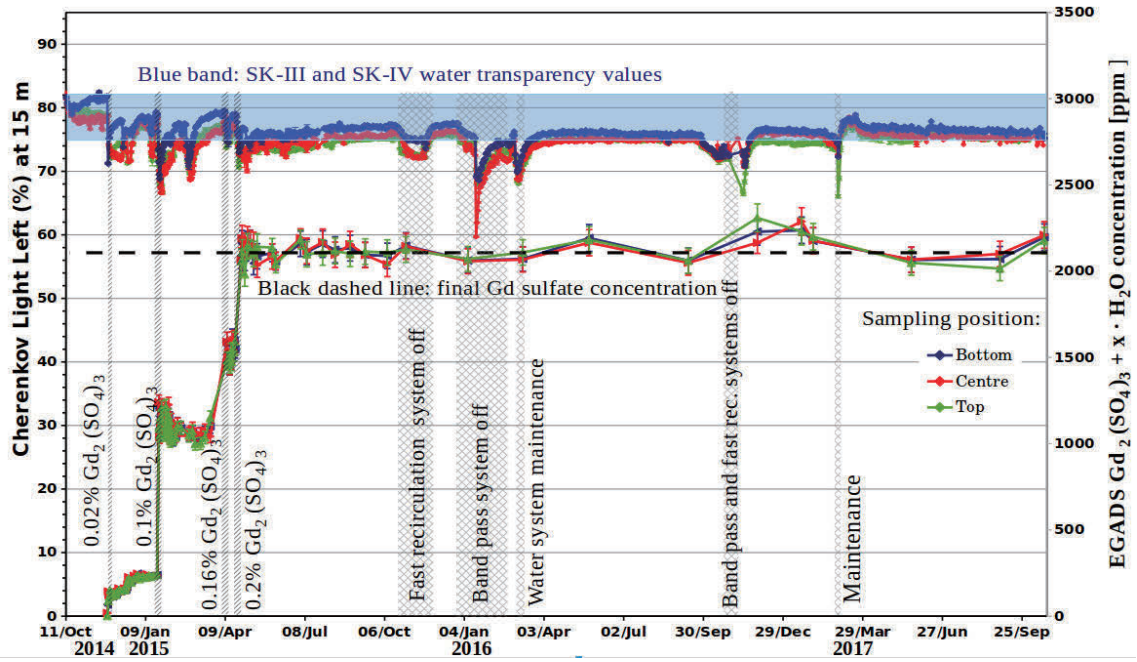


Fig. 22. Cerenkov light left at 15 m for Gd-loaded water in EGADS until September 2017. The horizontal blue band is the typical values for SK-III and SK-IV. The vertical lines show the injection dates, where we also indicate the concentration (% in mass) in the 200-ton tank. The black dashed line shows the final expected concentration.

have been tested in order to determine what is needed to ensure high water transparency in SK without a band-pass system. Figure 23 shows the time variation of LL15 since this loading until May 2020. From March 2018 to June 2018, a slow but continuous decrease in the water transparency has been observed with the fast recirculation system only. From June 2018 to August 2018, the use of the band-pass system was allowed for the recovery of high water transparency. Thereafter, the fast recirculation system has only been used.

In May 2019, the water system was stopped for about one week due to electrical damage following a power cut. This led to a reduction in the water transparency. After restarting, the water transparency was recovered. In September 2019, the water flow was modified so that only half of the flow passes through the special cation exchange resin. The water transparency remained stable and high. Finally, in November 2020, in order to simulate the future additional Gd loading in Super-Kamiokande, EGADS was loaded from 0.01% to 0.03% Gd concentration.

Ion exchange resin tests

Impurities in the water Cerenkov detector's water can be removed using anion and cation resins as a standard method.

In case of Gd-loaded water, standard cation exchange resins are expected to also remove Gd. Hence, a special cation exchange resin has been developed and installed in EGADS, in addition to the usual anion exchange resin. The installation was done in January-February 2019 (in January, the new cation exchange resin was used alone, leading to a water transparency drop). As shown in Figure 23, we observed an improvement in the water transparency compared to that with only anion exchange resin. This increase was enhanced following the replacement of the TOC and UV lamps in March 2019, which stresses the importance of the ionization lamps for the water transparency.

Cation and anion exchange resins are commercial products that can be discontinued by their manufacturers. When this happens, in order to find and test new resins for Super-Kamiokande, we are using EGADS to demonstrate the performance of replacement candidates.

In 2021, the AmberJet 4400 anion exchange resin was discontinued by its manufacturer. In May 2021, we tested AmberJet 4002, which allowed us to keep a high water transparency. The initial drops following the installation of this new resin were due to a too-short resin flushing period.

In 2022, the AmberJet 1020 (Gd) special cation resin was discontinued by its manufacturer. A substitute candidate, Amberlite IR120B (Gd), was installed in the water system in December 2021. Data after one and a half years showed acceptable results, though not as good as the AmberJet 1020 (Gd).

In 2023, Amberlite IR120B (Gd) will be discontinued by its manufacturer. In September 2023, we tested Amberlite HP1210 (Gd) in the EGADS water system, after two months of purge with purge water. Performances were equivalent to AmberJet 1020 (Gd).

DAQ operations

In June 2017, EGADS electronics were upgraded from the ATM electronics to SK's QBee electronics; the DAQ system was also upgraded to use these new electronics. Thanks to this upgrade, the stability of the DAQ has been greatly improved, especially at high rates. Several SN tests were performed, and demonstrated that EGADS is able to detect and process a 10-second-long burst of more than 100 kHz without trouble. This

is much more than what is expected from a very close galactic SN burst: in the case of Betelgeuse, about 25k events are expected according to Nakazato's model.

We developed an online fitter, HEIMDALL, based on SK WIT. It is able to reconstruct all the events online during a SN burst and then provides an alarm within a few seconds. HEIMDALL is looking for IBD candidates, therefore taking advantage of the delayed coincidence to reduce the background. Thanks to this, EGADS is able to look for SN in the far end of our galaxy. This enables us to instantly and autonomously detect a galactic SN and report to local experts and the neutrino and astronomy community.

Bibliography

[1] Marti, Ll. et al., NIM-A 959, 163549 (2020)

SK-Gd

In the SK-Gd project, the sensitivity of electron antineutrino identification has been improved significantly by detecting neutron signals due to the capture on gadolinium (Gd) (specifically, gadolinium sulfate octahydrate ($Gd_2(SO_4)_3 \cdot 8H_2O$)). The operation with 0.01% of Gd (about 13 tons in total weight of $Gd_2(SO_4)_3 \cdot 8H_2O$) has been completed. We achieved about 50% neutron capture fraction on Gd [1]. Current operation with 0.03% Gd continues, achieving 75% neutron capture fraction on Gd [2].

Diffuse supernova neutrino background search

Diffuse Supernova Neutrino Background (DSNB) is a cumulative neutrino radiation background emitted from past supernova explosions that have occurred since the early universe after the Big Bang. If we obtain information about DSNB, we could study the history of supernova explosions, such as when and how many supernova explosions have occurred in the universe. Many of the elements around us are believed to be created during nuclear fusion reactions in massive stars, during supernova explosions, or by mergers between neutron stars — high-density objects formed after supernova explosions. Therefore, understanding supernova explosions provides us with new insight into the synthesis of elements in the universe.

In 2023, we published our first DSNB result for the SK-Gd period with 552 days of SK-VI data [4]. The expected flux sensitivity obtained in this search is comparable to the world's most stringent sensitivity limit given by the pure-water phase SK data, which has five times the statistics [3].

In 2024, we developed a new method to identify the Gd neutron signal using a neural network, enabling the detection of DSNB signals while reducing background events more efficiently. The neural network was trained with 12 variables as input, including the number of PMT hits and the spatial spread of PMT hits. As shown in Figure 24, in addition to the capture by Gd, the capture by protons was efficiently identified, and the DSNB detection efficiency was 1.3 times higher than that of the previous method [4].

Furthermore, a significant reduction in the NCQE background event using the spatial hit spreading has been achieved. Under the new method, 80% of NCQE events were reduced while keeping DSNB signal events.

Adding the 404 days of SK-VII data, we update the DSNB search result. Figure 25 shows the energy spectrum of the final events using 552 days of SK-VI and 404 days of SK-VII. The p-value of the background-only hypothesis is lowered to 0.04 for the most significant energy bin. From the result that there is no significant excess over the background expectation, we placed observed upper limit and sensitivity with 90% confidence level for each energy bin, as shown in Figure 26. There are some updates to the stringent upper limit and sensitivity depending on the energy.

Bibliography

[1] K. Abe et al., Nucl. Instrum. Meth. A, 1027, 166248 (2022)

[2] K. Abe et al., Nucl. Instrum. Meth. A, 1065, 169480 (2024)

[3] K. Abe et al., Phys. Rev. D **104**, 122002 (2021)

[4] M. Harada et al., The Astrophysical Journal Letters, 951,L27 (2023)

T2K EXPERIMENT

[Spokesperson : Ken Sakashita]
KEK

The Tokai to Kamioka (T2K) experiment [1] is a long baseline neutrino oscillation experiment: a man-made beam of neutrinos is used to do precise studies of the oscillations of neutrinos. Accelerated protons are used to produce the neutrinos in the J-PARC center in the Ibaraki prefecture, which then travel 295 km to reach the Super-Kamiokande (Super-K) detector in the Gifu prefecture, where they can be detected after oscillations. A complex of near detectors located 280 meters away from the proton target is used to monitor the neutrino beam and constrain systematic uncertainties on the neutrino fluxes and interactions. T2K was the first long-baseline experiment to use the off-axis beam technique [2]: the beam is not aimed directly at Super-K, but in a direction making a 2.5° angle with the far detector direction. This gives increased sensitivity to neutrino oscillations while reducing the backgrounds by producing a narrow band neutrino beam centered on the energy corresponding to the first maximum of the $\nu_\mu \to \nu_e$ oscillation probability.

T2K realized the first observation of the appearance of a flavor of neutrinos through oscillation by detecting electron neutrinos in a beam of neutrinos produced in the muon flavor [3]. After achieving this milestone, the experiment has been using its ability to produce a beam of either neutrinos or antineutrinos to compare the oscillations of neutrinos and their antiparticles. This allows us to study the main remaining open questions in neutrino oscillations (CP symmetry and ordering of the neutrino mass states) by looking at the differences between the oscillations $\nu_\mu \to \nu_e$ and $\bar{\nu}_\mu \to \bar{\nu}_e$. At

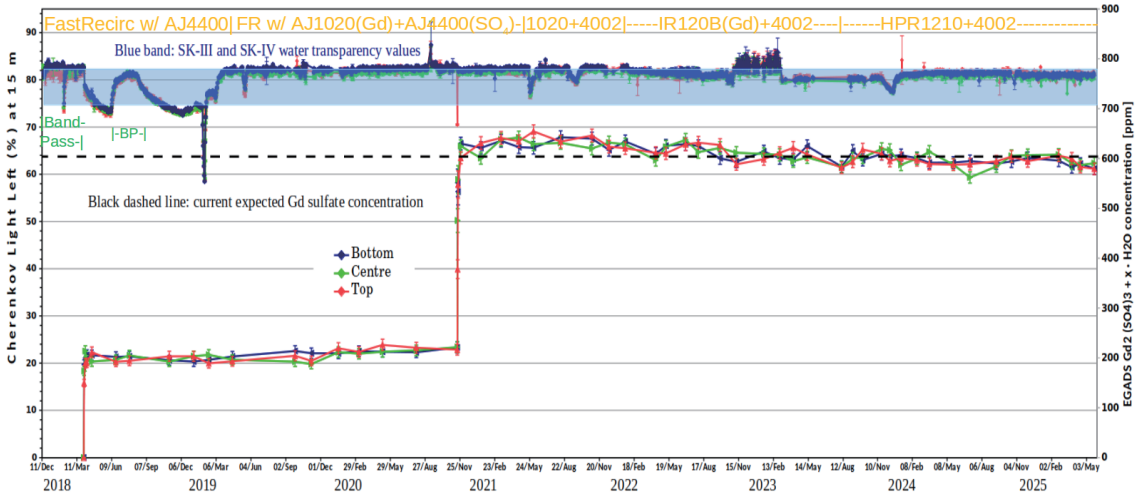


Fig. 23. Cerenkov light left at 15 m for Gd-loaded water in EGADS since December 2018. The horizontal blue band is the typical values for SK-III and SK-IV. The vertical lines show the injection dates, where we also indicate the concentration (% in mass) in the 200-ton tank. The black dashed line shows the final expected concentration.

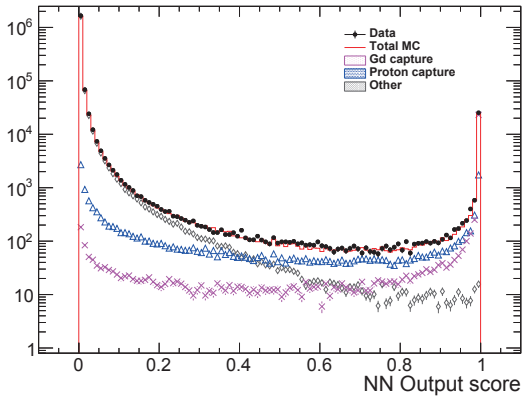


Fig. 24. Selection of neutron capture events by energy cut for the calibration data and its MC simulation with Am/Be neutron source

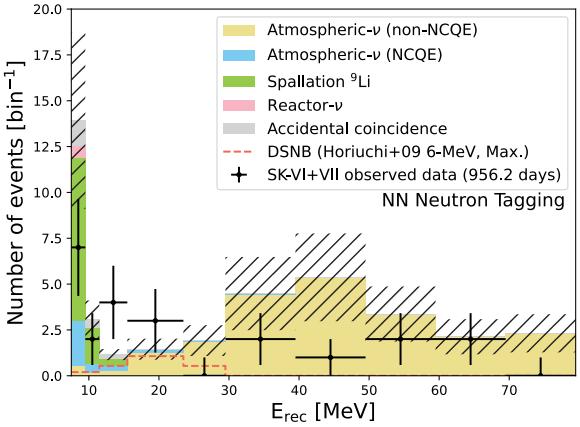


Fig. 25. Selection of neutron capture events by energy cut for the calibration data and its MC simulation with Am/Be neutron source

the same time, T2K's physics goals include the precise measurement of the neutrino oscillation parameters θ_{23} and Δm^2_{32} through a precise study of the pattern of the disappearance of the muon neutrinos in conjunction with the data used to study the oscillation to the electron flavor. The experiment additionally performs searches for physics beyond the standard model, such as oscillations due to sterile neutrinos and CPT violation. Finally, the near detectors are used to perform a wide range of neutrino and anti-neutrino cross-section measurements.

In J-PARC, protons are accelerated to 30 GeV by a series of three accelerators and hit a 1.9 interaction-length graphite target. The collisions produce hadrons, in particular charged pions and kaons, which are focused by three electromagnetic horns. The hadrons then go through a 96 m-long decay tunnel where they decay in flight into neutrinos. A beam dump at the end of the decay tunnel stops the remaining hadrons, while high-energy muons (5 GeV/c or higher) can pass through this beam dump and are measured to provide a first, indirect monitoring of the neutrino beam. The horns can be used either with a positive current (ν-mode), in which case the beam is mainly made of ν_μ, or with a negative current ($\bar{\nu}$-mode), which gives a mainly $\bar{\nu}_\mu$ beam.

The near detectors are separated into two groups. On the axis of the beam, the INGRID detector, made of fourteen identical modules, is used to monitor the beam direction and rate stabilities. Each module is made of a succession of iron plates to provide a large target mass (7.1 tons per module) alternating with scintillator planes for detection. Using the number of events reconstructed in each module, the beam direction can be measured daily with better than 0.4 mrad accuracy. Located in the direction of Super-K, the off-axis detector ND280 is made of several detectors located inside a 0.2T magnet. An upgrade of the off-axis near detectors was conducted and completed in May 2024. A set of new detectors has been installed to replace the π^0 detector in the upstream part of the ND280 detector complex. The new detectors will bring improved ability to study neutrino interactions, with a larger efficiency for high-angle events, a lower threshold to detect protons, and the ability to reconstruct neutron energy. The higher precision

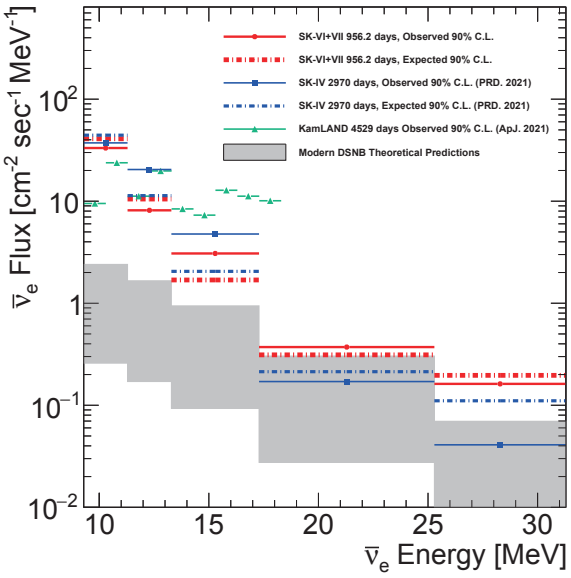


Fig. 26. Sensitivity of the DSNB flux of SK-VI and SK-VII (red dot–dashed line) and the upper limit obtained (red solid line)

of those off-axis detectors allows to do more detailed measurements of the unoscillated neutrino beam. In neutrino oscillation analyses, the ND280 is used to provide information on the ν_μ and $\bar{\nu}_\mu$ unoscillated spectra directed at SK, constrain the dominant backgrounds, and constrain the combination of flux and interaction cross sections.

The far detector, Super-K, is a 50 kton water Cherenkov detector, shielded from atmospheric muons by 1000 m of rock, or 2700 meters-water-equivalent (m.w.e.) mean overburden. To select events corresponding to the T2K beam, Super-K is synchronized via GPS to the J-PARC beamline. Hit information within $\pm 500 \mu s$ from the beam arrival timing is used for T2K data analysis. Events are reconstructed by detecting Cherenkov rings from charged particles produced by neutrino interactions. These events are separated into muon-like and electron-like events based on the light pattern of the most energetic ring, and additional selection cuts are applied to produce samples enriched in certain interaction modes. In 2020, Gadolinium was dissolved into the Super-Kamiokande detector at 0.01%, and the new phase of Super-K, SK-Gd, was started [4]. Additional gadolinium was loaded to Super-K in 2022, and the detector is currently operational with 0.03% gadolinium concentration. Additions of gadolinium significantly increased neutron detection capability, which will benefit T2K's neutrino interaction and oscillation measurements as well.

To study neutrino oscillations, the data recorded at the far detector are compared to the predictions of the three-flavor oscillation model for different values of the oscillation parameters. To this end, a model of the experiment is constructed: the fluxes of the different flavors of neutrinos reaching the detectors are predicted by a series of simulations, and the interactions of ν and $\bar{\nu}$ in the detectors are simulated using the NEUT Monte Carlo event generator [5]. First, the flux and properties of the proton beam reaching the target are measured by the proton beam line monitors. Interactions of the protons in the graphite target and production of secondary hadrons are then simulated using the FLUKA package [6]. Measurements from hadron production experiments, in particular NA61/SHINE [7], are used to tune this part of the simulation and the out-of-target interactions. The propagation and decay-in-flight of the hadrons in the decay tunnel are then simulated using the GEANT3 and GCALOR [8] packages. The predictions from this model are compared to the neutrino events observed in the near detectors to tune the predictions for the far detector by constraining the model parameters. The result of this near detector fit provides the initial values and uncertainties of the flux and interaction model parameters used in the far detector analysis to measure parameters describing neutrino oscillations.

T2K started collecting physics data in January 2010. Data up to run 10 were taken during the pure-water phase of the Super-K detector. Run 11 corresponds to the first data-taking period with gadolinium dissolved in Super-K water at 0.01% Gd concentration. The first large amount of data was taken after the accelerator upgrade happened in run 13, which started in November 2023 and ended in June 2024. In December 2023, stable operation was achieved with a record beam power of 760 kW, reaching for the first time the 750 kW design power of the facility. In parallel, the upgraded near detectors were partially installed in October 2023, and neutrino data were collected from run 13. In run 14, the first $\bar{\nu}$-mode after the accelerator upgrade was conducted, and the beam record was further increased to 800 kW. The installation of the remaining components of the upgraded near detectors was completed in May 2024, and data taking with the full upgraded near detectors was achieved in June 2024 (Fig. 27).

The details of the data that have been collected at the far detector can be found in Table 4. Over the whole period, the event rates and the beam directions were found to be consistent with the expectations and stable by the measurements of the muon monitor and the on-axis near detector. In particular, the beam direction remained stable well within the $\pm$1mrad target.

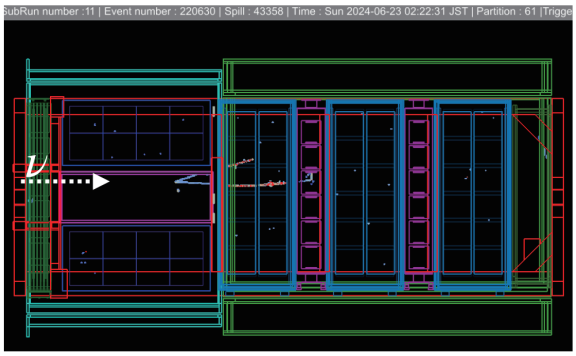


Fig. 27. An event display of the fully upgraded off-axis near detector, with a neutrino interaction candidate in the newly installed "Super-FGD", and a track is entering the original ND280 detectors. From [9].

Table 4. T2K data taking periods and integrated numbers of protons on target (POT) that can be used in the far detector analysis.

Run Period	Dates	$\times 10^{20}$ POT ν	$\overline{\nu}$
Run 1	Jan.2010 - Jun.2010	0.32	–
Run 2	Nov.2010 - Mar.2011	1.11	–
Run 3	Mar.2012 - Jun.2012	1.60	–
Run 4	Oct.2012 - May.2013	3.60	–
Run 5	May.2014 - Jun.2014	0.24	0.51
Run 6	Oct.2014 - Jun.2015	0.19	3.55
Run 7	Feb.2016 - May.2016	0.48	3.50
Run 8	Oct.2016 - Apr.2017	7.17	–
Run 9	Oct.2017 - May.2018	0.20	8.79
Run 10	Oct.2019 - Feb.2020	4.73	–
Run 11	Mar.2021 - Apr.2021	1.76	–
Run 12	Apr.2023 - Apr.2023	0.09	–
Run 13	Nov.2023 - Jun.2024	5.03	–
Run 14	Nov.2024 - Mar.2025	1.46	1.21
Total	**Jan.2010 - Mar.2025**	**28.02**	**17.56**

First joint oscillation analysis of Super-Kamiokande atmospheric and T2K accelerator neutrino data

T2K reported its first joint oscillation analysis of Super-Kamiokande atmospheric and T2K accelerator neutrino data [10]. The motivation for this joint approach lies in the complementary strengths of the two datasets, which have different neutrino energies and baselines. Atmospheric neutrinos, produced by cosmic ray interactions in the atmosphere, span a broad range of neutrino energies and baselines. They provide relatively weak constraints on $|\Delta m^2_{32}|$ and $\sin^2(2\theta_{23})$, but upward-going neutrinos undergo strong matter effects, offering unique sensitivity to the neutrino mass ordering. In contrast, T2K accelerator neutrinos have a fixed baseline of 295 km and a narrow neutrino energy spectrum peaked around 600 MeV. This enables precise measurements of muon neutrino disappearance, which in turn provides strong constraints on $|\Delta m^2_{32}|$ and $\sin^2(2\theta_{23})$. T2K data also provide some sensitivity to δ_{CP} and mass ordering; however, these effects are strongly degenerate and difficult to disentangle using accelerator data alone. The joint analysis addresses this degeneracy by utilizing the complementary sensitivities of these two datasets. Furthermore, both datasets benefit from common constraints from the T2K near detectors, which help to reduce systematic uncertainties related to neutrino interactions.

The analysis builds on previous studies from the two experiments [11, 12], with several modifications introduced to enable a coherent joint analysis. Neutrino oscillation parameters are measured by comparing the predicted and observed event rates and energy spectra for both atmospheric and accelerator neutrinos at SK. This analysis framework integrates common elements of the two experimental analyses where applicable, while preserving the individual methodologies where necessary. The neutrino flux models used in the two experiments are mostly independent, except for shared systematic uncertainties from hadron production in proton collisions. The SK atmospheric flux model is constrained using atmospheric muon measurements [13, 14], while the T2K flux model uses the NA61/SHINE experiment [15]. Correlated impacts of shared uncertainties on both data samples were evaluated. Event selection at SK follows the same criteria as in Refs. [12, 16] with one modification: an additional selection to remove neutron contamination from the Michel electron candidates. This is applied to both SK and T2K samples. Neutrino interactions are simulated with the NEUT generator v5.4.0 [5]. Due to the similarities in the neutrino energy spectra and event selections, T2K and low-energy atmospheric events are described using a common interaction and uncertainty model [11]. However, due to limited phase space overlap between the T2K near detectors and non-sub-GeV atmospheric samples, the T2K near detectors are used only to constrain the low-energy model and the correlated components of the high-energy model. Newly added uncertainties and other parts of the high-energy model are excluded from the near detector constraint. Detector-related uncertainties are estimated from comparisons between atmospheric data and simulations. By evaluating the impacts of detector parameters on event rates in both the SK and T2K samples simultaneously, correlated uncertainties are constructed.

The atmospheric neutrino dataset used in this study is slightly expanded from Ref. [12], including the full Super-Kamiokande IV period (2008–2018), for a total live time of 3224.4 days. The T2K dataset is identical to that used in Ref. [11], covering up to run 10. It corresponds to 19.7×10^{20} and 16.3×10^{20} POT in neutrino and antineutrino modes, respectively.

The oscillation analysis is performed using Bayesian and frequentist approaches. In the Bayesian analysis, the data favor the normal ordering and show a slight preference for the upper octant of θ_{23}. SK and T2K data prefer different octants, while both favor similar values of the *CP*-violation phase, as shown in Fig. 28. Figure 29 shows the exclusion of *CP*-conserving values of the Jarlskog invariant [17, 18, 19], defined as $J_{CP} = \sin\theta_{13}\cos^2\theta_{13}\sin\theta_{12}\cos\theta_{12}\sin\theta_{23}\cos\theta_{23}\sin\delta_{CP}$. The largest credible interval from this Bayesian analysis that excludes CP-conserving values is summarized in Table 5. The significance of this exclusion is affected by robustness studies using simulated datasets [11] generated with alternative models and fit using the nominal model. This result highlights a potential weakness in the uncertainty model of the nominal model.

Table 5. Largest credible interval from the Bayesian analyses not containing different CP-conserving values of J_{CP} and δ_{CP}. Values in parentheses indicate how these could change due to possible biases seen in robustness studies.

Value tested	Prior uniform in δ_{cp}	Prior uniform in $\sin(\delta_{CP})$
$J_{CP} = 0$	2.3σ (2.2σ)	2.0σ (1.9σ)
$\delta_{CP} = 0$	2.6σ (2.5σ)	2.3σ (2.2σ)
$\delta_{CP} = \pi$	2.1σ (1.9σ)	1.6σ (1.4σ)

The significance of *CP*-violation and the mass ordering is evaluated using the frequentist analysis based on ensembles of pseudoexperiments. The test statistic for *CP* conservation

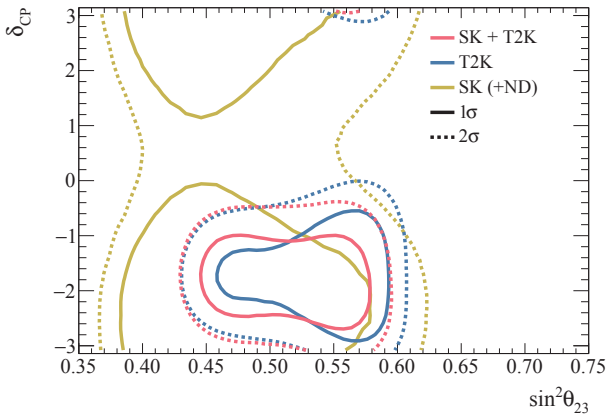


Fig. 28. The $(\sin^2(\theta_{23}, \delta_{CP})$ credible regions obtained with the SK, T2K, and combined datasets. The neutrino mass ordering is marginalized over, and a prior uniform in δ_{CP} is used.

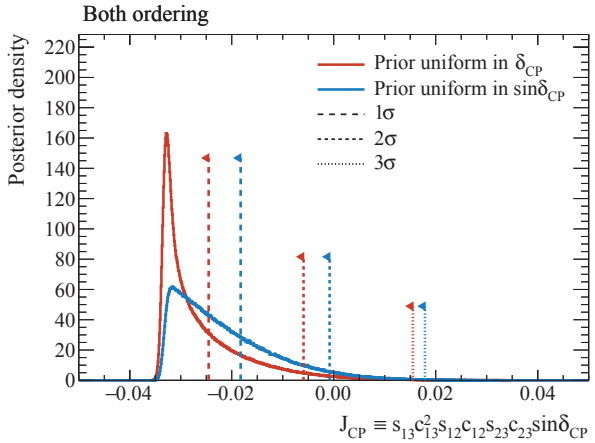


Fig. 29. Posterior density for the Jarlskog invariant with credible intervals overlaid, marginalized over both neutrino mass orderings, and assuming a uniform prior in δ_{CP} or $\sin\delta_{CP}$.

is defined as the log-likelihood ratio between *CP* conservation hypotheses and those without any assumption. Similarly, the log-likelihood ratio between normal and inverted ordering is used for the neutrino mass ordering (Fig. 30). *CP* conservation is disfavored with a lower p value($p = 0.037$), which is slightly more significant than that obtained using T2K data alone ($p = 0.047$). The inverted ordering is disfavored with $p = 0.079$, while the normal ordering shows good agreement with the data ($p = 0.58$). The best-fit values and 68.3% confidence intervals obtained using the Feldman-Cousins method [20] are $\delta_{cp} = -1.76^{+0.73}_{-0.95}$, $\sin^2\theta_{23} = 0.468^{+0.106}_{-0.025}$, where MO was treated as a nuisance parameter, and Δm^2_{32} $(|\Delta m^2_{31}|) = 2.520^{+0.048}_{-0.058}$ $(2.480^{+0.052}_{-0.048}) \times 10^{-3}\,\mathrm{eV}^2$ for normal (inverted) ordering.

The SK and T2K datasets both prefer similar values of the *CP* phase and the normal mass ordering, leading to an enhanced preference in the combined analysis. As shown in Fig. 29, *CP*-conserving values of J_{CP} ($J_{CP} = 0$) are excluded at the 2σ level. However, this significance drops below 2σ when accounting for the potential weakness of the uncertainty model by robustness studies. The constraints from the T2K

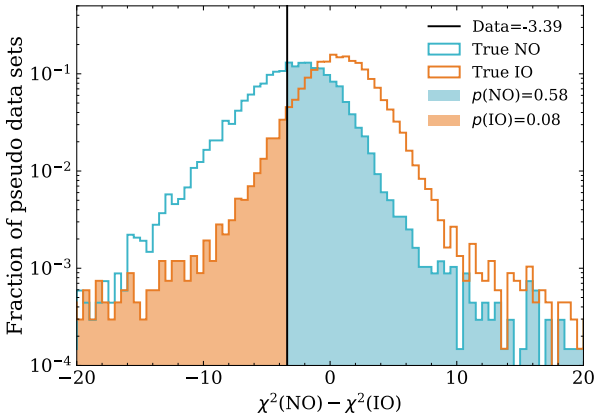


Fig. 30. Distribution of the neutrino mass ordering test statistic under true normal (NO) and inverted (IO) ordering hypotheses. The filled areas to the left (right) of the data result indicate the p values for the inverted (normal) hypotheses.

near detectors have a small impact on the measurement of δ_{CP} and the mass ordering. The dominant systematic uncertainties for δ_{CP} measurement arise from the atmospheric neutrino flux below 1 GeV, the $\sigma_{\nu_e}/\sigma_{\nu_\mu}$ cross section ratio, and the particle identification for single-ring events–none of which are well constrained by the near detectors. For the mass ordering, most of the sensitivity originates from high-energy atmospheric neutrinos, for which the near detectors are essentially insensitive. Thus, the improvement in mass ordering sensitivity in the joint analysis primarily results from the stronger constraint on $\sin\theta_{23}$ provided by the T2K data.

Bibliography

[1] K. Abe *et al.* (T2K Collaboration), Nucl. Instrum. Meth. A **659**, 106 (2011).

[2] D. Beavis, A. Carroll, I. Chiang, *et al.*, Long Baseline Neutrino Oscillation Experiment at the AGS (Proposal E889), 1995. Physics Design Report, BNL 52459.

[3] K. Abe *et al.* (T2K Collaboration), Phys. Rev. Lett. **112**, 061802 (2014).

[4] K. Abe *et al.* (Super-Kamiokande Collaboration), Nucl. Instrum. Meth. A **1027**, 166248 (2022).

[5] Y. Hayato, L. Pickering, Eur. Phys. J. Spec. Top. (2021)

[6] T. Bhlen *et al.*, Nucl. Data Sheets **120**, 211 (2014).

[7] N. Abgrall et al. (NA61/SHINE Collaboration), Eur. Phys. J. C **76**, 84 (2016).

[8] C. Zeitnitz and T. A. Gabriel, Proceedings of International Conference on Calorimetry in High Energy Physics (World Scientific, Corpus Christi, Texas, 1992), ISBN 9789810213039, pp. 394-404.

[9] C. Riccio, J-PARC PAC 39th Meeting (2025).

[10] K. Abe et al. (SuperKamiokande Collaboration and T2K Collaboration), Phys. Rev. Lett. **134**, 011801 (2025).

[11] K. Abe et al. (The T2K Collaboration), Eur. Phys. J. C **83**, 782 (2023).

[12] M. Jiang et al. (Super-Kamiokande Collaboration), Prog. Theor. Exp. Phys. 2019, 053F01 (2019).

[13] S. Haino et al., Phys. Lett. B 594, 35 (2004).

[14] K. Abe et al., Phys. Lett. B 564, 8 (2003).

[15] N. Abgrall et al. (The NA61/SHINE Collaboration), Eur. Phys. J. C **76**, 617 (2016).

[16] K. Abe et al. (The T2K Collaboration), Phys. Rev. D **103**, 112008 (2021)

[17] P. Krastev et al., Phys. Lett. B 205, 84 (1988).

[18] C. Jarlskog, Phys. Rev. Lett. 55, 1039 (1985).

[19] C. Jarlskog, Phys. Lett. B 609, 323 (2005).

[20] G. J. Feldman and R. D. Cousins, Phys. Rev. D 57, 3873 (1998)

XENON EXPERIMENT

XENON ICRR group
[Principal investigator : Shigetaka Moriyama]
Kamioka Observatory, ICRR, the University of Tokyo

Introduction

The XENONnT experiment [1] is the most sensitive direct dark matter search experiment conducted at LNGS in Italy. The XENON collaboration includes about 200 collaborators from 30 institutions in 12 countries. From Japan, the University of Tokyo (ICRR and Kavli IPMU), Nagoya University, and Kobe University have participated since 2017. The XENON group uses liquid xenon and employs a time projection chamber (TPC) shown in Fig. 31, characterized by its ability to discriminate between nuclear and electron recoil. The Japanese group is making a significant contribution toward the discovery of DM particles based on a purification technology for liquid xenon developed in XMASS and the neutron detection technology developed for Super-Kamiokande. The XENON collaboration completed XENONnT detector construction in 2020 and started data taking in 2021.

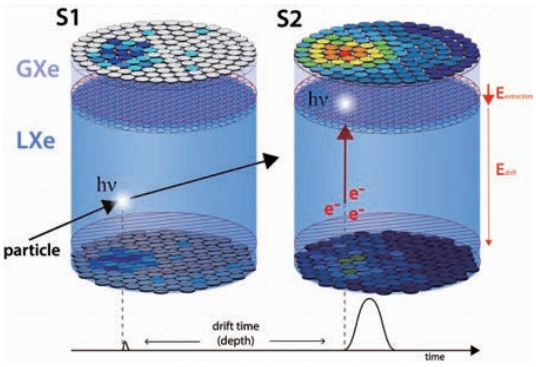


Fig. 31. Principle of operation of liquid xenon time projection chamber (TPC). The interaction of dark matter produces scintillation light S1, and electrons drifted by an electric field give a delayed signal S2; the observed pattern of S2 can identify the planar location of the interaction, and the time difference between S1 and S2 provides depth information. The ratio of S1 to S2 also holds information about the type of particle that caused the interaction. Figure from the XENON collaboration.

Neutron background tagging utilizing SK-Gd technology

Background reduction is critical in rare event searches. One of the most important backgrounds in XENONnT is neutrons emitted from instrument components. The Japanese group is contributing to the realization and operation of a neutron veto (NV) detector that tags these neutrons and reduces the background by event basis, using the gadolinium-doped water Cherenkov detector technology developed at Kamioka for Super-Kamiokande [3]. Figure 32 shows a full view of

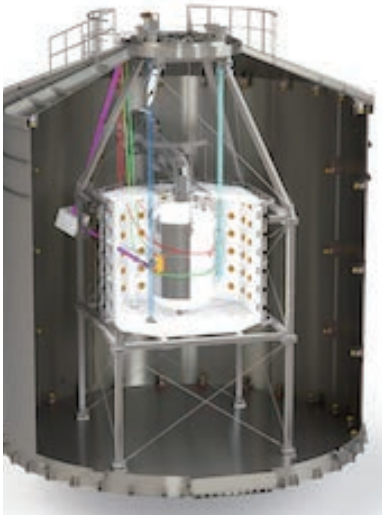


Fig. 32. Overview of the XENONnT detector. The white part is the neutron veto detector. The liquid xenon TPC is at the center, surrounded by the white reflective material, and 120 PMTs are used to detect the Cherenkov lights produced by gamma rays when neutrons are captured by gadolinium or other nuclei, and used to identify the neutrons. The water tank is 10 m in diameter and 10 m in height, and 0.2 % of gadolinium will be added to the entire system. Figure from the XENON collaboration.

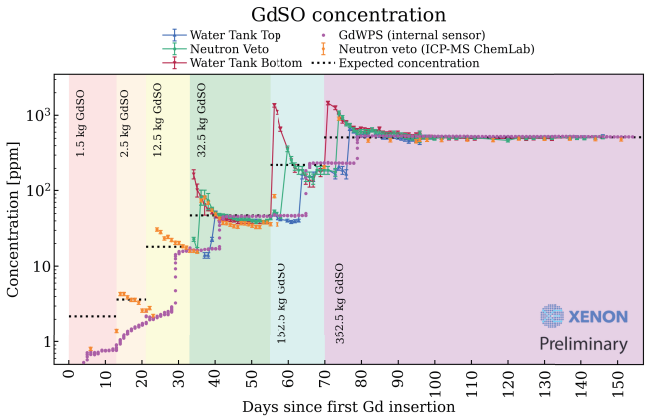


Fig. 33. Measured GdSO concentration during loading: Conductivity measurements of samples from water tank top (blue), inside NV region (green), bottom of water tank (red), conductivity measured at GdWPS (magenta), direct measurements via mass spectrometry (ICP-MS at LNGS chemistry lab, yellow).

the XENONnT detector, which is entirely housed in a water tank with a white reflective material optically isolating the NV immediately surrounding the liquid xenon TPC at its center. The NV is equipped with 120 PMTs. By adding 0.2% of Gd to the water in the whole tank, neutrons emitted from the detector components are expected to be captured by Gd with a high probability if they reach the NV after recoiling from xenon nuclei in the TPC. After capturing the neutron on Gd, we expect PMTs in the NV detector to observe Cherenkov light caused by gamma rays emitted from the Gd nucleus that captured the neutron. This enables us to tag neutrons that cause background for the WIMP search and thus maximize the experiment's sensitivity. XENONnT aims to tag approximately 87% of such neutron events that are otherwise indistinguishable from dark matter events. Preparation of about 3 tons of the purest grade of gadolinium sulfate octahydrate (GdSO) in Japan [4] and design of the Gd-Water Purification System (GdWPS) for our application were done with the help of the Super-Kamiokande collaboration.

In 2021, the installation of a GdWPS was completed, and in 2022, the plant was commissioned to optimize performance using pure water and Gd-loaded water. For the science run 0 (SR0) dataset collected from July 6, 2021, the NV operated with pure water, achieving 53% of the neutron tagging efficiency to reject neutron-originated background events. This meant that we could reduce the neutron background by a factor of two.

The first Gd loading at 10% of the target concentration

A 0.02% Gd loading into the water tank was performed for the commissioning of the GdWPS, for testing the procedure of GdSO insertion and dissolution, and for physics data acquisition with improved neutron tagging efficiency. The loading started in October 2023. In total, 352.5 kg of GdSO was loaded in 6 steps over a period of 80 days. Figure 33 shows the GdSO concentrations measured during the introduction period; the concentration of the Gd mass 0.2% corresponds to 500 ppm of GdSO. GdSO concentration in the system can be estimated with direct measurements of Gd via mass spectrometry (ICP-MS in the LNGS chemistry lab), conductivity of samples from WT, and conductivity measured by GdWPS inner sensor. The figure clearly shows the upward spread of the concentrated solution introduced at the bottom, as expected from the internal water flow within the tank.

The characteristics of the detector response to neutrons were evaluated using an AmBe neutron calibration source. As shown in Fig. 34, efficiency at 5 PE signal in NV is about 77% with 500 ppm of GdSO. This represents another factor of two reduction in the neutron background compared to pure water. Science Run 2 (SR2) data were collected with this improved NV performance, and the analysis is currently underway.

First Indication of Solar ^{8}B Neutrinos via Coherent Elastic Neutrrino-Nucleus Scattering with XENONnT [5]

Coherent elastic neutrino-nucleus scattering (CEνNS) is a Standard Model process with low momentum transfer, which allows neutrinos to scatter coherently with nuclei. This process has recently been observed using a pulsed spallation neutron source (SNS). The detection of CEνNS events from solar neutrinos is challenging due to the lower flux and energy, as well as the lack of timing information. Therefore, it requires minimal background and maximizing the sensitive region of interest with a low-energy threshold. Liquid xenon detectors searching for dark matter particles fulfill these requirements; solar ^{8}B neutrinos are expected to contribute the largest detectable number of coherent neutrino-xenon scattering events, albeit at low nuclear recoil (NR) energies. XENONnT experiment made the first detection of CEνNS induced by solar neutrinos ^{8}B. This is the first detection of elastic NRs from

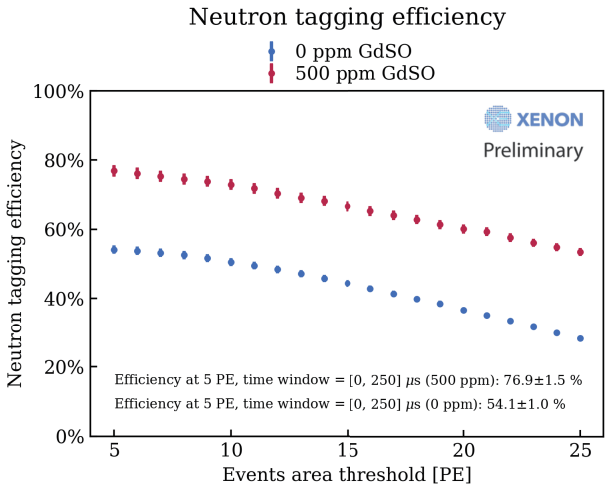


Fig. 34. Neutron tagging efficiency for 0.02% Gd (red, equivalent to 500 ppm GdSO) and pure water (blue) as a function of the number of PEs observed in NV. The tagging efficiency describes more specifically how efficiently the NV tags those neutrons that perform a single-scatter nuclear recoil in the region of interest for the WIMP search. It is estimated by evaluating how many neutron captures in NV occur after a single nuclear recoil in the TPC with a 250 us time window, during AmBe calibration.

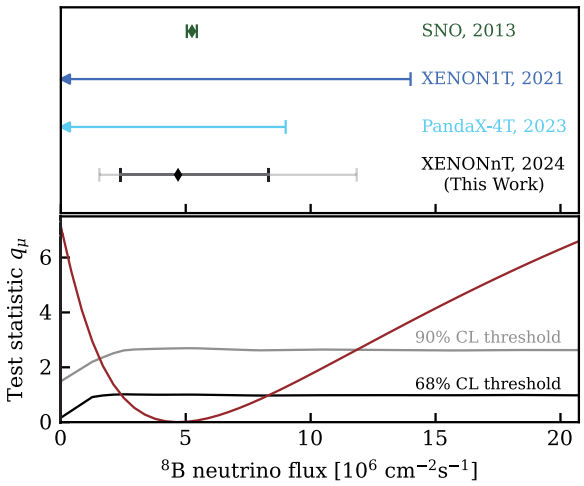


Fig. 35. Constraints on solar ^{8}B neutrino flux. Top: the 68 % (90 %) measurement of solar ^{8}B neutrino flux from this work is shown in black (gray). The 68 % CL measurement from SNO, and 90 % CL upper limits from XENON1T and PandaX-4T are also shown. Bottom: the solid red line shows the profile likelihood ratio test statistics q_μ as a function of solar ^{8}B neutrino flux. The constraints are derived with Feldman-Cousins construction at 68 % (90 %) CL, indicated by the black (gray) curve.

astrophysical neutrinos, the first measurement of the CEνNS process with a Xe target, and the first step into the "neutrino fog" by a dark matter experiment. "Neutrino fog" is the range of dark matter parameter space where the neutrino-induced signals become a background.

The search uses two datasets with a total live time of 316.5 days after accounting for dead time from data acquisition and vetoes. The first dataset, taken between July 6, 2021, and November 28, 2021, is referred to as the SR0 dataset with a live time of 108.0 days. The second dataset was collected between May 19, 2022, and August 8, 2023, a period referred to as SR1, with a live time of 208.5 days. After considering the field distortion correction and removing events with the interaction in the region where an understanding of the detector and backgrounds is insufficient, the fiducial volume mass for SR0 and SR1 are (3.97 $\pm$ 0.20) and (4.10 $\pm$ 0.19) t, respectively. The total exposure in this analysis is 3.51 t$\times$yr.

By lowering the S1 and S2 thresholds, we are able to include NR signals as low as 0.5 keV. Various techniques have been developed to reduce the dominant accidental background. Various calibrations, including ^{88}YBe and ^{37}Ar, are performed to understand the detector response, signal, and background modeling.

After unblinding, 9 and 28 events are observed in SR0 and SR1, respectively. The observed number of events is consistent with the expected ^{8}B CEνNS signal on top of the background. A four-dimensional binned likelihood analysis is performed after modeling signals and background components, accidental (AC) background, electronic recoil (ER) background, and radiogenic neutrons. The best-fit values of background components and ^{8}B CEνNS signal from the unconstrained fit are shown in Tab.6. The unconstrained best-fit number of ^{8}B CEνNS signals is $10.7^{+3.7}_{-4.2}$, consistent with the expectation of $11.9^{+4.5}_{-4.2}$ events. The background-only hypothesis, with no ^{8}B CEνNS signals, is disfavored with a p-value of 0.003, corresponding to a statistical significance of 2.73 σ.

Table 6. The expected and best-fit number of events from signal and background components in the ROI.

Component	Expectation	Best-fit
AC (SR0)	7.5 ± 0.7	7.4 ± 0.7
AC (SR1)	17.8 ± 1.0	17.9 ± 1.0
ER	0.7 ± 0.7	$0.5\ ^{+0.7}_{-0.6}$
Neutron	$0.5^{+0.2}_{-0.3}$	0.5 ± 0.3
Total background	$26.4\ ^{+1.4}_{-1.3}$	26.3 ± 1.4
^{8}B	$11.9\ ^{+4.5}_{-4.2}$	$10.7\ ^{+3.7}_{-4.2}$
Observed	37	

Assuming the flux-weighted CEνNS cross section $\sigma_{CE\nu NS}$ predicted by the SM, Fig. 35 shows the XENONnT constraint on the solar ^{8}B neutrino flux of $(4.7^{+3.6}_{-2.3}) \times 10^6$ cm^{-2}s^{-1} at 68 % CL. With the solar ^{8}B neutrino flux being constrained by SNO, Fig. 36 shows the first measurement of the flux-weighted CEνNS cross section $\sigma_{CE\nu NS}$ on Xe as $(1.1^{+0.8}_{-0.5}) \times 10^{-39}$ cm^2, consistent with the SM prediction of 1.2 $\times$ 10^{-39}cm^2. As XENONnT continues to take data, more precise measurements are expected in the future.

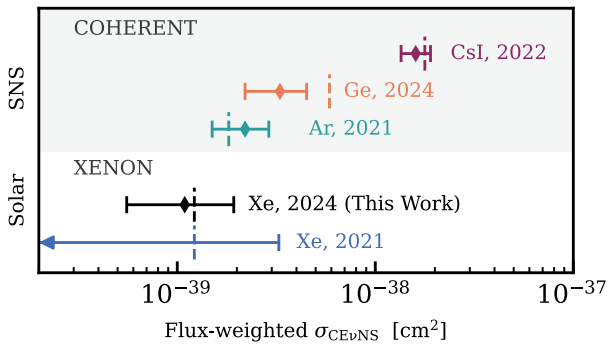


Fig. 36. The measurements with neutrinos from the SNS by the COHERENT collaboration using CsI (red), Ge (orange), and Ar (green) nuclei are also shown. For comparison, the SM predictions are shown by vertical dashed lines. Measurements of the flux-weighted CEνNS cross section $\sigma_{CE\nu NS}$. The measurement using Xe nuclei solar ^{8}B neutrinos from this work is shown in black. The 90 % CL upper limit from XENON1T is shown in blue.

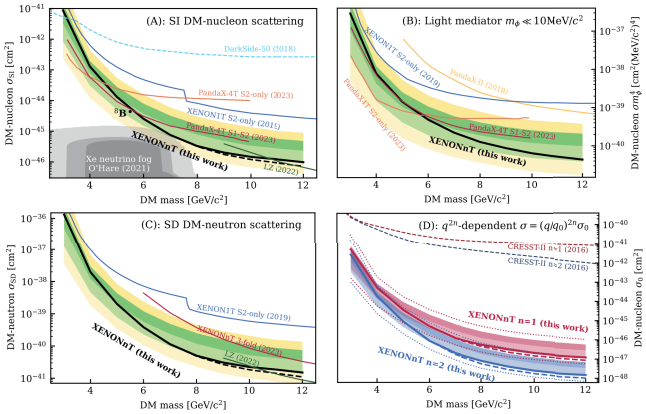


Fig. 37. Dark matter cross section upper limit at 90% confidence level with the 1 σ (green) and 2 σ (yellow) sensitivity band. The results with and without sensitivity -1σ PCL are shown by solid and dashed lines, respectively.

First Search for Light Dark Matter in the Neutrino Fog with XENONnT [6]

The search for light dark matter was conducted by using the same dataset and analysis techniques for solar ^{8}B neutrino search [5] described in the previous section. The dark matter models considered in this analysis involve nuclear recoils from the elastic scattering of dark matter particles on xenon nuclei with a mass ranging from 3 to 12 GeV/c^2. This mass range is favored by various models such as WIMP, asymmetric dark matter, and self-interacting dark matter. We examine spin-independent (SI) and spin-dependent (SD) interactions mediated by a heavy mediator with mass $m_\phi \gg q_0/c \equiv 10\,\mathrm{MeV/c^2}$, where q_0 represents the typical momentum transfer in this search. We also consider SI interactions mediated by a scalar or vector light mediator (SI-LM) with mass $m_\phi \ll q_0/c$. The differential rate is proportional to $\sigma m_\phi^4/(q^2/c^2+m_\phi^2)^2 \approx \sigma m_\phi^4 c^4/q^4$, where q denotes the momentum transfer, and σ is the cross section of dark matter nucleon scattering. Momentum-dependent dark matter scattering (MDDM) is also considered, characterized by a modified SI interaction cross section of the form $\sigma_{\chi N} = (q/q_0)^{2n}\sigma_0$, where $n \in \{1,2\}$ and σ_0 is the cross section of dark matter nucleon scattering. In addition, we search for mirror dark matter characterized by a differential cross section resembling Rutherford scattering.

Analysis techniques for deriving detector observables from produced photons and electrons, background reduction, and event selections are basically the same as those developed in ^{8}B CEνNS analysis. After unblinding, SR0 and SR1 reveal 9 and 28 events, respectively. The discovery p-value for the dark matter of SI interaction indicates no significant excess, with a minimum p-value of 0.18 at 3 GeV/c^2. The results for SI, SI-LM, SD, and MDDM are shown in Fig. 37 with previous limits. Our results tighten the constraints across the parameter spaces for all listed dark matter models. The cross section (4.4×10^{-45} cm^2) for ^{8}B CEνNS equivalent dark matter of 5.5 GeV/c^2 is also shown in the SI limit. The SD limit is susceptible to the current $\sim$ 10% uncertainty of the nuclear form factors. As the uncertainty predominantly changes the expected recoil rate, the results presented here can be rescaled. In addition, we exclude all metallic components (heavy mirror atoms such as mirror oxygen) of mirror dark matter, specifically ruling out mirror oxygen with a 90% upper limit. Mirror atoms are the mirror-sector counterpart of ordinary atoms, composed of mirror protons and neutrons, and are potential dark matter candidates because they interact weakly with ordinary matter. We achieve the world-leading sensitivity for light dark matter candidates within the ^{8}B CEνNS neutrino fog shown in Fig.37 (A). The background-only model yields a best-fit of $11.4^{+2.0}_{-3.6}$ ^{8}B CEνNS events with constrains based on the standard solar model ^{8}B neutrino spectrum and the measured flux of $(5.25\pm0.20)\times10^6\,\mathrm{cm^{-2}s^{-1}}$ from SNO. The ^{8}B CEνNS emerges as the most significant background in the 6 GeV/c^2 model, accounting for 60% of the total background in the signal-like region, marking the first step into the neutrino fog.

Search for Light Dark Matter in Low-Energy Ionization Signals from XENONnT [7]

The search for light dark matter was conducted with single- and few-electron signals in the SR0. The SR0 dataset was divided into two subsets. The first dataset (D1) with a live-time of 14.3 days was collected in November 2021 at the end of SR0 and is used to refine our data selections. The second dataset (D2) with 16.5 days is collected in September and October of 2021, is used for the blinded search.

In this analysis, only S2 signals were used because elastic scattering interactions rarely produce detectable S1 signals for dark matter particles below $\sim 6\,\mathrm{GeV/c^2}$. A large instrumental background of single- and few-electron S2s has been observed that persists $\mathcal{O}(100)$ ms following particle interactions. We mitigate this background by developing stringent spatial and temporal vetos for the smallest S2s and limit our region of interest to S2s with sizes subject to these veto requirements. Significant background rates likely originate from photoionization of electronegative impurities and delayed electron emission after higher-energy interactions. Thus, we restrict

our search region to time periods and volumes of the detector that minimize the rate of these backgrounds. These selections were optimized using D1. Various techniques are applied to establish a detector response framework, including a specific structure of the detector, such as support wires aligned perpendicular to the grid of both the gate and the anode.

After event selections based on our novel detector response framework, we observed 634 (189) events in the analysis region in D2 (D1). We compute the 90% confidence level upper limits on the physics parameters of the various dark matter models shown in the Fig. 38. The upper limits in bold solid (dashed) lines are computed using D2 (D1). Panel A-D in Fig. 38 show the 90% confidence level upper limits on the cross section of dark matter electron scattering as a function of the dark matter mass, obtained in this work by considering both halo dark matter with a velocity distribution from the standard halo model and solar-reflected dark matter (SRDM) which are halo dark matter particles upscattered by the Sun. For SRDM shown in Panels A and C, we are sensitive to dark matter masses down to 2 and 10 keV under the heavy and light mediator scenarios, respectively. The upper limits obtained in this work are stronger than the ones reported directly by previous experiments, but less stringent than the results from XENON1T S2-only data and XENON1T Low-ER data in the heavy mediator scenario. Panels B and D indicate the values of the cross section of dark matter electron scattering required to obtain the correct relic abundance from freeze-out and freeze-in production, respectively. Panel E shows the 90% confidence level upper limits on the kinetic mixing parameter by considering the dark photon (DP) model. DP can interact with electrons through a kinetic mixing (denoted by ε) with the photon in the standard model. Systematic uncertainty arises due to DP absorption in different electron shells. Panel F shows the 90% confidence level upper limits on the axion-electron coupling strength computed by considering the axion-like particle (ALP) model. ALPs are absorbed by bound electrons through the axioelectric effect with axion-electron coupling strength g_{ae}.The ALP parameter space is also constrained by other direct dark matter detection experiments. Both of AP and ALP models result in monoenergetic depositions corresponding to particle masses.

These constraints on the cross section of dark matter electron scattering are weakened by the elevated single-electron background rates. This only affects masses where the expected signal is concentrated in the 1-2 electron populations. DP and ALP models with masses heavier than 0.1 keV produce more electrons and are hence less affected by the increased rates of single-electron background events. This is can be seen from panels E-F in Fig. 38 from the convergence of the upper limits computed from D1 and D2 for larger DP or ALP mass. Future work can improve on these results through the development of a predicted background model for delayed electron emission, which will allow leveraging the full XENONnT exposure to probe new parameter space.

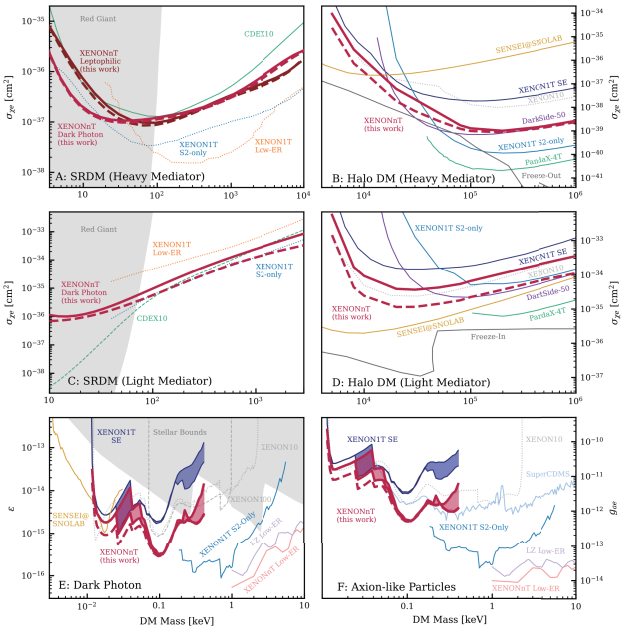


Fig. 38. The 90% confidence level upper limits on the various physics model parameters computed using dataset D2 (D1) are shown in solid (dashed) red lines. Panel A (C) shows the upper limits on dark matter-electron scattering cross section by considering solar-reflected dark matter under the heavy (light) mediator scenario, while panels B (D) show the limits by considering halo dark matter under the heavy (light) mediator scenario. Panel E shows the 90% confidence level upper limits on the kinetic mixing parameter computed by considering Dark Photon models, while panel F shows the 90% confidence level upper limits on the axion-electron coupling by considering Axion-like Particle models.

Bibliography

[1] E. Aprile *et al.* (XENON collaboration), JCAP 11 (2020) 031.

[2] E. Aprile *et al.* (XENON collaboration), Phys. Rev. Lett. 131, 041003 (2023).

[3] L. Marti, *et al.* (Super-Kamikande collaboration), Nucl. Instrum. Meth. A, 959, 163549 (2020); K. Abe *et al.* (Super-Kamiokande collaboration), Nucl. Instr. Meth. A, 1027 (2022) 166248.

[4] E. Aplile *et al.* (XENON collaboration), Eur. Phys. J. C (2022) 82:599.

[5] E. Aprile *et al.* (XENON collaboration), Phys. Rev. Lett. 133, 191002 (2024).

[6] E. Aprile *et al.* (XENON collaboration), Phys. Rev. Lett. 134, 111802 (2025).

[7] E. Aprile *et al.* (XENON collaboration), Phys. Rev. Lett. 134, 161004 (2025).

HYPER-KAMIOKANDE

[Co-Spokespersons: Masato Shiozawa[1], Francesca Di Lodovico[2]]
1: Kamioka Observatory, ICRR, The University of Tokyo
2: Department of Physics King's College London

Introduction

The Hyper-Kamiokande (Hyper-K or HK) project [1] is the world-leading international scientific research project hosted by the University of Tokyo and High Energy Accelerator Research Organization (KEK) consisting of a next-generation underground water Cherenkov detector and upgraded Japan Proton Accelerator Research Complex (J-PARC) neutrino beam. The Hyper-K project was approved by the Japanese Diet in 2020 and officially started.

Figure 39 shows a schematic drawing of the Hyper-K cylindrical detector. The detector is filled with 0.260 million metric tons of ultra-pure water, which serves an order of magnitude larger fiducial mass of 0.188 million metric tons than Super-K, equipped with newly developed high-sensitivity photosensors, and a high-intensity neutrino beam produced by an upgraded J-PARC accelerator facility. It provides enormous potential to discover leptonic charge-parity (CP) violation by observing neutrino and anti-neutrino beams from J-PARC, investigate the Grand Unified Theory by exploring proton decay, and determine the neutrino mass ordering by observing atmospheric neutrinos combining beam data. Hyper-K will also have far better capabilities to observe solar neutrinos and neutrinos from other astronomical sources than those of predecessor experiments.

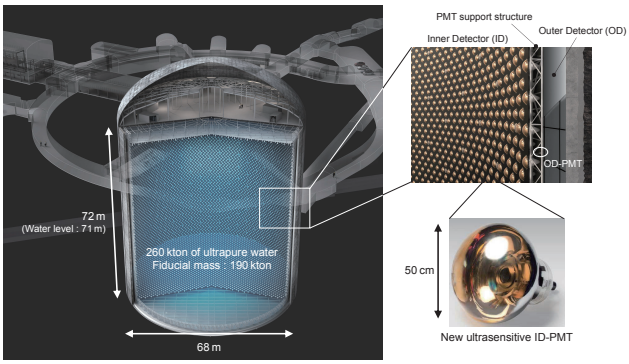


Fig. 39. Schematic view of the Hyper-K water tank and approach tunnel.

The Hyper-K international collaboration consists of about 640 researchers from 22 countries (June 2025, 75% from overseas). The detector technology has been developed on the basis of the successful Super-K experiment, and feasibility studies have been completed by the international group. The Hyper-K operation is scheduled to start in 2028.

Physics

Hyper-K will have the capability to measure the magnitude of the CP violation with high precision, which could explain the baryon asymmetry in the Universe. Figure 40 shows the expected significance of the CP violation discovery by ten years of operation. With expected systematic error improvement, Hyper-K covers 60% of the parameter space with 5σ or more, as the red dotted line shows in the figure. More than 8σ significance will be expected if $\delta_{CP} = -\pi/2$ as suggested by T2K [2] and NOνA [3] results.

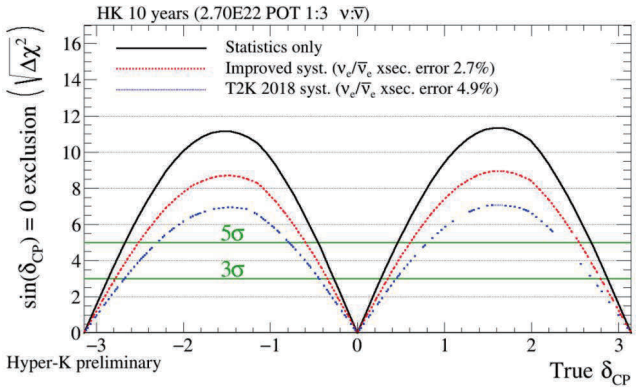


Fig. 40. Significance of the leptonic CP violation discovery with a 10-year observation in Hyper-K (HK) as a function of the unknown CP phase assuming the normal neutrino mass hierarchy. The red dotted line shows the result with the expected systematic error improvement, the blue dotted line shows the result with the achieved systematic error by T2K 2018, and the black line shows the result with only statistical error.

A proton decay $p \to e^+\pi^0$ is an important signal favored by many Grand Unified Theory models with a prediction close to the current limit of the lifetime of the proton decay. Highly sensitive Hyper-K PMTs result in a strong background (atmospheric neutrinos) reduction and $p \to e^+\pi^0$ search in Hyper-K is expected to be "background-free" particularly in the free-proton enhanced signal region. Figure 41 shows the 3σ discovery potential for the $p \to e^+\pi^0$ mode as a function of year. Hyper-K is the only realistic proposal that can go beyond the proton lifetime of 1×10^{35} years.

In addition to the supernova burst neutrino that was successfully observed in Kamiokande at once, undiscovered supernova relic neutrinos, accumulated by all supernovae since the beginning of the universe, are interesting events for exploring the history of heavy elements and the onset of stellar formation.

Construction status

The Hyper-K cavern is the largest artificial underground cavity in the world. The construction of the cavern and the water tank is a crucial part of the Hyper-K project. Figure 42 is a schematic drawing of the Hyper-K tunnels and the cavern. The excavation of the 1873.5 m access tunnel started in May 2021 and was completed in February 2022. Then, excavation of the approach tunnel followed and was finished in June 2022.

After completion of the approach tunnel, the excavation of the Hyper-K cavern started. Figure 43 shows the dome section

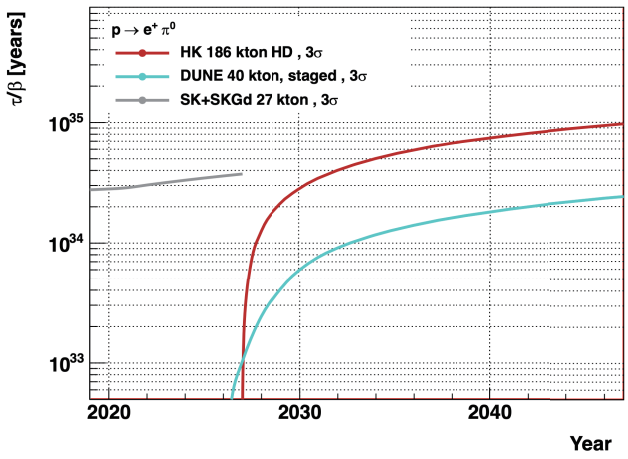


Fig. 41. The $p \to e^+\pi^0$ discovery reach in proton lifetime with 3σ significance as a function of year. It shows the Hyper-K (HK) planning to start in 2027, superimposed with the ongoing Super-K (SK) and planned DUNE experiments. The DUNE project assumes 10 kton operation from 2026, toward full 40 kton by increasing 10 kton every year [4].

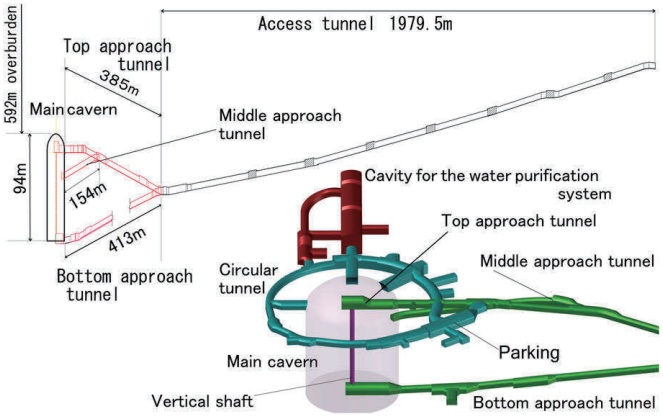


Fig. 42. Overview of the Hyper-Kamiokande excavation. The access tunnel, about 2 km, is connected to approach tunnels about 400 m to reach the top and bottom of the main cavern.

of the main cavern that was completed in October 2023. The diameter of the cavern is 69 m and the height of the ceiling is 21 m. Then the last part, excavation of the cylindrical section below, has begun. As shown in Figure 44, the work is ongoing steadily and reached a depth of 61 m in March 2025. The excavation will be completed to a depth of 73 m in July 2025.

20-inch PMT, Delivery and inspection

The newly developed photomultiplier tubes R12860 by Hamamatsu Photonics K.K is shown in Fig. 45. The total detection efficiency of R12860 for a single photon is twice higher than that of the Super-K PMT due to 1.4 times higher quantum efficiency (about 32%) and improved photoelectron collection efficiency. The timing and charge resolutions at single photoelectron also become much better as 1.1 ns and 35%, which can be compared with 2.1 ns and 53% of the Super-K PMT, respectively. The pressure tolerance of the PMT was also improved up to the depth of 125 m, so that the new PMT can be used below the depth of 70 m of the detector water.



Fig. 43. The main cavern dome section (diameter: 69m, height: 21m) was completed in October 2023.

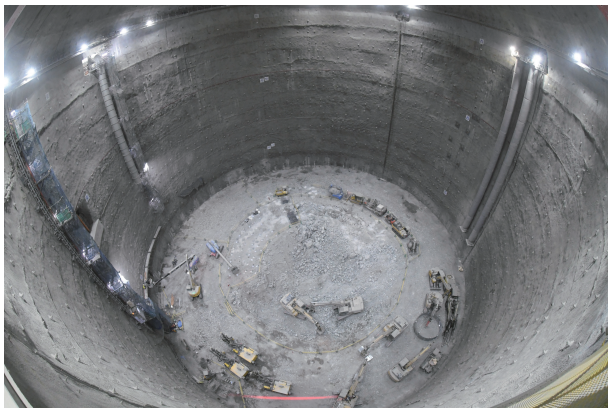


Fig. 44. The excavation of the cylindrical section is ongoing (September 2024).

Since the start of mass production in October 2020, the delivery of 400 PMTs for every month has been ongoing. The total number of deliveries reached about 14,000 in March 2025 without any delay in the schedule. At the facility where the PMTs were delivered, inspections of the PMTs are also ongoing. The inspection consists of visual inspection for bulb and waterproof quality, signal check for signal property and noise rate, and long-term stability check. Figure 46 shows the dark

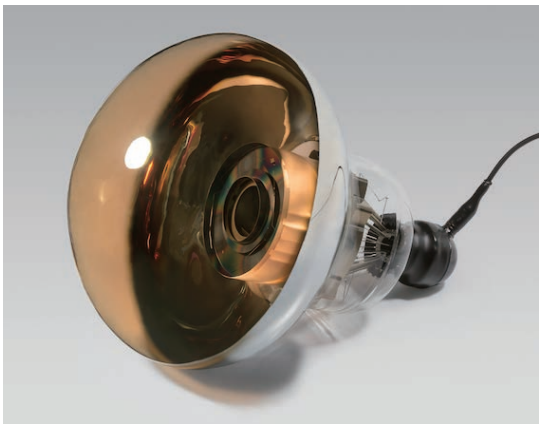


Fig. 45. New 50 cm photomultiplier tube with a box-and-line dynode (R12860, Hamamatsu Photonics K.K.).

room to check the long-term stability of 100 PMTs simultaneously. The delivery of PMTs continues until September 2026.

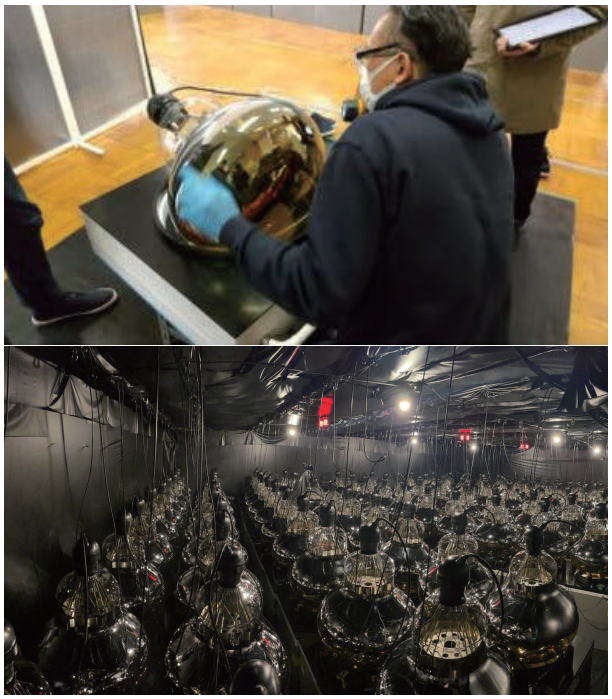


Fig. 46. Visual inspections of PMTs (top). Dark room for long-term stability check of 100 PMTs (bottom).

Electronics

The HK front-end electronics will be placed underwater near the PMTs to avoid a long analog cable and degradation of the PMT signal. This is another challenge of the HK project. We have made a lot of effort to develop water-tight equipment, high-reliability front-end electronics, and communication underwater.

Frontend electronics prototypes have been developed and validated to work as a system before starting mass production. The Figure 47 shows the system test of frontend electronics on the table before being assembled into a water-tight vessel. The system consists of two digitizer boards, a communication board, and HV/LV modules.

Figure 48 shows an underwater test with 1 MPa-tolerant water-tight vessel. The vessel contains a full setup of frontend electronics and is connected to 24 PMTs and a DAQ system via optical fiber. Performance and functionalities have been comprehensively tested and validated. Then mass production of the components is ready to start.

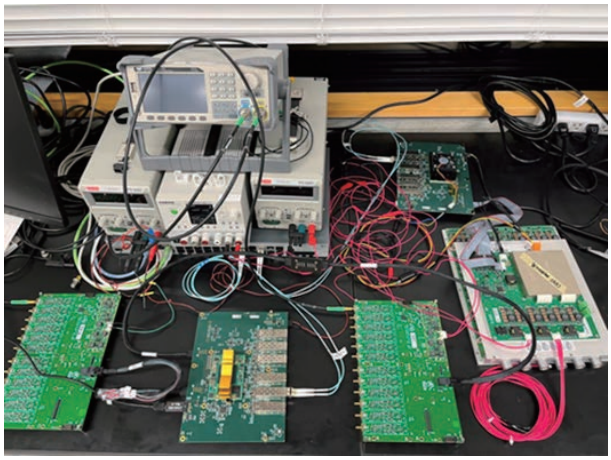


Fig. 47. System test of the frontend electronics on the table before assembling it into a water-tight vessel. The system consists of two digitizer boards, a communication board, and HV/LV modules.

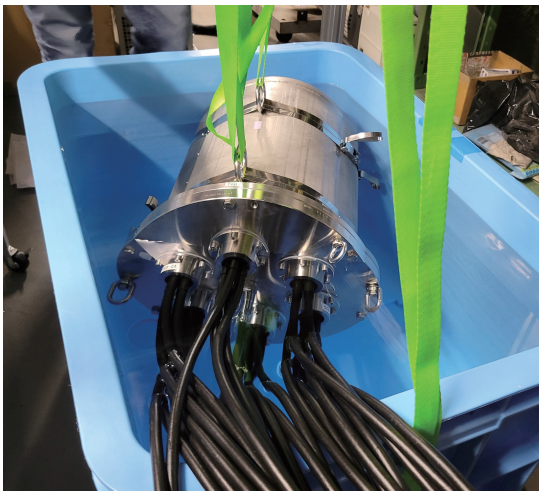


Fig. 48. Underwater test with 1MPa 1MPa-tolerant water-tight vessel. The vessel contains a full setup of frontend electronics and is connected to 24 PMTs and a DAQ system.

Bibliography

[1] "Hyper-Kamiokande Design Report," arXiv: 1805.04163.

[2] K. Abe *et al.* [T2K Collaboration], Nature 580, 339-344 (2020).

[3] P. Adamson *et al.* [NOνA Collaboration], Phys. Rev. Lett. 118, 231801.

[4] R. Acciarri *et al.* [The DUNE Collaboration], arXiv:1601.05471 [physics.ins-det].

HIGH ENERGY COSMIC RAY DIVISION

Overview

There are three major experimental research activities in the High Energy Cosmic Ray Division, the study of high-energy gamma rays and the development of the next generation gamma-ray telescopes by the Cherenkov Cosmic Gamma Ray group, the study of extremely high-energy cosmic rays by the Telescope Array (TA) group, and the study of very high-energy cosmic rays and gamma rays by the Tibet ASγ/ALPACA group.

Other activities, such as experiments utilizing the Akeno observatory, the Norikura observatory, the Mt. Chacaltaya observatory (jointly operated with Bolivia) are closely related to inter-university joint research programs. The High Energy Astrophysics group was created in the fiscal year 2009 aims to explore various high-energy astrophysical phenomena, through theoretical and observational approaches.

The CANGAROO telescopes had been in operation in South Australia since 1992, with a 3.8 m small telescope and then with four 10 m telescopes. The major scientific objective was the study of Very High Energy (VHE) gamma-ray sources in our galaxy in the southern hemisphere. The mission of these telescopes was completed, and the CANGAROO observation site was closed in 2011.

The MAGIC Collaboration constructed the first large atmospheric imaging Cherenkov telescope, MAGIC-I, in 2004, with a mirror surface of 236 m^2 at an altitude of approximately 2200 m, near the summit of the Roque de los Muchachos in La Palma, Canary Islands, Spain. In 2009, the second telescope with the same characteristics, MAGIC-II, was installed 85 m from MAGIC-I. The energy threshold achieved so far by the stereo observation is 25 GeV. Since 2010, more than ten researchers affiliated with ICRR have joined the MAGIC collaboration, contributing to its operations, observations, and data analysis.

For further development of VHE gamma-ray astronomy, the Cherenkov Cosmic Gamma Ray group is working on the design study and development, and construction of the next generation international ground-based gamma-ray observatory CTAO, which will offer an order of magnitude better sensitivity than currently running Cherenkov telescopes, three times better angular resolution, and wider energy coverage from 20 GeV to 100 TeV or higher. The construction of the first Large-Sized Telescope (LST) was completed on the CTAO-North site in La Palma in 2018. The construction of the second to fourth LSTs is progressing fast, and those three LSTs are planned to be completed in 2026. High Energy Astrophysics Facility in Canarias was established as a base for the project in April 2019.

At the Akeno observatory, a series of air shower arrays of increasing geometrical sizes were constructed and operated to observe extremely high-energy cosmic rays (EHECRs). The Akeno Giant Air Shower Array (AGASA) was operated from 1991 to January 2004 and covered the ground area of 100 km^2 as the world largest air shower array. In 13 years of operation, AGASA observed a handful of cosmic rays exceeding the theoretical energy end of the extra-galactic cosmic rays (GZK cutoff) at around 10^{20} eV.

The Telescope Array (TA), a large plastic scintillator array with air fluorescence telescopes, has been constructed in Utah, USA, which succeeds AGASA and measures the EHECRs with an order of magnitude larger aperture than that of AGASA for the further study of EHECRs. The full-scale TA is accumulating data as the largest array viewing the northern sky and observing the energy spectrum with high statistics, which is in good agreement with the GZK suppression and found evidence for anisotropies of arrival directions of EHECRs. The TAx4, which is aimed at quadrupling TA, was partially constructed by March 2019.

An air shower experiment aiming to search for celestial gamma-ray point sources started in 1990 with Chinese physicists at Yangbajing (Tibet, 4,300 m a.s.l.). This international collaboration is called the Tibet ASγ Collaboration. An extension of the air shower array was completed in 1995, and an emulsion chamber has been combined with this air shower array since 1996 to study the primary cosmic rays around the knee energy region. After successive extensions carried out in 1999, 2002, and 2003, the total area of the air shower array amounts to 37,000 m^2. The sun's shadow in cosmic rays affected by the solar magnetic field was observed for the first time in 1992, utilizing its good angular resolution in the multi-TeV energy region. The group added underground water Cherenkov muon detectors and successfully detected cosmic gamma rays above 100 TeV. The group is constructing a new air shower array, called ALPACA, to cover the sky in the Southern hemisphere, and started the operation of its partial array in Bolivia in 2023.

The High Energy Astrophysics group is conducting theoretical research on high-energy astrophysical phenomena, such as relativistic jets from active galactic nuclei, gamma-ray bursts, pulsars, and the merger of binary neutron stars. In this field, there remain many unsolved problems. The group especially studies the formation of relativistic outflows, particle acceleration in jets, emission mechanisms of electromagnetic waves or neutrinos from high-energy particles. The research supports multi-messenger astronomy, which probes astronomical phenomena through collaborating observations of electromagnetic waves, cosmic rays, neutrinos, and gravitational waves.

Cherenkov Cosmic Gamma-Ray Group

CTAO Project (Cherenkov Telescope Array Observatory)

CTAO-Japan Consortium
[Spokesperson : H. Kubo, T. Saito]

Collaboration list:
Institute for Cosmic Ray Research, The University of Tokyo, Chiba, Japan; Department of Physics, Aoyama Gakuin University, Tokyo, Japan; International Center for Hadron Astrophysics (ICEHAP), Chiba University, Chiba, Japan; Department of Physics, Hiroshima University, Hiroshima, Japan; Hiroshima Astrophysical Science Center, Hiroshima University, Hiroshima, Japan; Faculty of Engineering, Gifu University, Gifu, Japan; Faculty of Science, Ibaraki University, Ibaraki, Japan; Institute of Particle and Nuclear Studies, High Energy Accelerator Research Organization (KEK), Ibaraki, Japan; Institute of Space and Astronautical Science (ISAS), Japan Aerospace Exploration Agency (JAXA), Kanagawa, Japan; Faculty of Engineering, Kanagawa University, Kanawaga, Japan Department of Physics, Konan University, Hyogo, Japan; Faculty of Medical Engineering and Technology, Kitasato University, Kanagawa, Japan; Graduate School of Science and Technology, Kumamoto University, Kumamoto, Japan; Research Center for Advanced Particle Physics, Kyushu University, Fukuoka, Japan; Department of Physics, Kyoto University, Kyoto, Japan; Department of Applied Physics, University of Miyazaki, Miyazaki, Japan; Department of Physics, Nagoya University, Aichi, Japan; Solar-Terrestrial Environment Laboratory, Nagoya University, Aichi, Japan; Kobayashi-Maskawa Institute, Nagoya University, Aichi, Japan; Division of Science, National Astronomical Observatory of Japan, Tokyo, Japan; Department of Earth and Space Science, Osaka University, Japan; Astrophysical Big Bang laboratory, RIKEN, Wako, Japan; Department of Physics, Rikkyo University, Tokyo, Japan; Department of Physics, Saitama University, Saitama, Japan; National Institute of Technology, Sendai College, Miyagi, Japan; Department of Physics, Tokai University, Kanagawa, Japan; Faculty of Integrated Arts and Sciences, The University of Tokushima, Tokushima, Japan; Department of Astronomy, The University of Tokyo, Tokyo, Japan; Department of Physics, The University of Tokyo, Tokyo, Japan; Department of Physics, Graduate School of Science, Tokyo Metropolitan University, Tokyo, Japan; Astronomical Institute, Tohoku University, Sendai, Miyagi, Japan Faculty of Science and Engineering, Waseda University, Tokyo, Japan; Department of Physics, Yamagata University, Yamagata, Japan; Faculty of Management Information, Yamanashi Gakuin University, Yamanashi, Japan. Yukawa Institute for Theoretical Physics, Kyoto University, Kyoto, Japan; College of Engineering Science, Yokohama National University, Kanagawa, Japan;

Introduction of the CTAO project

During the past years, very-high-energy (VHE) gamma-ray astronomy has made spectacular progress and has established itself as a vital branch of astrophysics. To advance this field even further, we are constructing telescopes for the Cherenkov Telescope Array Observatory (CTAO) [1], the next-generation VHE gamma-ray observatory, in the framework of a worldwide, international collaboration. CTAO is the ultimate VHE gamma-ray observatory, whose sensitivity and broad energy coverage will attain an order of magnitude improvement above those of current Imaging Atmospheric Cherenkov Telescopes (IACTs). By observing the highest energy photons known, CTAO will clarify many aspects of the extreme Universe, including the origin of the highest energy cosmic rays in our Galaxy and beyond, the physics of energetic particle generation in neutron stars and black holes, as well as the star formation history of the Universe. CTAO will also address critical issues in fundamental physics, such as the identity of dark matter and the nature of space and time.

VHE gamma rays from $\sim$50 GeV to $\sim$100 TeV can be observed with ground-based current IACTs. The history of VHE gamma-ray astronomy began with the discovery of VHE gamma rays from the Crab Nebula by the Whipple Observatory in 1989. To date, the current generation IACTs featuring new technologies, such as H.E.S.S., MAGIC, and VERITAS, have discovered more than 300 Galactic and extragalactic sources of various types[3].

CTAO is designed to achieve superior sensitivity and performance, utilizing established technologies and experiences gained from the current IACTs. The project is presently in its construction phase, with international efforts from Japan, USA, EU, and other countries. It will consist of several tens of IACTs of three different sizes: Large-Sized Telescopes (LST), Middle-Sized Telescopes (MST), and Small-Sized Telescopes (SST) (See Fig. 1). CTAO has two sites in each Hemisphere to observe all sky: (1) CTAO's northern hemisphere array (CTAO-North), located on the island of La Palma in the Canary Islands, Spain, (2) CTAO's southern hemisphere array (CTAO-South), located in northern Chile in the Atacama Desert. With a factor of 10 increase in sensitivity, together with a much broader energy coverage from 20 GeV up to 300 TeV. CTAO will bring forth further dramatic advances for VHE gamma-ray astronomy. The discovery of more than 1000 Galactic and extragalactic sources is anticipated with CTAO.

CTAO will allow us to explore numerous diverse topics in physics and astrophysics [2]. The century-old question of the origin of cosmic rays is expected to be finally settled through detailed observations of supernova remnants (SNRs) and other Galactic objects, along with the diffuse Galactic gamma-ray emission, which will also shed light on the physics of the interstellar medium. Observing pulsars and associated pulsar wind nebulae will clarify physical processes in the vicinity of neutron stars and extreme magnetic fields. The physics of accretion onto supermassive black holes, the long-standing puzzle of the origin of ultra-relativistic jets emanating from them, as well as their cosmological evolution, will be addressed by extensive studies of active galactic nuclei (AGN). Through dedicated observing strategies, CTAO will also elucidate many aspects of the mysterious nature of gamma-ray bursts (GRBs), the most energetic explosions in the Universe. Detailed studies of both AGNs and GRBs can also reveal the origin of the highest-energy cosmic rays in the Universe,

*[3] https://tevcat.org/

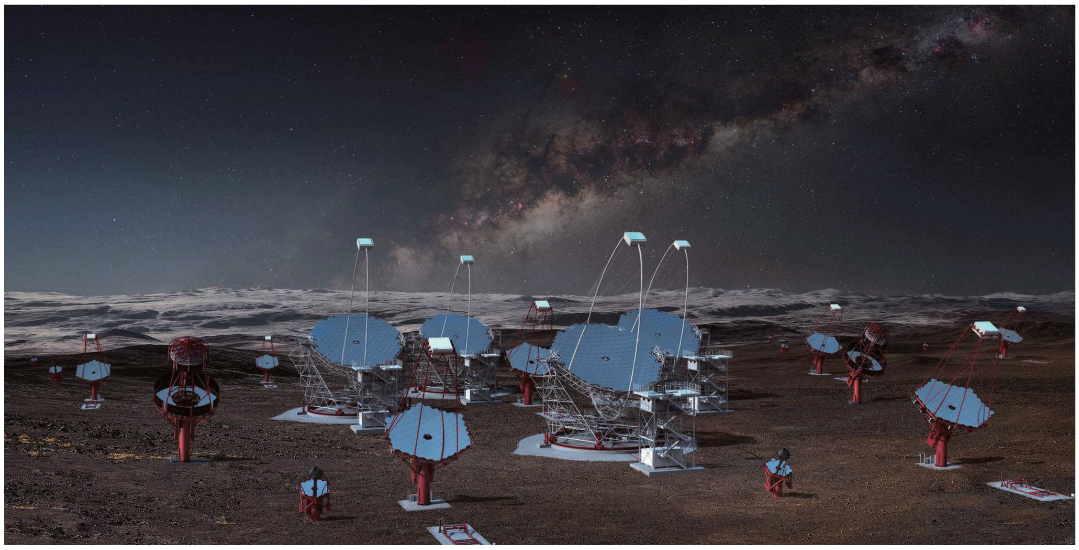


Fig. 1. Artist view of the Cherenkov Telescope Array observatory (CTAO). CTAO consists of three types of telescopes, Large-Sized Telescopes (23 m diameter), Medium-Sized Telescopes (12 m), and Small-Sized Telescopes (4 m), and covers the broad energy band from 20 GeV to 300 TeV. [Credit: Gabriel Pérez Diaz (IAC)/Marc-André Besel (CTAO)/ESO/ N. Risinger (skysurvey.org)]

probe the cosmic history of star formation, including the very first stars, and provide high-precision tests of theories of quantum gravity. Finally, CTAO will search for signatures from elementary particles constituting dark matter with the highest sensitivity yet. Realisation of the rich scientific potential of CTAO is very much feasible, thanks to the positive experiences gained from the current IACTs.

To maximize the scientific impact, the CTAO needs to carry out science projects that require large amounts of observing time spread over multiple observing periods and a structured organization capable of performing data analysis in a coherent and systematic way. For this purpose, CTAO will define the Key Science Project (KSP) Framework, which has been established considering the CTAO Access Policy.

The CTAO-Japan consortium [3] is contributing particularly to the construction of the LSTs (Fig. 2) and is involved in their development and commissioning. The LST telescope array covers the low-energy domain from 20 GeV to 3 TeV and is especially important for studies of high-redshift AGNs and GRBs. The diameter and area of the mirror are 23 m and 368 m^2, respectively, in order to achieve the lowest possible energy threshold of 20 GeV. All optical elements, photodetectors, and readout boards require state-of-the-art specifications, such as, among others, high reflectivity, collection efficiency, quantum efficiency, and ultra-fast digitization of signals. For this purpose, CTAO-Japan has developed high precision segmented mirrors (Fig. 3) [4] and high quantum efficiency photomultipliers (PMTs) and ultrafast readout electronics (Fig. 4) [5]. Building on the experience gained from the construction of the MAGIC telescope, the Max-Planck-Institute for Physics in Munich is responsible for the design of the 23-m diameter telescope structure, based on a carbon fiber tube space frame. The LSTs require very fast rotation (180 degrees in 20 seconds) to promptly observe GRBs.

The CTAO project was selected in 2023 as one of 12 projects shown on the “Roadmap 2023” as the Fundamental Concepts for Promoting Large Scientific Research Projects that the Working Group of the Ministry of Education, Culture, Sports, Science and Technology (MEXT) formulated on Large Scientific Projects.

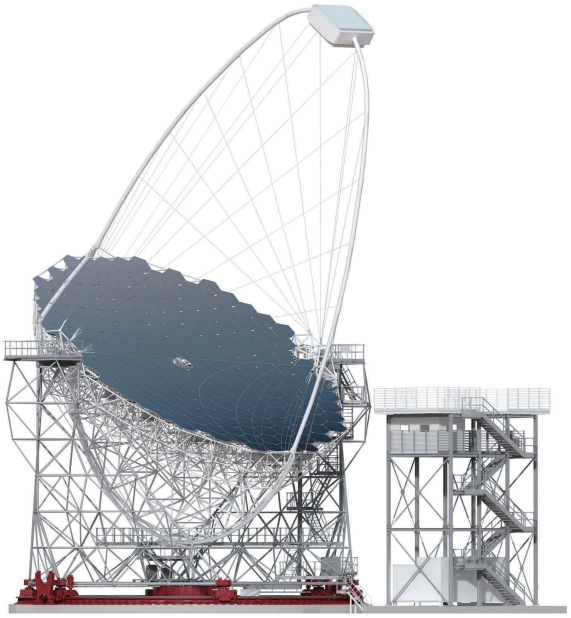


Fig. 2. Large-Sized Telescope (23 m diameter) designed by the Max–Planck-Institute for Physics. CTAO-Japan is contributing to the design, construction, and commissioning of the imaging camera at the focal plane, ultrafast readout electronics, and high-precision segmented mirrors.

Current status of the LST

LST-1

The first LST (LST-1) was built at the CTAO-North site in 2018, and it is now in the engineering run phase (Fig. 5). This is the first prototype telescope for the CTAO, and the LST-1 successfully passed the critical design review held in



Fig. 3. The high-precision segmented mirrors for the Large-Sized Telescope were developed by CTAO-Japan in cooperation with Sanko Co.LTD. The mirror is made of a 60-mm-thick aluminum honeycomb sandwiched by 3-mm-thick glass on both sides. A surface protection coat consisting of the materials SiO_2 and HFO_2 is applied to enhance the reflectivity and to elongate the lifetime.

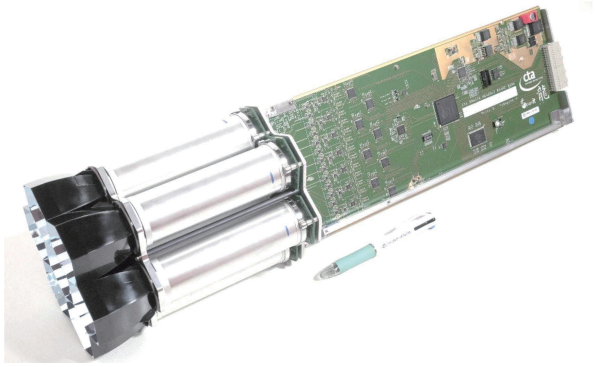


Fig. 4. Camera cluster for the Large-Sized Telescope developed by CTAO-Japan. This cluster consists of seven high quantum efficiency photomultipliers (R11920-100), Cockcroft-Walton High Voltages, pre-amplifier, Slow Control Board, DRS4 Ultra fast waveform recording system, and Trigger. The LST camera can be assembled with 265 of these clusters, cooling plates, and camera housing.



Fig. 5. LST-1 constructed at Observatory de Roque de los Muchachos (ORM), which is now in an engineering run phase. The diameter of the telescope mirror dish is 23 m and the mirror surface area is 400 m^2.



Fig. 6. LST2–4 construction at ORM (Dec. 2024). Credit: IAC

2020 by CTAO engineers and external experts from high-energy physics. In January 2025, CTAO became a legal entity, CTAO-ERIC (European Research Infrastructure Consortium), under European Union law, and CTAO-Japan participates as a strategic international partner. The discussion about how and when to hand over the telescopes to the CTAO is ongoing. Meanwhile, the LST-1 has been regularly observing gamma-ray sources based on the proposals evaluated within the LST collaboration. We already published several early science results using LST-1 [6, 7].

LST-2–4

The construction of the second to fourth LSTs (LST-2–4) is progressing fast. Fig. 6 shows the current status of the CTAO-North site in La Palma. The foundation, the drive rail, and the camera access tower of all three telescopes were already built. The mirror dishes were also mounted on all three telescopes in FY2024, and the camera support structures were also connected to two of the remaining three telescopes in FY2024.

We also installed the mirrors into the LST-4 telescope in November 2024. CTAO-Japan members joined the mirror installation campaign (See Fig. 7). We also started to install the mirrors into the LST-3 telescope at the end of March 2025, and the installation was successfully completed in May 2025[4]. The last mirror installation on LST-2 is expected during this summer.

We performed the final integration test of the cameras of LST-2–4 in the Institute of Astrophysics in the Canary Islands (IAC) in Tenerife, and the cameras were waiting for the transportation to La Palma island. As of the beginning of FY2025, the camera of LST-4 was already transported and installed into the telescope in May 2025[5] (See Fig. 8), and the other two cameras are expected to be installed within FY2025. We plan to start the commissioning tests for each telescope once we confirm that all the subsystems work as expected.

*4 https://www.ctao.org/news/the-lst-collaboration-finalises-mirror-installation-on-lst-3/

*5 https://www.ctao.org/news/camera-installation-marks-completion-of-lst-4-construction/

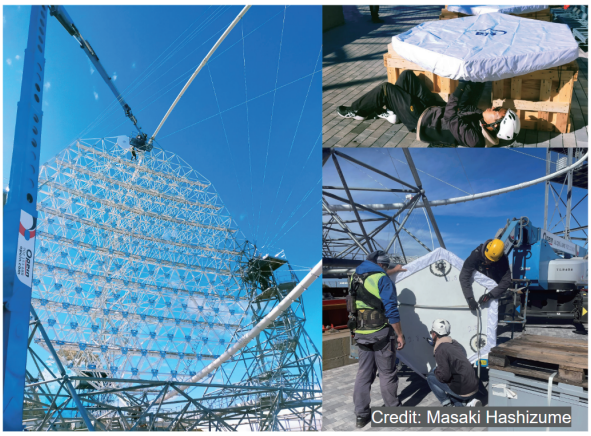


Fig. 7. LST4 mirror installation (Nov. 2024). Credit: Masaki Hashizume.



Fig. 8. LST4 camera installation (May 2025). Credit: LST collaboration.

LST South

In addition to the ongoing construction of LSTs at the CTAO-North site, up to four more LSTs are expected to be built at the CTAO-South site in Paranal, Chile [8]. The funding of two LSTs at the CTAO-South site is secured by the CTAO-Italy group. The CTAO-Italy group has already started to purchase the components of each subsystem. CTAO-Japan group is cooperating with them to prepare each subsystem based on our knowledge and experience – as well as providing access to the control software we've developed. We also contribute to the preparation for the mass production of the light guide to be used for LST South.

Small-Sized Telescope

CTAO-Japan consortium (especially members from ISEE, Nagoya University) has also been contributing to the development of the SST camera using silicon photomultiplier (SiPM) (See Fig. 9). Nine prototype telescopes are under construction on Tenerife Island, Canary Islands, Spain as ASTRI Mini-Array project [9]. Our members from the CTAO-Japan group have been performing SiPM tests to install the camera on the first prototype camera.

Since we plan to build more than 40 SSTs with 2,048

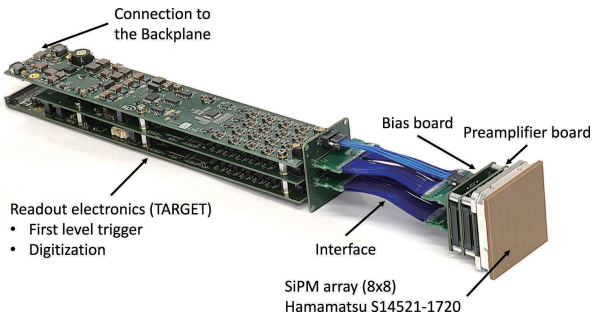


Fig. 9. SiPM module for the SST camera [10]. The camera consists of 32 identical modules, each containing 64 SiPMs.

SiPMs, it is important to understand their failure modes and rates. In an initial test, we measured the leakage current of two SiPM modules, totaling 128 SiPMs, for more than half a year. In this test, a SiPM exhibited a 10-fold increase in the leakage current, no visible increase was observed in its dark count rate, indicating that the increase was not caused by a higher dark count rate. Furthermore, the voltage dependence of the leakage current exhibited resistor-like behavior, verifying the existence of a current source parallel to the SiPMs. Visual inspection of the surface of the SiPM found damage to the electrode, and temperature measurement by far-infrared verified localized ohmic heating in this region. From this evidence, we concluded that the damage to the aluminum electrode is the root cause of the large current increase. The manufacturer plans to screen out this kind of damage by automatic visual inspection in future productions.

The leakage current in 20% of the SiPMs jumped by fixed amounts, and some SiPMs exhibited several jump modes. We speculate that these modal jumps are caused by the activation and deactivation of a certain defect, and that multimodal behavior is caused by multiple defects. In fact, we observed localized visual light emission from hot-carrier luminescence at these defect sites and found that the luminosity was proportional to the excess dark current, indicating that the majority of the excess dark current is caused by these emission sites. We also found that the jumps of the current coincide with the brightness changes of the emission sites. Observations by a photo-emission microscope revealed that there are many emission sites, and bright spots are always located near the corners of microcells where the electric field is high. From these observations, we conclude that the excess dark currents are caused by defects. The electric field dictates the brightness and the dark current caused by defects. This indicates that we may be able to reduce excess dark current by lowering the field strength through design improvement. These studies were presented at [11].

Activities of CTAO-Japan members

In this section, some activities contributed by CTAO-Japan consortium members are introduced.

Computing Center at the CTAO-North site

The computing center is being upgraded to accommodate the control and operation of the new telescopes LST-2–4. During FY2024, the dedicated servers for LST-2–4 were delivered

to La Palma. Since they could not be installed due to missing containers to host them, the existing server `lst104` was fully set up from scratch, operating on ALMA Linux 9. The software required to operate the camera and drive system of LST-4 has been successfully installed and is fully functional. To streamline future deployments, an automated setup procedure was developed, allowing for efficient preparation of additional servers.

In addition to the preparations for LST-2–4, several maintenance activities were carried out. The computing center job submission system was reconfigured to reflect current operational priorities. The updated priority order is as follows: 1) data taking, 2) real-time analysis, 3) onsite analysis pipeline, 4) fast offline analysis, 5) MAGIC-CTA-pipe data processing, 6) Monte Carlo production, 7) other data analyses of the LST collaboration members.

Local software repositories were updated to support continued operation under the CentOS 7 operating system. Given the end of official support for CentOS 7 in FY2024, the latest available packages were secured and mirrored locally to ensure stability.

Lastly, the expired batteries in the uninterruptible power supply (UPS) system were replaced to maintain reliable backup power for the IT infrastructure. These upgrades and maintenance measures are essential to ensure a robust and scalable IT environment that supports both current and upcoming scientific operations at the La Palma observatory.

LST-1 performance study with the Crab Nebula observations

We observed the Crab Nebula with the LST-1 telescope during the commissioning period to evaluate the telescope's performance in single-telescope mode as summarized in our first performance paper [12]. Although the trigger threshold was not fully stable at the beginning of the commissioning phase, it has been stable since August 2021, thanks to the dedicated threshold control system, and the trigger threshold is 20 GeV, increasing to around 30 GeV after analysis cuts. The angular resolution is around 0.17° for $E > 1$ TeV and around 0.34° at E = 100 GeV after the baseline cuts (70% gamma ray retainment efficiency) used to derive the spectra. The energy resolution reaches the level of 20% for $E > 1$ TeV, and 35% at E=100 GeV for low-zenith observations with the same cuts.

Fig. 10 shows the energy spectrum of the Crab Nebula obtained with the standard analysis. This spectrum is very close (within 10%) to the spectrum determined with the MAGIC telescopes. We also find a smooth connection between the LST-1 spectrum and the *Fermi*-LAT one, especially when the possible systematics in the background normalization in the LST-1 near-threshold analysis are taken into account.

Fig. 11 shows the differential sensitivity of the LST-1. In addition to the standard source-independent analysis, we also performed source-dependent analysis with a priori knowledge of the gamma-ray source position to compute the sensitivity. Although the source-dependent analysis provides slightly better energy resolution and smaller bias below 50 GeV, the differential sensitivity is almost similar between the two analysis methods. The 50-hour sensitivity above 100 GeV is about 1.5 times worse than that of the MAGIC telescopes that operate

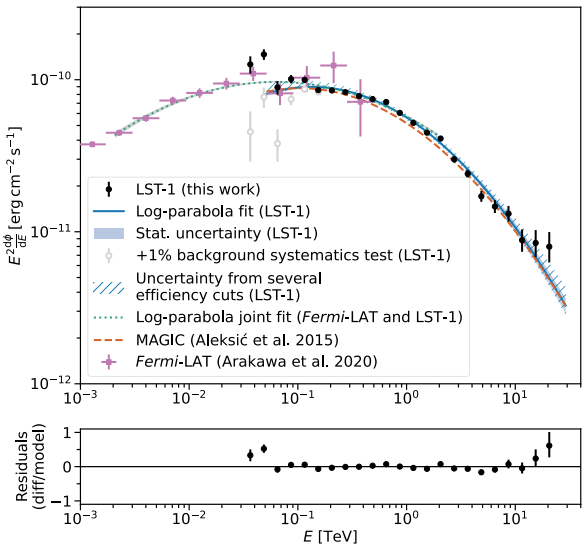


Fig. 10. SED of the Crab Nebula for the entire LST-1 dataset obtained with the source-independent analysis [12]. Flux points (black circles) and best-fit model (solid blue line) correspond to the dataset with a cut in image intensity above 80 p.e., and energy-dependent gammaness and theta selection cuts with 70% gamma ray retainment efficiency. The solid error band illustrates the statistical uncertainty of the fit. Open markers represent the effect of increasing the background normalization by 1%, to show that even such a small systematic error can have a large effect, well beyond the statistical uncertainty, on the flux at the lowest energies. The joint fit of the *Fermi*-LAT and LST-1 spectra is represented by the dotted line (accompanied by its statistical uncertainty band).

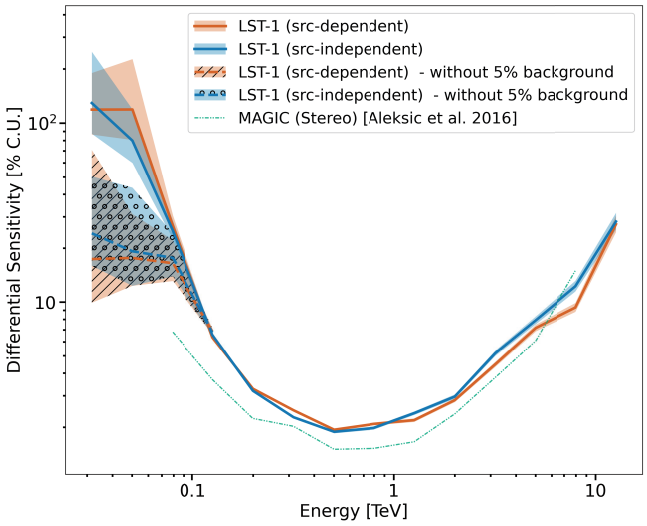


Fig. 11. Differential sensitivity of LST-1 for source-dependent and source-independent analyses, versus reconstructed energy, with and without including the condition that the signal-to-background ratio has to be at least 5% [12]. The MAGIC reference is taken from [13].

in a similar energy range in stereoscopic mode, as expected. The optimal 50-h differential sensitivity achieved is around 1.7% C.U. at 800 GeV using source-independent analysis. The best integral sensitivity of the instrument is 1.1% C.U. above 250GeV in 50 hours (12.4% C.U. in 0.5 hours).

We have prepared the repository including code and data to reproduce the figures (only the data points, not the entire

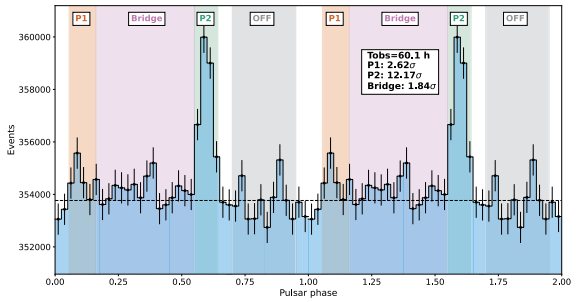


Fig. 12. Phase diagram of the Geminga pulsar observed with LST-1, where the emission of the second pulse (P2) is significantly detected [14].

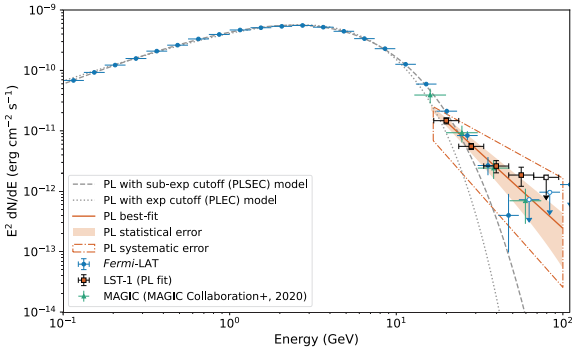


Fig. 13. Spectral Energy Distribution of the Geminga pulsar, showing compatibility between LST-1 and MAGIC results [14].

data analysis) of the LST-1 performance paper [6].

Geminga Pulsar with LST-1

The gamma-ray emission mechanism of pulsars is not fully understood, and observation above 10 GeV is particularly important. That is one of the main physics targets of CTAO. Geminga is the second gamma-ray pulsar firmly detected by LST-1 after the Crab pulsar [14].

The LST-1 phase diagram of the Geminga pulsar (Fig. 12) reveals statistically significant emission ($\sim 12\sigma$) for the second pulse (P2). This complements the previously published results of *Fermi*-LAT and MAGIC [15]. It should be noted that this phase diagram was obtained with 60 hours of observations, while MAGIC needed 80 hours to detect the pulsation with a lower statistical significance. The first pulse (P1), which is not detected with MAGIC, also reaches a significance of $\sim 2.6\sigma$ in our LST-1 observations. The best-fit model for the spectrum of P2 was found to be compatible with the previous results obtained by the MAGIC (Fig. 13). The overall results prove the high sensitivity of LST-1 at the lowest energies ($10-30$ GeV).

Background tool development

IACTs detect air showers initiated not only by gamma rays but also by the isotropic cosmic ray (CR) flux. Despite advances in background rejection techniques, a fraction of CR-induced events produce electromagnetically dominated cascades that are indistinguishable from gamma-ray showers [16, 17, 18]. These gamma-like events pass standard selection cuts and contribute a background across the full field of view (FoV).

Analyses of diffuse emission, overlapping sources, or sources with uncertain positions require image-based 3D analysis methods that critically depend on an accurate background model. The shape and intensity of this background vary with observational conditions such as atmospheric quality and telescope pointing [19]. Consequently, background levels must be either measured directly or estimated via Monte Carlo simulations. However, simulations are computationally intensive and suffer from larger uncertainties in the modelling of hadronic interactions compared to electromagnetic showers [20].

Our group has developed and maintains the `pybkgmodel` software package[7] [21], which reconstructs the IACT background in the full camera FoV. Its modular design supports various input formats and reconstruction techniques, such as from [22], allowing users to adapt the background estimation method to the needs of each analysis, balancing statistical and systematic uncertainties. The open source package is fully compatible with the CTAO software ecosystem and produces outputs in the standard gamma-ray data format (GADF)[8], ensuring compatibility with tools such as `gammapy` [23].

`pybkgmodel` has reached a stable release and is already widely used within the CTAO-LST collaboration. It plays a key role in several analyses presented here, including the studies of the Galactic Center and the Cygnus region drift scan.

LST-1 drift scan observations of the Cygnus cocoon region

The Cygnus cocoon is one of the most-studied star-forming regions in the Galaxy and has already been observed in the gamma-ray band with *Fermi*-LAT [24], HAWC [25] and LHAASO [26] telescopes. However, its large $r_{68} \simeq 3$ deg extension [27], comparable or larger than the field of view of the ground-based Cherenkov telescopes, precluded their conventional pointing observations due to the source and background regions confusion.

To resolve this problem, we performed the so-called "drift scan" observations of the Cygnus cocoon region with LST-1. In the drift scan mode, the telescope is kept at a fixed azimuth/altitude position for the duration of the entire observation, allowing the source to pass its field of view as the Earth rotates. With telescope performance generally depending on the pointing azimuth/altitude, such observations yield the most stable telescope sensitivity and counting rates over time.

A preliminary view of the Cygnus cocoon from LST-1 drift scan data is given in Fig. 14. The sky map in this figure covers a large, roughly $10^\circ \times 3^\circ$ region centered on the cocoon position, far exceeding the LST-1 instantaneous field of view.

*6 https://github.com/cta-observatory/lst-crab-performance-paper-2023

*7 https://github.com/cta-observatory/pybkgmodel

*8 https://gamma-astro-data-formats.readthedocs.io/en/v0.3/

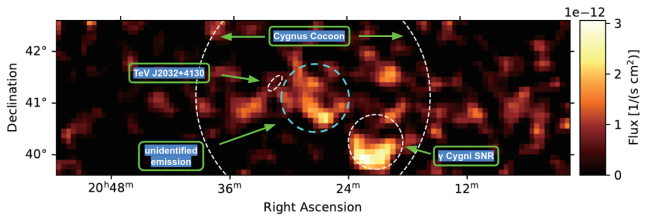


Fig. 14. Sky map of the Cygnus cocoon region in the 0.1-10 TeV energy range, obtained from the LST-1 drift scan observations. White contours mark some of the known γ-ray sources in the region – the γ Cygni supernova remnant and the binary system TeV J2032+4130 as well as the expected extension of the Cocoon's γ-ray emission. Also marked is the unidentified extended emission that may be linked to the Cocoon's central part. The sky map is smeared with the 0.1° Gaussian kernel for better readability.

Despite the limited exposure of only 12 hours, LST-1 observations reveal the well-known γ Cygni supernova remnant and a binary system TeV J2032+4130 (visible only at higher energies, thus not standing out in this picture). Importantly, these observations indicate the presence of a more extended Cocoon emission with LST-1 likely resolving its central part.

Due to the novelty of the drift scan technique for CTAO and LST collaborations, the analysis of these data is still ongoing. With the associated developments and know-how, these observations may further serve as a pathfinder for future drift scan observations with the entire CTAO array.

Galactic Center

The current IACTs, such as H.E.S.S., MAGIC, and VERITAS, have detected VHE gamma-ray emission in the Galactic Center region. A highlighted hypothesis, also known as the PeVatron scenario, suggests that the supermassive black hole Sagittarius A* (Sgr A*) accelerates cosmic rays to PeV energies, producing diffuse gamma-ray emission extending up to tens of TeV spanning a few hundred parsecs along the Central Molecular Zone (CMZ) [31]. However, previous IACT observations have reported discrepant results due to methodological differences, limiting the comparability and interpretability of the spectral features. For instance, H.E.S.S. initially reported a power-law spectrum within an annular region spanning 20–60 pc from Sgr A*, while recent MAGIC observations have indicated a $\sim 2\sigma$ hint of a spectral cutoff near 20 TeV in the emission integrated over the central ridge [32]. In contrast, no such evidence for a cutoff has been reported by H.E.S.S. or VERITAS for an extended component in the region.

The LST-1 provides sensitivity enhanced in the TeV energy range under large zenith-angle observations, despite an unavoidable increase in the energy threshold. In addition, the relatively wide field of view ($\sim 4.5^\circ$ in diameter) of LST-1 allows for more uniform coverage of the Galactic ridge compared to other IACTs in the Northern Hemisphere. In this study, LST-1 observations of the Galactic Center region, illustrated in Fig. 15, reveal a stronger hint than the MAGIC study for a spectral cutoff around 20 TeV with a statistical preference of approximately 3σ over a simple power-law model. This result highlights LST-1's capability to perform spatially extended TeV gamma-ray measurements and contributes to a more refined understanding of particle acceleration processes in the Galactic Center. We note that a PhD thesis presenting these results was successfully defended in this fiscal year [34], in addition to presentations at international conferences [33].

Dark Matter

Dark matter (DM) remains one of the most compelling unresolved problems in modern physics. Among the various theoretical candidates, Weakly Interacting Massive Particles (WIMPs) are particularly well-motivated due to their natural emergence in extensions of the Standard Model. At VHE, some channels of WIMP interactions are predicted to produce gamma rays. The Galactic Center region is, owing to its relative proximity and anticipated high DM density, regarded as one of the most promising targets for such indirect searches. IACTs have placed some of the most stringent constraints on WIMP models in this region.

In our study, we develop a DM analysis dedicated to LST-1, and perform the first sensitivity evaluation for WIMP searches with LST-1, with background realistically estimated from observational data. This evaluation demonstrates that LST-1 is already sufficiently competitive compared to the current-generation telescopes despite the monoscopic view, on account of the large-zenith-angle observations and the wide field of view. These results contribute to shaping the strategic direction of DM searches with LST-1, the upcoming LST sub-array, and the future CTAO-North full array. As a result, CTAO-North will be newly taken into account, in addition to CTAO-South, for DM searches in the Galactic Center region. Our study, which reshapes the design of the key science projects for the consortium, has been recognized as an impactful contribution within the framework of international collaboration.

SNR G17.8+16.7

G17.8+16.7 is a recently identified supernova remnant (SNR) characterized by its shell-like morphology and non-thermal radio spectrum [28] in the vicinity of the gamma-ray source FHES J1723.5−0501 listed in the Fermi High-Latitude Extended Sources Catalog. Araya et al. (2022) [28] conducted a comprehensive analysis of GeV gamma rays and discussed some of the characteristics of the SNR. The estimated age of the SNR was determined to be $\sim$10 kyr based on the morphological and brightness characteristics. The large diameter in GeV energies ($\sim 1.4^\circ$) facilitates the investigation of the origin of the gamma-ray emission (SNR or pulsar wind nebula) and the interaction with the surrounding matter using the point spread function of an IACT experiment.

It is important to acknowledge the fact that this extended SNR is situated at a high Galactic latitude. This SNR is a rare and valuable example for studying particle acceleration in low-density gas. SN 1006 (G327.6+14.6) was previously the only SNR with this feature, and G17.8+16.7 might be a future (evolved) figure of SN 1006 given its estimated age of 10 kyr determined by Araya et al. (2022) [28]. This provides a unique opportunity to study particle acceleration in a middle-aged SNR embedded within a low-density gas. Indeed, SN 1006 and this source are thought to be the only two

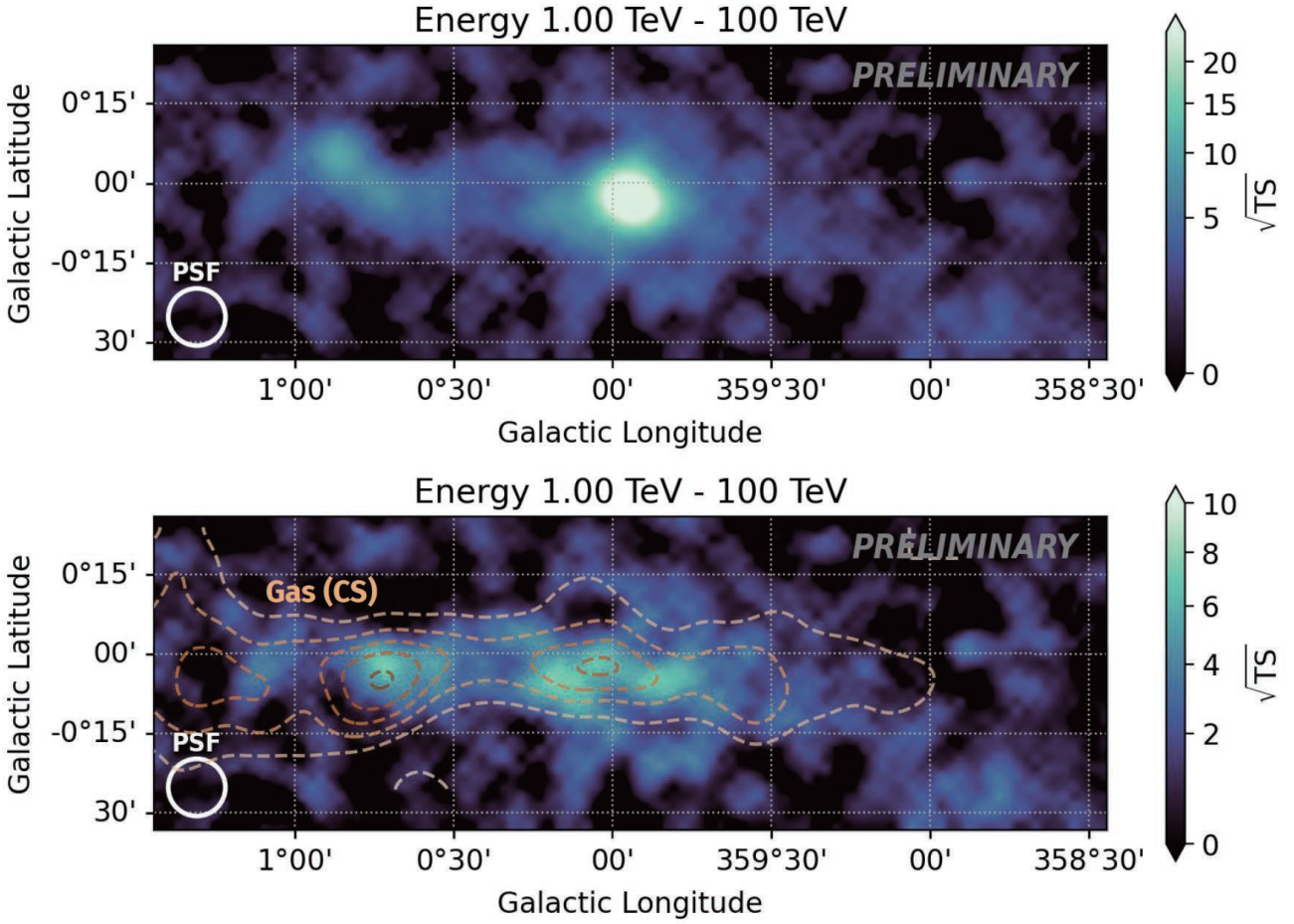


Fig. 15. Sky map of the Galactic Center region obtained from LST-1 observations. The maps are smoothed using a Gaussian kernel with a standard deviation of 0.06°. The circle in the lower left corner indicates the 68% containment radius of the point-spread function (PSF). *Top:* Sky map in units of statistical significance. *Bottom:* Residual sky map after subtracting the best-fit models for Sgr A* and G0.9+0.1. Overlaid contours represent the gas distribution traced by CS molecular line emission, velocity-integrated and smoothed accordingly, based on data from [30].

SNRs whose gamma-ray emission processes are definitely leptonic, owing to their low gas densities.

The gamma-ray emission from G17.8+16.7 exhibits a hard spectrum, and a simple one-zone leptonic model can naturally explain the multi-wavelength non-thermal fluxes of the source. However, the high-energy cutoff in the particle distribution was not constrained because of *Fermi*-LAT's insufficient sensitivity above 100 GeV. To investigate this energy regime, we carried out the observation of the SNR with the LST-1. The total observation time was nearly 11 hours. We applied quality cuts based on the stability of the shower rates for the dark-night observations, yielding 6.8 hours of good-quality data used for subsequent analysis. The preliminary results of the analysis yielded upper limits on the SED, which can put a constraint on the maximum energy of the accelerated particles. These preliminary results were presented in [29], and more detailed results will be reported elsewhere.

LST-1 observations of active galactic nuclei

The extragalactic VHE sky observed by the ground-based IACTs is dominated by a special subclass of active galactic nuclei (AGNs) called "blazars". Blazars are radio-loud AGNs whose relativistic jets are aligned closely to our line of sight, characterised by broadband non-thermal emission and rapid variability spanning the radio to very high energy (VHE) gamma-ray bands. In recent years, LST-1 has detected a few well-known blazars with redshifts ranging from 0.03 to 0.997, owing to its high sensitivity down to a few tens of GeV. From February to April of 2023, LST-1 observed a TeV blazar 1ES 1218+304 at a redshift of 0.182 during a moderately active state and detected it with 5.8σ significance (preliminary) with 4.4 hours of good-quality data. The VHE spectral slope is consistent with the previous observations of 1ES 1218+304 reported by other VHE telescopes. We modeled the broadband spectral energy distribution of 1ES 1218+304 using a leptonic one-zone synchrotron self-Compton scenario and obtained physical parameters compatible with the literature. During this period, 1ES 1218+304 was simultaneously observed by the neighboring MAGIC telescope in the VHE band, and by the Neil Gehrels Swift Observatory in the optical–UV–X-ray band. With a preliminary analysis, we obtained 7.2σ significance with only 2.2 hours of joint LST-1 + MAGIC observation of 1ES 1218+304, demonstrating the improvement of sensitivity with a joint IACT system over monoscopic IACT. We have reported these results in several conferences [35, 36]. Our results indicate a signif-

icant advancement of AGN research in the near future with the upcoming stereoscopic system consisting of four LSTs, as its enhanced sensitivity will lead to the detection of numerous new AGNs and improved time-resolved analysis of known sources.

GRB 221009A: The "Brightest-Of-All-Time" Gamma-Ray Burst

Gamma-ray bursts (GRBs) are the most luminous electromagnetic transient phenomena in the universe. GRBs with durations longer than a few seconds are believed to be triggered when the fast-rotating core of a massive star collapses to a black hole or a highly magnetized neutron star, giving rise to powerful, transient ultrarelativistic jets. However, the basic nature and formation mechanism of such jets remain mysterious.

GRB 221009A was the brightest GRB discovered to date, and nicknamed the "brightest-of-all-time (BOAT) GRB". The event provided a unique opportunity to scrutinize a long GRB in unprecedented detail. The most notable finding from extensive multiwavelength observations of GRB 221009A was the first strong evidence of a "structured jet" in a long GRB. In order to explain the entire multiwavelength dataset, the jet must consist of a fast and narrow inner jet component, surrounded by a slower and wider outer jet component. This contrasts with earlier studies of less bright events in which jets with a simpler assumed structure were sufficient to explain all of the data. Such inferences for GRB 221009A offer a new window onto the poorly understood physics of jets in GRBs.

Unfortunately for Cherenkov telescopes, including LST-1, the GRB occurred during conditions with strong moonlight, which severely limited its sensitivity. Nevertheless, follow-up observations were performed as much as possible for the first 20 days or so after the GRB. Dedicated analysis of the data revealed a 4.1 σ excess over the background at $\sim$1.3 days after the burst, but the spectrum was not well constrained. At later times, only upper limits could be derived.

Despite the apparently limited results, the LST-1 data actually constitute a critical piece in the puzzle. Fig.16 compares observed data versus theoretical models for the light curve of gamma rays in the 0.3-5 TeV band. In between data from LHAASO up to $\lesssim$3000 sec and upper limits from H.E.S.S. at $\gtrsim$2 day, our LST-1 data at $\sim$1.3 day actually fills a gap in the VHE data. Moreover, this turns out to be crucial for discriminating between different models. The three models shown in the plot are different types of structured jet models, all of which are consistent with the LHAASO data at earlier times, but then diverge from each other at $\gtrsim 10^4$ sec, differing by more than an order of magnitude at $\sim$1.3 day. If our 4.1 σ excess is a true gamma-ray signal, it seems most consistent with Zhang et al. 2025. While it may also be marginally consistent with Ren et al. 2024, it disfavors Zheng et al. 2024.

Future observations of GRBs in less unfortunate conditions, as well as a complete LST array, will likely allow significantly better spectral and temporal coverage. Such data promises to offer new insight into the mystery of how jets form and propagate in GRBs.

More details can be found in a paper in press for the Astrophysical Journal Letters, the very first letter for CTAO [37]. Of the four corresponding authors, two are Japanese: Kenta Terauchi played a crucial role in the data analysis, and Susumu Inoue led the theoretical interpretation.

Theoretical modeling on gamma-ray pulsars

Based on a unique, innovative methodology, we established a toy model for fitting gamma-ray phase diagrams of pulsars. Our toy model assumes a north-south symmetric configuration as well as a circularly symmetric beam per hemisphere. We highlight that some geometrical effects and physical effects (e.g. Time Delay, Doppler Shift) could collectively deform a pulse profile to the asymmetric form that we detect.

Doppler Shift is the most innovative and critical element of our methodology. Because of the Doppler Shift, photons with the same E_{det} (Doppler-shifted energy in the detector's frame) but at different phases actually correspond to different E_{psr} (Unshifted energy in the pulsar's frame).

We performed case studies on Crab, Geminga, Dragonfly & Vela pulsars, which are the brightest gamma-ray pulsars. We obtained satisfactory fits between our model predictions and the observational results. Our fitting results [38] preliminarily suggest that the third components of these four pulsars could be interpreted as Doppler-boosted tails of Beam2. Besides, our inferred emission site locations and beam axis directions give endorsement to some wind models. Moreover, for the Crab pulsar, we report a preliminary qualitative correlation between the X-ray polarisation angle and the dominating γ-ray pulse component.

Other contributions by CTAO-Japan members

On top of the above-mentioned activities, CTAO-Japan members have been contributing to many other projects. There are some examples of results that were presented at domestic and international conferences.

- Pipeline to detect AGN flare using *Fermi*-LAT data for LST ToO observations [39]
- LST-1 first detection of Flat spectrum radio quasar (FSRQ) OP313 using IACT [40, 41, 42]
- Classical TeV-blazar observations with LST-1 (Mrk 421, Mrk 501, 1ES 1959+650, 1ES 0647+250, PG 1553+113) [43, 44]
- Observation of Seyfert galaxy NGC 1068[45]
- Search for Primordial Black Holes [46]
- Reconstruction of gamma-ray showers using the time evolution of Cherenkov Photons [47, 48]

In addition to the main research topics discussed above, several of the group members are working on some smaller projects promising advances for further scientific research with LSTs.

Bibliography

[1] Design Concepts for The Cherenkov Telescope Array, The CTA Consortium, Exper. Astron. 32 (2011) 193-316.

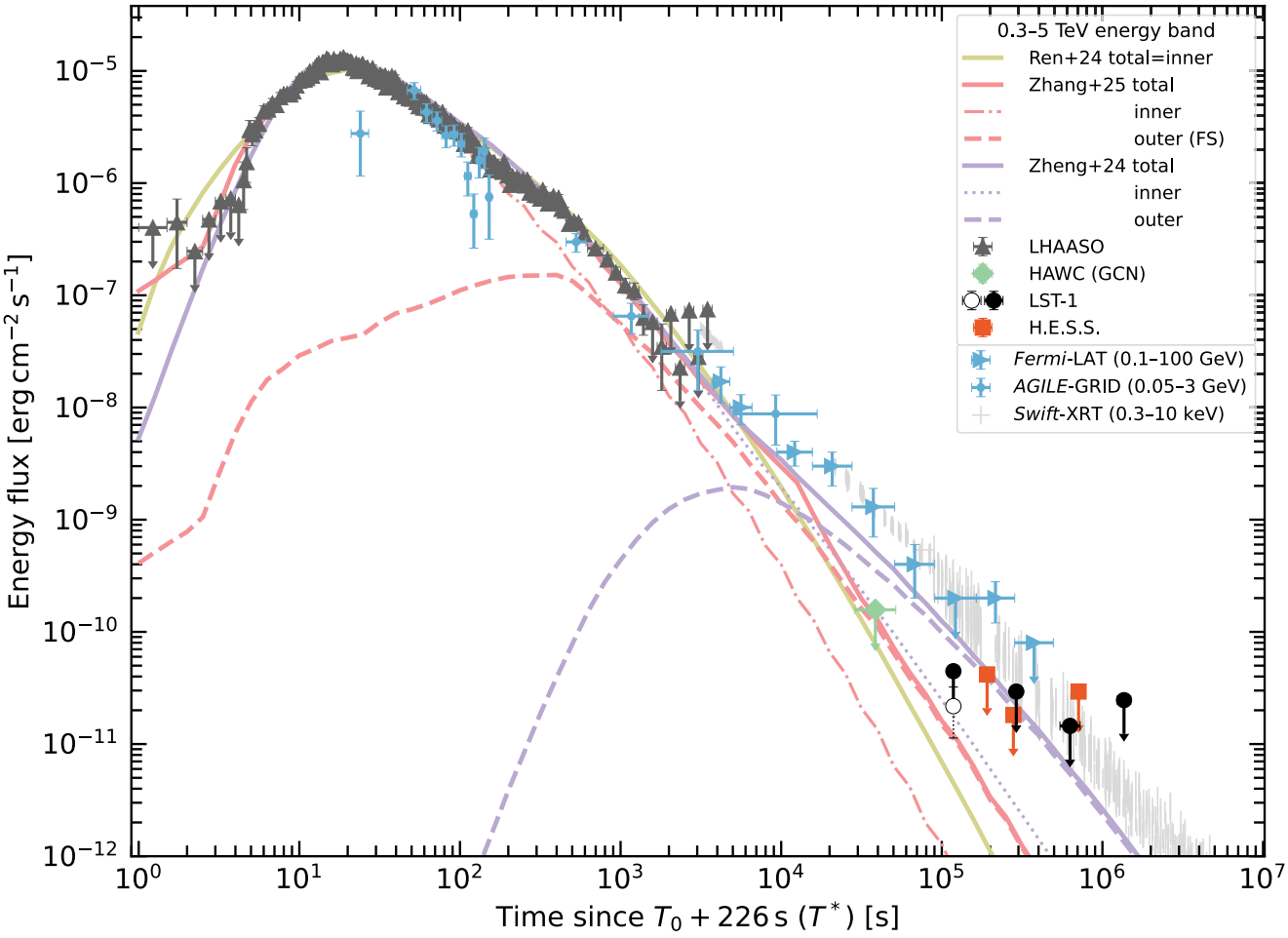


Fig. 16. GRB 221009A light curve compared with models. Energy flux at 0.3-5 TeV versus time since the burst trigger (T_0) shifted by +226 s. Data from LHAASO (dark gray vertical triangles), HAWC (green diamond), LST-1 (black filled and empty circles for upper limits and the energy flux point, respectively), and H.E.S.S. (orange squares). Model curves from Ren et al. 2024, Zheng et al. 2024, and Zhang et al. 2025 in gold, purple, and red, respectively. For the latter two, the contributions from the inner and outer jet regions are also shown separately. For more details, see [37]

[2] Science with the Cherenkov Telescope Array, arXiv:1709.07997

[3] CTAO Consortium website: http://www.cta-observatory.jp/ and http://www.ctao.org/.

[4] Design and production of segment mirrors for the Large-Sized Telescopes of the Cherenkov Telescope Array, T. Inada et al., Proceedings of SPIE Astronomical Telescopes + Instrumentation 2020, 11451 (2020)

[5] Development and quality control of PMT modules for the large-sized telescopes of the Cherenkov Telescope Array Observatory, T. Saito et al., NIM A, 1073, 170229 (2025)

[6] Multiwavelength study of the galactic PeVatron candidate LHAASO J2108+5157, K. Abe et al., A&A, 691, A328 (2024)

[7] Detection of RS Oph with LST-1 and modelling of its HE/VHE gamma-ray emission, K. Abe et al., A&A, 695, A152 (2025)

[8] The CTA LST South as part of the CTA+ program, L.A. Antonelli et al., PoS, ICRC2023, 444, 755.

[9] The ASTRI Mini-Array Gamma-Ray Experiment, EPJ Web of Conferences 319, 01003 (2025)

[10] Silicon photomultipliers for the SST camera of the Cherenkov Telescope Array, NIM. A, 1060, 169047 (2024)

[11] Study on dark-current long-term instability in SiPM and light emission from APD cells, R. Kawarasaki et al., JPS meeting (Sapporo)

[12] Observations of the Crab Nebula and Pulsar with the Large-sized Telescope Prototype of the Cherenkov Telescope Array, H. Abe et al., ApJ, 956, 80 (2023)

[13] The major upgrade of the MAGIC telescopes, Part II: A performance study using observations of the Crab Nebula, J. Aleksić et al., Astroparticle Physics, 72, 76 (2016)

[14] Detection of the Geminga pulsar at energies down to 20 GeV with the LST-1 of CTAO, CTAO-LST Project, Abe et al., A&A Accepted arXiv:2505.21632 (2025)

[15] Detection of the Geminga pulsar with MAGIC hints at a power-law tail emission beyond 15 GeV, MAGIC Collaboration, Acciari et al., A&A 643 L14 (2020)

[16] A Cocoon of Freshly Accelerated Cosmic Rays Detected by Fermi in the Cygnus Superbubble, G. Maier & J. Knapp Astrop. Phys., 28, 1, 72-81, 2007.

[17] The background from single electromagnetic subcascades for a stereo system of air Cherenkov telescopes, D. Sobczyńska J. Phys. G: Nucl. Part. Phys., 36, 125201, 2009.

[18] Nature of the low-energy, gamma-like background for the Cherenkov Telescope Array, J. Sitarek et al. Astrop. Phys., 97, 1-9, 2018.

[19] Background modelling in very-high-energy gamma-ray astronomy, D. Berge et al. A&A, 466, 1219–1229, 2007.

[20] Effect of the uncertainty in the hadronic interaction models on the estimation of the sensitivity of the Cherenkov telescope array, M. Ohishi et al. J. Phys. G: Nucl. Part. Phys., 48, 075201, 2021.

[21] Pybkgmodel- a background modelling toolbox for the CTA, M. Strzys et al. PoS, ICRC2023, 894, 2023.

[22] Spatial likelihood analysis for MAGIC telescope data, I. Vovk et al. A&A, 619, A7, 2018.

[23] Gammapy: A Python package for gamma-ray astronomy, A. Donath et al. A&A, 678, A157, 2023.

[24] A cocoon of freshly accelerated cosmic rays detected by Fermi in the Cygnus superbubble, M. Ackermann, M. Ajello, A. Allafort, et al. Science, 334(6059):1103, November 2011.

[25] HAWC observations of the acceleration of very-high-energy cosmic rays in the Cygnus Cocoon, A. U. Abeysekara et al. Nature Astron., 5(5):465–471, 2021. [Erratum: Nature Astron. 5, 724–724 (2021)].

[26] An ultrahigh-energy gamma-ray bubble powered by a super PeVatron, LHAASO Collaboration. Science Bulletin, 69(4):449–457, February 2024.

[27] Multiple emission components in the Cygnus cocoon detected from Fermi-LAT observations, X. Astiasarain, L. Tibaldo, P. Martin, J. Knödlseder, and Q. Remy. A&A, 671:A47, March 2023.

[28] G17.8 + 16.7: A new supernova remnant, Araya M., Hurley-Walker N., Quir´os-Araya S., 2022, MNRAS, 510, 2920

[29] Observation of SNR G17.8+16.7 with LST-1, H. Katagiri et al., ASJ meeting (Mito)

[30] Dense Molecular Clouds in the Galactic Center Region. I. Observations and Data, M. Tsuboi et al., 1999, ApJS, 120, 1

[31] Acceleration of petaelectronvolt protons in the galactic centre, HESS Collaboration, Nature, 531 (2016) 476.

[32] MAGIC observations of the diffuse emission in the vicinity of the galactic center, MAGIC Collaboration, A&A 642 (2020) A190.

[33] Galactic Center Observations with CTAO LST-1, Shotaro Abe, Abhishek, Michele Doro, Tomohiro Inada, Marcel Strzys, Masahiro Teshima, and Ievgen Vovk for the CTAO-LST Project, EPJ Web Conf. 319 (2025) 05006.

[34] TeV Gamma-Ray Emission across the Galactic Center Ridge with the First CTA Large-Sized Telescope, S. Abe, Doctoral Dissertation (2025).

[35] LST-1 observations and multiwavelength study of blazar 1ES 1218+304, A. Roy et al., HEAC2024 (Yerevan)

[36] Very High Energy observations and multiwavelength study of blazar 1ES 1218+304, A. Roy et al., ASJ meeting (Mito)

[37] GRB 221009A: Observations with LST-1 of CTAO and implications for structured jets in long gamma-ray bursts, Astrophysical Journal Letters, in press

[38] A mechanism-independent methodology for modeling γ-ray phaseograms of pulsars in the framework of north-south symmetry, Yeung et al., submitted to MNRAS

[39] CTAO report 233: Status of the AGN ToO Observations with CTAO LST-1, S. Nozaki et al., JPS meeting (online)

[40] Detection of explosive VHE gamma-ray flare from the distant quasar OP313 with the LST-1 of CTAO, S. Nozaki et al., COSPAR2024 (Busan)

[41] LST-1's Early Achievements in AGN Observations: Discovery of the Farthest Blazar OP 313, J. Baxter et al., Gamma2024 (Milano)

[42] LST-1's Early Achievements in AGN Observations: Discovery of the Farthest Blazar OP 313, J. Baxter et al., ASJ meeting (Kobe)

[43] Study of the variable VHE gamma-ray emission of bright AGN with LST-1, R. Takeishi et al., TeVPA2024 (Chicago)

[44] CTAO report 229: Observation of Active Galactic Nuclei with the Large-Sized Telescope prototype of the Cherenkov Telescope Array, R. Takeishi et al., JPS meeting (Sapporo)

[45] CTAO Report 234: Observation of the NGC 1068 with the CTAO Large-Sized Telescope, Y. Yao, JPS meeting (online)

[46] CTAO report 236: Plan of Primordial Blackhole Search with CTAO/LST-1, M. Takahashi et al., JPS meeting (online)

[47] CTAO Report 231: The possibility of using the time evolution of the number of Cherenkov photons in the reconstruction of the position of the gamma-ray shower, B. Sunghyun et al, JPS meeting (Sapporo)

[48] CTAO Report 237: Reconstruction of Gamma-Ray Showers using the time evolution of Cherenkov photons, B. Sunghyun et al, JPS meeting (online)

TA: Telescope Array Experiment

Spokespersons: S. Ogio[1] (Dec. 2017 - Dec. 2023), Y. Tsunesada[2] (Dec. 2023 - present), J.N. Matthews[3]

1 : ICRR, The Univ. of Tokyo
2 : Graduate School of Science, Osaka Metropolitan Univ.
3 : Dept. of Physics and Astronomy, Univ. of Utah

Collaborating Institutions:

Academia Sinica, Taipei, Taiwan; Chubu Univ., Kasugai, Japan; ERI, Univ. of Tokyo, Tokyo, Japan; Hiroshima City Univ., Hiroshima, Japan; Hanyang Univ., Seoul, Korea; ICRR, Univ. of Tokyo, Kashiwa, Japan; INR, Moscow, Russia; CEICO, Inst. of Phys, Czech Acad. of Sci., Prague, Czech Republic; Kanagawa Univ., Yokohama, Japan; KEK/IPNS, Tsukuba, Japan; Kochi Univ., Kochi, Japan; Loyola Univ. Chicago, Chicago, USA; Moscow M.V. Lomonosov State University, Moscow, Russia; National Centre for Nuclear Research, Warsaw, Poland; NICT, Tokyo, Japan; Osaka Electro-Comm. Univ., Neyagawa, Japan; Osaka Metropolitan Univ., Osaka, Japan; RIKEN, Wako, Japan; Shibaura Inst. Tech., Tokyo, Japan; Shinshu Univ., Nagano, Japan; SKKU, Suwon, Korea; Tokyo City Univ., Tokyo, Japan; ULB, Brussels, Belgium; UNIST, Ulsan, Korea; Univ. of Nova Gorica, Nova Gorica, Slovenia; Univ. of Utah, Salt Lake City, USA; Univ. of Yamanashi, Kofu, Japan; Yonsei Univ., Seoul, Korea

Introduction

The Telescope Array (TA) is the largest Ultra-High Energy Cosmic Ray (UHECR) observatory in the northern hemisphere. The main aim of TA is to explore the origin and nature of UHECRs by measuring the energy spectrum, arrival direction distribution and mass composition. The TA collaboration consists of approximately 150 researchers from the USA, Russia, Korea, Belgium, Czech Republic, Slovenia, Poland, Taiwan, and Japan.

The TA detector consists of a surface array of 507 plastic scintillator detectors (SD) and three stations of fluorescence detectors (FD). It is located in the desert, approximately 200 km south of Salt Lake City in Utah in USA. The SDs were deployed on a square grid with 1.2-km spacing, and the SD array covers an area of approximately 700 km^2. Each SD has two layers of 1.2-cm-thick scintillator with an area of 3 m^2. The full operation of SDs started in March 2008. The duty cycle is approximately 95% on average. One northern FD station at the Middle Drum (MD) site uses 14 refurbished HiRes telescopes. Two southern FD stations at the Black Rock Mesa (BRM) and Long Ridge (LR) sites were built newly each with 12 telescopes. The MD FD views 3° - 31° and the BRM and LR FDs view 3° - 33° above the horizon. All three FD stations started the observation in November 2007, and have duty cycles of approximately 10%.

TA found evidence for intermediate-scale anisotropy of arrival directions of cosmic rays with greater than 5.7×10^{19} eV of energy [1]. With enhanced statistics, it is expected to observe the structure of the hotspot along with other possible excesses and point sources, along with the correlations with extreme phenomena in the nearby universe. TA proposed the TAx4 project to quadruple the effective area of the TA SD aperture, including the existing TA SD array by installing additional 500 newly designed SDs on a square grid with wider, 2.08-km spacing between each. The layout of TAx4 is shown in Fig. 1.

The design of SD for the TAx4 experiment is identical to the design of SD for the TA Low energy Extension(TALE) experiment, which will be described in detail later. The basic design is common to TA, but the number and arrangement of wavelength shifter fibers (WLSF), the performance of the photomultiplier tubes (PMTs), and the wireless LAN module and used protocols are different. In the TAx4 and TALE, we use a PMT with significantly improved quantum efficiency and surface uniformity. This has allowed us to reduce the total length of WLFSs by 67% while maintaining the performance of the SD as a whole. A new wireless LAN module is used for the TAx4 and TALE SDs because the one used in TA was out of production.

Detector installation for TAx4 began in 2019, and 257 SDs were deployed in February and March 2019. By this installation, the total coverage area with SDs, including the original TA SD array, has been increased by a factor of 2.5. The new SD array started the data acquisition in April 2019. Since the new SD array is divided into two lobes, two FD stations are required to overlook each lobe in order to increase the number of hybrid events for the measurement of $X_{\rm max}$ and to confirm the energy scale. These FD stations consist of refurbished HiRes telescopes: four telescopes at the MD site and eight telescopes at the BR site. The TAx4 FD station at the northern site was constructed and started stable observation in June 2018. The TAx4 FDs at the southern site were constructed and started observation in 2019. The recent status of TAx4 was reported in [2].

The TA Low energy Extension (TALE) enables detailed studies of the energy spectrum and composition from $\sim10^{16.5}$ eV. The main objective of TALE is to clarify the transition from galactic to extragalactic cosmic ray origins based on a comparison between Monte Carlo (MC) simulations created using the latest LHC experimental results and observed air shower data. The TALE detector is located north of the TA site (at around the MD FD station). The TALE FD station consists of 10 refurbished HiRes telescopes. The TALE FD views 31° - 59° in elevation angle. The TALE detectors are located at the northern corner of the TA detectors. The TALE FD operation was commenced in the spring of 2013. The TALE SD

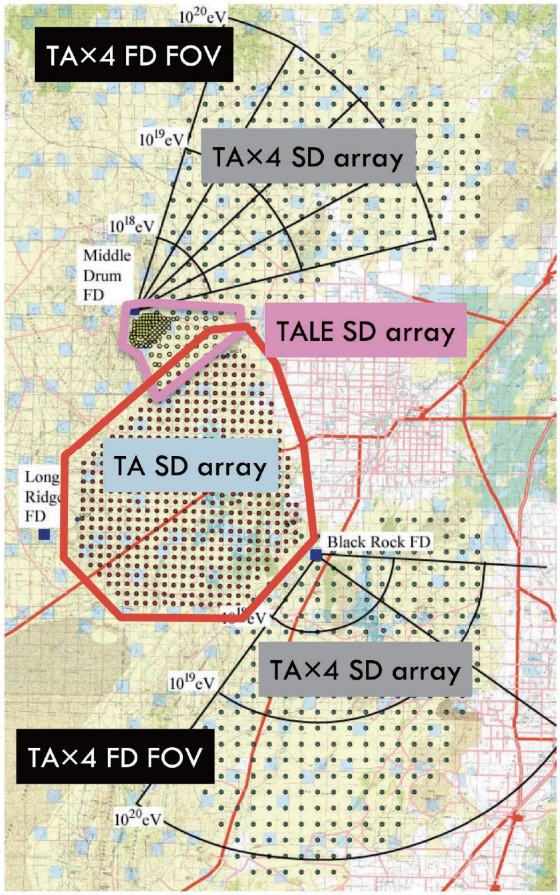
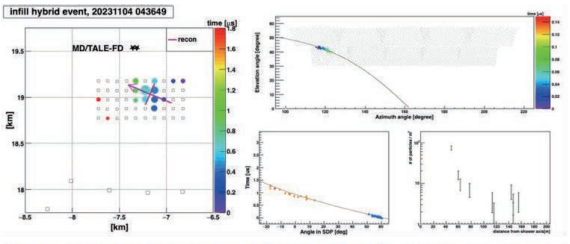


Fig. 1. The layout of the TA, TAx4, and TALE. The array of 507 SDs is the original TA SD array. There are three TA FD stations (Middle Drum to the north, Long Ridge to the west, and Black Rock Mesa to the east of the TA SD array) with black square symbols. The array of surface detectors to the north of the TA SD array is the TALE SD array. The additional TAx4 500 surface detectors will be located in separate lobes on the northeast and southeast sides of the TA SD array. The 257 SDs have already been deployed for TAx4. Two additional FD stations with refurbished HiRes telescopes for the TAx4 are located at the Middle Drum and Black Rock Mesa sites, and view to the northeast and southeast, as denoted by the frame of the fan.

array consists of 80 SDs (40 SDs with 400-meter spacing and 40 SDs with 600-meter spacing). The TALE SD array was completed in February 2018 and is in stable operation. The mode energy of TALE hybrid events is $10^{16.8}$ eV.

The TALE infill experiment is a further extension of TA-TALE detectors to observe low-energy cosmic rays down to the PeV region. TALE infill uses existing TALE-FD detectors and newly developed "infill" SDs with 100m spacing. 50 SDs used in the TALE infill array were manufactured at the Akeno observatory of ICRR in October 2021. In the summer of 2022, these detectors were transported to the TA site and installed in the area between the TALE FD station and the TALE SD array in October 2022. The TALE infill array started routine hybrid observations with TALE FDs in October 2023. An example of events detected by this hybrid system is shown in Fig. 2. The mode energy of TALE infill SD array events is $10^{15.5}$ eV.



Result.	θ[deg]	φ[deg]	Rp[km]	ψ[deg]	coreX[km]	coreY[km]	X_{max}[g/cm^2]	log(E/eV)
infill	45.0	113.2	0.47	117.5	-7.33	19.10	650	15.12

Fig. 2. An example of a hybrid event detected by the TALE infill experiment. The table below shows the parameters of the primary cosmic rays obtained from the event reconstruction. The energy is very small, about a quarter of the mode energy.

Publications in refereed journals

The following articles are selected from those published in refereed journals in JFY 2024 through the TA Collaboration.

Estimation of Mass Composition from the Arrival Direction Distribution of UHECRs Observed by the TA SD Array

We reported an estimate of the injection mass composition for UHECRs in the energy region above 10 EeV[3]. The mass composition was estimated by comparing the energy-dependent arrival direction distribution of UHECR events observed by the TA SD array over 14 years with the large-scale structure of the local universe within 250 Mpc. An example of such an analysis is shown in Fig. 3, where cosmic rays with energies above 100 EeV are considered. The colored contour map represents the probability distribution of the arrival directions, assuming a value of $\theta_{100} = 10^\circ$, a parameter that characterizes the angular spread due to isotropic smearing. The white dots indicate the arrival directions of the events observed by the TA SD array. The observed distribution appears to be inconsistent with the expected arrival distribution under the assumption of $\theta_{100} = 10^\circ$. By varying θ_{100}, we searched for the value that matched the observed and expected distributions.

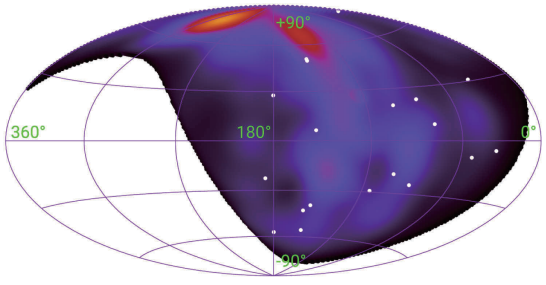


Fig. 3. Cosmic rays with energies above 100 EeV are considered. The colored contour map represents the probability distribution of the arrival directions, assuming a value of $\theta_{100} = 10^\circ$, a parameter that characterizes the angular spread due to isotropic smearing. The white dots indicate the arrival directions of the events observed by the TA SD array. The observed distribution appears to be inconsistent with the expected arrival distribution under the assumption of $\theta_{100} = 10^\circ$.

The same analysis was also performed on mock datasets

generated under assumptions about the source distribution of cosmic rays, magnetic-field distributions, and the injection mass composition. In this way, we obtain an estimate of the mass composition. Fig. 4 shows the result under the assumption that the extragalactic magnetic field (EGMF) is negligibly small. The estimated composition indicates a relatively light injection composition at around E = 10 EeV, and a very heavy composition at E $>$ 100 EeV.

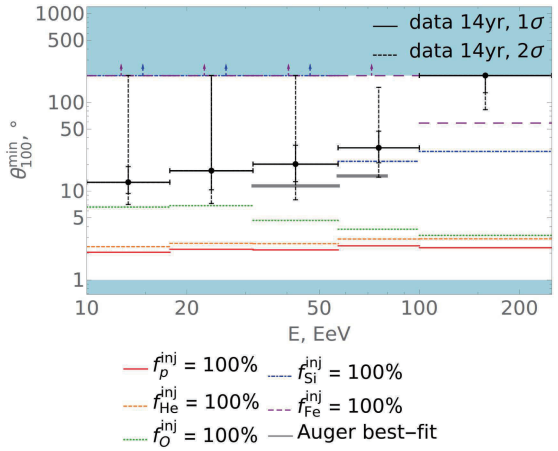


Fig. 4. The distribution of the test-statistics minima, θ_{100}^{min}, for the data compared to several injected composition models. The regular GMF model is used, and deflections in EGMF are neglected.

Fig. 5 presents the result under the assumption that the EGMF is at the maximum strength allowed by current observational constraints. Even in this case, the inference that the composition becomes very heavy at E $>$ 100 EeV remains valid. However, in the lower-energy region, the composition may become lighter if a strong EGMF is present.

Additionally, a companion paper[4] demonstrates that these results are robust against uncertainties in the UHECR injection spectrum, the experimental energy scale, and the Galactic magnetic field.

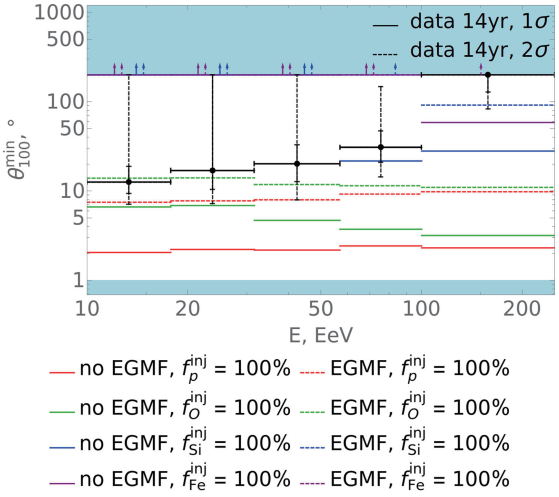


Fig. 5. Test statistics for the data compared to various pure nuclei injected composition models. Results without EGMF and with extremely strong EGMF.

Other physics results

Analysis of Inclined Air Shower Events Observed by the TA×4 SD array and by the TA SD array

Until now, air shower events used in the standard analyses of the TA SD and TAx4 SD arrays have been limited to zenith angles up to 55°, and events with larger zenith angles have not been included. In this study[5][6], we extended the air shower reconstruction method for observed data from the TAx4 SD array to include large zenith angle events. Using simulation data, we improved the method for constructing energy estimation tables used in the TAx4 SD event reconstruction process and extended them to zenith angles up to 70°. We confirmed that the difference in estimated energies between the new and the conventional energy estimation tables for the TAx4 SD array remains within 10% bias.

Subsequently, using simulation data, we evaluated the reconstruction accuracy of energy and other reconstructed parameters based on the new energy estimation tables developed in this study. We confirmed that the reconstruction of events with zenith angles greater than 55° achieves a comparable level of accuracy to that in the conventional zenith angle range.

To validate whether the simulation data appropriately reproduces the observed data, we compared the reconstructed distributions of various parameters between the observed data and the simulation for both (1) all events, including large zenith angle events, and (2) large zenith angle events only. In both cases, we confirmed that there are no significant discrepancies between the data and the simulation.

Using data from the TAx4 SD array collected over a 3-year period, we then performed the first measurement of the energy spectrum of UHECRs with energies higher than $10^{18.8}$ eV, including events with a large zenith angle made analyzable by this study. The result is shown in Fig. 6. The energy spectrum, including large zenith angle events, agrees, within statistical uncertainties, with the results of previous analyses using TA SD and TAx4 SD data. In particular, the spectrum fully agrees with the conventional TAx4 SD result at all data points within statistical error, demonstrating that the analysis of large zenith angle events is consistent with previous analyses conducted in the conventional zenith angle region.

Moreover, the number of observed events in the real data increased by approximately a factor of 1.5 due to the extension of the zenith angle range achieved in this study, significantly enhancing the available event statistics.

We plan to apply the zenith angle extension method developed in this study to the TA SD array as well. This expansion not only increases the number of observed events but also enlarges the observable region of the sky. Taking advantage of this, we will conduct more detailed studies of anisotropy and the energy spectrum. In particular, we expect improved understanding of the so-called ”spectrum anisotropy”—the observed difference in the energy spectra between the Southern Hemisphere, measured by Auger, and the Northern Hemisphere, measured by TA.

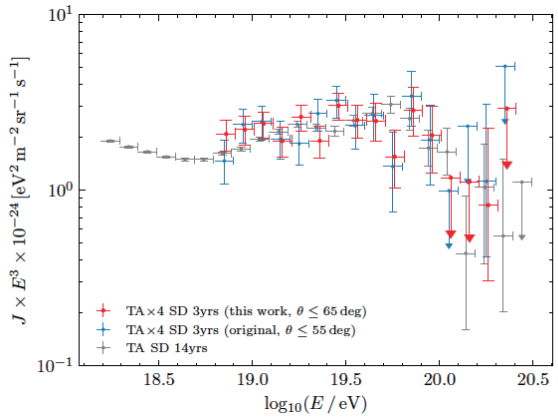


Fig. 6. UHECR energy spectrum, including the large zenith air shower events. The red dots represent the energy spectrum measured in this study. The blue dots represent the conventional energy spectrum of TA×4 SD, and the gray dots represent the energy spectrum observed over 14 years by TA SD.

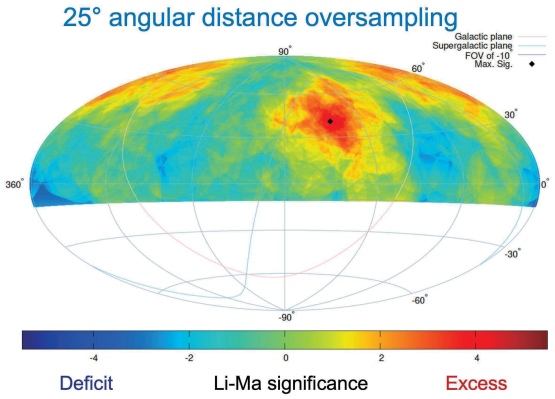


Fig. 7. The sky map of the TA Hotspot using Hammer projection and the growth of the Hotspot. The Li-Ma significance using a 25° circle angular window is shown in equatorial coordinates for 16 years of SD events with energies greater than 5.7×10^{19} eV. The black diamond indicates the maximum Li-Ma significance position measured at (144.0°, 40.5°). The color code indicates an excess (red) and a deficit (blue) of events compared to isotropy.

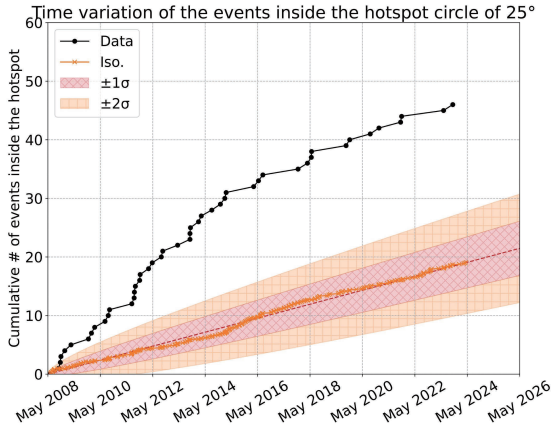


Fig. 8. The black dots represent the cumulative number of events falling inside the hot spot circle of 25○ from the most significant excess to the isotropy at (144.0°, 40.5°). The orange cross indicates the cumulative number of isotropic background expectations. The estimated isotropic event rate is depicted with the red dashed line, showing $\pm 1\sigma$ (pink) and $\pm 2\sigma$ (orange) deviations from the linear increase rate.

Medium-scale Anisotropy Analyses

Building on the historical development of the TA hotspot analysis, we analyzed 16 years of data collected by the TA SD array[7]. The left panel of Fig. 7 presents a sky map of the TA hotspot using a Hammer projection. This dataset includes a total of 228 events with energies exceeding 5.7×10^{19} eV. An oversampling analysis with a radius of 25° revealed a maximum Li-Ma significance of 4.9σ at equatorial coordinates (144.0°, 40.5°). Within this 25° radius circle, 46 out of the 228 events were observed, compared to an expectation of 19.1 events from an isotropic distribution. The color scale indicates event excesses (red) and deficits (blue) relative to isotropy. The black diamond marks the location of the maximum Li-Ma significance at (144.0°, 40.5°).To estimate how frequently such excesses would appear randomly in an isotropic UHECR sky, Monte Carlo event sets were generated. Each simulation set contains the same number of events as the real dataset, isotropically distributed and modulated by the geometric exposure of the TA SD array. A trial is considered successful if the maximum Li-Ma significance in the simulated map, S_{MC}, exceeds or equals the observed value, S_{obs}. The probability of randomly finding an excess of this magnitude somewhere in the field of view is calculated to be 2.1×10^{-3}, corresponding to approximately 2.9σ.

The Fig. 8 shows the growth of events within the hotspot. The black dots represent the cumulative number of events within a 25° radius around (144.0°, 40.5°), while the orange Xs show the expected cumulative background based on isotropy. The estimated isotropic event rate is indicated by a red dashed line, with $\pm 1\sigma$(pink) and $\pm 2\sigma$(orange) bands representing statistical deviations from the expected linear increase. This visualization highlights both the deviation of the observed excess from the isotropic expectation and the evolution of statistical fluctuations over time.

A modest excess as shown in Fig. 9 was identified in a slightly lower energy range (E $> 10^{19.4}$ eV). In the 16-year TA SD dataset, the number of events observed above energy thresholds of $10^{19.4}$ eV, $10^{19.5}$ eV, and $10^{19.6}$ eV were 1186, 767, and 464, respectively. Oversampling analyses were performed on a grid in equatorial coordinates with 0.1° steps in right ascension (0°– 360°) and declination (−15.7°– 90°).

The oversampling analysis yielded the following maximum Li-Ma significances: 3.7σ at (17.9°, 35.2°), 3.9σ at (19.2°, 35.2°), and 3.7σ at (21.8°, 36.2°). At each energy threshold, consistent excesses were observed within angular distances of 7.7°, 7.4°, and 8.3°, respectively, from the direction of the Perseus-Pisces Supercluster (PPSC). Celestial maps indicating the excess toward the PPSC at each energy threshold are shown in Fig. 9.

The PPSC, apart from the local supercluster, is the closest supercluster to us. It is located near the local void, where magnetic fields are expected to be weaker than in other cosmic web structures. This makes the PPSC a unique and important structure within the TA experiment's field of view, lending significance to the observed excess in its direction.

Multiple Monte Carlo event sets were generated to estimate the probability of such excesses occurring by chance under an isotropic arrival direction distribution. The chance probabilities for an excess with comparable significance and proximity to the PPSC were estimated to be 3.1σ for E $>$ $10^{19.4}$ eV, 3.2σ for E $> 10^{19.5}$ eV, and 3.0σ for E $> 10^{19.6}$ eV.

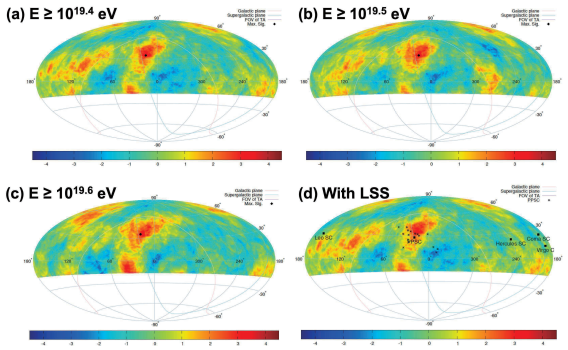


Fig. 9. The sky maps of the Perseus-Pisces Supercluster (PPSC) excess using the Hammer projection. The Li-Ma significance using a 20° circle angular window is shown in equatorial coordinates for different energy thresholds: (a) E $> 10^{19.4}$ eV, (b) E $> 10^{19.5}$ eV, and (c) E $> 10^{19.6}$ eV. The black diamonds indicate the maximum Li-Ma significance positions for each energy threshold. Additionally, (d) shows the nearby major large-scale structures (LSS) overlaid with the Li-Ma significance map for E $> 10^{19.4}$ eV. The color code indicates an excess *(red)* and a deficit *(blue)* of events compared to isotropy.

Energy Spectrum Measured by the TA SD array

We analyzed the data collected by the TA SD array over a 16-year period, from May 11, 2008, to May 11, 2024, and derived the cosmic-ray energy spectrum. Fig. 10 shows the resulting energy spectrum and its fit to a broken power-law model[8]. The data points are represented by black dots with error bars, and the red thick line indicates the fit using a triple broken power-law function, which includes three break points ($E_{\rm ankle}$, $E_{\rm shoulder}$, and $E_{\rm cutoff}$) and four spectral indices (p_1, p_2, p_3, and p_4).

The first break point, known as the "ankle" feature, is found at $E_{\rm ankle} = 10^{18.70\pm0.01}$ eV, with spectral indices $p_1 = -3.28 \pm 0.02$ below the ankle and $p_2 = -2.62 \pm 0.03$ above it. The second break point, referred to as the "softening feature" or "shoulder", occurs at $E_{\rm shoulder} = 10^{19.15\pm0.08}$ eV, followed by a spectral index of $p_3 = -2.83 \pm 0.04$.

The third break point, the "cutoff" feature, appears at $E_{\rm cutoff} = 10^{19.83\pm0.03}$ eV, with a spectral index of $p_4 = -4.61 \pm 0.41$ beyond the cutoff.

The fitted curve is overlaid on the plot.

We evaluated the statistical significance of the observed cutoff at $10^{19.83}$ eV. If the cutoff feature were absent, the expected number of events above this energy would be 173.7, whereas only 97 events were observed. This deviation corresponds to a probability of 1.6×10^{-10}, indicating a statistical significance of 6.3σ.

Similarly, we evaluated the statistical significance of the observed shoulder feature at $10^{19.15}$ eV. If this feature were absent, the expected number of events in the energy range between $10^{19.15}$ eV and $10^{19.83}$ eV would be 2156.4, while the observed number is 1921. This difference corresponds to a chance probability of 1.3×10^{-7}, or a statistical significance of 5.2σ.

This observation is consistent with the "instep" softening feature reported by the Auger experiment at $10^{19.11\pm0.03}$ eV. When applying an overall energy rescaling of +9%, this feature shifts to approximately $10^{19.15}$ eV. The agreement between the TA and Auger results confirms that this softening feature is consistently observed in both the Northern and Southern Hemispheres.

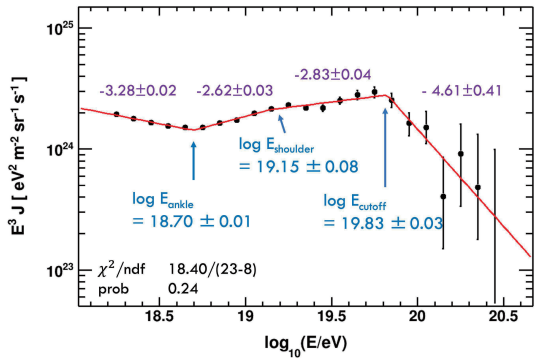


Fig. 10. Energy spectrum using 16-year SD data. The data points are represented by black points with error bars, while a fit to the broken power law is shown with the red solid line.

Cosmic Ray Composition Measurement between 3 PeV to 30PeV with the TALE Hybrid Detector

We reported on the mass composition of cosmic rays as measured by the TALE hybrid detector[9]. The TALE hybrid system consists of ten high-elevation angle fluorescence telescopes and an air shower array composed of 80 SDs, of which 40 are spaced at 400 meters and the remaining 40 at 600 meters. The system began operation in 2017.

In 2023, to lower the energy threshold of the hybrid mode into the PeV region for the purpose of measuring the mass composition around the knee in the cosmic ray spectrum, we constructed a new SD array consisting of 50 detectors spaced at 100 meters. Through 540 hours of hybrid observation using this new array and the FDs, we measured the average depth of shower maximum, $< X_{\rm max} >$, in the energy range from $10^{15.5}$ eV to $10^{16.4}$ eV, obtaining an elongation rate of $D_{10} = 15 \pm 4$ g/cm^2 per decade. This result indicates that the average mass composition of cosmic rays becomes heavier as energy increases in this range. Fig. 11 presents this result in combination with previous TALE hybrid observations using the TALE SD + TALE FD hybrid mode. The earlier data were based on a preliminary analysis presented at ICRC 2023 [10], covering hybrid observations from November 2017 to March 2023, and providing measurements of $< X_{\rm max} >$ in the energy range from $10^{16.5}$ eV to $10^{18.5}$ eV.

In that result, the observed elongation rate showed a clear break just above 10^{17} eV. The elongation rate before the break was 23 ± 5 g/cm^2 per decade, while after the break it increased sharply to 98 ± 5 g/cm^2 per decade. In contrast,

the expected elongation rate under the assumption of a pure composition is approximately 60 g/cm^2 per decade in both regimes.

Based on these findings, we conclude that the average mass composition increases (i.e., becomes heavier) in the energy range from $10^{15.5}$ eV to 10^{17} eV, followed by a reversal to a lighter composition at higher energies.

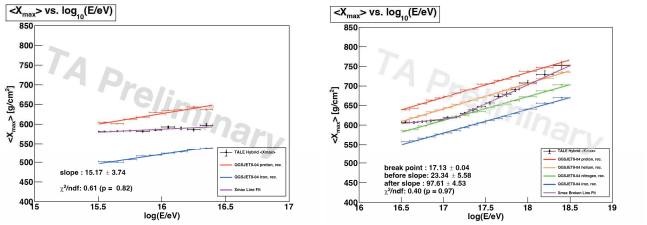


Fig. 11. Preliminary results of $< X_{\max} >$ as a function of energy. *(left)* $< X_{\max} >$ measurement bythiswork. For the comparison, the $< X_{\max} >$ of proton/iron are displayed as well. *(right)* Our previous $< X_{\max} >$ measurement in the energy range of $10^{16.5}$ eV to $10^{18.5}$ eV is also shown for the comparison.

Performance Evaluation of the TALE Infill SD Array

Operation of the TALE infill SD array began in November 2023. Since then, the array has been recording over 20,000 cosmic-ray events per day. A reconstruction program was developed to determine the energy and arrival direction of cosmic rays from the data collected by the TALE infill SD array. In parallel, improvements were made to the Monte Carlo (MC) simulations used for evaluating the performance of the reconstruction and for analyzing the energy spectrum[11][12].

The angular resolution of the arrival direction was evaluated as the opening angle between the true and reconstructed directions in the simulations. As shown in Fig. 12, the angular resolution improves with increasing energy, reaching 1.7° at $10^{15.3}$ eV and 1.0° at $10^{16.7}$ eV. Compared to the standard TALE SD array, which has an angular resolution of approximately 3° at its lowest observable energy (around $10^{16.5}$ eV), the TALE infill SD array demonstrates a significant improvement in angular resolution around this energy.

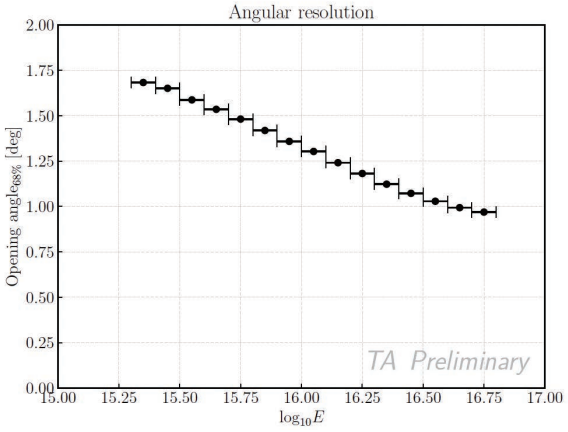


Fig. 12. Angular resolution of TALE infill SD array.

Since arrival direction accuracy can also be validated using real data alone, we applied the even-odd method to evaluate it independently of simulations. In the even-odd method, the full detector array is split evenly into two sub-arrays, labeled "odd" and "even", and each sub-array is analyzed separately. Fig. 13 illustrates how the TALE infill SD array was divided into even and odd sub-arrays. Note that each sub-array contains half the number of detectors, and the spacing between detectors becomes $\sqrt{2}$ times larger. Consequently, the angular resolution using the full array corresponds to half the opening angle between the two reconstructed directions from the sub-arrays.

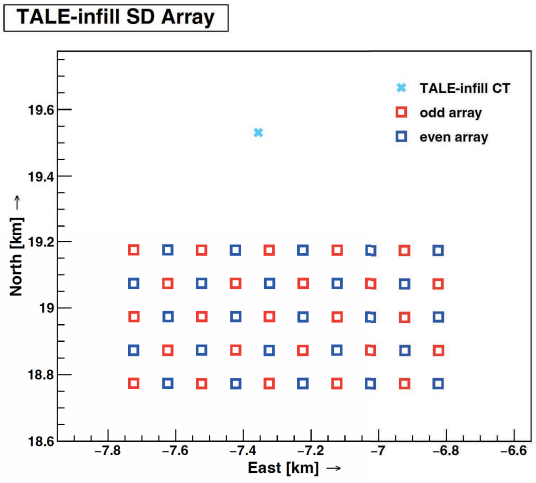


Fig. 13. *Red square* indicates the odd sub-array and *blue square* indicates the even sub-array. Each sub-array consists of half of the original SDs, arranged with $\sqrt{2}$ times the spacing of the full array. *Blue cross* marks the locations of the communication towers.

The left panel of Fig. 14 shows the distribution of opening angles between the even and odd sub-array reconstructions, based on data collected from November 1, 2023, to June 28, 2024. The red dashed line indicates the angle that contains 68 % of the distribution, $\delta_{68\%}^{\text{even-odd}}$, which was found to be 3.15°. Thus, the angular resolution using the full array is estimated to be half of this value, or 1.6°, which is consistent with the resolution obtained from MC simulations. This confirms that the installed detectors are performing as expected.

The right panel of Fig. 14 presents the relationship between the reconstructed energy and $\delta_{68\%}^{\text{even-odd}}$. The best angular resolution—i.e., the smallest $\delta_{68\%}^{\text{even-odd}}$—is observed around $10^{16.4}$ eV.

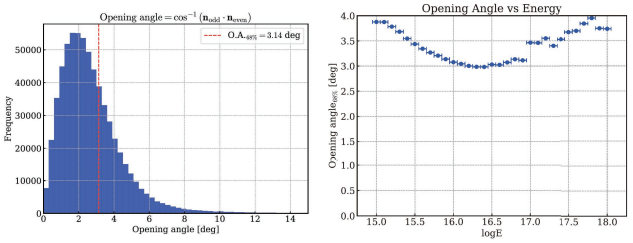


Fig. 14. *(left)* Angular resolution analyzed and verified using the even-odd method on actual data. *(right)* Energy dependence of angular resolution.

Other activities

Other research results and activities reported at UHECR2024, JPS meetings and/or other conferences are listed and introduced below.

- Development of an analysis method for neutrino-induced air showers with the Telescope Array surface detectors [13]
- The fractional analysis of mass composition measured by the Telescope Array FADC fluorescence detectors in hybrid mode [14]
- Calibration of the TA Fluorescence Detectors and Systematic Uncertainties in UHECR Analysis [15]
- Update on full-sky searches for large- and medium-scale anisotropies in the UHECR flux using the Pierre Auger Observatory and the Telescope Array [16]
- Approaching UHECR astronomy using mass-sensitive data from the Pierre Auger Observatory and the Telescope Array Project [17]
- Updates on TALE SD energy spectrum
- TAx4 mass composition analysis

Research and development of next-generation detectors

The TA experiment site is also a facility for the development of next-generation detectors, and prototype detectors for Auger@TA [18] EUSO [19][20], FAST [21][22] and CRAFFT [23] have been installed and are being used for joint observations with the TA experiment.

Discussions are also underway for the next-generation observatories, to measure the properties of the highest-energy cosmic rays with unprecedented accuracy in the future such as TA2 and GCOS (The Global Cosmic Ray Observatory) [24].

Bibliography

[1] R.U. Abbasi, *et al.*, "INDICATIONS OF INTERMEDIATE-SCALE ANISOTROPY OF COSMIC RAYS WITH ENERGY GREATER THAN 57 EeV IN THE NORTHERN SKY MEASURED WITH THE SURFACE DETECTOR OF THE TELESCOPE ARRAY EXPERIMENT", ApJL, 790, L21, 2014

[2] E. Kido, *et al.*, "Updates of the surface detector array of the TAx4 experiment", PoS(ICRC2023), 239, 2023.

[3] R.U. Abbasi, *et al.*, "Isotropy of Cosmic Rays beyond 10^{20} eV Favors Their Heavy Mass Composition", PRL 133, 041001, 2024

[4] R.U. Abbasi, *et al.*, "Mass composition of ultrahigh energy cosmic rays from distribution of their arrival directions with the Telescope Array", PRD 110, 022006, 2024

[5] C. Koyama, *et al.*, "Analysis of Inclined Air Shower Events Observed by the TAx4 SD", PoS(UHECR2024)099, 2025

[6] C. Koyama, "Measurement of the highest- energy cosmic ray energy spectrum using inclined air showers with the extended surface detector array of the Telescope Array experiment", M. Sc. thesis, U. of Tokyo, 2025

[7] J.H. Kim, *et al.*, "Telescope Array Surface Detector Medium-scale Anisotropy Analyses", PoS(UHECR2024)097, 2025

[8] J.H. Kim, *et al.*, "Energy Spectrum Measured by the Telescope Array Surface Detectors", PoS(UHECR2024)037, 2025

[9] K. Fujita, *et al.*, "Cosmic Ray Composition Measurement between 3 PeV to 30 PeV with the TALE Hybrid Detector", PoS(UHECR2024)042, 2025

[10] K. Fujita, *et al.*, "Cosmic ray mass composition measurement with the TALE hybrid detector", PoS(ICRC2023)401, 2024

[11] Y. Kawachi, *et al.*, "Measurement of cosmic rays with energies down to the PeV region using the TALE-infill SD array", PoS(UHECR2024)096, 2025

[12] Y. Kawachi, *et al.*, "Measurement of the energy spectrum of cosmic rays with energies down to the knee region with the TALE-infill SD array", M. Sc. thesis, Osaka Metropolitan University, 2025

[13] K. Takahashi, *et al.*, "Development of an analysis method for neutrino-induced air showers with the Telescope Array surface detectors", PoS(UHECR2024)026, 2025

[14] J.H. Kim, *et al.*, "The fractional analysis of mass composition measured by the Telescope Array FADC fluorescence detectors in hybrid mode", PoS(UHECR2024)098, 2025

[15] T. Tomida, *et al.*, "Calibration of the TA Fluorescence Detectors and Systematic Uncertainties in UHECR Analysis", PoS(UHECR2024)120, 2025

[16] A. Abdul Halim, *et al.*, "Update on full-sky searches for large- and medium-scale anisotropies in the UHECR flux using the Pierre Auger Observatory and the Telescope Array", PoS(UHECR2024)009, 2025

[17] K. Watanabe, *et al.*, "Approaching UHECR astronomy using mass-sensitive data from the Pierre Auger Observatory and the Telescope Array Project", PoS(UHECR2024)017, 2025

[18] S. Mayotte, *et al.*, "Auger@TA: An Auger-like surface detector micro-array embedded within the Telescope Array Project", PoS(ICRC2023), 368, 2023.

[19] Z. Plebaniak *et al.*, "The EUSO-TA ground-based detector: results and perspectives", PoS(ICRC2023), 385, 2023.

[20] M. Bertaina "An overview of the JEM-EUSO program and results", PoS(ICRC2021), 406, 2021.

[21] S. Sakurai, "Detecting ultra-high-energy cosmic rays with prototypes of the Fluorescence detector Array of Single-pixel Telescopes (FAST) in both hemispheres", PoS(ICRC2023), 302, 2023.

[22] F.W. Bradfield, "Reconstruction procedure of the Fluorescence detector Array of Single-pixel Telescopes", PoS(ICRC2023), 303, 2023.

[23] Y. Tameda *et al.*, "Detector optimization and observation plan of the CRAFFT project for the next generation UHECR observation", PoS(ICRC2023), 329, 2023.

[24] R. Alves Batista *et al.*, "Science with the Global Cosmic-ray Observatory (GCOS)", PoS(ICRC2023), 281, 2023.

Tibet ASγ Experiment

[Spokesperson: M. Takita]

ICRR, The Univ. of Tokyo, Kashiwa, Chiba 277-8582

Experiment

The Tibet air shower experiment has been successfully operated at Yangbajing (90°31′ E, 30°06′ N; 4300 m above sea level) in Tibet, China, since 1990. It has continuously made a wide field-of-view (approximately 2 steradian) observation of cosmic rays and gamma rays in the northern sky.

The Tibet I array was constructed in 1990, and it was gradually upgraded to the Tibet II by 1994, which consisted of 185 fast-timing (FT) scintillation counters placed on a 15 m square grid covering 36,900 m^2, and 36 density (D) counters around the FT-counter array. Each counter has a plastic scintillator plate of 0.5 m^2 in area and 3 cm in thickness. All the FT counters are equipped with a fast-timing 2-inch-diameter photomultiplier tube (FT-PMT), and 52 out of 185 FT counters are also equipped with a wide dynamic range, 1.5-inch-diameter PMT (D-PMT) by which we measure up to 500 particles which saturates the FT-PMT output, and all the D-counters have a D-PMT. A 0.5 cm-thick lead plate is put on the top of each counter in order to increase the counter sensitivity by converting gamma rays into electron-positron pairs in an electromagnetic shower. The mode energy of the triggered events in Tibet II is 10 TeV.

In 1996, we added 77 FT counters with a 7.5 m lattice interval to a 5,200 m^2 area inside the northern part of the Tibet II array. We called this high-density array Tibet HD. The mode energy of the triggered events in Tibet HD is a few TeV.

In the late fall of 1999, the array was further upgraded by adding 235 FT-counters so as to enlarge the high-density area from 5,200 m^2 to 22,050 m^2, and we call this array and further upgraded one Tibet III. In 2002, all of the 36,900 m^2 area was covered by the high-density array by adding 200 FT-counters more. Finally, we set up 56 FT-counters around the 36,900 m^2 high-density array and equipped 8 D-counters with FT-PMT in 2003. At present, the Tibet air shower array consists of 761 FT-counters (249 of which have a D-PMT) and 28 D-counters as in Fig. 1.

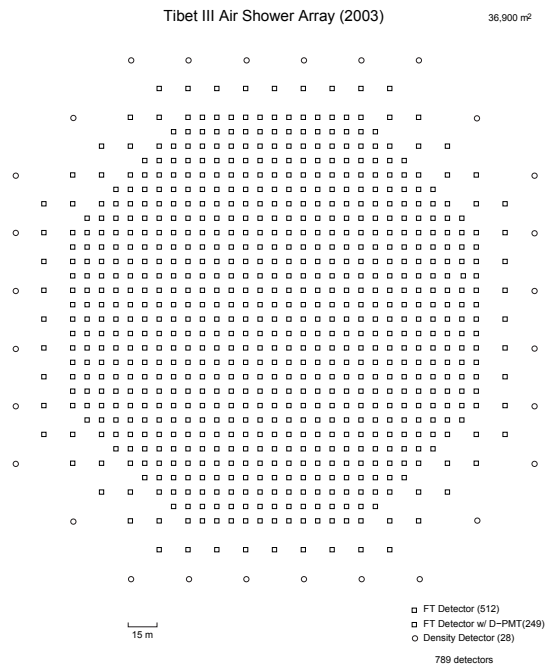


Fig. 1. Schematic view of Tibet III.

The performance of the Tibet air shower array has been well examined by observing the Moon's shadow (approximately 0.5 degrees in diameter) in cosmic rays. The deficit map of cosmic rays around the Moon demonstrates the angular resolution to be around 0.9° at a few TeV for the Tibet III array. The pointing error is estimated to be better than $\sim$0.02°, as shown in Fig. 2, by displacement of the shadow center from the apparent center in the north-south direction, as the east-west component of the geomagnetic field is very small at the experimental site. On the other hand, the shadow center displacement in the east-west direction due to the geomagnetic field enables us to spectroscopically estimate the energy scale uncertainty at $\pm$12% level, as shown in Fig. 3. Thus, the Tibet air shower experiment introduces a new method for energy scale calibration, other than the conventional estimation by the difference between the measured cosmic-ray flux by an air shower experiment, and the higher-energy extrapolation of cosmic-ray flux measured by direct measurements by balloon-borne or satellite experiments.

In 2007, a prototype 100-m^2 underground water Cherenkov muon detector was successfully constructed in Tibet to demonstrate the technical feasibility, cost estimate, validity of our Monte Carlo simulation. Data analyses demonstrate that our MC simulation reproduces real data quite reasonably.

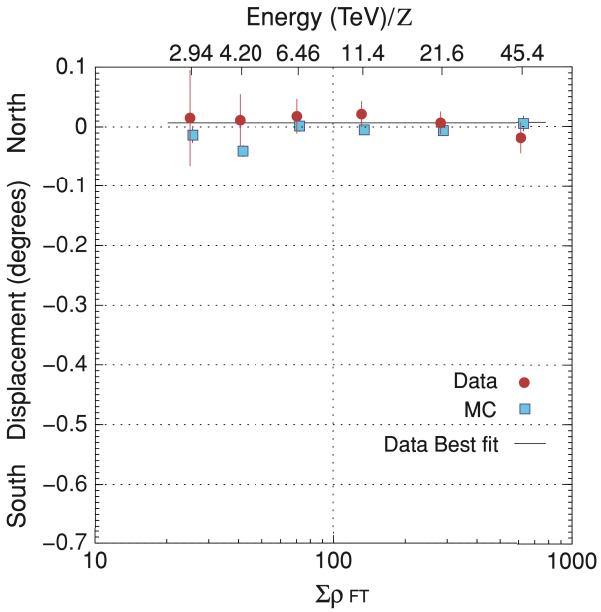


Fig. 2. From [1]. The Moon's shadow center displacement from the apparent position in the north-south direction as a function of energy, observed by Tibet III.

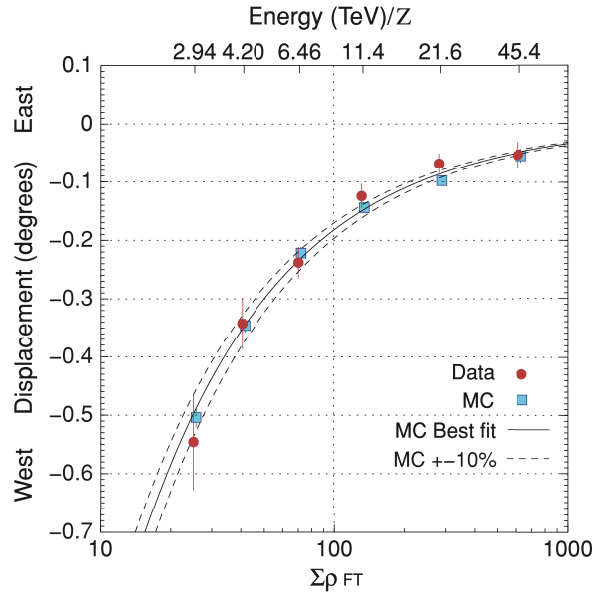


Fig. 3. From [1]. The Moon's shadow center displacement from the apparent position in the east-west direction as a function of energy, observed by Tibet III.

After the success of the prototype underground muon detector, we added a large underground muon detector (MD) array, and the experimental configuration was changed starting from February 2014. The current array consists of 597 plastic scintillation detectors with an area of 0.5 m^2 as shown by small dots in Fig. 4, covering an area of 65,700 m^2. The Tibet MD array (3,400 m^2 in total area) consists of 64 water-Cherenkov-type detectors located at 2.4 m underground of the AS array, as shown by open squares in Fig. 4. Each detector is a waterproof concrete cell filled with water up to 1.5 m in depth, 7.35 m $\times$ 7.35 m in area, equipped with a 20-inch-diameter downward-facing photomultiplier tube (PMT) on the ceiling. The inner walls and floor have a white Tyvek sheet lining to efficiently gather catoptric water Cherenkov light. The electromagnetic component is shielded by the soil overburden, which corresponds to $\sim$19 radiation lengths. The energy threshold for muons is approximately 1 GeV. A photon-induced air shower has much less muons compared with a cosmic-ray-induced one. The Tibet MD array enables us to significantly discriminate a cosmic-ray background event from a photon signal by means of counting the number of muons in an air shower.

Physics Results

Our current research theme is classified into 4 categories:

(1) Celestial gamma-ray point/diffuse sources,

(2) Chemical composition and energy spectrum of primary cosmic rays in the knee energy region,

(3) Cosmic-ray anisotropies in the multi-TeV region with high precision,

(4) Global 3-dimensional structure of the solar and interplanetary magnetic fields by observing the Sun's shadow in cosmic rays.

We will introduce a part of the results obtained in this fiscal year [3, 4, 9] on discussions for recent Galactic diffuse gamma-ray observation, and γ/p separation with machine learning.

Standard gamma-ray point-source analysis

A photon-induced air shower contains much less muons compared with a cosmic-ray-induced air shower. Therefore, the MD array enables us to distinguish a photon signal event from a cosmic-ray-induced background event. Using the AS and MD arrays, we analyzed the air shower data and muon data during 719 live days from February 2014 to May 2017.

Figure 4 (a) and (b) show the event display and the lateral distribution, respectively, of a typical photon-like event observed with $E = 251$ TeV from the Crab nebula [5]. The total uncertainty of the energy ΔE is defined as the quadratic sum of the absolute energy-scale error (12%) [1] and the energy resolution estimated by using MC events with the same zenith angle (θ) and core distance from the array center (R). The ΔE of the 251 TeV photon-like event is estimated to be $^{+45}_{-43}$ TeV.

We reconstruct the arrival direction of an air shower by means of the relative timing information recorded at each scintillation detector. The color scale and circle size in Fig. 4 (a) stand for the relative timing (t) and the particle density (ρ) in an air shower. In the first place, we estimate the air shower core location weighted by ρ. The arrowhead position and direction in the figure indicate the estimated core position and azimuthal direction. The t's in the air shower front are fitted by a conical shape, and its cone angle is optimized by the MC

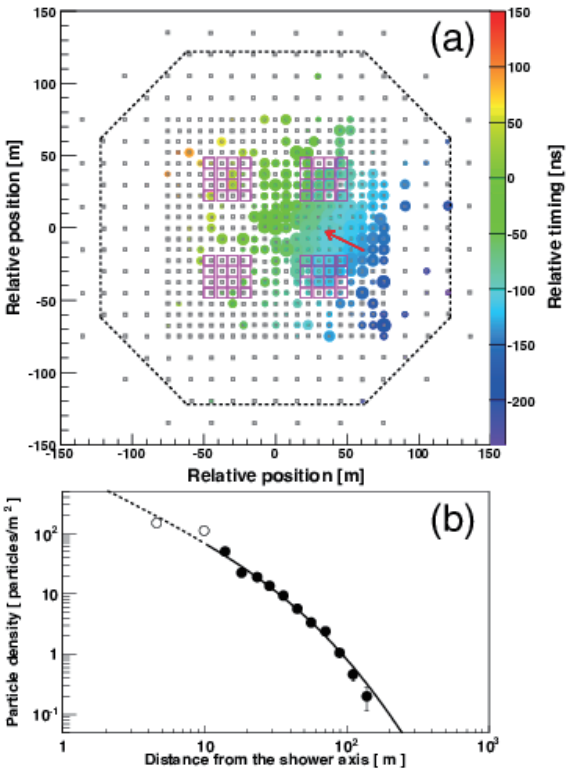


Fig. 4. From Ref.[5], references therein. (a) An event display of the observed photon-like AS of energy 251 TeV. The size and color of each circle represent the logarithmic particle density and the relative timing in each detector, respectively. The arrowhead and direction indicate the AS core location and incident direction, respectively. Dots and open squares denote scintillation detectors and underground MDs, respectively. The enclosed area by the dashed line indicates the fiducial area of the AS array. (b) Lateral distribution of the photon-like shower event in panel (a). The solid circles and curve show the experimental data and the fitting result by the Nishimura-Kamata-Greisen (NKG) function to the data recorded by detectors more than 10 m apart from the AS axis. The dashed curve and open circles are an extrapolation of the NKG function fitting and the unused data within 10 m from the AS axis.

simulation depending on the air shower size. The angular resolutions (50% containment) are estimated to be approximately 0.5° and 0.2° for 10 TeV and 100 TeV photon, respectively.

The secondary particles in an air shower deposit energy, which is proportional to ρ, in a scintillator. The ρ at each detector is defined as the PMT output charge divided by the single particle peak which is monitored every 20 minutes to correct the temperature dependence of each detector gain. The energy of each air shower is reconstructed using the lateral distribution of ρ, above 10 TeV. Figure 4 (b) shows an example of the lateral distribution of ρ. As an energy estimator, we use $S50$ [6], which is defined as ρ at a distance of 50 m from the air shower axis in the best-fit Nishimura-Kamata-Greisen (NKG) function. The energy resolutions with $S50$, which depend on the air shower core location and zenith angle, are roughly estimated to be 40% at 10 TeV and 20% at 100 TeV. On the other hand, the energy below 10 TeV was estimated directly from $\Sigma\rho$ corresponding to the sum of the particle density measured by each scintillation detector, as the number of hit detectors is too low to fit $S50$. The absolute energy scale uncertainty is estimated to be 12% by the westward displacement of the Moon's shadow position.

The electromagnetic cascade in the air shower is strongly suppressed by the bremsstrahlung process in the overburden, while muons and a part of the hadronic components penetrate into the underground MD array. The number of detected particles at an MD (N_μ) is defined as the output charge divided by the single muon peak, which is monitored every 20 minutes. The sum of detected particles in all MDs (ΣN_μ) is used as a parameter to separate between photon and cosmic-ray induced air showers.

An event trigger is issued at any 4-fold coincidence with detectors recording more than 0.6 particles within the area enclosed by the dashed lines in Fig. 4. At air shower energies smaller than 10 TeV, we employ the same selection criteria and estimate the event energy as in the previous work [1], except for the MD selection criterion. At air shower energies greater than 10 TeV, we employ the following event selections: (1) zenith angle of arrival direction (θ) should be $\theta < 40^\circ$; (2) number of available detectors for the air shower reconstruction should be ≥ 16; (3) among 6 detectors recorded with the largest ρ's, 5 should be contained in the fiducial area enclosed by the dashed lines in Fig. 4; (4) $\log(S50)$ should be > -1.2; (5) age parameter (s) in the best-fit NKG function should be $0.3 < s < 1.3$. (6) ΣN_μ should be $\Sigma N_\mu < 2.1 \times 10^{-3} (\Sigma\rho)^{1.2}$ or $\Sigma N_\mu < 0.4$, where $\Sigma\rho$ is the sum of particle density measured by the AS array. The MD cut is optimized for photon detection by our MC simulation.

To estimate the background contribution from cosmic rays, we adopt the Equi-Zenith Angle method, which is the same as in our previous works [1]. The background counts are estimated from the number of events averaged over 20 off-source bins of the same size as the on-source bin located at the equi-zenith angle. The radius of the on/off-source bin is set to $R_{\rm sw}(\Sigma\rho) = 6.9/\sqrt{\Sigma\rho}$ (deg.). In order to efficiently extract signals in the higher energy region at a low background level, the lower limit of $R_{\rm sw}$ is set to 0.5°, which corresponds to $\sim 90\%$ containment of photons above 100 TeV.

To generate air shower events in the atmosphere, Employed is the CORSIKA code v7.4000 with EPOS-LHC for the high-energy hadronic interaction model and FLUKA code v2011.2b for the low-energy hadronic interaction model. The very-high-energy photons at the top of the atmosphere are inputted, assuming a power-law spectrum with a differential index -2.9 above 0.3 TeV. The generated secondary particles in an air shower are fed into the detector response simulation for the AS array developed based on the GEANT4 code v4.10.00. The MC simulation for the MD array, considering the overburden, has been developed based on the GEANT4 code. The electromagnetic and hadronic cascades by the secondary particles in the overburden, as well as the ray tracing of Cherenkov lights emitted in the water cells, are simulated by the GEANT4 code. The number of photoelectrons detected in the 20-inch PMT is converted to N_μ referring to the single muon peak in each cell. The muon cut is determined to maximize the figure of merit $N_\gamma^{\rm MC}/\sqrt{N_\gamma^{\rm MC} + N_{\rm CR}^{\rm DATA}}$, where $N_\gamma^{\rm MC}$ and $N_{\rm CR}^{\rm DATA}$ denote the expected number of photons by the MC and the number of background events in the data af-

ter the muon cut. The photon-like events are defined as the remaining events after the muon cut.

With the Tibet AS+MD array, we have successfully observed sub-PeV gamma rays from the Crab Nebula for the first time [5]. Subsequently, we also succeeded in detecting sub-PeV diffuse gamma rays from the Galactic plane for the first time, and measured the sub-PeV gamma-ray spectra of several sources.

Positional correlation between Tibet Galactic diffuse gamma rays above 398 TeV and 1LHAASO catalog gamma-ray sources above 100 TeV

The Tibet ASγ experiment succeeded in the first detection of sub-PeV Galactic diffuse gamma rays above 100 TeV along the Galactic disk [7]. The hadronic origin of the Tibet ASγ Galactic diffuse gamma-ray emission (GDE) events is supported by the observation of Galactic neutrinos by IceCube, as the energy spectrum of the Tibet ASγ diffuse gamma rays converted into the neutrino flux assuming the hadronic interaction model smoothly connects at $\simeq 60$ TeV with the all-sky Galactic-neutrino flux in the field of view of the Tibet ASγ experiment.

Surprisingly, there was no overlap between the Tibet ASγ GDE events above 398 TeV with the known TeV sources along the Galactic disk, supporting the diffuse nature of them. Recently, the LHAASO collaboration published their first catalog (1LHAASO catalog) of gamma-ray sources detected in $1\,\mathrm{TeV} < E < 25\,\mathrm{TeV}$ and/or $E > 25\,\mathrm{TeV}$, among which 43 sources are also detected above 100 TeV with more than $4\,\sigma$ detection significance [8]. The detection of the sub-PeV gamma-ray sources in the 1LHAASO catalog provides us with a good chance to investigate how much these sources contribute to the Tibet ASγ GDE events above 398 TeV.

Shown in Fig. 5, are the incoming directions of the Tibet ASγ GDE events (red points) above 398 TeV and the positions and extensions of the sub-PeV LHAASO sources (blue circles; [8]). Assuming a two-dimensional Gaussian morphology, we calculate the extensions of 95% containment radii from the published extensions of the 39% containment radii [8]. We show the 95% upper limits on the extensions for point sources.

Astonishingly again, no Tibet ASγ GDE events above 398 TeV have their arrival directions within the extensions of the sub-PeV LHAASO sources. Therefore, none of the sub-PeV LHAASO sources is the origin of the Tibet ASγ GDE events above 398 TeV. The number of accidental overlaps between the Tibet ASγ GDE events above 398 TeV and the sub-PeV LHAASO sources is estimated to be 0.86, while the expected number of gamma-ray events from the 22 newly-reported sub-PeV LHAASO sources is 1.2. Therefore, it is statistically consistent that there is no overlap between the Tibet ASγ GDE events above 398 TeV and the sub-PeV LHAASO sources. No overlap between the Tibet ASγ GDE events above 398 TeV and the sub-PeV LHAASO sources supports the diffuse nature of the Tibet ASγ GDE events above 398 TeV again.

For more details on this topic, see [3].

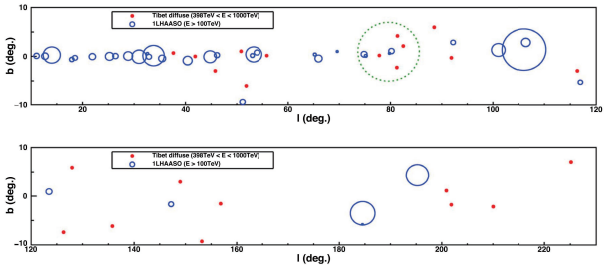


Fig. 5. Figures and captions from Ref.[3], references therein. Incoming directions of the Galactic diffuse gamma-ray events above 398 TeV observed by the Tibet ASγ experiment (red points) and the positions and extensions of the sub-PeV LHAASO sources: the gamma-ray sources detected by LHAASO above 100 TeV (blue circles; [8]) in the Galactic coordinates. The extensions of the sub-PeV LHAASO sources have 95% containment radii assuming a two-dimensional Gaussian morphology. For point-like sources, the 95% upper limits on the extensions are shown. The green dashed circle with a 6° radius encloses the Cygnus region centered at $(l, b) = (79.^\circ 62, 0.^\circ 96)$, the position of HAWCJ2030 + 409. Note that some of the sub-PeV LHAASO sources have $|b| > 10^\circ$ and thus are not shown in the plot.

Constraint on the contribution of resolved gamma-ray sources to the sub-PeV Galactic diffuse gamma-ray flux

We reported on the gamma-ray source contributions in the Galactic diffuse gamma-ray emission (GDE), which has been successfully observed in 2021 [7]. The Tibet ASγ experiment achieved the world's first observation of GDE in the UHE energy region using data recorded during about two years of live time.

Subsequently, the LHAASO experiment confirmed GDE in the UHE region, but the flux intensity was $\sim$30% that of the Tibet ASγ experiment. This may be caused by a difference in the source mask scheme when analyzing the GDE flux. It was a fact that the masked region of the LHAASO is conservatively wider than that of the Tibet ASγ experiment. In this work, we first investigate how much of the source contributions in the GDE flux observed by the Tibet ASγ experiment, assuming the LHAASO UHE gamma-ray sources (1st LHAASO catalog).

We found that the contamination of known gamma-ray sources is less than 30%, as shown in Fig. 6. Furthermore, we found that the difference in GDE flux between the Tibet ASγ and LHAASO experiments can be explained by the way the gamma-ray sources are masked in terms of their mask coverage, assuming the existing model distribution of the GDE.

For more details on this topic, see [4].

γ/p separation with the machine learning

The Tibet ASγ experiment has observed cosmic gamma rays and cosmic rays in the energy range from TeV to several tens of PeV using a surface detector array since 1990. Gamma-ray flux is estimated by identifying arrival direction excesses above the cosmic-ray background. In 2014, an underground water Cherenkov muon detector (MD) was added to distinguish between gamma rays and background cosmic rays based on their muon-poor air showers, enabling hybrid observations.

In this work, we developed methods to separate gamma-ray and hadronic air showers using only surface array data, fo-

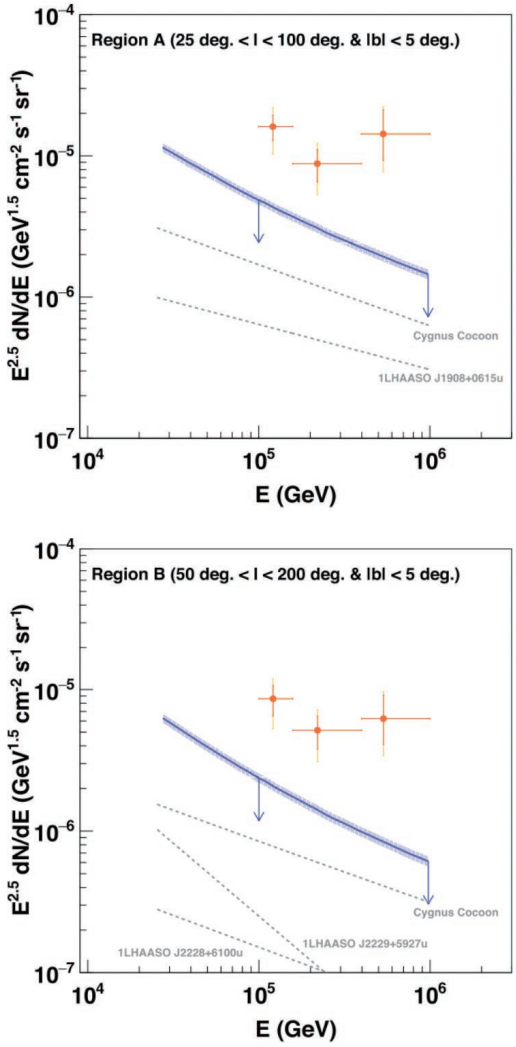


Fig. 6. Figures and captions from Ref.[4], references therein. Tibet diffuse flux (orange points) compared with the total gamma-ray flux of the sub-PeV LHAASO sources plus the Cygnus Cocoon that is not masked in the Tibet diffuse analysis (source flux, blue solid curve). The comparison is made for regions A (upper panel) and B (lower panel). The blue shaded band shows the error of the source flux. The downward arrows at 100 TeV and 1 PeV indicate that the calculated source flux should be regarded as the upper limit in the sub-PeV energy range. The gray lines show the best-fit energy spectra of some sources that largely contribute to the source flux in the sub-PeV energy range.

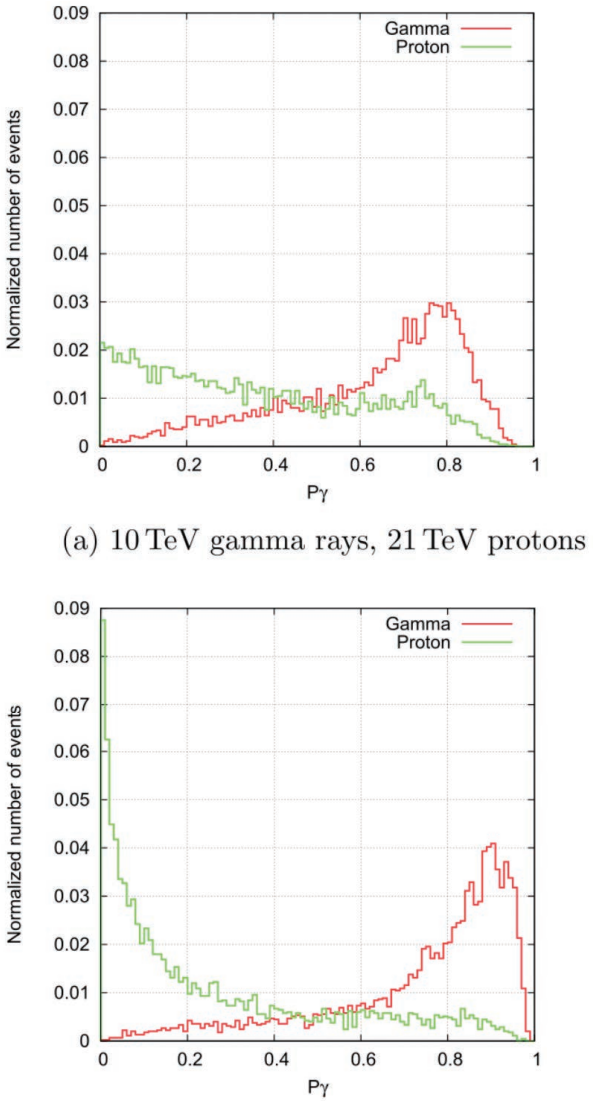


Fig. 7. The normalized distributions of P_γ obtained using the CNN. Panel (a) shows the separation results for 10 TeV gamma-ray showers and 21 TeV proton showers, while panel (b) presents the results for 100 TeV gamma rays and 165 TeV protons. The red histograms represent gamma-ray showers, and the green histograms represent proton showers.

cusing on the pre-MD period. Two neural network approaches were tested: one using features describing the lateral spread of particles, and another using shower image data.

Monte Carlo simulations of vertically incident gamma-ray and proton showers were analyzed. For single-feature classification, the best feature gave AUC values of 0.701 at 10 TeV and 0.808 at 100 TeV. A multilayer perceptron (MLP) using multiple features improved AUC to 0.761 and 0.854, respectively, which represents an improvement of approximately 5% in the AUC value compared with the single-feature case.

Figure 7 shows the normalized distributions of P_γ obtained using the convolutional neural network (CNN). The CNN using shower images achieved AUC values of 0.781 at 10 TeV and 0.901 at 100 TeV, outperforming the MLP method by roughly 5%. Applying the CNN to simulated Crab Nebula events (10–100 TeV) yielded AUCs of 0.753–0.879 and improved the gamma-ray excess significance by a factor of 1.3–1.8 compared to no separation.

For more details on this topic, see [9].

Other Activities

The emulsion-pouring facilities can meet the demands for making any kind of nuclear emulsion plates, which are used for cosmic ray or accelerator experiments. The thermostatic emulsion-processing facilities are operated in order to develop nuclear emulsion plates or X-ray films. Using these facilities, it is also possible to make and develop an emulsion pellicle in 600-micron thickness each. In this way, these facilities have

been open to all the qualified scientists who want to carry out joint research programs successfully. Recently, however, the shrinking demand for the facilities led us to decide that we should suspend calls for joint research programs to utilize the emulsion-pouring facilities, starting from 2012.

Ongoing Research Plans

(1) Modeling of TeV Galactic Cosmic-ray Anisotropy

Cosmic rays do not arrive at Earth uniformly. Recent experiments have consistently observed small anisotropies, with amplitudes of approximately 0.2%, in the arrival directions of cosmic rays at TeV energies. In this study, we model the cosmic-ray anisotropy at TeV energies using the intensity-mapping method based on Liouville's theorem [10]. Our results indicate unrealistically small-scale anisotropies, with angular scales of less than $\sim 10^{\circ}$ in the distribution of the cosmic-ray relative intensity at the outer boundary of the heliosphere. One potential issue is that the experimental data spans a ten-year period, while the magnetohydrodynamic (MHD) heliospheric model used in this work represents only a single snapshot in time. Performing intensity mapping for multiple snapshots of the MHD heliosphere and averaging the results could improve the accuracy of this study.

(2) Chemical composition of primary cosmic rays, making the knee in the all-particle energy spectrum

We have measured the energy spectra of primary cosmic ray protons, helium, and all particles around the knee energy region. The main component responsible for making the knee structure in the all particle energy spectrum is heavier nuclei than helium. The next step is to identify the chemical component making the knee in the all-particle energy spectrum. We have a plan to install a Yangbajing Air shower Core detector array (YAC) near the center of Tibet III to distinguish the chemical component making the knee. We completed construction of YAC2 (124 detectors over $\sim 500 \mathrm{m}^2$ in area), as is shown in Fig. 8, and started data-taking in 2014. YAC2 aims mainly to study the energy spectra of proton and helium components in the knee energy region.

(3) Gamma-ray astronomy in the 100 TeV region

For the purpose of detecting high-energy cosmic gamma rays with an air shower array, a large underground muon detector [11] is very effective to reduce cosmic-ray background. We added a large ($\sim$3,400 m^2) underground water Cherenkov muon detector (Tibet-MD) array under the present Tibet air shower array (Tibet AS $\sim$65,700 m^2). By Tibet AS + MD, we aim at background-free detection of celestial point-source gamma rays around 100 TeV with the world-best sensitivity and at locating the origins (PeVatrons) of cosmic rays accelerated up to the knee (PeV) energy region in the northern sky. The measurement of cut-off energies in the energy spectra of such gamma rays in the 100 TeV region may contribute significantly to the understanding of the cosmic-ray acceleration



Fig. 8. YAC2 set up at Yangbajing.

limit at the acceleration sites. Above 100 TeV, the angular resolution of Tibet AS with 2-steradian wide field of view is 0.2° and the hadron rejection power of Tibet MD is typically 1/1000 for a point-like source.

As described in the text, we succeeded in the first detection of photons with energies above 100 TeV from the Crab in the world, opening a new energy (sub-PeV) window in astronomy. We have also succeeded in the detection of gamma rays in the 100 TeV region from G106.3+2.7, Cygnus OB1 and OB2 regions, HESS J1843-033, HESS J1849-000, as well as sub-PeV diffuse gamma rays from the galactic disk. Analyses are underway in search of other sub-PeV gamma-ray sources.

Bibliography

References

[1] "Multi-TeV Gamma-Ray Observation from the Crab Nebula Using the Tibet-III Air Shower Array Finely Tuned by the Cosmic-Ray Moon's Shadow", M. Amenomori *et al.*, Astrophysical Journal, **692** , 61-72 (2009).

[2] "Observation of Gamma Rays up to 320 TeV from the Middle-aged TeV Pulsar Wind Nebula HESS J1849-000", M. Amenomori *et al.*, Astrophy. J. **954**, 200 (2023).

[3] "On the Source Contribution to the Galactic Diffuse Gamma Rays above 398 TeV Detected by the Tibet ASγ Experiment", S. Kato *et al.*, Astrophy. J. **961**, L13 (2024).

[4] "Quantitative Constraint on the Contribution of Resolved Gamma-Ray Sources to the Sub-PeV Galactic Diffuse Gamma-Ray Flux Measured by the Tibet ASγ Experiment", S. Kato *et al.*, Astrophy. J. **977**, L3 (2024).

[5] "First Detection of Photons with Energies beyond 100 TeV from an Astrophysical Source", M. Amenomori*et al.*, Physical Review Letters, **123** :051101-1-6 (2019).

[6] "Energy determination of gamma-ray induced air showers observed by an extensive air shower array", K. Kawata *et al.*, Experimental Astronomy, **44** 1-9 (2017).

[7] "First Detection of sub-PeV Diffuse Gamma Rays from the Galactic Disk: Evidence for Ubiquitous Galactic Cosmic Rays beyond PeV Energies", M. Amenomori*et al.*, Physical Review Letters, **126** :041101-1-7 (2021).

[8] "The First LHAASO Catalog of Gamma-Ray Sources", Z. Cao *et al.*, Astrophy. J. Supplement **271**, 25 (2024).

[9] "Neural networks for separation of cosmic gamma rays and hadronic cosmic rays in air shower observation with a large area surface detector array", S. Okukawa *et al.*, Machine Learning: Science and Technology, **5** id.025016 (p1-21) (2024).

[10] "Modeling of TeV Galactic Cosmic-ray Anisotropy based on Intensity Mapping in an MHD Model Heliosphere", M. Amenomori*et al.*, J. Phys.: Conf. Ser. **2742** 012014 (2024).

[11] "Exploration of a 100 TeV gamma-ray northern sky using the Tibet air-shower array combined with an underground water-Cherenkov muon-detector array", T.K. Sako *et al.*, Astroparticle Physics, **32** , 177-184 (2009).

The Tibet ASγ Collaboration, as of 2024

M. Amenomori[1], Y. W. Bao[2], X. J. Bi[3], D. Chen[4], T. L. Chen[5], W. Y. Chen[3], Xu Chen[3,4], Y. Chen[2], Cirennima[5], S. W. Cui[6], Danzengluobu[5], L. K. Ding[3], J. H. Fang[3,7], K. Fang[3], C. F. Feng[8], Zhaoyang Feng[3], Z. Y. Feng[9], Qi Gao[5], Q. B. Gou[3], Y. Q. Guo[3], Y. Y. Guo[3], Y. Hayashi[10], H. H. He[3], Z. T. He[6], K. Hibino[11], N. Hotta[12], Haibing Hu[5], H. B. Hu[3], K. Y. Hu[3,7], J. Huang[3], H. Y. Jia[9], L. Jiang[3], P. Jiang[4], H. B. Jin[4], K. Kasahara[13], Y. Katayose[14], C. Kato[10], S. Kato[15], I. Kawahara[14], T. Kawashima[15], K. Kawata[15], M. Kozai[16], Labaciren[5], G. M. Le[17], A. F. Li[3,9,18], H. J. Li[5], W. J. Li[3,10], Y. Li[4], Y. H. Lin[3,7], B. Liu[19], C. Liu[3], J. S. Liu[3], L. Y. Liu[4], M. Y. Liu[5], W. Liu[3], H. Lu[3], T. Makishima[14], Y. Masuda[10], S. Matsuhashi[14], M. Matsumoto[10], X. R. Meng[5], Y. Meng[3,7], A. Mizuno[15], K. Munakata[10], Y. Nakamura[15], H. Nanjo[1], C. C. Ning[5], M. Nishizawa[20], R. Noguchi[14], M. Ohnishi[15], S. Okukawa[14], S. Ozawa[21], X. Qian[4], X. L. Qian[22], X. B. Qu[23], T. Saito[24], M. Sakata[25], T. Sako[15], T. K. Sako[15], T. Sasaki[11], J. Shao[3,9], T. Shibasaki[26], M. Shibata[14], A. Shiomi[26], H. Sugimoto[27], W. Takano[11], M. Takita[15], Y. H. Tan[3], N. Tateyama[11], S. Torii[28], H. Tsuchiya[29], S. Udo[11], R. Usui[14], H. Wang[3], S. F. Wang[5], Y. P. Wang[5], Wangdui[5], H. R. Wu[3], Q. Wu[5], J. L. Xu[4], L. Xue[8], Z. Yang[3], Y. Q. Yao[4], J. Yin[4], Y. Yokoe[15], Y. L. Yu[3,7], A. F. Yuan[5], L. M. Zhai[4], H. M. Zhang[3], J. L. Zhang[3], X. Zhang[2], X. Y. Zhang[8], Y. Zhang[3], Yi Zhang[30], Ying Zhang[3], S. P. Zhao[3], Zhaxisangzhu[5], X. X. Zhou[9] and Y. H. Zou[3,7]

[1]Department of Physics, Hirosaki University, Hirosaki 036-8561, Japan.
[2]School of Astronomy and Space Science, Nanjing University, Nanjing 210093, China.
[3]Key Laboratory of Particle Astrophysics, Institute of High Energy Physics, Chinese Academy of Sciences, Beijing 100049, China.
[4]National Astronomical Observatories, Chinese Academy of Sciences, Beijing 100012, China.
[5]Department of Mathematics and Physics, Tibet University, Lhasa 850000, China.
[6]Department of Physics, Hebei Normal University, Shijiazhuang 050016, China.
[7]University of Chinese Academy of Sciences, Beijing 100049, China.
[8]Institute of Frontier and Interdisciplinary Science and Key Laboratory of Particle Physics and Particle Irradiation (MOE), Shandong University, Qingdao 266237, China.
[9]Institute of Modern Physics, SouthWest Jiaotong University, Chengdu 610031, China.
[10]Department of Physics, Shinshu University, Matsumoto 390-8621, Japan.
[11]Faculty of Engineering, Kanagawa University, Yokohama 221-8686, Japan.
[12]Faculty of Education, Utsunomiya University, Utsunomiya 321-8505, Japan.
[13]Faculty of Systems Engineering, Shibaura Institute of Technology, Omiya 330-8570, Japan.
[14]Faculty of Engineering, Yokohama National University, Yokohama 240-8501, Japan.
[15]Institute for Cosmic Ray Research, University of Tokyo, Kashiwa 277-8582, Japan.
[16]Polar Environment Data Science Center, Joint Support-Center for Data Science Research, Research Organization of Information and Systems, Tachikawa 190-0014, Japan.
[17]National Center for Space Weather, China Meteorological Administration, Beijing 100081, China.
[18]School of Information Science and Engineering, Shandong Agriculture University, Taian 271018, China.
[19]Department of Astronomy, School of Physical Sciences, University of Science and Technology of China, Hefei 230026, China.
[20]National Institute of Informatics, Tokyo 101-8430, Japan.
[21]National Institute of Information and Communications Technology, Tokyo 184-8795, Japan.
[22]Department of Mechanical and Electrical Engineering, Shangdong Management University, Jinan 250357, China.
[23]College of Science, China University of Petroleum, Qingdao 266555, China.
[24]Tokyo Metropolitan College of Industrial Technology, Tokyo 116-8523, Japan.
[25]Department of Physics, Konan University, Kobe 658-8501, Japan.
[26]College of Industrial Technology, Nihon University, Narashino 275-8575, Japan.
[27]Shonan Institute of Technology, Fujisawa 251-8511, Japan.
[28]Research Institute for Science and Engineering, Waseda University, Tokyo 162-0044, Japan.
[29]Japan Atomic Energy Agency, Tokai-mura 319-1195, Japan.
[30]Key Laboratory of Dark Matter and Space Astronomy,

Purple Mountain Observatory, Chinese Academy of Sciences, Nanjing 210034, China.

ALPACA Project

[Spokesperson: M. Takita]
ICRR, The Univ. of Tokyo, Kashiwa, Chiba 277-8582

Cosmic rays are supposed to be accelerated up to the knee energy (PeV) region at supernova remnants (SNRs), star formation regions, and PWNe in the Galaxy. Therefore, we naturally expect gamma rays at 100 TeV energies, which originate in π^0 decays produced by the accelerated cosmic rays interacting with matter surrounding the acceleration sites. The gamma-ray emission of electron origin might be highly suppressed above 10 TeV due to the rapid decrease of inverse-Compton cross section by the Klein-Nishina effect as well as synchrotron radiation energy loss in the magnetic field around the acceleration sites. The detection and spectral measurement of gamma rays in the 100 TeV region from their celestial sources, together with multi-wavelength (radio, X-ray, gamma-ray) observations, will be an important experiment enabling us to discriminate between the hadronic and leptonic processes, to locate the acceleration site (PeVatron which accelerate cosmic rays up to PeV energies) of cosmic rays and to verify the standard acceleration model of cosmic rays. Furthermore, diffuse gamma rays from the Fermi bubbles reported by the Fermi-LAT group and sub-PeV neutrino events [1] detected by IceCube suggest that the Fermi bubbles are a PeVatron candidate. Similarly, the energy spectrum of diffuse gamma rays from the extended region around the Galactic center marginally measured by H.E.S.S. up to approximately 40 TeV also strongly indicates the existence of PeVatron [2], from which we expect to detect gamma rays at 100 TeV energies. In 2021, the Tibet ASγ experiment succeeded in the first detection of sub-PeV diffuse gamma rays from the Galactic disk. The natural interpretation is that the sub-PeV gamma rays are of cosmic ray origin. Therefore, this is the first experimental evidence that PeVatrons exist in the Galaxy. However, there has been no agreed-upon PeVatron in the northern sky so far. Thus, a wide field-of-view gamma-ray imaging at 100 TeV energies in the southern sky, where the H.E.S.S. sources [3], the Fermi bubbles, and the Galactic center are located withinthe field of view, will be a key experiment.

Experiment

The Andes Large area PArticle detector for Cosmic ray physics and Astrophysics [4],[5] (ALPACA) is a cosmic-ray experiment with a large surface air shower array with a large underground muon detector array. The experimental site (approximately 500 m$\times$500 m $\sim$250,000 m^2 in total area) is located on a flat high land called Chacaltaya Plateau (4,740 m above sea level, 16°23' S, 68°08' W), as shown in Fig. 1, around Mount Chacaltaya, near La Paz, Bolivia. In a part of this area, our array is under construction and is partly in operation.



Fig. 1. From Ref.[4]. Experimental site for the ALPACA experiment, Chacaltaya Plateau (4,740 m above see level, 16°23' S, 68°08' W), near Mount Chacaltaya, in Bolivia.

We plan to set up a 3,600 m^2 underground (below 2 m soil overburden) muon detector array (MD) and an 83,000 m^2 air shower array (AS). MD of water Cherenkov type is composed of four pools, with each pool (approximately 1.5 m deep) containing sixteen 56 m^2 unit detectors. AS is made up of 401 1 m^2 plastic scintillation counters at 15 m spacing.

The AS field of view is roughly 2 steradian. The expected angular resolution of AS is approximately 1 degree at 5 TeV and 0.2 degrees around 100 TeV for gamma rays. For 100 TeV gamma rays, the AS energy resolution is estimated to be $\sim$20-25%. The hadron rejection power of MD is more than 99.9% at 100 TeV, while keeping most of the gamma-ray events. Long-term detector stability, angular resolution, pointing accuracy, and energy scale can be calibrated by the cosmic-ray shadow in the Moon as well as by some of the bright stable TeV gamma ray sources in the southern sky.

Covered Physics

The research target of ALPACA is divided into four :

1. Measurement of high-energy (5 TeV – 1 PeV) cosmic gamma rays.

2. Measurement of cosmic-ray energy spectra around the Knee energy region (100 TeV – 100 PeV).

3. Measurement of cosmic-ray anisotropy $>$ 5 TeV at sidereal time frame.

4. Measurement of the Sun shadow in cosmic rays $>$ 5 TeV.

We aim at low-background detection of celestial gamma rays in the 100 TeV region with the world-best sensitivity (an order of magnitude better than any previous/existing experiments) and at locating the origins of cosmic rays accelerated up to the knee energy region in the southern sky. Presuming a

Crab-like gamma-ray source extending up with power-law index -2.6 located in the southern sky, the ALPACA experiment is sensitive to the source with ∼15% Crab intensity during one calendar year, as is demonstrated in Fig. 2.

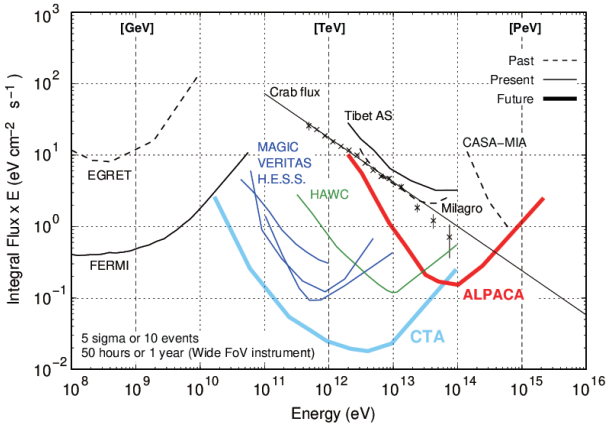


Fig. 2. Sensitivity of ALPACA to high-energy gamma-ray point source. Experimental data points are from HEGRA. The ALPACA sensitivity is evaluated from Ref.[6].

The AS + MD in the southern hemisphere will be a unique/complementary experiment to ongoing experiments (FERMI, CALET, DAMPE, H.E.S.S., VERITAS, MAGIC, Tibet ASγ, HAWC, LHAASO) and future projects (CTA, SWGO) in this field, which are either located in the northern hemisphere or aiming at gamma-ray astronomy below 10 TeV region, or having a narrow field-of-view, or not expected to start operation in the near future (within 5 to 10 years). Thus, the new energy window in the 100 TeV region observing gamma rays with a wide field-of-view will be opened first in the southern sky by the ALPACA experiment. We expect to detect more than a score of known TeV sources, i.e., young SNRs (SN1006, RX J1713.7-3946, RX J0852.0-4622), Pulsar Wind Nebulae, the Galactic center, etc, in the 100 TeV region, some of which may be cosmic-ray PeVatron candidates. Furthermore, our wide field-of-view sensitivity to diffuse gamma rays allows us to study extremely diffuse gamma-ray sources that are difficult to detect by IACTs. The diffuse gamma rays from the Fermi bubbles may be clearly detected, if they extend up to the 100 TeV region. Similarly, detection of diffuse gamma rays above 100 TeV from an extended region from the Galactic center is promising, where the gamma-ray energy spectrum strongly suggests the existence of PeVatron. The sub-PeV diffuse gamma rays along the Galactic disk in the southern sky are an interesting target to understand the PeV cosmic-ray propagation in the Galaxy. Detection and spectral measurement of gamma rays in the 100 TeV region from these celestial sources, together with multi-wavelength (radio, X-ray, gamma-ray) observations, are key points enabling us to discriminate between the hadronic and leptonic processes, to locate the acceleration site of cosmic rays and to examine the standard acceleration and propagation model of cosmic rays. From the astronomical point of view, we will open the ultra-high-energy (above 100 TeV) window in gamma-ray astronomy in the southern sky. Besides, gamma-ray emission from nearby extragalactic sources such as M87 and Cen A, gamma rays of dark matter origin, those from the Sun disk recently observed by HAWC [9] are also interesting subjects.

We also aim at measuring energy spectra of proton, helium, and iron components separately around the knee energy region with the new AS + MD. The standard cosmic-ray acceleration model at SNR predicts the knee energy of each nucleus component to be proportional to Z (atomic number). We can discriminate between proton and iron components by MD, as an iron nucleus produces approximately 2 times more muons than a proton with the same energy. Thus, the cosmic-ray acceleration scenario (SNR shock acceleration) will be verified by observing the linearly Z(atomic number)-dependent knee(=bent) positions of proton, helium, and iron components around the knee energy region.

Precise cosmic-ray anisotropy measurement at the sidereal time frame in the TeV energy region in the southern sky provides unique data for the community to understand the magnetic field structure in the heliosphere. The ALPACA experiment gives complementary data in the TeV region to that from IceCube above a few tens of TeV.

Furthermore, measurement of the Sun's shadow in cosmic rays above the TeV energy region in the southern hemisphere also helps understand the modeling of the magnetic fields between the Sun and the Earth, complementary to the observations in the northern hemisphere.

ALPAQUITA

As a prototype experiment, the ALPAQUITA [7] air shower array, which is ∼25 % of the ALPACA air shower array in area, has been constructed at the experimental site, Chacaltaya Plateau. The containers, including materials and equipment necessary to construct the ALPAQUITA air shower array, arrived at La Paz, Bolivia, in early 2019. The main infrastructures, including electricity, experimental hut, fence, cable guide drains were ready in 2021. Due to COVID-19 problems, the construction of the ALPAQUITA air shower array in the central part of ALPACA, as shown in a black octagon in Fig. 3 was delayed, but was completed in 2023, as is seen in Fig. 4. Since then, the ALPAQUITA surface array has continued stable operation. We will expand the ALPAQUITA air shower array, as shown in a red octagon in Fig. 3, under which we will add a 900 m^2 muon detector pool in 2025. The design of the muon detector pool is completed, collaborating with the Bolivian design company, as shown in Fig. 5.

The ALPAQUITA sensitivity to gamma rays from a point source is estimated by a Monte Carlo simulation [7], as is shown in Fig. 6. Even with the ALPAQUITA air shower array with a 900 m^2 MD, we expect to detect several bright 100 TeV gamma-ray sources. We also found that by considering the lateral distribution of muons, the sensitivity improves by 5–15% between 10–100 TeV as shown in Fig. 7 [8].

Analyses of the initial ALPAQUITA data are ongoing. We succeeded in the detection of the Moon shadow in cosmic rays $> 10\,\sigma$ statistical significance with the ALPAQUITA array, as shown in Fig. 8. The number of cumulative deficit events in the Moon shadow linearly evolves as a function of the number of recorded cosmic-ray events, indicating a stable operation of

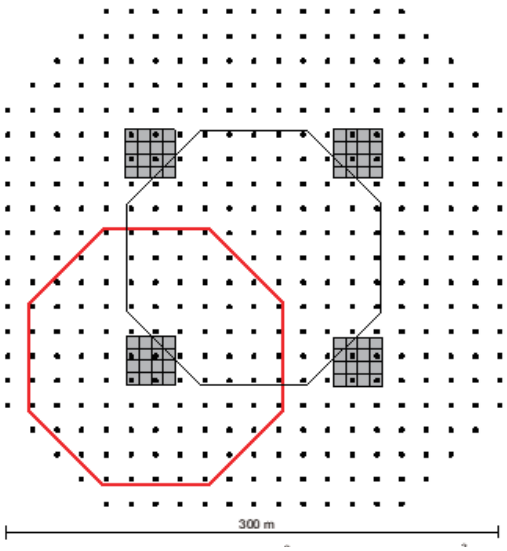


Fig. 3. Layout of the ALPACA and ALPAQUITA arrays. Each small dot indicates a scintillating counter, while the gray hatched area indicates the MD. ALPACA covers 300 m×300 m area containing 401 counters and 4 MD pools. The current ALPAQUITA surface array contains 97 counters enclosed by the solid-black line, while the ALPAQUITA + MD, to be constructed soon, is enclosed by the solid-red line.



Fig. 4. ALPAQUITA air shower array completed in 2023 in front of the Chacaltaya mountain.

the ALPAQUITA array. The evolving rate is consistent with the angular resolution of approximately 1°, which is expected for cosmic rays around 5-10 TeV by a Monte Carlo simulation.

In addition to the air shower data, the ALPAQUITA array records the counting rates of scintillating detectors at coincidence levels from 1 to 4. Figure 9 shows the time profiles of the Any1 and Any2 counting rates in the middle of May 2024. According to a passage of a large ICME on May 10, a strong Forbush decrease was observed by the world-wide Neutron Monitor and Muon telescope networks. The strong suppression of the CR intensity in the ALPAQUITA Any1 channel seen in Fig. 9 (black curve) is consistent with the other measurements, taking into account the median rigidity of Any1, 76 GV. On the other hand, non-detection of the decrease in the Any2 channel (red curve) with a median rigidity of 960 TV marginally constrains a simple power law behavior of the FD

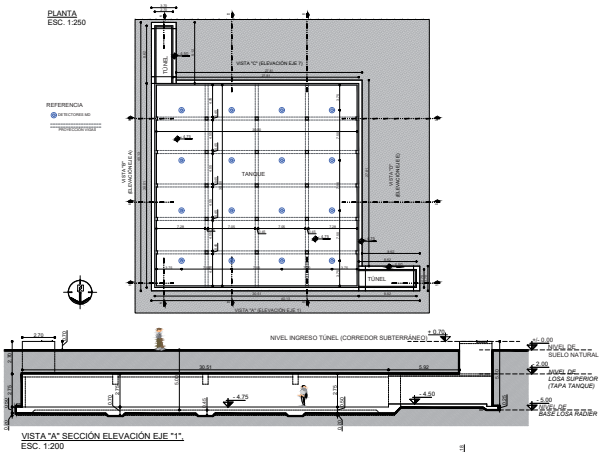


Fig. 5. Design of the ALPACA muon detector.

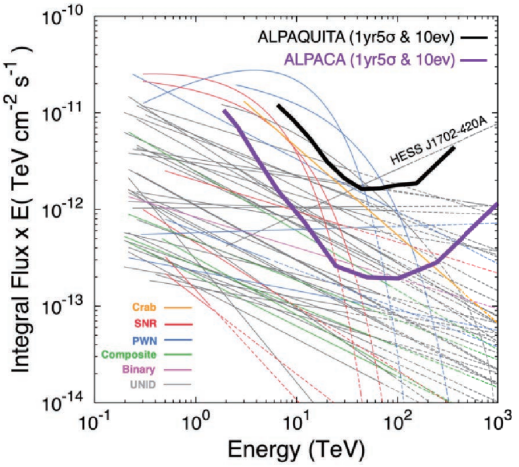


Fig. 6. From [7]. Sensitivity of the ALPAQUITA air shower array with a 900 m^2 MD (black curve) to point-like gamma-ray sources. The measured energy spectra of the H.E.S.S. sources are represented by solid curves, while the dashed curves represent the extrapolations of the measured spectra.

amplitude with rigidity. Any2 measurement is found to provide a unique rigidity coverage compared with the other measurements.

ALPACA

The budget to construct ALPACA was funded in 2022. We will set up ALPACA, a 3,600 m^2 underground muon detector array (MD) and an 83,000 m^2 air shower array (AS), shown in Fig. 3 (full area). MD of water Cherenkov type is composed of four pools, with each pool containing sixteen 56 m^2 unit detectors. AS is made up of 401 1 m^2 plastic scintillation counters at 15 m spacing. We will finish construction of ALPACA by operating the ALPAQUITA + MD arrays.

Bibliography

Papers and references

[1] C. Lunardini et al., PRD, **92**, 021301-1-5 (2015).

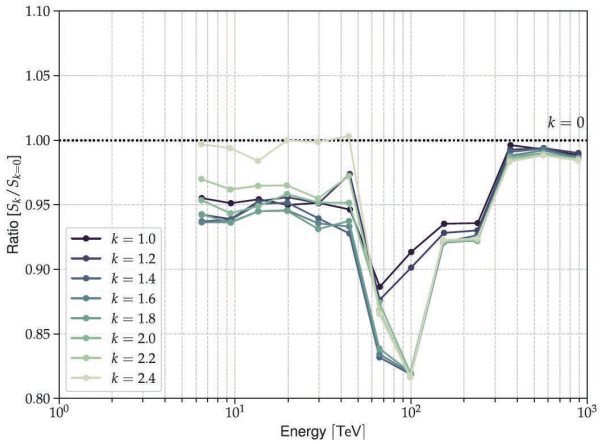


Fig. 7. Sensitivity improvement factors as a function of gamma-ray energy when considering the muon lateral distribution. Various weighting factors k are tested and k=1.6 is found to give the best sensitivity while k=0 is the conventional analysis.

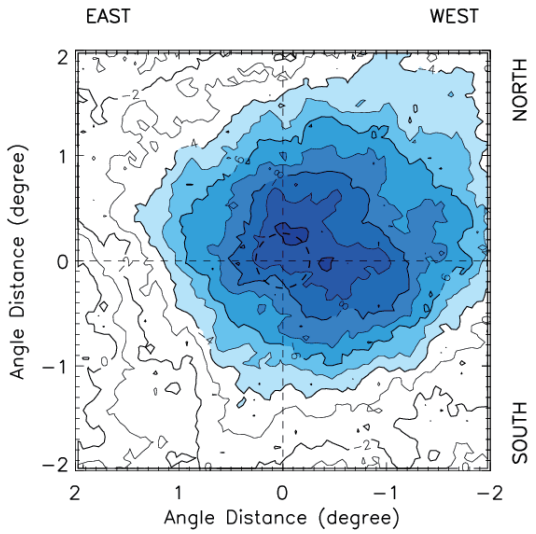


Fig. 8. Moon shadow observed by the ALPAQUITA air shower array. The detection significance is $> 10\,\sigma$, based on the data taken from April 2023 to April 2024.

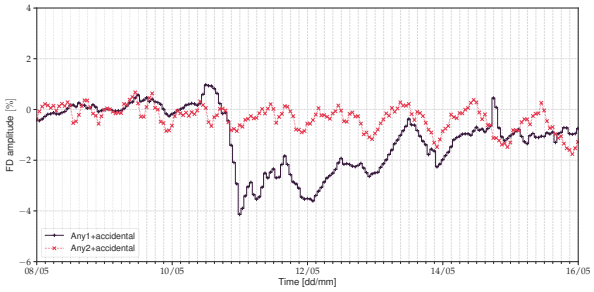


Fig. 9. Moon shadow observed by the ALPAQUITA air shower array. The detection significance is $> 10\,\sigma$, based on the data taken from April 2023 to April 2024.

[2] A. Abramoswski et al., Nature, **531**, 476 (2016).

[3] H. Abdalla et al., A&A **612**, A1 (2018).

[4] M. Takita for the ALPACA Collaboration, THE EUROPEAN PHYSICAL JOURNAL, **145**, 01002-1-3, (2017).

[5] F. Aceves de la Cruz et al. (The ALPACA Collaboration), Proc. of ICRC2021, POS(ICRC2021)733, Online, July 12-23, (2021).

[6] T. K. Sako et al., Astroparticle Physics, **32**, 177 (2009).

[7] S. Kato et al. (The ALPACA Collaboration), Experimental Astronomy, **52**, 85-107 (2021).

[8] M Anzorena et al. (The ALPACA Collaboration), Experimental Astronomy, **59**, 13 (2025).

[9] A. Albert et al. (The HAWC Collaboration), Phys. Rev. Lett., **131**, 051201 (2023).

The ALPACA Collaboration, as of 2024

M. Anzorena[1], D. Blanco[2], E. de la Fuente[3,4], K. Fujita[1], R. Garcia[1], K. Goto[5], Y. Hayashi[6], K. Hibino[7], N. Hotta[8], G. Imaizumi[1], A. Jimenez-Meza[9], Y. Katayose[10], C. Kato[6], S. Kato[24], T. Kawashima[1], K. Kawata[1], T. Koi[11], H. Kojima[12], T. Makishima[10], Y. Masuda[6], S. Matsuhashi[10], M. Matsumoto[6], R. Mayta[13,14], P. Miranda[2], A. Mizuno[1], K. Munakata[6], Y. Nakamura[1], C. Nina[2], M. Nishizawa[15], Y. Noguchi[10], S. Ogio[1], M. Ohnishi[1], S. Okukawa[10], A. Oshima[5,11], M. Raljevich[2], T. Saito[16], T. Sako[1], T. K. Sako[25], J. Salinas[2], T. Shibasaki[17], S. Shibata[12], A. Shiomi[17], M. A. Subieta Vasquez[2], F. Sugimoto[1], N. Tajima[18], W. Takano[7], M. Takita[1], Y. Tameda[19], K. Tanaka[20], R. Ticona[2], I. Toledano-Juarez[21,22], H. Tsuchiya[23], Y. Tsunesada[13,14], S. Udo[7], R. Usui[10], R. I. Winkelmann[2], K. Yamagishi[10], K. Yamazaki[11] and Y. Yokoe[1]

[1]Institute for Cosmic Ray Research, University of Tokyo, Kashiwa 277-8582, Japan.
[2]Instituto de Investigaciones Físicas, Universidad Mayor de San Andrés, La Paz 8635, Bolivia.
[3]Departamento de Física, CUCEI, Universidad de Guadalajara, Guadalajara, México.
[4]Doctorado en Tecnologías de la Información, CUCEA, Universidad de Guadalajara, Zapopan, México.
[5]College of Engineering, Chubu University, Kasugai 487-8501, Japan.
[6]Department of Physics, Shinshu University, Matsumoto 390-8621, Japan.
[7]Faculty of Engineering, Kanagawa University, Yokohama 221-8686, Japan.
[8]Faculty of Education, Utsunomiya University, Utsunomiya 321-8505, Japan.
[9]Departamento de Tecnologías de la Información, CUCEA, Universidad de Guadalajara, Zapopan, México.
[10]Faculty of Engineering, Yokohama National University, Yokohama 240-8501, Japan.
[11]College of Science and Engineering, Chubu University, Kasugai 487-8501, Japan.
[12]Chubu Innovative Astronomical Observatory, Chubu University, Kasugai 487-8501, Japan.

[13]Graduate School of Science, Osaka Metropolitan University, Osaka 558-8585, Japan.
[14]Nambu Yoichiro Institute for Theoretical and Experimental Physics, Osaka Metropolitan University, Osaka 558-8585, Japan.
[15]National Institute of Informatics, Tokyo 101-8430, Japan.
[16]Tokyo Metropolitan College of Industrial Technology, Tokyo 116-8523, Japan.
[17]College of Industrial Technology, Nihon University, Narashino 275-8575, Japan.
[18]RIKEN, Wako 351-0198, Japan.
[19]Faculty of Engineering, Osaka Electro-Communication University, Neyagawa 572-8530, Japan.
[20]Graduate School of Information Sciences, Hiroshima City University, Hiroshima 731-3194, Japan.
[21]Doctorado en Ciencias Físicas, CUCEI, Universidad de Guadalajara, Guadalajara, México.
[22]Maestría en Ciencia de Datos, Departamento de Métodos Cuantitativos, CUCEA, Universidad de Guadalajara, Zapopan, México.
[23]Japan Atomic Energy Agency, Tokai-mura 319-1195, Japan.
[24]Inst. D'Astrophysique de Paris, Sorbonne Univ.
[25]Nagano Pref. Inst. of Tech.

High Energy Astrophysics Group

[Spokesperson: K. Asano]

ICRR, The Univ. of Tokyo, Kashiwa, Chiba 277-8582

Overview

The high energy astrophysics group has been making theoretical studies of violent astrophysical phenomena, in which nonthermal cosmic-ray particles are being accelerated. Targets of the group's study include high-energy astrophysical objects such as supernova remnants/explosions, pulsars, pulsar wind nebulae, black hole/neutron star mergers, jets from active galactic nuclei (AGNs), and gamma-ray bursts (GRBs). We especially study the formation of relativistic outflows, particle acceleration in jets, emission mechanisms of electromagnetic waves or neutrinos, and electromagnetic counterparts for compact binary mergers. Our research carries the multi-messenger astronomy forward, which probes astronomical phenomena through collaborative observations of electromagnetic waves, cosmic rays, neutrinos, and gravitational waves.

Research Topic 1: GRB Afterglow

GRBs are the most luminous explosions in the Universe. Their enormous energy is promptly released within a few seconds to minutes, followed by a gradually fading afterglow radiation. The afterglow emissions provide unique information to study the particle acceleration mechanism in relativistic shocks, the physical properties of the GRB jet, and the circumstances of the progenitor stars.

A large fraction of GRBs show X-ray afterglows with a decay index of < 0.5 during the initial $\sim 10^3$ s. This shallow decay phase (or plateau phase) is one of the unsolved problems in the GRB afterglow physics. We simulate the emission in the shallow decay phase of gamma-ray burst afterglows using a time-dependent code. We test four models: the energy injection (EI) model, evolving the injection efficiency of nonthermal electrons (EE), evolving the amplification of the magnetic field (EB), and the wind model with a relatively low bulk Lorentz factor. All four models can reproduce the typical X-ray afterglow lightcurve. The spectral shape depends on not only the parameter values at the time corresponding to the observer time but also the past evolution of the parameters. The model differences appear in the evolution of the broadband spectrum, especially in the inverse Compton component. Future gamma-ray observations with imaging atmospheric Cherenkov telescopes such as the Cherenkov Telescope Array will reveal the mechanism of the shallow decay phase.

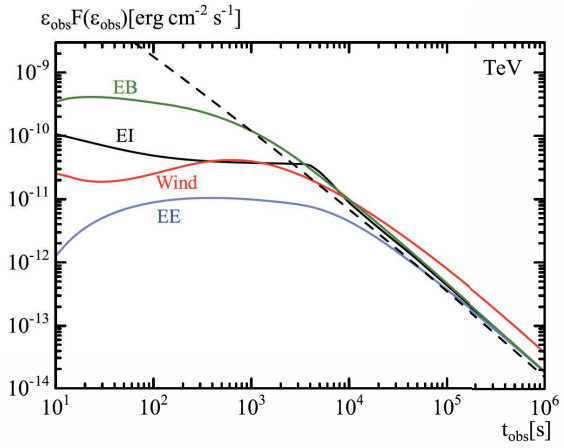


Fig. 1. Afterglow TeV lightcurves for EI, EE, EE and wind models [16]. Future detections of TeV photons will distinguish the mechanism of the shallow decay phase.

We also study the ejecta property dependence of the GRB afterglow. We carry out spherically symmetrical one-dimensional special relativistic magnetohydrodynamic simulations of magnetized outflows with an adaptive mesh refinement method. The Lorentz factor evolutions of forward and reverse shocks induced by the interaction between magnetized ejecta and an ambient medium are investigated for a wide range of magnetization and width of the ejecta. The forward shock evolution is described by the magnetic acceleration, coasting, transition, and self-similar deceleration phases. According to our simulation results, we numerically calculate the corresponding radiation. Based on our numerical results, to model afterglow light curves in general cases, we construct semi-analytical formulae for the Lorentz factor evolutions. The magnetization and ejecta width dependence are clearly seen in the reverse shock light curves. The transition phase with a reasonable ejecta width can reproduce the shallow decay phase in the observed GRB afterglow. The inverse Compton emission in the magnetic acceleration phase can be responsible for the very steep rise of the early TeV emission

in GRB 221009A.

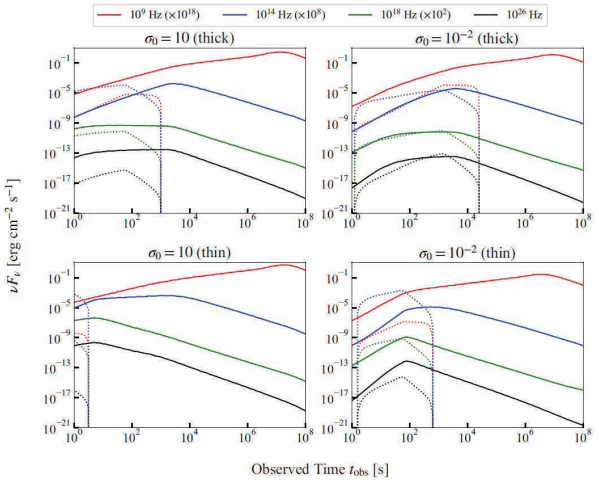


Fig. 2. The afterglow light curves combined with the forward and reverse shock radiation [31]. Each panel corresponds to the different initial magnetization and width of the ejecta. The solid line is the forward shock light curve, and the dotted one is the reverse shock light curve.

Research Topic 2: Radio Halos in Galaxy Cluster

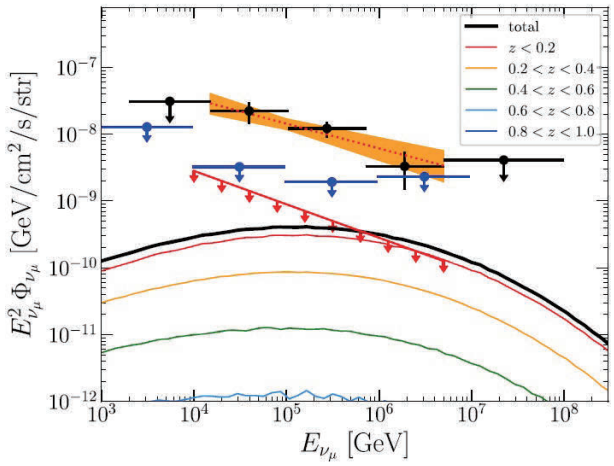


Fig. 3. The spectrum of the isotropic neutrino background from galaxy clusters [30]. The contributions from various redshift bins are shown with colored lines. The red line with arrows shows the 90% confidence level (CL) upper limit derived from the stacking analysis of the Planck-SZ galaxy clusters using the distance-weighting scheme. The blue arrows show the upper limits in quasi-differential energy bins.

A giant radio halo (RH) is a diffuse synchrotron emission observed on the scale of megaparsecs, typically found in the central region of merging galaxy clusters. Its large size and steep spectrum suggest that it originates from the reenergization of an aged population of cosmic-ray electrons (CREs), while the secondary leptons produced in the pp hadronic collision of cosmic-ray protons (CRPs) may contribute to the emission. In this study, we investigate the reacceleration model, including both primary and secondary CREs, assuming that the primary cosmic rays (CRs) originate from internal galaxies. In our new method, we follow the cosmological evolution of each cluster and calculate the energy spectra and 1D spatial distributions of CRs. The primary CRE model with a ~ 3 Gyr duration of reacceleration successfully reproduces the statistical properties of the RHs observed in the recent LOFAR survey, as well as the spectrum and profile of the Coma cluster. The gamma-ray and neutrino emissions produced by reaccelerated CRPs are consistent with the upper limits. However, if the CRP injection rate is high and the secondary CREs become significant, the model with the required ~ 3 Gyr reacceleration overproduces the number of RHs. The limit on the CRP injection rate, $L_{\rm p} \lesssim 10^{41}$ erg s^{-1}, is significantly lower than that expected from the early starburst activity or jets from active galactic nuclei. This discrepancy requires a revision of either the model of CR supply from galaxies or the turbulent reacceleration model.

Research Topic 3: Magnetar Bursts

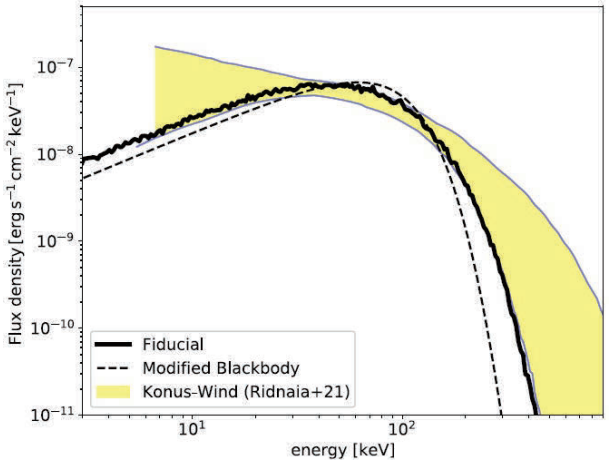


Fig. 4. X-ray spectrum at 5–900 keV of our magnetar burst model (thick solid) [39]. The vertical axis is the flux density, and the horizontal axis is the photon energy. The dashed black line is the modified blackbody spectrum for reference. The luminosity distance to the magnetar is set to 7 kpc. The yellow-shaded region is the 99.7% error region of the X-ray short burst associated with FRB 20200428A, which is detected from SGR 1935+2154 by the Konus- Wind.

An X-ray short burst associated with a Galactic fast radio burst was observed in 2020, distinguished by its X-ray cutoff energy significantly exceeding that of other X-ray short bursts. X-ray photons of these short bursts are believed to originate from fireballs within the magnetospheres of magnetars. If a fireball forms near a magnetic pole, it expands along the magnetic field lines, subsequently emitting photons and generating plasma outflows that may account for the observed radio bursts. We numerically study the radiative acceleration and X-ray spectrum of such outflowing fireballs consisting of pure electron–positron pairs and radiation, employing spherically symmetric relativistic radiation hydrodynamics calculations with the effects of strong magnetic fields. Using a Monte Carlo scheme in the radiation calculation, we consistently incorporate both the acceleration of the fluid by radiation and the scattering of radiation by the fluid, both of which

are enhanced by the cyclotron resonant scattering. Our calculation reveals that cyclotron resonant scattering accelerates the plasma outflow significantly and broadens the X-ray spectrum. The plasma outflow is accelerated up to ultrarelativistic velocities, with Lorentz factors exceeding 100. The calculated X-ray spectrum broadened due to scattering is similar to the observed X-ray spectrum in the Galactic fast radio burst.

The shape of a magnetar is not perfectly spherical due to the Lorentz force exerted by its strong magnetic fields and is described as a triaxial body. We study the unstable free precession in a triaxial magnetar; one of the principal axes undergoes an upside-down flip. This flip is known as the Dzhanibekov effect. We find that during the flip, the Euler force can suddenly disturb the force balance on the surface layer of the magnetar, potentially leading to plastic flow of the layer. This, in turn, may trigger different forms of magnetar activity, such as the emission of bursts and/or of gravitational waves.

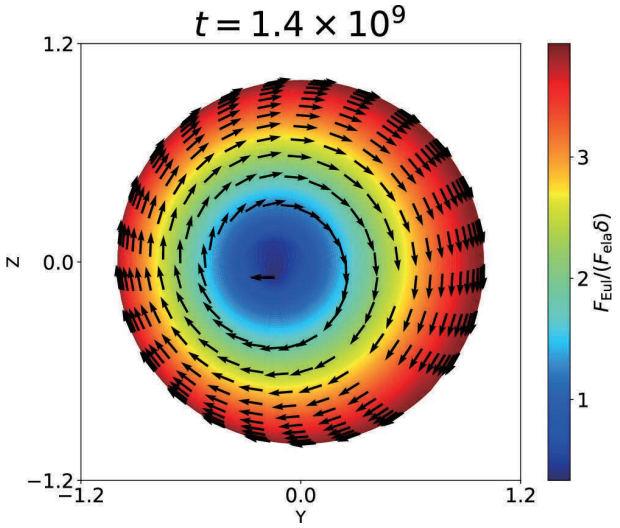


Fig. 5. Direction and strength of the Euler force on the magnetar surface [17].

Research Topic 4: Radiation Process in Relativistic MHD Waves

Turbulence in highly magnetized plasma can be relativistic and induce an electric field comparable to the background magnetic field. Such a strong electric field can affect the emission process of nonthermal electrons. As the first step toward elucidating the emission process in relativistic turbulence, we study the radiation process of electrons in relativistic circularly polarized Alfvén waves. While the induced electric field boosts the average energy of low-energy electrons with a Larmor radius smaller than the wavelength, the emissivity for such electrons is suppressed because of the elongated gyromotion trajectory. The trajectory of high-energy electrons is shaken by the small-scale electric field, which enhances the emissivity. Since the effective Lorentz factor of $E \times B$ drift is $\simeq \sqrt{2}$ in the circularly polarized Alfvén waves, the deviation from the standard synchrotron emission is not so prominent. However, a power-law energy injection in the waves can produce a concave photon spectrum, which is similar to the GeV extra component seen in GRB spectra. If the turbulence electric field is responsible for the GeV extra component in GRBs, the estimates of the typical electron energy and magnetic field should be largely altered.

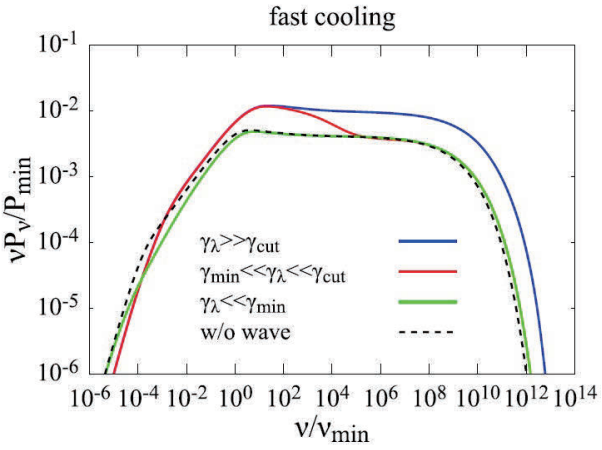


Fig. 6. The synchrotron radiation spectra in relativistic circularly polarized Alfvén waves with a power-law ($p = 2$) distribution for injection in the fast-cooling case [1]. The colored solid lines show the results for different γ_λ, which corresponds to the electron Lorentz factor, at which the Larmor radius is comparable to the wavelength of the Alfvén wave. The case without the wave is shown with the dashed black line.

Research Topic 5: Fermi and eROSITA Bubbles

The Fermi and eROSITA bubbles (FBs and eRBs) are the largest gamma-ray- and X-ray-emitting objects in the sky, respectively. They look like nearly symmetrical pairs of bubbles rising above and below the center of our Galaxy. In the last decade, most of the literature has suggested that the FBs and eRBs were formed by 1-10 Myr past Galactic center (GC) burst-like activities, implying that the bubbles are evanescent structures of the Milky Way (MW). However, the true formation mechanisms are still unknown.

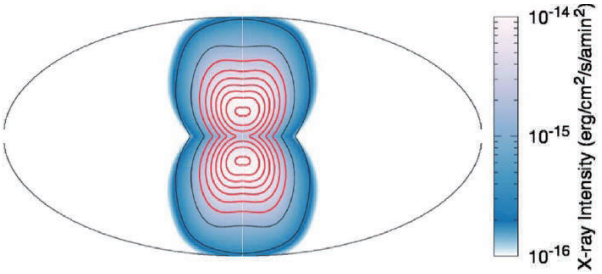


Fig. 7. The intensity sky maps of the hadronic gamma-ray and X-ray observed from $(R, z) = (8.5\text{kpc}, 0\text{kpc})$ [18]. The contour shows the 1 GeV gamma-ray intensity. The red contours indicate the intensity larger than 0.5×10^{-6} cm^{-2} s^{-1} str^{-1}. The color shows the X-ray intensity for the 0.6-1 keV band.

We propose a scenario for FBs and eRBs as the by-products of steady star formation activity. To simultaneously explain the star formation history of the MW and the metallicity of $\sim Z_\odot$ at the Galactic disk, a steady Galactic wind driven by CRs is required. For tenuous gases with a density of

$\lesssim 10^{-3}$ cm^{-3}, CR heating dominates over radiative cooling, and the gas can maintain the virial temperature of ~ 0.3 keV, ideal for escape from the Galactic system as the wind. A part of the wind falls back onto the disk like a Galactic fountain flow. We model the wind dynamics according to the Galactic evolution scenario and find that the scale height and surface brightness of the X-ray and the hadronic gamma-ray emissions from such fountain flow regions can be consistent with the observed properties of the FBs and eRBs. This implies that the bubbles are persistent structures of the MW existing over (at least) the last ~ 1 Gyr rather than evanescent structures formed by nontrivial, ~ 10 Myr past Galactic center transient activities.

Research Topic 6: Supermassive Black Holes with MHD Simulations

The Comparison of multi-wavelength observations with MHD numerical simulations is essential to probe the accretion flow onto supermassive black holes.

Strong soft X-ray emission, called soft X-ray excess, is often observed in luminous AGNi. It has been suggested that the soft X-rays are emitted from a warm ($T = 10^6$-10^7 K) region that is optically thick for the Thomson scattering (warm Comptonization region). Motivated by the recent observations that soft X-ray excess appears in changing look AGN (CLAGN) during the state transition from a dim state without broad emission lines to a bright state with broad emission lines, we performed global three-dimensional radiation MHD simulations, assuming that the mass accretion rate increases and becomes around 10% of the Eddington accretion rate. The simulation successfully reproduces a warm, Thomson-thick region outside the hot, radiatively inefficient accretion flow near the black hole. The warm region is formed by efficient radiative cooling due to inverse Compton scattering. The calculated luminosity 0.01-0.08 $L_{\rm Edd}$ is consistent with the luminosity of CLAGN. We also found that the warm Comptonization region is well described by the steady model of magnetized disks supported by azimuthal magnetic fields. When the antiparallel azimuthal magnetic fields supporting the radiatively cooled region reconnect around the equatorial plane of the disk, the temperature of the region becomes higher by releasing the magnetic energy transported to the region.

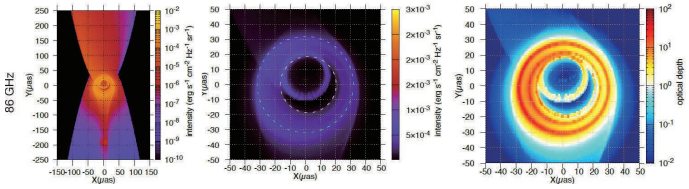


Fig. 8. The intensity maps and the optical depth maps when the observational frequency is 86 GHz [12]. The left panel is the log-scale Intensity map, the middle panel is the linear-scale intensity map, and the right panel is the optical depth map. The white dotted circle in the linear-scale intensity map represents the position of the photon ring. The diameter of the cyan dotted circle in the middle panel is 64μas, which is almost as large as the ring-like images observed with GMVA, ALMA, and GLT at 86 GHz.

By performing general relativistic radiative transfer calculations, we show the radio images of relativistic jets, including highly magnetized regions inside jet funnels, based on steady, axisymmetric, and semi-analytic general relativistic MHD models. It is found that multiple ring images appear at the photon frequency of 230 GHz for nearly pole-on observers, because of the strong light-bending effect on photons generated at the separation surfaces, which is the boundary between the inflow and outflow flows in the jet funnel. A bright teardrop-shaped component, which extends from the bright rings of the separation surface, also appears in the counter jet region. The diameter of the brightest outermost ring originated from the counter jet is $\sim 60\mu$as, which is consistent with the ring-like images of M87 at 86 GHz observed with GMVA, ALMA, and GLT, whose ring diameter is $\sim 64\mu$as. The thinner and smaller-diameter rings are exhibited when the black-hole spin magnitude is higher. These morphological features are expected to appear without being prominently affected by the detailed MHD-plasma parameters of our GRMHD jet model, since the location of the separation surfaces is mainly regulated by the black hole spin. Our GRMHD model and the emission features of the images in the horizon-scale, highly magnetized jet funnel may be tested by future observations, e.g., the next-generation Event Horizon Telescope and the Black Hole Explorer.

Research Topic 7: Nuclear Reactions in Supernovae

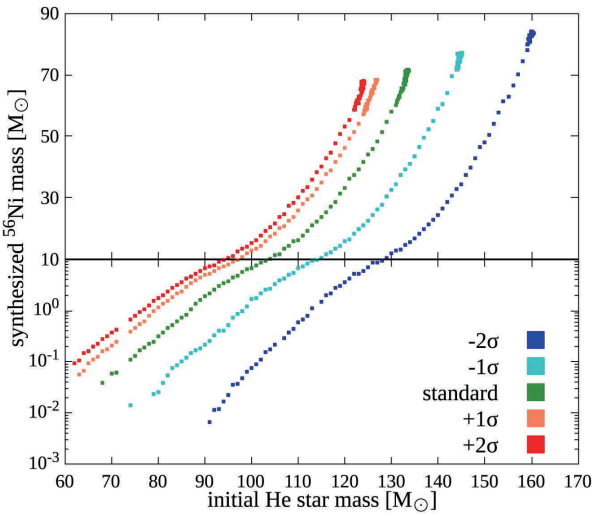


Fig. 9. The relationship between the synthesized radioactive nickel mass and the initial He core mass for different ^{12}C(α,γ)^{16}O reaction rates [10].

Nuclear reactions are key to our understanding of stellar evolution, particularly the ^{12}C(α,γ)^{16}O rate, which is known to significantly influence the lower and upper ends of the black hole mass distribution due to pair-instability supernovae (PISNe). However, these reaction rates have not been sufficiently determined. We use the MESA stellar evolution code to explore the impact of uncertainty in the ^{12}C(α,γ)^{16}O rate on PISN explosions, focusing on nucleosynthesis and explosion energy by considering the high resolution of the initial mass. Our findings show that the mass of synthesized radioactive nickel (^{56}Ni) and the explosion energy increase with

$^{12}C(\alpha,\gamma)^{16}O$ rate for the same initial mass, except in the high-mass edge region. With a high (about twice the starlib standard value) rate, the maximum amount of nickel produced falls below 70 $M_{\odot}$, while with a low rate (about half of the standard value) it increases up to 83.9 $M_{\odot}$. These results highlight that carbon 'preheating' plays a crucial role in PISNe by determining core concentration when a star initiates expansion. Our results also suggest that the onset of the expansion, which means the end of compression, competes with collapse caused by helium photodisintegration, and the maximum mass that can lead to an explosion depends on the $^{12}C(\alpha,\gamma)^{16}O$ reaction rate.

Research Topic 8: CALET Project

We have joined CALET, CALorimetric Electron Telescope, which is a mission for the Japanese Experiment Module-Exposed Facility (JEM-EF) on the International Space Station. The CALET mission aims at revealing unsolved problems in high-energy phenomena of the Universe by carrying out accurate measurements of high-energy spectra of electrons, gamma-rays, and nuclei.

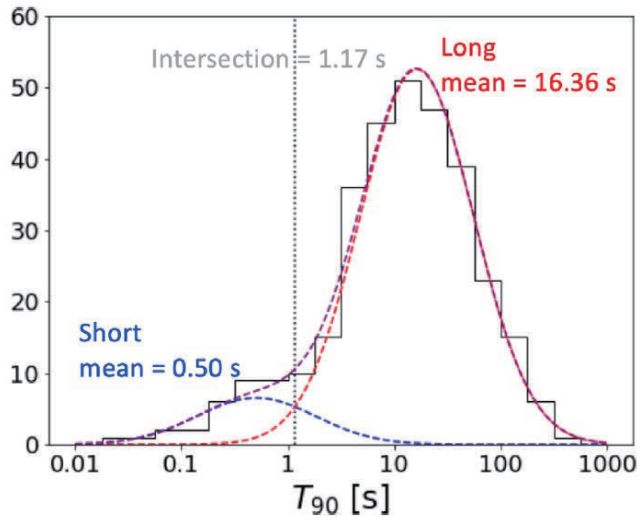


Fig. 10. Gamma-ray burst duration distribution measured by CALET/SGM (40-1000 keV) [23].

The CALET gamma-ray burst monitor (CGBM), designed to observe prompt emissions of GRBs in the hard X-ray (7-1000 keV) and soft gamma-ray (SGM, 40 keV-20 MeV) band, has been providing all-sky monitoring, with 60% duty cycle and without any problems, since October 2015. The gamma-ray bursts are also monitored by the calorimeter, whose threshold is decreased to 1 GeV whenever a trigger signal is produced by the CGBM. CALET covers the energies from 7 keV to 10 TeV. Fig. 10 presents the time duration distribution of GRBs observed by CGBM/SGM. As of the end of June 2023, the CGBM has detected 327 GRBs, including 31 short GRBs by classifying GRBs with the intersection of two logarithmic normal distributions.

Bibliography

Papers in refereed journals

[1] Ryota Goto, & Katsuaki Asano "Radiation Process in Relativistic MHD Waves: The Case of Circularly Polarized Alfvén Waves", Astrophys. J. **965**, 178(9pp) (2024)

[2] H. Abe, S. Abe, J. Abhir, et al. "The Variability Patterns of the TeV Blazar PG 1553+113 from a Decade of MAGIC and Multiband Observations", Mon. Not. R. Astron. Soc. **529**, 3894-3911 (2024)

[3] S. Abe, J. Abhir, V. A. Acciari, et al. "Performance and First Measurements of the MAGIC Stellar Intensity Interferometer", Mon. Not. R. Astron. Soc. **529**, 4387-4404 (2024)

[4] S. Abe, J. Abhir, V. A. Acciari, et al. "First Characterization of the Emission Behavior of Mrk 421 from Radio to VHE Gamma Rays with Simultaneous X-ray Polarization Measurements", Astron. Astrophys. **684**, A127(24pp) (2024)

[5] H. Abe, S. Abe, J. Abhir, et al. "Constraints on Axion-like Particles with the Perseus Galaxy Cluster with MAGIC", Phys. Dark Univ. **44**, 101425(13pp) (2024)

[6] Kensuke Kakiuchi, Takeru K. Suzuki, Shu-ichiro Inutsuka, Tsuyoshi Inoue, & Jiro Shimoda "MHD Simulation in Galactic Center Region with Radiative Cooling and Heating", Astrophys. J. **966**, 230(19pp) (2024)

[7] S. Abe, J. Abhir, V. A. Acciari, et al. "Insights into the Broadband Emission of the TeV Blazar Mrk 501 during the First X-Ray Polarization Measurements", Astron. Astrophys. **685**, A117(18pp) (2024)

[8] Taichi Igarashi, Hiroyuki R. Takahashi, Tomohisa Kawashima, Ken Ohsuga, Yosuke Matsumoto, & Ryoji Matsumoto "Radiation MHD Simulations of Soft X-ray Emitting Regions in Changing Look AGN", Astrophys. J. **968**, 121(15pp) (2024)

[9] Naoki Ogino, Makoto Arimoto, Hamid Hamidani, Takanori Sakamoto, Daisuke Yonetoku, Tatsuya Sawano, Motoko Serino, Katsuaki Asano, & Nobuyuki Kawai "Possible X-Ray Cocoon Emission from GRB 050709", Pub. Astron. Soc. Japan **76**, 550-559 (2024)

[10] Hiroki Kawashimo, Ryo Sawada, Yudai Suwa, Takashi J. Moriya, Ataru Tanikawa, & Nozomu Tominaga "Impacts of the $^{12}C(\alpha,\gamma)^{16}O$ Reaction Rate on ^{56}Ni Nucleosynthesis in Pair-Instability Supernovae", Mon. Not. R. Astron. Soc. **531**, 2786-2801 (2024)

[11] Kanji Morikawa, Yutaka Ohira, & Takumi Ohmura "Particle Acceleration and Magnetic Field Amplification by Relativistic Shocks in Inhomogeneous Media", Astrophys. J. Lett. **969**, L1(6pp) (2024)

[12] Taiki Ogihara, Tomohisa Kawashima, & Ken Ohsuga "Radio Images inside Highly Magnetized Jet Funnels Based on Semianalytic GRMHD Models", Astrophys. J. **969**, 22(11pp) (2024)

[13] Kai Matsunaga, Hiroyuki Uchida, Rei Enokiya, Toshiki Sato, Ryo Sawada, Hideyuki Umeda, Takuto Narita, & Takeshi Go Tsuru "Progenitor Constraint-Incorporating Shell Merger: The Case of Supernova Remnant G359.0—0.9", Astrophys. J. **970**, 4(8pp) (2024)

[14] S. Abe, J. Abhir, A. Abhishek, et al. "Constraints on Lorentz Invariance Violation from the Extraordinary Mrk 421 Flare of 2014 using a Novel Analysis Method", J. Cos. Astropart. Phys. **2024-07**, 044(23pp) (2024)

[15] S. Abe, J. Abhir, A. Abhishek, et al. "Dark Matter Line Searches with the Cherenkov Telescope Array", J. Cos. Astropart. Phys. **2024-07**, 047(63pp) (2024)

[16] Katsuaki Asano "Multiwavelength Modeling for the Shallow Decay Phase of Gamma-Ray Burst Afterglows", Astrophys. J. **970**, 141(8pp) (2024)

[17] Tomoki Wada, & Jiro Shimoda "The Dzhanibekov Effect as a Possible Source of Magnetar Activity", Astrophys. J. **972**, 58(6pp) (2024)

[18] Jiro Shimoda, & Katsuaki Asano "Fermi and eROSITA Bubbles as Persistent Structures of the Milky Way Galaxy", Astrophys. J. **973**, 78(10pp) (2024)

[19] Motoki Kino, Hyunwook Ro, Masaaki Takahashi, Tomohisa Kawashima, Jongho Park, Kazuhiro Hada, Yuzhu Cui "Mapping the Distribution of the Magnetic Field Strength along the NGC 315 Jet", Astrophys. J. **973**, 100(12pp) (2024)

[20] K. Abe, S. Abe, F. Acero, et al. "Prospects for γ-Ray Observations of the Perseus Galaxy Cluster with the Cherenkov Telescope Array", J. Cos. Astropart. Phys. **2024-10**, 004(104pp) (2024)

[21] Shogo Yoshioka, Shin Mineshige, Ken Ohsuga, Tomohisa Kawashima, & Takaaki Kitaki "Radiation and Outflow Properties of Super-Eddington Accretion Flows around Various Mass Classes of Black Holes: Dependence on the Accretion Rates", Pub. Astron. Soc. Japan **76**, 1015-1025 (2024)

[22] K. Abe, S. Abe, A. Abhishek, et al. "A Detailed Study of the Very High-Energy Crab Pulsar Emission with the LST-1", Astron. Astrophys. **690**, A167(12pp) (2024)

[23] Y. Akaike, O. Adriani, K. Asano, et al. "The Calorimetric Electron Telescope (CALET) on the International Space Station: Results from the First Eight Years on Orbit", Adv. Sp. Res. **74**, 4353-4367 (2024)

[24] O. Adriani, Y. Akaike, K. Asano, et al. "Direct Measurements of Cosmic-Ray Iron and Nickel with CALET on the International Space Station", Adv. Sp. Res. **74**, 4368-4376 (2024)

[25] K. Abe, S. Abe, J. Abhir, et al. "A New Method of Reconstructing Images of Gamma-Ray Telescopes Applied to the LST-1 of CTAO", Astron. Astrophys. **691**, A328(16pp) (2024)

[26] S. Abe, J. Abhir, A. Abhishek, et al. "Standardised Formats and Open-Source Analysis Tools for the MAGIC Telescopes Data", J. High Ene. Astrop. **44**, 266-278 (2024)

[27] S. Abe, J. Abhir, A. Abhishek, et al. "Constraints on VHE Gamma-Ray Emission of Flat Spectrum Radio Quasars with the MAGIC Telescopes", Mon. Not. R. Astron. Soc. **535**, 1484-1506 (2024)

[28] J. C. Algaba, M. Balković, S. Chandra, et al. "Broadband Multi-Wavelength Properties of M87 during the 2018 EHT Campaign including a Very High Energy Flaring Episode", Astron. Astrophys. **692**, A140(44pp) (2024)

[29] Yuh Tsunetoe, Tomohisa Kawashima, Ken Ohsuga, Shin Mineshige "Survey of Non-Thermal Electrons around Supermassive Black Holes through Polarization Flips", Pub. Astron. Soc. Japan **76**, 1211-1227 (2024)

[30] Kosuke Nishiwaki, & Katsuaki Asano "Low Injection Rate of Cosmic-Ray Protons in the Turbulent Reacceleration Model of Radio Halos in Galaxy Clusters", Astrophys. J. **978**, 62(22pp) (2025)

[31] Yo Kusafuka, & Katsuaki Asano "Ejecta Width and Magnetization Reflected in Gamma-Ray Burst Early Afterglows: Implication for Reverse Shock Component and Shallow Decay Phase", Mon. Not. R. Astron. Soc. **536**, 1822-1837 (2025)

[32] S. Abe, J. Abhir, A. Abhishek, et al. "Cosmic-Ray Acceleration and Escape from Supernova Remnant W44 as Probed by Fermi-LAT and MAGIC", Astron. Astrophys. **693**, A255(14pp) (2025)

[33] S. Abe, J. Abhir, A. Abhishek, et al. "Characterization of Markarian 421 during its Most Violent Year: Multiwavelength Variability and Correlations", Astron. Astrophys. **694**, A195(20pp) (2025)

[34] S. Abe, J. Abhir, A. Abhishek, et al. "Time-Dependent Modelling of Short-Term Variability in the TeV-Blazar VER J0521+211 during the Major Flare in 2020", Astron. Astrophys. **694**, A308(18pp) (2025)

[35] S. Abe, J. Abhir, A. Abhishek, et al. "Combined Search in Dwarf Spheroidal Galaxies for Branon Dark Matter Annihilation Signatures with the MAGIC Telescopes", J. Cos. Astropart. Phys. **2025-03**, 020(17pp) (2025)

[36] K. Abe, S. Abe, A. Abhishek, et al. "Detection of RS Oph with LST-1 and Modelling of its HE/VHE Gamma-Ray Emission", Astron. Astrophys. **695**, A152(18pp) (2025)

[37] K. Abe, S. Abe, J. Abhir, et al. "Insights from the First Flaring Activity of a High-Synchrotron-Peaked Blazar with X-Ray Polarization and VHE Gamma Rays", Astron. Astrophys. **695**, A217(18pp) (2025)

[38] J. Röder, M. Wielgus, A. P. Lobanov, et al. "A Multifrequency Study of Sub-Parsec Jets with the Event Horizon Telescope", Astron. Astrophys. **695**, A233(21pp) (2025)

[39] Tomoki Wada, & Katsuaki Asano “Radiative Acceleration and X-ray Spectrum of an Outflowing Pure Electron-Positron Pair Fireball in Magnetar Bursts”, Prog. Theo. Exp. Phys. **2025**, 033E01(25pp) (2025)

ASTROPHYSICS AND GRAVITY DIVISION

Overview

Astrophysics and Gravity Division consists of Gravitational Wave Group, Observational Cosmology Group, Primary Cosmic Ray Group, and Theory Group.

The Gravitational Wave Group conducts experimental research on gravitational waves with researchers of gravitational wave experiments and theory in Japan. The main items are the construction of the large-scale cryogenic interferometer (KAGRA) at Kamioka underground and the operation of CLIO. For this purpose, the KAGRA observatory was established at the beginning of the fiscal year of 2016 to assist the construction of the KAGRA gravitational wave telescope.

The Observational Cosmology Group studies cosmic history based on deep multi-wavelength observations in collaboration with worldwide researchers. This group has started a new optical and near-infrared deep survey project with the wide-field instrument of Prime Focus Spectrograph mounted on the Subaru telescope.

Theory Group conducts both theoretical studies of the Universe and astroparticle physics.

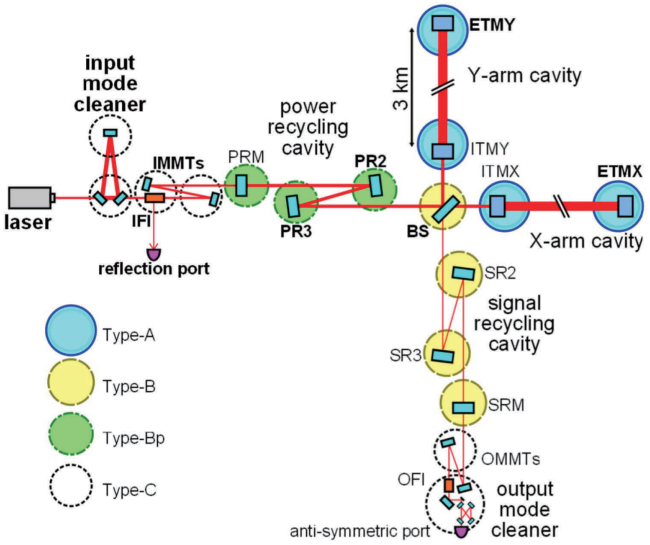


Fig. 1. Schematic view of the bKAGRA interferometer[3]. Type-A, Type-B, Type-Bp, and Type-C are the names of vibration isolation systems for each mirror.

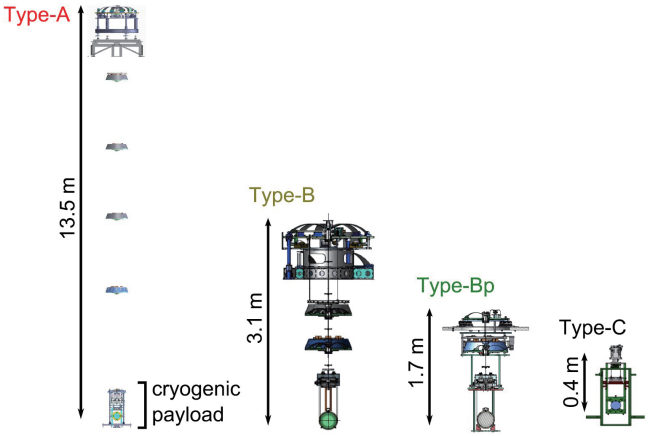


Fig. 2. KAGRA vibration isolation systems[3]. KAGRA equips four kinds of vibration isolation systems as Type-A, Type-B, Type-Bp, and Type-C.

Gravitational Wave Group

KAGRA Project Status

[Spokesperson : Shinji MIYOKI]

ICRR, The Univ. of Tokyo, Hida, Gifu 506-1205

Overview

KAGRA, the Large-scale Cryogenic Gravitational Wave Telescope, aims to detect gravitational waves and contribute to the development of gravitational wave astronomy, which was established by the first detection of gravitational waves by LIGO. KAGRA employs a 3 km L-shaped laser interferometer with cryogenic mirror systems, located underground at Kamioka [1]. The development of KAGRA is divided into two stages: initial KAGRA (iKAGRA) and baseline KAGRA (bKAGRA). The iKAGRA interferometer is a simple Michelson interferometer with a 2-watt laser, room-temperature mirrors, and a basic vibration isolation system. We completed the iKAGRA interferometer and performed a test run in April 2016 [2], after which we proceeded to bKAGRA.

Figures 1 and 2 show a schematic view of the optical layout of the bKAGRA interferometer and the KAGRA vibration isolation systems. Table 1 shows the design parameter of the bKAGRA interferometer[3]. The bKAGRA interferometer will employ a Resonant Sideband Extraction (RSE) interferometer with a 180-Watt laser, cryogenic Sapphire mirrors, and several kinds of vibration isolation systems. The bKAGRA interferometer should attain a sensitivity high enough for the detection of gravitational waves with the help of the high-power laser and RSE interferometer to reduce the quantum noise, the cryogenic Sapphire mirrors to reduce the thermal noise, and the vibration isolation systems to reduce the seismic noise. Figure 3 shows the designed sensitivities of bKAGRA in the cases of Broadband RSE (BRSE) and of Detuned RSE (DRSE), where the incoherent sum of the fundamental noise sources is assumed. The observation range for an in-spiral and merger of a neutron-star binary reaches 135 Mpc in BRSE and 153 Mpc in DRSE with the same definition of the observation range as LIGO and Virgo.

The KAGRA observatory signed three documents be-

Table 1. The design parameters of the bKAGRA interferometer[3]

Arm cavity length	3000 m	Test mass size	ϕ22 cm × 15 cm
Laser wave length	1064 nm	Mass of test mass	22.8 kg
Input power at PRM	67W	Temperature of test mass	22 K
Arm intra-cavity power	340 kW	Beam radius at test mass	3.5 cm
ITM transmittance	0.4 %	PRC/SRC lengths	66.6 m
PRM transmittance	10 %	Detuning angle	3.5 deg
SRM transmittance	15 %	Homodyne angle	135.1 deg

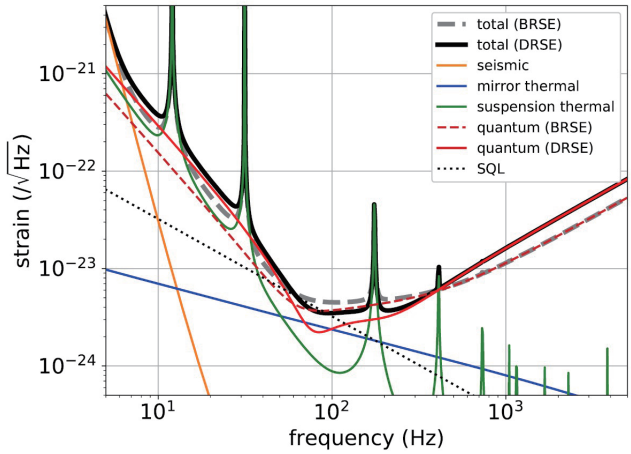


Fig. 3. The designed sensitivity of the bKAGRA interferometer[3]. "total", "seismic", "mirror thermal", "suspension thermal", "quantum", and "SQL" mean total sum of fundamental noise sources shown in this figure, seismic noise including gravity gradient noise, mirror thermal noise, suspension thermal noise, quantum noise, and standard quantum limit, respectively. The figure shows "total" and "quantum noise" in both Broadband RSE (BRSE) and Detuned RSE (DRSE) cases. The observation range for an in-spiral and merger of a neutron-star binary reaches 135 Mpc in BRSE and 153 Mpc in DRSE with the same definition of the observation range as LIGO and Virgo.

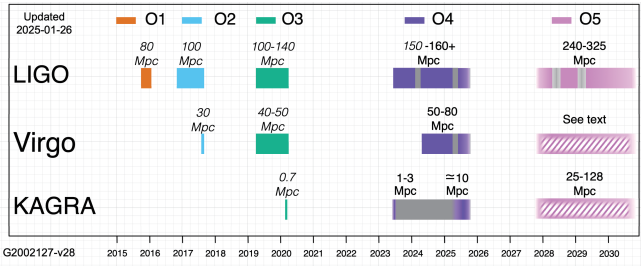


Fig. 4. International observation scenario[7]. The next international collaborative observation, called O4, started on May 24, 2023. O4 end was extended to November 2025. KAGRA performed the observation from May 24 to June 21, 2023, and resumed commissioning works. KAGRA resumed the observation from June 2025.

tween LIGO and VIRGO on October 4, 2019, to enable international joint observations. The documents are the Memorandum of Agreement between VIRGO, KAGRA, and LIGO (main part)[4], Memorandum of Agreement between Virgo, KAGRA, and LIGO (Attachment A)[5], and Letter of Intent for KAGRA to Join the O3 Run[6].

Figure 4 shows the international collaborative observation scenario[7] as of June 15, 2025. LIGO conducted Observation 1 (O1) from September 12, 2015, to January 19, 2016, and Observation 2 (O2) from November 30, 2016, to August 25, 2017. Virgo joined O2 on August 1, 2017. LIGO and Virgo started Observation 3 (O3) on April 1, 2019. Initially, O3 was planned to continue until the end of April 2020, but was suspended on March 27, 2020, due to the influence of COVID-19[8]. After the finish of O3, KAGRA conducted the first international joint observation run with GEO600 from April 7 to 21, 2020. This observation, referred to as O3GK, was officially recognized as an official joint observation with GEO600 by LIGO, VIRGO, and KAGRA. During O3GK, a sensitivity range of approximately 0.7 Mpc and the duty factor of 53 % were achieved.

The current international collaborative observation run, known as O4, began on May 24, 2023, and its end has been extended to November 18, 2025 [7]. KAGRA participated in the observation from May 24 to June 21, 2023, after which it resumed commissioning activities according to the agreement with LIGO and Virgo. During this observation period, a sensitivity range of approximately 1.3 Mpc and a duty factor of 80 % were achieved. Details of the observations conducted during O4 are provided in the "Observation" section, and information on the commissioning activities carried out afterward is presented in the "Commissioning" section.

In FY2023, two large earthquakes occurred on the Noto Peninsula, located about 100 km north of KAGRA. The first earthquake struck on May 5, 2023, with a magnitude of 6.5. As a result, KAGRA lost the alignment of all mirrors inside the vacuum chambers. Fortunately, we were able to recover the alignments remotely without venting the vacuum chambers, and the observing run began on May 24, 2023.

The second large earthquake occurred on January 1, 2024, with a magnitude of 7.6. The seismic intensity levels were 5– (on the Japan Meteorological Agency scale) at the surface near the KAGRA site and 3 at the underground facility. These were the highest vibration levels recorded in Hida City, Gifu Prefecture, in the past 100 years.

Fortunately, there were no power outages, fires, or vacuum leaks, and the cryogenic systems continued to operate normally. However, several turbo-molecular pumps stopped due to errors caused by excessive vibration of their blades. More critically, we found malfunctions in 10 mirror suspension systems. These included: (i) detachment of many magnets from the mirrors, (ii) unintended contact within the suspension sys-

tems, and (iii) severe mirror misalignments that could not be corrected remotely.

We started repairing the suspension systems immediately after the earthquake. All mechanical repairs were completed around early July, and then we started recovering the operations of KAGRA. The Fabry–Perot Michelson Interferometer (FPMI) configuration was restored in August 2025, followed by the recovery of the power-recycled FPMI (PRFPMI) configuration using RF signals in September 2025. Finally, we achieved the PRFPMI configuration with DC readout, reaching an improved sensitivity of approximately 2 Mpc, an improvement over the 1.3 Mpc sensitivity achieved during O4a.

Thanks to an increase in injected laser power from 1 W to 10 W and a reduction in beam jitter noise caused by a fixed mirror on the optical bench in the IFI vacuum tank, KAGRA's sensitivity reached approximately 4 Mpc. Further improvements, including optimization of the beam spot positions on the input mirrors and reduction of suspension thermal noise via cooling of the mirrors, reduction of coil driver circuit noise to ETMX by a factor of $1/2$, and many mirrors' alignment tweaking, pushed the binary neutron star (BNS) sensitivity over 7 Mpc in June 2025.

The rapidly progressing status of KAGRA was presented at many international conferences. Many papers about the progress of KAGRA were also published [11, 12, 13, 14, 15, 16, 17, 18, 19]. We also presented activities on our web page.[20]

Bibliography

[1] "KAGRA: 2.5 generation interferometric gravitational wave detector", KAGRA collaboration, Nature Astronomy, Vol. 3, pp.35-40, January (2019)

[2] "Construction of KAGRA: an underground gravitational-wave observatory", KAGRA collaboration, Prog. Theor. Exp. Phys. 2018, 013F01 (2018)

[3] "First cryogenic test operation of underground km-scale gravitational-wave observatory KAGRA", KAGRA collaboration, Class. Quantum Grav. 36 165008 (2019)

[4] https://gwdoc.icrr.u-tokyo.ac.jp/cgi-bin/DocDB/ShowDocument?docid=10663

[5] https://gwdoc.icrr.u-tokyo.ac.jp/cgi-bin/DocDB/ShowDocument?docid=10664

[6] https://gwdoc.icrr.u-tokyo.ac.jp/cgi-bin/DocDB/ShowDocument?docid=10813

[7] https://observing.docs.ligo.org/plan/

[8] https://www.ligo.caltech.edu/news/ligo20200326

[9] "First joint observation by the underground gravitational-wave detector KAGRA with GEO 600", The LIGO Scientific Collaboration, the Virgo Collaboration, and the KAGRA Collaboration, Prog. Theor. Exp. Phys., 063F01 (2022)

[10] "Performance of the KAGRA detector during the first joint observation with GEO 600 (O3GK)", The KAGRA Collaboration, Progress of Theoretical and Experimental Physics, ptac093, (2022)

[11] "Search for gravitational-lensing signatures in the full third observing run of the LIGO-Virgo network", The LIGO Scientific Collaboration, the Virgo Collaboration, the KAGRA Collaboration, ApJ, 970, 191 (2024)

[12] "A Joint Fermi-GBM and Swift-BAT Analysis of Gravitational-Wave Events from the GWTC-3 Catalog", C. Fletcher et al, ApJ, 964, 149 (2024)

[13] "Overview of KAGRA: Data Transfer and Management", T. Akutsu et al, Progress of Theoretical and Experimental Physics, Volume 2023, (2023)

[14] "Status of the underground gravitational wave detector KAGRA", the KAGRA Collaboration, PoS TAUP2023, 441.0116 (2024)

[15] "Detector characterization of KAGRA for the fourth observing run", Yuzurihara H, on behalf of the KAGRA Collaboration, PoS ICRC2023, 444, 1564 (2024)

[16] "The first joint observation by KAGRA with GEO 600", Uchikata N, on behalf of the KAGRA Collaboration, PoS ICRC2023, 444, 1579 (2024)

[17] "Investigation of the environmental noise at KAGRA detector", Yokozawa T, on behalf of the KAGRA Collaboration, PoS ICRC2023 444, 1557 (2024)

[18] "Evaluation of Microseismic Motion at the KAGRA Site Based on Ocean Wave Data", S Hoshino , Y Fujikawa , M Ohkawa , T Washimi , T Yokozawa, Prog. Theor. Exp. Phys. 2024 103F01 (2024)

[19] "Extension of the characterization method for non-Gaussianity in gravitational wave detector with statistical hypothesis test", Shunsei Yamamura, Hirotaka Yuzurihara, Takahiro Yamamoto, Takashi Uchiyama, Class. Quantum Grav. 41, 20, 205008 (2024)

[20] http://gwcenter.icrr.u-tokyo.ac.jp/en/

Commissioning

[Spokesperson : Takafumi USHIBA]

ICRR, The Univ. of Tokyo, Hida, Gifu 506-1205

In fiscal year 2024, commissioning activities were categorized into two groups: recovering the interferometer from damage caused by the Noto earthquake and improving sensitivity. The recovery of the interferometer — locking the Power Recycled Fabry–Pérot Michelson Interferometer (PRFPMI) with room-temperature sapphire mirrors — was finished in October 2024. Subsequently, interferometer commissioning to improve sensitivity was conducted for achieving 10 Mpc sensitivity.

Recovery of the interferometer After repairing the damaged suspensions, a health check was conducted on all suspensions before and after vacuum evacuation. The health checks were completed by the end of July, confirming that all suspensions were healthy.

Starting in April 2024, we conducted a full-scale initial alignment and lock acquisition to recover the interferometer from the Noto earthquakes. The Input Mode Cleaner (IMC) alignment was performed first and finished in April. Then, the X and Y arm alignments were completed in May and June, respectively. The alignment to the Output Mode Cleaner (OMC) was finished in July, after which lock acquisition began.

At first, the Auxiliary Lock System (ALS) with a green laser was recovered in July, and the FPMI was locked with RF signals in August. The PRFPMI lock with RF signals was also achieved in August, after which the Alignment Sensing and Control (ASC) was implemented. Then, the PRFPMI with DC readout was achieved in October, and the sensitivity of about 1 Mpc was recovered, which is the sensitivity before the Noto earthquakes.

Sensitivity improvement Before the Noto earthquakes, the sensitivity was limited by the acoustic noise around the OMC. Therefore, a detailed commissioning of the OMC was first conducted. It was then found that the vibration isolation stack for the OMC was not functioning well, resulting in much larger vibrations than expected. Therefore, the OMC stack was deconstructed and repaired. Additionally, the second resonance of the OMC stack occurred at the same frequency as the resonance of the OMC suspensions, enhancing the OMC vibration at that frequency. To avoid this situation, the number of stacks was reduced from three to two, making the stack resonance higher. Thanks to these modifications to the OMC stacks, the effect of the acoustic noise around the OMC was reduced, and a sensitivity of about 2 Mpc was achieved.

Starting at the end of 2024, four sapphire mirrors were cooled down to reduce thermal noise, which limited sensitivity around 100 Hz. The temperatures of all four mirrors reached around 90 K, and PRFPMI with four cooled mirrors was achieved in January. Then, the input laser power was increased from 1.2 W to 10 W to reduce shot noise, which limited the sensitivity at high frequencies. Due to the reduction of thermal and shot noise, a sensitivity of about 3.5 Mpc was achieved in February 2025.

The noise source of the 126 Hz peak was investigated from March 2025. Several investigations were performed at the corner station, which confirmed that the noise source is most likely in the Input Faraday Isolator (IFI) vacuum tank. Therefore, the IFI vacuum tank was vented and opened to investigate the inside of the vacuum chamber. It was then found that one of the steering mirrors in the IFI chamber was loose, causing large beam jitter around 126 Hz. After securing the steering mirror, a sensitivity of about 6 Mpc was achieved.

Vacuum

[Spokesperson : Takashi Uchiyama]
ICRR, The Univ. of Tokyo, Hida, Gifu 506-1205

The impact of the Noto Peninsula earthquake that occurred on January 1, 2024, was not caused by serious damage such as vacuum leaks, and fortunately, only one of the 40 turbo molecular pumps was stopped abnormally. On the other hand, there were many problems with the mirror suspension systems installed inside the vacuum chambers, so 23 vacuum chambers were opened, and recovery works were carried out. It was in July that all recovery works were completed and everything returned to vacuum.

During the restoration work, it was found that there was an oily liquid on the bottom of the EYA vacuum chamber. There was about 1L of liquid, and all of it was pumped out from the vacuum chamber. The inside of the vacuum chamber was cleaned using neutral detergents and solvents. The liquid was analyzed for ingredients, and it was presumed to be a glycerin fatty acid ester, and vegetable oil lubricants became a strong candidate. The composition analysis of the lubricant stored in KAGRA was found to be different from the liquid. As a result, the inflow route of the liquid and its substance remains unknown.

In preparation for the cooling of the mirrors, an interlock system was introduced to prevent contamination of the cooled mirror surface due to the deterioration of the vacuum pressure. The interlock is a system that closes 7 large GVs in KAGRA by a PLC device that monitors the vacuum pressure. While the interlocking function, if the vacuum pressure near the GV exceeds the set pressure due to vacuum leaks, etc., the large GV will automatically shut down. This can be expected to reduce the effect of atmospheric components attaching to the cooled mirror.

Cryogenic system

[Spokesperson : Nobuhiro KIMURA]
ICRR, The Univ. of Tokyo, Hida, Gifu 506-1205

One of KAGRA's unique features is the use of cryogenic sapphire mirrors in the 3 km-long arm cavity. The cryogenic system cooling the cryogenic sapphire mirrors was operated for 18 months from July 2022 to January 2024. During the period from March to October 2024, upgrade work and maintenance inspections were performed to correct problems identified during the continuous operation of the cryogenic system. Commissioning of the cryogenic system for O4c observations began in October 2024.

Maintenance and Improvement of Cryogenic System The cryogenic system of the KAGRA interferometer began cooling in July 2023 and continued operation for about 18 months until January 2024.

In January 2024, it was decided to return three cryogenic sapphire mirrors (ITMX, ETMX, and ETMY) to room temperature to repair interferometer equipment damaged by the earthquake, and warming was started. Subsequently, the decision was made to warm the remaining cryogenic sapphire mirror (ITMY), and four cryogenic sapphire mirrors were warmed back to room temperature by March 2024. The cryogenic system shutdown period due to the repair of damaged interferometer equipment was used to improve the cryogenic system and perform maintenance work. The following is a list

of the cryogenic system problems identified during the period of continuous operation and the actions taken to correct them.

(i) Instability of cooling characteristics was observed in some of the 24 pulse tube cryocoolers in the cryogenic system.

In order to improve the stability, the pressure of helium gas in all helium compressors was adjusted to prevent the instability from occurring during continuous operation.

(ii) An abnormal shutdown, presumably caused by overheating of the equipment, occurred in some of the 24 compressors supplying compressed helium gas to the pulse tube cryocoolers.

Based on analysis of inspection records, it was estimated that the cause of the overheating was deterioration of the cooling water passing through the heat exchanger that cools the compressed helium gas and contamination of the surface of the heat exchanger cooling channel.

To improve the cooling characteristics of the heat exchangers, the water cooling system of all compressors and three cooling water chillers that supply cooling water to the compressors were cleaned. In addition, measures were taken to prevent deterioration of the cooling water by adding chemicals to the circulating cooling water to modify the water as the cooling medium.

To detect overheating in the compressor, a new temperature monitoring system was constructed to constantly monitor the helium gas flowing in the compressor and the temperature of the cooling water. Any abnormality detected by this temperature monitoring system is immediately communicated to those involved in the cryogenic system.

Return of KAGRA cryogenic system Upon completion of maintenance and inspection of the cryogenic equipment, the cryogenic equipment began to be re-cooled on October 18, 2025. The cooling of the KAGRA cryogenic equipment was conducted in three phases. In the first stage, the duct shields on both sides of the cryostat were cooled, and the moisture in the residual gas in the adiabatic vacuum chamber of the cryostat was adsorbed around the duct shields. During the cooling of the duct shields, the residual gas components in each cryostat were continuously monitored with a quadrupole mass spectrometer. The moisture pressure of the residual gas component decreased to about 1/3 of that at room temperature in response to the progressive cooling of the duct shield. Based on the temperature distribution of the duct shield, the decrease in moisture pressure is assumed to be the result of moisture solidifying on the surface of the duct shield and on the surface of the super-insulation that surrounds the duct shield.

On December 16, 2025, about two months after the start of duct shield cooling, cooling of the double radiation shields of the four cryostats began, and the temperature of each duct shield was between 160 K and 170 K at the start of double radiation shield cooling. The cryogenic sapphire mirrors were cooled to about 250 K by radiation cooling from each duct shield.

On February 18, 2026, cooling of the two cryogenic sapphire mirrors (ETMX and ETMY) began.

Figure5 shows the temperatures of the four cryogenic sapphire mirrors at the end of March 2026. As a result, the temperatures of the cryogenic sapphire mirrors have almost returned to the state before the Noto Peninsula earthquake.

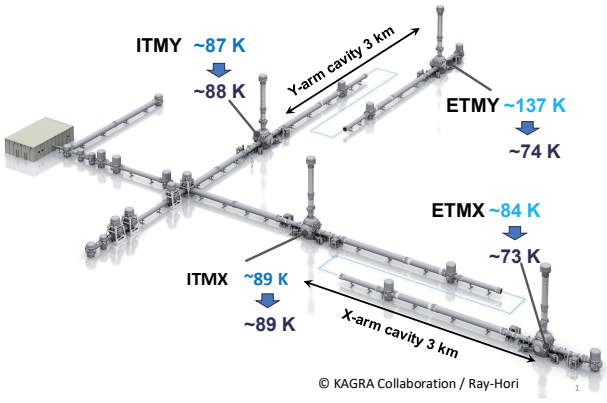


Fig. 5. Temperatures of cryogenic sapphire mirrors. The upper low shows the temperature at the time of the Noto Peninsula earthquake, and the lower low shows the temperature of each cryocooled sapphire mirror at the end of March 2025.

Environment Monitors

[Spokesperson : Takaaki YOKOZAWA]

ICRR, The Univ. of Tokyo, Hida, Gifu 506-1205

Since the amplitude of the GW is extremely small, vibration from essential instruments, sound from outside the experimental area, etc., can produce noise source contamination that limits KAGRA sensitivity. To evaluate the noise sources, many sensors are installed at the KAGRA site, including seismometers, microphones, magnetometers, and accelerometers. The first is to characterize underground and cryogenic environments. The KAGRA detector has two unique features, an underground and cryogenic environment, and these features are essential for next-generation detectors. We installed various PEMs, including accelerometers, microphones, magnetometers, thermometers, and weather stations. The second is to evaluate whether the current KAGRA sensitivity is limited by environmental noise or not.

After the recovery of the interferometer from the large Noto earthquake, we performed the noise evaluation around the OMC (Output Mode Cleaner) first. With the improvement of the stacks and damping for the OMC, we expected to reduce the effect of the environmental noise, compared to the O4a run.

In addition to this, we generated the large coil and performed the magnetic injection test using it. We concluded that the current noise level might not be limited by magnetic noise.

We investigated various ground motions using seismometers. Microseismic noise, which is the ground motion of $\sim$ 0.2 Hz caused by the sea wave, affects the efficiency of the commissioning. So we forecast the microseismic noise using machine learning of past data. Compared with the PCA method, the accuracy of the forecast may be improved. Also,

the ground motion from the blasting, near construction work, and nearby earthquake was investigated.

Digital system

[Spokesperson : Shoichi OSHINO]
ICRR, The Univ. of Tokyo, Hida, Gifu 506-1205

In preparation for the upcoming international joint observation of gravitational waves starting in FY2025, we have made significant progress in upgrading and maintaining the digital system infrastructure at KAGRA.

A new workstation was installed inside the clean booth of the center area for working inside the clean booth more efficiently. The MTP fiber cable connecting the first and second floors of the X-end station was laid. This cable will be used for the new IO chassis to be introduced in the future. The operating systems of the workstations and monitor PCs were upgraded sequentially. Additionally, a full backup of the digital system was taken to ensure data integrity and recovery readiness.

To address the issue of IPC glitches affecting gravitational wave data, we implemented several countermeasures. These included replacing network interface cards, balancing data rates, and reducing the total data volume. As a result, the frequency of glitches has been significantly reduced.

We also introduced a new NAS (Network Attached Storage) system to improve data redundancy. We installed new ADC (Analog-to-Digital Converter) and DAC (Digital-to-Analog Converter) units to improve data acquisition and control capabilities.

Furthermore, we have been updating many of the RT models in preparation for improving the stability and sensitivity of the interferometer.

Detector Charcterization

[Spokesperson : Hirotaka Yuzurihara]
ICRR, The Univ. of Tokyo, Hida, Gifu 506-1205

Data sharing with LIGO and Virgo The data from GW observatories (LIGO, Virgo, and KAGRA) are collected by the cluster at the California Institute of Technology (CIT). To search for the gravitational wave signals in the KAGRA data, it is necessary to know in advance which times of the data should be analyzed or which times should be excluded from the analysis. This information is called the data quality (DQ) flag.

The task of the KAGRA Detector Characterization is to provide LVK members with the DQ flags of the KAGRA data. We regularly updated the DQ flags based on knowledge during the commissioning phase. The updated DQ flags covered disturbances due to environmental noise as well as noise transients coming from instrument electrical glitches, operational errors caused by human activities, and so on. The DQ flags for O4a data were automatically generated at the KAGRA site, uploaded to the dedicated server, and shared with the data analysis members in the LIGO-Virgo-KAGRA collaboration.

Data quality evaluation for KAGRA data One of the essential roles of Detector Characterization is to prevent the false detection of gravitational waves. Gravitational waves (GWs) are very weak signals buried by various disturbances, such as the vibration of the mirrors that constitute an interferometer and the instability of the laser power and frequency. Such disturbances can also be detected as false GW events. Understanding the behavior and statistics of the detector noise is essential for separating GWs from such false events.

It is known that the strain data contains many transient or non-stationary disturbances. Therefore, we provided various tools for understanding and mitigating noise sources. By using the tools, we evaluated the KAGRA data. In the study of non-Gaussian noise, we developed a tool to evaluate the non-Gaussianity of the strain data. The developed tool processes and analyzes the strain data once an hour. The results are available on the internal web page. Monitoring the time variability of Gaussianity effectively contributed to noise hunting during commissioning, identifying unknown noise, and characterizing the number of occurrences and problematic frequency bands. One significant example is the discovery and visualization of scattered noise in the O4a data through monitoring of Gaussianity.

S.Yamamura *et al.* extended the conventional method to evaluate non-Gaussian noise, called the Rayleigh statistic, using a statistical hypothesis test to determine a threshold for non-Gaussian noise. This extension can contribute to the initial detection of non-Gaussian noise and lead to further investigation of its origin. The results, including the new algorithm and its application to the simulation data and the observing run data, were submitted in fiscal year 2023 and published as a refereed paper in CQG [1] in fiscal year 2024.

Lockloss investigation Long-term operation with stable control is essential for detecting gravitational waves. The detection probability of gravitational waves depends on the observing time and the observable volume, which is proportional to the cube of the detectable distance. Therefore, the possibility of detecting gravitational waves can be increased if the observation time can be extended by achieving stable interferometer operation.

The length and angle control to keep the interferometer in resonance are performed by software called Guardian. Various environmental disturbances, control oscillations, and the overflow of the control can cause the interferometer to fall out of its controlled state. This phenomenon is called lockloss. To identify the cause of the lockloss, it is essential to collect information on the type of disturbance that occurred, which control was oscillating, and the oscillation frequency as quickly as possible. Based on this information, the interferometer control can be improved to reduce the number of lockloss. To achieve stable operation, lockloss should be minimized as much as possible.

For this purpose, the system that automatically identifies the possible causes of lockloss has been developed for the O4a observing run. The time of the lockloss, the state of the interferometer before the lock loss, the lock duration, and the possible causes of the lockloss are collected and summarized on the internal web page. In fiscal year 2024, we started the

lockloss investigation during the commissioning data by using this system. The developed system has helped save time in investigating the cause of lockloss and improve the stability of the interferometer controls.

Bibliography

[1] Shunsei Yamamura, Hirotaka Yuzurihara, Takahiro Yamamoto, Takashi Uchiyama, Class. Quantum Grav. 41 205008 (2024)

Operations

[Spokesperson : Takahiro Sawada]

ICRR, The Univ. of Tokyo, Hida, Gifu 506-1205

The Operations Division leads the end-to-end coordination of scientific operations, including the calibration and quality assurance of interferometer data, its timely delivery to analysis teams, and public release in accordance with open data policies. The Division also manages computing infrastructure and software environments, oversees the low-latency alert system for gravitational-wave (GW) event notifications, and plays a central role in organizing observing run schedules and synchronizing operational schedules—such as observing, commissioning, and maintenance—across observatories within the international GW network. It supervises six key groups—Calibration, Detector Characterization, Computing and Software, Low Latency, Open Data, and the Run Planning Committee—each contributing essential capabilities to enabling reliable scientific results and maximizing their yield through the joint international operation of the detectors. In fiscal year 2024, the Division undertook a broad range of initiatives, as described below, in addition to the regular responsibilities of its constituent groups. These efforts aimed to strengthen KAGRA's responsiveness, reliability, and integration within the global multi-detector network.

To support the timely vetting of GW event candidates during observing runs, the Division enhanced its functional capacity within the Rapid Response Team (RRT)—a global collaboration operating on a 24/7 shift-based system and comprising several hundred researchers. The Division maintained and strengthened internal systems for rapid validation and advanced the development of training plans and operational procedures. These efforts were led by the Division's RRT Managers, who oversaw the preparation and readiness processes. During actual event responses, the Division's Site Advocate played a leading role in coordinating discussions. These measures ensured effective contribution to the RRT via channels such as GCN Circulars.

The Run Coordinator from the Division played a key role in managing operational software integrity through active involvement in the Software Change Control Board (SCCB) under the IGWN Computing & Software Committee. The SCCB is charged with assessing proposed changes to software environments or configurations, ensuring they have undergone proper testing, packaging, and scientific review before being considered. The Run Coordinator held final approval authority for such changes during observation periods, thereby contributing to stable and coordinated operations of the GW network.

The Division contributed to the assessment and maintenance of the Low Latency Alert Infrastructure (LLAI), a system supporting low-latency GW event notifications. It worked with the LLAI Review Team to evaluate the technical robustness of the infrastructure, including its architecture, operational behavior, and fault tolerance mechanisms. Additionally, the Low-Latency Group Chair and Division Chair contributed to the design of the Low-Latency Production Integration Challenge (LLPIC). This end-to-end test campaign verifies the stable, consistent, and non-invasive operation of alert-generation and annotation pipelines within the production environment. Only those pipelines that pass LLPIC validation are authorized for use during observing runs.

Data Analysis, Computing environment

[Spokesperson : Nami Uchikata, Tatsuya Narikawa, Soichiro Morisaki, Hideyuki Tagoshi]

ICRR, The Univ. of Tokyo, Kashiwa, Chiba, 277-8582

Activities in the LVK Observational Science Division

The KAGRA data analysis is now performed jointly with LIGO and Virgo under the LIGO-Virgo-KAGRA Memorandum of Agreement (MoA). The MoA defines the policy of joint data analysis and data sharing. In the Observational Science Division of the LIGO-Virgo-KAGRA (LVK) Collaboration, there is a Data Analysis Council (DAC), which is a committee managing data analysis activities in LVK. Under DAC, there are four working groups regarding the gravitational wave signal search, Compact Binary Coalescence working group (CBC), Burst working group (Burst), Continuous Wave Working Group (CW), and Stochastic Background Working Group (Stochastic). From ICRR, Hideyuki Tagoshi is serving as a co-chair of DAC, and Tatsuya Narikawa is serving as a review co-chair of the CBC group. Further, Nami Uchikata is managing the remote meeting of the Test of General Relativity Subgroup under the CBC group.

O4 activities

KAGRA is planning to join the O4c run from spring 2025. Although the expected binary neutron star range is at most 10 Mpc, which is much lower than the current LIGO and Virgo, it might be possible to find a signature of gravitational wave signals in the KAGRA data if we use the information of observed signals by LIGO and Virgo. A dedicated pipeline to search for CBC signals in the KAGRA data, targeting the detected signals by LIGO and Virgo, is under development. This pipeline is planned to be applied to KAGRA O4c data. The project is led by Takashi Kato and Hideyuki Tagoshi.

After the O4a run, the LVK collaborations are working on various analyses for the observed events during the run and preparing collaboration papers including those results. Among those collaboration papers, N. Uchikata is contributing to the O4a Tests of General Relativity (TGR) paper as a member of the paper writing team. The paper is planned

to be released around the summer of 2025. N. Uchikata and T. Narikawa are also working on gravitational wave echo analysis, which will be included in the O4a TGR paper, using the analysis pipeline developed from FY2023. The Python package to generate the gravitational wave echo waveform model used in this analysis is available in public (R. K. L. Lo and N. Uchikata [1].

Accurately inferring the spin distribution of merging black holes from gravitational-wave data is crucial for understanding their formation channels. M. Iwaya, K. Kobayashi, and S. Morisaki revisited a previous analysis conducted by the LVK Collaboration and found that the numerical method used to compute a key quantity for likelihood evaluation introduces non-negligible numerical errors. To overcome this, they developed an analytical method that avoids these issues [2]. Applying their approach to existing gravitational-wave events, they recovered a spin distribution nearly identical to that obtained in the earlier analysis, suggesting that the numerical errors are not significant for current datasets. However, as the number of detected events grows, these errors may accumulate, making their analytical method increasingly important for future analyses.

Gravitational-wave detectors, owing to their extreme sensitivity, can also be used to search for phenomena beyond gravitational waves, such as ultralight dark matter. S. Morisaki and collaborators have been investigating the potential of these detectors to probe various dark matter candidates, including dark photons and axions. In the current fiscal year, they analyzed the statistical properties of signals induced by ultralight dark matter and developed an optimal data analysis method to extract such signals [3]. They are currently developing a search pipeline that implements this technique and plan to apply it to data from O4.

Studies on the effect of the tidal deformability of neutron stars on binary neutron star signals have also been done in the group. This year, T. Narikawa wrote a review article on this topic [4].

Managing computing environment

As one of the main computing resources in KAGRA, the KAGRA main data server has been working at ICRR Kashiwa. The first main data server (System A) was decommissioned in November 2023, and System B is now operational. It has 4PB data storage and 512 computing cores.

All data taken by the KAGRA detector at the Kamioka site are packed into one file every 32 seconds and continuously transferred to the main data server at Kashiwa. In addition to this, low-latency data transfer is also done by packing only the gravitational wave channel and a few other channels into one file every 1 second. For low-latency data transfer, a latency of about 3.5 seconds is achieved from Kamioka to Kashiwa (this time includes the time necessary for calibration). In order to share the low-latency data file among LIGO-Virgo-KAGRA, the low-latency data files are transferred to LIGO and Virgo. The low-latency data files of the LIGO and Virgo detectors are transferred to the KAGRA main data server.

We have another computing cluster that is mainly used for data analysis tasks. During FY2024, we introduced an additional computing node, and the total computing cores of the system became 1188 cores.

Bibliography

[1] https://git.ligo.org/echoes_template_search/echoes_waveform_models

[2] M. Iwaya, K. Kobayashi, S. Morisaki, K. Hotokezaka and T. Kinugawa, Phys. Rev. D **111**, no.10, 103046 (2025) doi:10.1103/PhysRevD.111.103046 [arXiv:2412.14551 [gr-qc]].

[3] S. Morisaki, J. Kume, T. Fujimori and Y. Michimura, [arXiv:2503.04484 [hep-ph]].

[4] T. Narikawa, Butsuri, Vol. 79, No. 10 (2024)

IGWN

Currently, the LIGO, Virgo, and KAGRA collaborations are preparing to transition from the existing LIGO-Virgo-KAGRA framework —established under the current Memorandum of Agreement — to a unified collaboration, the International Gravitational Observatory Network (IGWN).

The primary motivation for this transition is to enhance the efficiency of international joint observing runs and data analysis, thereby facilitating the timely and effective production of scientific results.

It is now widely recognized that a new organizational structure is essential to fully realize the scientific potential of the LIGO-Virgo-KAGRA (LVK) network. In order to effectively achieve our scientific objectives, a coordinated and unified framework is required — one that defines shared scientific goals and establishes their priorities based on scientific merit and the availability of resources.

The current system, which relies on parallel, independent, and at times redundant decision-making processes, has proven to be inefficient. Moving forward, a streamlined structure that eliminates such inefficiencies is necessary.

There are numerous activities within the network that can and should be consolidated, rather than duplicated. To support the operations of a unified observatory network, efforts to secure additional resources have already been initiated. A single organizational entity will be essential to ensure the fair and efficient allocation of these resources.

Furthermore, the integration of infrastructure and operations across the entire network must proceed in a seamless and coordinated manner.

The LIGO Scientific Collaboration, the Virgo Collaboration, and the KAGRA Collaboration are expected to be formally unified under IGWN through a process of constructive consolidation. While IGWN will serve as an overarching framework composed of multiple observatories, the individual independence and autonomy of each observatory will be maintained.

At present, efforts are underway to draft and establish the governance and operational rules necessary for the formation of IGWN.

The current target is to officially establish IGWN and begin its operations in January 2027. From the fifth observation run (O5) onward, scientific observations and data analysis will

be conducted under the IGWN framework. As of now, the anticipated start date for O5 is January 2028.

Observational Cosmology Group

[Spokesperson: Yoshiaki Ono]

ICRR, The Univ. of Tokyo, Kashiwa, Chiba 277-8582

JWST, ALMA, and Keck Spectroscopic Constraints on the UV Luminosity Functions at $z \sim 7$–14: Clumpiness and Compactness of the Brightest Galaxies in the Early Universe [1]

In collaboration with the members of Waseda University, University College London, National Astronomical Observatory of Japan, University of Arizona, Harvard–Smithsonian Center for Astrophysics, University of Melbourne, The University of Texas at Austin, University of Edinburgh, Spanish Astrobiology Center, Saint Mary's University, Toba College, Space Telescope Science Institute, Aix-Marseille University, McDonald Observatory, UCO/Lick Observatory, SOKENDAI, Ehime University, and Nagoya University.

We present the number densities and physical properties of the bright galaxies spectroscopically confirmed at $z \sim 7$–14. Our sample is composed of 60 galaxies at $z_{\rm spec} \sim 7$–14, including recently confirmed galaxies at $z_{\rm spec} = 12.34$–14.18 with JWST, as well as new confirmations at $z_{\rm spec} = 6.583$–7.643 with $-24 < M_{\rm UV} < -21$ mag using ALMA and Keck. Our JWST/NIRSpec observations have also revealed that very bright galaxy candidates at $z \sim 10$–13 identified from ground-based telescope images before JWST are passive galaxies at $z \sim 3$–4, emphasizing the necessity of strict screening and spectroscopy in the selection of the brightest galaxies at $z > 10$. The UV luminosity functions derived from these spectroscopic results are consistent with a double power-law function, showing tensions with theoretical models at the bright end. To understand the origin of the overabundance of bright galaxies, we investigate their morphologies using JWST/NIRCam high-resolution images obtained in various surveys, including PRIMER and COSMOS-Web. We find that $\sim 70\%$ of the bright galaxies at $z \sim 7$ exhibit clumpy morphologies with multiple subcomponents, suggesting merger-induced starburst activity, which is consistent with SED fitting results showing bursty star formation histories. At $z \gtrsim 10$, bright galaxies are classified into two types: extended ones with weak high-ionization emission lines, and compact ones with strong high-ionization lines including [NIV]λ1486, indicating that at least two different processes (e.g., merger-induced starburst and compact star formation/AGN) are shaping the physical properties of the brightest galaxies at $z \gtrsim 10$ and are responsible for their overabundance (Figure 1).

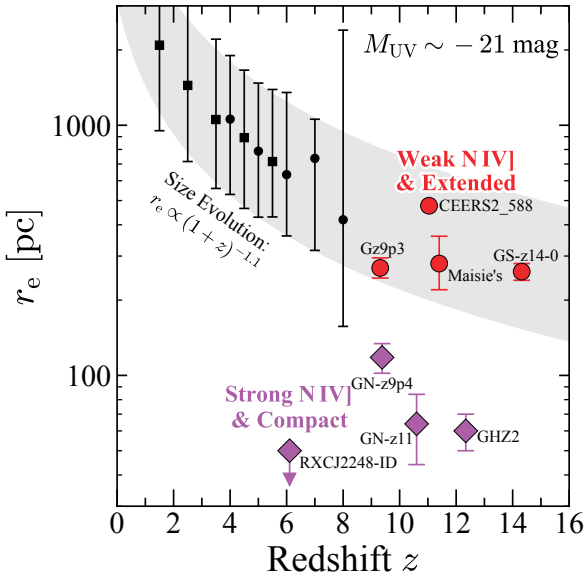


Fig. 1. Rest-frame UV effective radius of galaxies as a function of redshift. The black symbols are size measurements for bright galaxies with $M_{\rm UV} \sim -21$ mag at $z = 0$–8 and the gray shaded region shows the size evolution for galaxies with $M_{\rm UV} \sim -21$ mag and its 1σ dispersion in the literature. The red circles are bright galaxies at $z > 9$ whose sizes follow the redshift evolution measured at $z \sim 0$–8 and the magenta diamonds are compact galaxies whose effective radii are smaller than ~ 100 pc in the literature. Bright galaxies at $z \gtrsim 10$ can be classified into two types: extended galaxies with weak high-ionization emission lines (the red circles), and compact galaxies with strong high-ionization lines, such as NIV]λ1486 (the magenta diamonds). The extended galaxies with sizes of $r_e \sim 200$–500 pc do not exhibit prominent rest-UV high-ionization emission lines and sometimes show a signature of merger activity. In contrast, the compact galaxies exhibit strong high-ionization lines, such as CIVλ1549, HeIIλ1640, and NIV]λ1486 (e.g., EW(NIV]λ1486) $\sim$ 10–30 Å), suggesting compact and intense starburst or AGN activity.

Bibliography

[1] Harikane, Y.; Inoue, A. K.; Ellis, R. S.; Ouchi, M.; Nakazato, Y.; Yoshida, N.; Ono, Y.; Sun, F.; Sato, R. A.; Fujimoto, S.; Kashikawa, N.; McLeod, D. J.; Perez-Gonzalez, P. G.; Sawicki, M.; Sugahara, Y.; Xu, Y.; Yamanaka, S.; Carnall, A. C.; Cullen, F.; Dunlop, J. S.; Egami, E.; Grogin, N.; Isobe, Y.; Koekemoer, A. M.; Laporte, N.; Lee, C.-H.; Magee, D.; Matsuo, H.; Matsuoka, Y.; Mawatari, K.; Nakajima, K.; Nakane, M.; Tamura, Y.; Umeda, H.; Yanagisawa, H., 2025, The Astrophysical Journal, 980, 138

JWST Measurements of Neutral Hydrogen Fractions and Ionized Bubble Sizes at $z = 7$–12 Obtained with Lyα Damping Wing Absorptions in 27 Bright Continuum Galaxies [2]

In collaboration with the members of National Astronomical Observatory of Japan.

We present volume-averaged neutral hydrogen fractions $x_{\rm HI}$ and ionized bubble radii R_b measured with Lyα damping wing absorption of galaxies at the epoch of reionization. We

combine JWST/NIRSpec spectra taken by the CEERS, GO-1433, DDT-2750, and JADES programs and obtain a sample containing 27 bright UV-continuum ($M_{\rm UV} < -18.5$ mag) galaxies at $7 < z < 12$. We construct four composite spectra binned by redshift and find the clear evolution of the softening break toward high redshift at rest-frame 1216 Å, suggesting an increase of Lyα damping wing absorption. We estimate Lyα damping wing absorption in the galaxy spectra with realistic templates including Lyα emission and circumgalactic medium absorptions (Figure 2). Assuming the standard inside-out reionization picture having an ionized bubble with radius R_b around a galaxy embedded in the intergalactic medium with $x_{\rm HI}$, we obtain $x_{\rm HI}$ (R_b) values generally increasing (decreasing) from $x_{\rm HI} = 0.53^{+0.18}_{-0.47}$ to $0.92^{+0.08}_{-0.10}$ ($\log R_b = 1.67^{+0.14}_{-0.16}$ to $-0.69^{+0.89}_{-0.24}$ comoving Mpc) at redshift $z = 7.12^{+0.06}_{-0.08}$ to $9.91^{+1.49}_{-1.15}$. The redshift evolution of $x_{\rm HI}$ indicates a moderately late reionization history consistent with the one previously suggested from the electron scattering of cosmic microwave background and the evolution of UV luminosity function with an escape fraction $f_{\rm esc} \sim 0.2$. Our R_b measurements suggest that bubble sizes could be up to a few dex larger than the cosmic average values estimated by analytic calculations for a given $x_{\rm HI}$, while our R_b measurements are roughly comparable with the values for merged ionized bubbles around bright galaxies predicted by recent numerical simulations.

Bibliography

[2] Umeda, H.; Ouchi, M.; Nakajima, K.; Harikane, Y.; Ono, Y.; Xu, Y.; Isobe, Y.; Zhang, Y., 2024, The Astrophysical Journal, 971, 124

Dynamics of a Galaxy at $z > 10$ Explored by JWST Integral Field Spectroscopy: Hints of Rotating Disk Suggesting Weak Feedback [3]

In collaboration with the members of National Astronomical Observatory of Japan, University of Tsukuba, and Waseda University.

We investigate the dynamics of GN-z11, a luminous galaxy at $z = 10.60$, carefully analyzing the public deep integral field spectroscopy (IFS) data taken with the JWST NIRSpec integral field unit. While the observations of the IFS data originally targeted an HeII clump near GN-z11, we find that the CIII]$\lambda\lambda$1907,1909 emission from ionized gas at GN-z11 is bright and spatially extended significantly beyond the point-spread function (PSF). The spatially extended CIII] emission of GN-z11 shows a velocity gradient with red- and blueshifted components in the north and south directions, respectively, which cannot be explained by the variation of the [CIII]λ1907/CIII]λ1909 line ratios. Assuming the velocity gradient is produced by disk rotation, we perform forward modeling with GalPak^{3D}, including the effects of PSF smearing and line blending, and obtain a rotation velocity of $v_{\rm rot} = 257^{+138}_{-117}$ km s^{-1}, a velocity dispersion of $\sigma_v = 91^{+18}_{-32}$ km s^{-1}, and a ratio of $v_{\rm rot}/\sigma_v = 2.83^{+1.82}_{-1.41}$. The $v_{\rm rot}/\sigma_v$ value would suggest a rotation-dominated disk existing at $z > 10$,

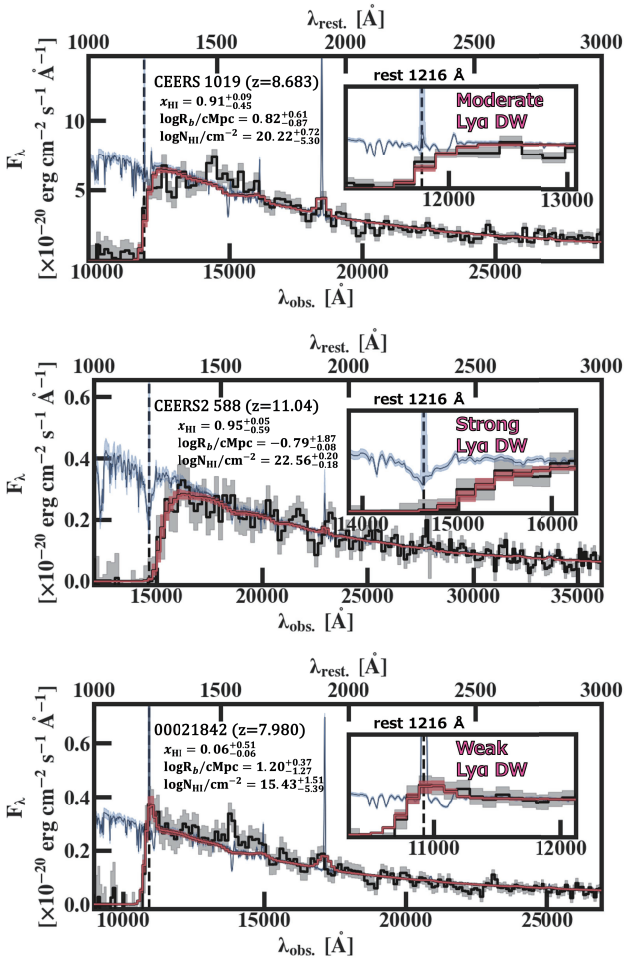


Fig. 2. Fitted spectrum for the case of moderate, strong, and weak Lyα damping wing absorption features seen in CEERS_1019, CEERS2_588, and 000021842 from the top to bottom panels, respectively. The black line and shading represent the observed spectrum and its error, respectively. The red (blue) line and shading represent the model spectrum and its uncertainty after (before) Lyα absorptions applied and smoothed with PRISM resolution, respectively. The black dotted line represents rest-frame 1216 Å at the systemic redshift. The inset panel shows a zoom-in view of the spectrum around rest-frame 1216 Å. The best-fit values and uncertainties for $x_{\rm HI}$, $\log R_b$, and $\log N_{\rm HI}$ for each object are also written inside each panel. The x-axes in the top and bottom panels represent the observed and rest-frame wavelength, respectively.

albeit with large uncertainties (Figure 3). The rotation velocity agrees with that of numerical simulations predicting a rotating disk formed in the early Universe under the conditions of mass compaction and weak feedback. While the velocity gradient is consistent with the rotating-disk solution, we recognize that galactic outflows can also explain the velocity gradient, as well as the extended morphology and the high velocity dispersion found in the outskirts. Higher signal-to-noise ratio and higher-resolution data are necessary to conclude the physical origin of the velocity gradient in GN-z11.

Bibliography

[3] Xu, Y.; Ouchi, M.; Yajima, H.; Fukushima, H.; Harikane, Y.; Isobe, Y.; Nakajima, K.; Nakane, M.; Ono, Y.; Umeda,

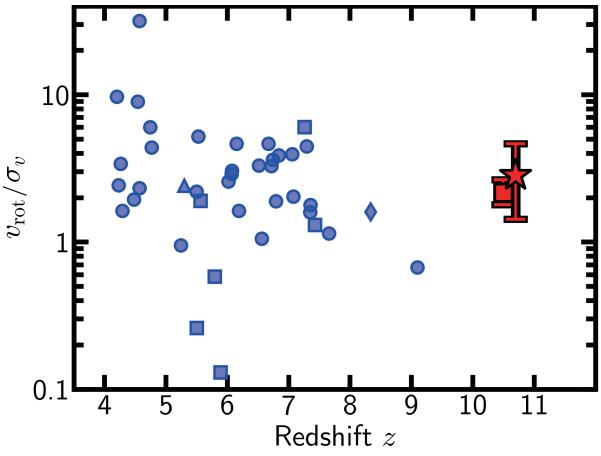


Fig. 3. $v_{\rm rot}/\sigma_v$ of GN-z11 compared to those obtained by previous studies at different redshifts. Our results of GN-z11 are shown with the red star and square, which show $v_{\rm rot}/\sigma_v$ obtained with GalPak$^{\rm 3D}$ modeling and the observed kinematic ratio $\Delta v_{\rm obs}/\sigma_{\rm med}$, respectively. The blue circles are galaxies whose [CII] kinematics are measured with ALMA, taken from the literature. The blue squares are recent JWST results using the NIRSpec MSA, taken from the literature, while the blue triangles and diamonds are taken from the literature, which uses the NIRCam WFSS.

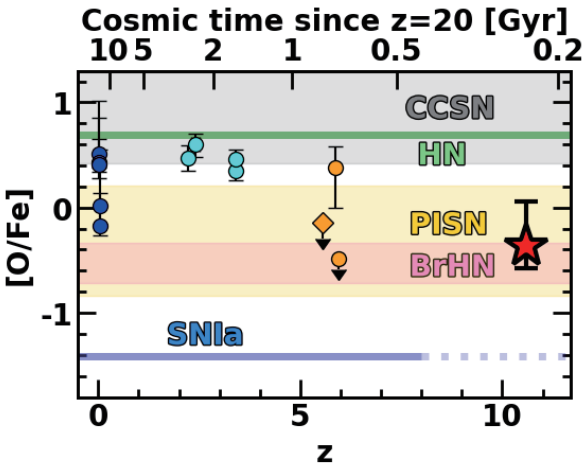


Fig. 4. Abundance ratio of O/Fe as a function of redshift. The red star symbol indicates our measurements from spectral fitting to the spectra of GN-z11. The cyan and orange circles show the measurements in the fitting method for composite spectra of galaxies at $z \sim 2$–3 and $z \sim 6$, respectively, taken from the literature. The blue circles indicate the measurements for local EMPGs in the literature. The gray, green, violet, yellow, and blue shaded regions represent the yields of CCSNe, HNe, BrHNe, PISNe, and SNe Ia, respectively, taken from the literature.

H.; Yanagisawa, H.; Zhang, Y., 2024, The Astrophysical Journal, 976, 142

Low [O/Fe] Ratio in a Luminous Galaxy at the Early Cosmic Epoch ($z > 10$): Signature of Short Delay Time or Bright Hypernovae/Pair-instability Supernovae? [4]

In collaboration with the members of National Astronomical Observatory of Japan, Konan University, and Waseda University.

We present an [O/Fe] ratio of a luminous galaxy GN-z11 at $z = 10.60$ derived with the deep public JWST/NIRSpec data. We fit the medium-resolution grating (G140M, G235M, and G395M) data with the model spectra consisting of BPASS-stellar and CLOUDY-nebular spectra in the rest-frame UV wavelength ranges with Fe absorption lines, carefully masking the other emission and absorption lines in the same manner as previous studies conducted for lower-redshift ($z \sim$ 2–6) galaxies with oxygen abundance measurements. We obtain an Fe-rich abundance ratio $[{\rm O/Fe}] = 0.37^{+0.43}_{-0.22}$, which is confirmed with the independent deep prism data as well as by the classic 1978 index method. This [O/Fe] measurement is lower than that measured for star-forming galaxies at $z \sim 2$–3. Because $z = 10.60$ is an early epoch after the Big Bang ($\sim$ 430 Myr) and the first star formation (likely $\sim$ 200 Myr), it is difficult to produce Fe by Type Ia supernovae (SNe Ia), which require sufficient delay time for white-dwarf formation and gas accretion. The Fe-rich abundance ratio in GN-z11 suggests that the delay time is short or that the major Fe enrichment is not accomplished by SNe Ia but by bright hypernovae (BrHNe) and/or pair-instability supernovae (PISNe), where the yield models of BrHNe and PISNe explain Fe, Ne, and O abundance ratios of GN-z11 (Figure 4). The [O/Fe] measurement is not too low to rule out the connection between GN-z11 and globular clusters (GCs) previously suggested by the nitrogen abundance, but rather supports the connection with a GC population at high [N/O] if a metal dilution process exists.

Bibliography

[4] Nakane, M.; Ouchi, M.; Nakajima, K.; Harikane, Y.; Tominaga, N.; Takahashi, K.; Yanagisawa, H.; Watanabe, K.; Nomoto, K.; Isobe, Y.; Kashino, D.; Nishigaki, M.; Ishigaki, M. N.; Ono, Y.; Takeda, Y., 2024, The Astrophysical Journal, 976, 122

Balmer Decrement Anomalies in Galaxies at $z \sim 6$ Found by JWST Observations: Density-bounded Nebulae or Excited HI *Clouds?* [5]

In collaboration with the members of National Astronomical Observatory of Japan, University of Tsukuba, and Japan Aerospace Exploration Agency (JAXA).

We investigate the physical origins of the Balmer decrement anomalies in GS-NDG-9422 and RXCJ2248-ID galaxies at $z \sim 6$ whose Hα/Hβ values are significantly smaller than 2.7, the latter of which also shows anomalous Hγ/Hβ and Hδ/Hβ values beyond the errors. Because the anomalous Balmer decrements are not reproduced under the Case B recombination, we explore the nebulae with optical depths smaller and larger than the Case B recombination by physical modeling. We find two cases quantitatively explaining the anomalies: (1) density-bounded nebulae that are opaque only up to around Lyγ–Ly8 transitions, and (2) ionization-bounded nebulae partly/fully surrounded by optically thick excited HI

clouds (Figure 5). The case of (1) produces more Hβ photons via Lyγ absorption in the nebulae, requiring fine-tuning in optical depth values, while this case helps ionizing photon escape for cosmic reionization. The case of (2) needs the optically thick excited HI clouds with $N_2 \sim 10^{12}$–10^{13} cm^{-2}, where N_2 is the column density of the hydrogen atom with the principal quantum number of $n = 2$. Interestingly, the high N_2 values qualitatively agree with the recent claims for GS-NDG-9422, with the strong nebular continuum requiring a number of 2s-state electrons, and for RXCJ2248-ID, with the dense ionized regions likely coexisting with the optically thick clouds. While the physical origin of the optically thick excited HI clouds is unclear, these results may suggest gas clouds with excessive collisional excitation caused by an amount of accretion and supernovae in the high-z galaxies.

Bibliography

[5] Yanagisawa, H.; Ouchi, M.; Nakajima, K.; Yajima, H.; Umeda, H.; Baba, S.; Nakagawa, T.; Nakane, M.; Matsumoto, A.; Ono, Y.; Harikane, Y.; Isobe, Y.; Xu, Y.; Zhang, Y., 2024, The Astrophysical Journal, 974, 180

Theory Group

Overview

The theory group conducts active research in both elementary particle physics and astroparticle physics, with particular emphasis on particle phenomenology and particle cosmology. In the domain of particle physics, key topics include theoretical investigations of dark matter, cosmic inflation, and various extensions of the Standard Model. In astroparticle physics, the group focuses on inflationary dynamics, the thermal history of the early universe, dark matter, baryogenesis, and Big Bang nucleosynthesis (BBN).

Following the discovery of the Higgs boson, the Large Hadron Collider (LHC) has yet to provide definitive evidence for physics beyond the Standard Model. In light of this, there is a growing need to critically reassess prevailing theoretical frameworks and to explore new paradigms and strategies for uncovering novel phenomena. Consequently, our research on physics beyond the Standard Model continues to diversify in both scope and methodology.

Since the first direct detection of gravitational waves (GWs) by the LIGO collaboration on 14 September 2015—from the merger of two black holes—a new era of gravitational wave astronomy has emerged. Numerous GW events have since been observed, including the landmark detection from a binary neutron star merger. This event provided compelling evidence for the existence of kilonovae, which are believed to be key sites for the production of heavy r-process elements. As the catalogue of GW events continues to grow, elucidating the astrophysical origins of such sources remains a central and highly active area of research.

Supersymmetric (SUSY) extensions of the Standard Model remain among the most theoretically compelling frameworks for new physics. SUSY offers a natural solution to the hierarchy problem associated with the Higgs boson mass and aligns well with grand unified theories (GUTs). Although superpartners have not yet been detected at the LHC, SUSY scenarios continue to be leading candidates for beyond-the-Standard-Model physics. Our group has long investigated both the phenomenological and cosmological implications of the models.

Recent high-precision cosmological observations, notably those from the Planck satellite, have robustly determined the mean densities of matter and baryons in the Universe, firmly establishing the presence of non-baryonic dark matter. Among the viable candidates, weakly interacting massive particles (WIMPs) are of particular interest, acting as cold dark matter in the formation of large-scale structures. Our research includes the construction of particle physics models for dark matter and the study of their detectability in both direct detection experiments and indirect astrophysical searches.

The study of the early universe is deeply intertwined with developments in elementary particle physics. Advances such as grand unification and supersymmetry have provided profound insights into the fundamental processes that shaped the early cosmos. In particular, the inflationary paradigm posits that quantum fluctuations of the inflaton field seeded the primordial density perturbations, ultimately giving rise to the large-scale structure observed today. Conversely, cosmological and astrophysical observations serve as powerful probes of new theoretical models in particle physics, making particle cosmology a central theme of our research.

Big Bang nucleosynthesis remains a cornerstone of modern cosmology. The predicted abundances of light elements are highly sensitive to the details of the early universe. Physics beyond the Standard Model often introduces new particles that may have been present during the BBN epoch, potentially altering the nucleosynthesis outcomes. Such considerations impose stringent constraints on new particle species and theoretical models.

Grand unified theories predict that the universe underwent multiple vacuum phase transitions in its early stages. These transitions generally result in the formation of topological defects—such as monopoles, cosmic strings, and domain walls—depending on the symmetry-breaking patterns involved. Our group has studied the formation and evolution of various types of topological defects and their cosmological consequences.

Particle Phenomenology

[Spokesperson : Masahiro Ibe]
ICRR, The University of Tokyo, Kashiwa, Chiba 277-8582

Small instanton effects on composite axion mass **[1]**

In collaboration with the members of ICRR and Kavli IPMU.

This paper investigates the impact of small instanton effects on the axion mass in composite axion models. In particular, we focus on the Composite Accidental Axion (CAA) models, which are designed to address the axion quality prob-

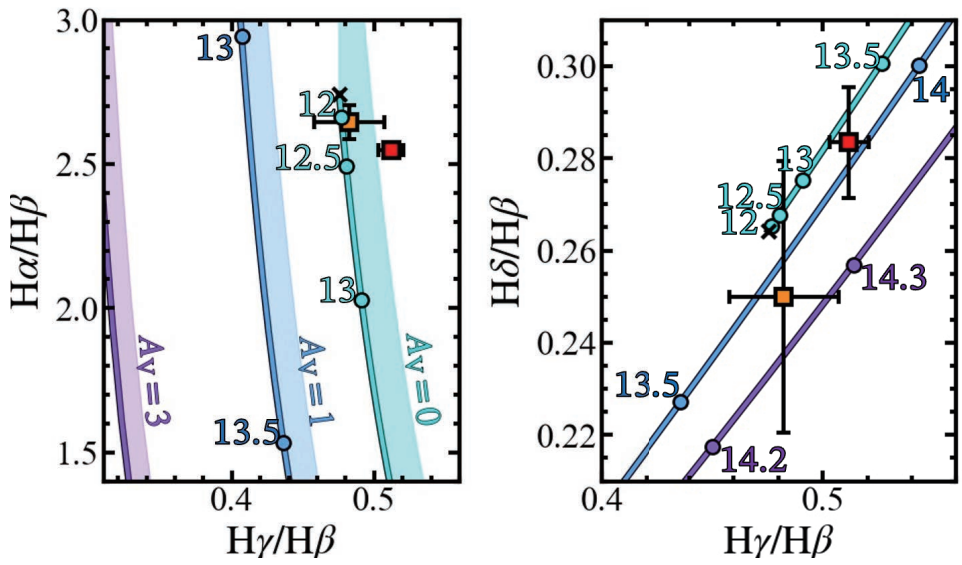


Fig. 5. Comparisons between the observed Balmer line ratios and theoretical Balmer line ratios, including the effects of the optical depths of the Balmer lines. The squares are the same as Figure 1. The orange and red squares represent the values of GS-NDG-9422 and RXCJ2248-ID in the literature. The black crosses indicate the Case B values for $T_{\rm e} = 20{,}000$ K and $n_{\rm e} = 10^3$ cm^{-3}. The cyan, blue, and purple lines and circles denote the Balmer line ratios, including the effects of the optical depths with $A_{\rm V} = 0$, 1, and 3, respectively. The numbers shown beside the circles represent the values of $\log N_2$. The cyan, blue, and purple shaded regions in the left panel indicate the regions that can be reproduced by an interstellar shock in the case of $A_{\rm V} = 0$, 1, and 3, respectively.

lem, and where the Peccei-Quinn (PQ) symmetry emerges accidentally. In the CAA models, the QCD gauge symmetry is embedded in a larger gauge group at high energy. These models contain small instantons not included in low-energy QCD, which could enhance the axion mass significantly. However, in the CAA models, our analysis reveals that these effects on the axion mass are non-vanishing but are negligible compared to the QCD effects. The suppression of the small instanton effects originates from the global chiral U(1) symmetries, which are not broken spontaneously and play a crucial role in eliminating θ-terms in the hidden sectors through anomalies. We find these U(1) symmetries restrict the impact of small instantons in hidden sectors on the axion mass. Our study provides crucial insights into the dynamics within the CAA models and suggests broader implications for understanding small instanton effects in other composite axion models.

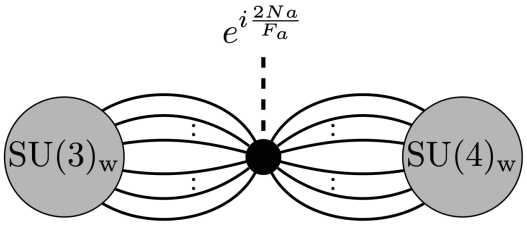


Fig. 6. Non-vanishing contributions to the vacuum amplitude. Two gray blobs denote the 't Hooft vertices associated with an $\mathrm{SU}(3)_{\rm w}$ and an $\mathrm{SU}(4)_{\rm w}$ instanton. (Taken from Ref. [1])

***Nucleon decay as a probe of flavor symmetry: the case of fake unification* [2]**

In collaboration with the members of ICRR and Kavli IPMU.

This paper explores nucleon decay within the framework of a "fake Grand Unified Theory (GUT)" combined with the Froggatt-Nielsen (FN) mechanism. In this fake GUT framework, quarks and leptons may have distinct high-energy origins but fit into complete SU(5) multiplets at low energies without requiring force unification, setting it apart from conventional GUTs. By introducing flavor symmetry through the FN mechanism, the model addresses the flavor puzzle of quark and lepton mass hierarchies and mixing patterns. Our analysis demonstrates that nucleon decay rates and branching fractions in the fake GUT are sensitive to flavor symmetry, providing a means to distinguish it from conventional GUT predictions. These findings underscore the importance of nucleon decay searches in probing both baryon number violation and the underlying flavor structure.

***Gravitational waves from metastable cosmic strings in supersymmetric new inflation model* [3]**

In collaboration with the members of ICRR and Kavli IPMU.

Recent observations by pulsar timing arrays (PTAs) indicate a potential detection of a stochastic gravitational wave (GW) background. Metastable cosmic strings have been recognized as a possible source of the observed signals. In this paper, we propose an R-invariant supersymmetric new inflation model. It is characterized by a two-step symmetry breaking $\mathrm{SU}(2) \to \mathrm{U}(1)_G \to$ nothing, incorporating metastable cosmic strings. The field responsible for the initial symmetry breaking acts as the inflaton, while the second symmetry breaking occurs post-inflation, ensuring the formation of the cosmic string network without monopole production. Our model predicts symmetry-breaking scales consistent with the string tensions favored by PTA data, $G_{\rm N}\mu_{\rm str} \sim 10^{-5}$, where

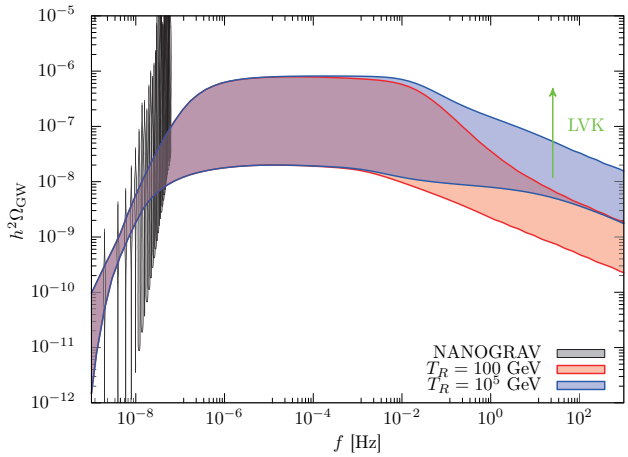


Fig. 7. The GW energy density spectrum for the META-LS scenario. (Taken from Ref. [3])

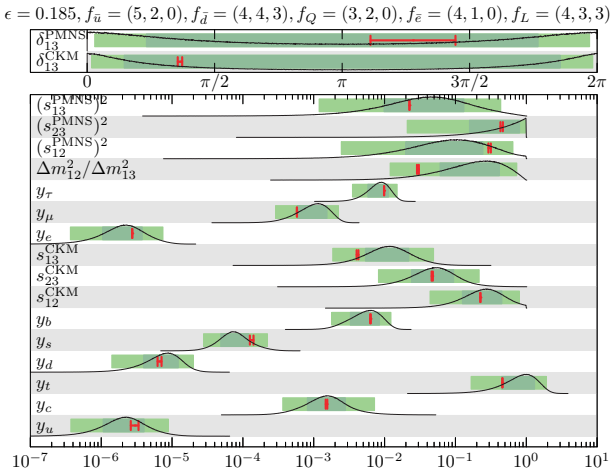


Fig. 8. Example of predictions (the prior distributions) from $\mathcal{O}(1)$ distributions of κ's with a FN charge assignment. (Taken from Ref. [4])

$G_{\rm N}$ is the Newton constant. Notably, a low reheating temperature is required to suppress non-thermal gravitino production from the decay of inflaton sector fields. This also helps evade LIGO-Virgo-KAGRA constraints, while yielding a distinctive GW signature that future PTA and interferometer experiments can detect. Additionally, we examine the consistency of this scenario with non-thermal leptogenesis and supersymmetric dark matter.

***Comprehensive Bayesian exploration of Froggatt-Nielsen mechanism* [4]**

In collaboration with the members of ICRR and Kavli IPMU.

The Froggatt-Nielsen (FN) mechanism successfully explains the hierarchical structure of fermion Yukawa couplings by introducing a U(1) flavor symmetry with distinct charge assignments for different fermion generations. While some FN charge assignments have been proposed, their evaluation has largely relied on heuristic approaches. This paper systematically investigates viable FN charge assignments within the Standard Model, including both the quark and lepton sectors, using Bayesian statistical analysis. The study explores scenarios involving both the seesaw mechanism and dimension-five operators for neutrino mass generation. A comprehensive parameter scan over FN charges reveals a wide range of charge assignments consistent with observed fermion masses and mixing angles. Interestingly, negative FN charges and significant generational differences in charges are found to be viable, contrary to conventional assumptions. The analysis also compares the seesaw mechanism and dimension-five operator scenarios, finding no strong preference between them for optimal charge assignments. Furthermore, predictions for the lightest neutrino mass and effective Majorana mass relevant for neutrinoless double-beta decay are presented, highlighting regions of parameter space accessible to upcoming experiments. Implications for nucleon decay are studied, demonstrating that different FN charge assignments predict significantly different nucleon decay lifetimes and branching ratios, providing a potential experimental probe for FN models.

***Global Neutrino Constraints on the Minimal U(1)$_{L_\mu - L_\tau}$ Model* [5]**

In collaboration with the members of ICRR and Kavli IPMU.

We examine the minimal U(1)$_{L_\mu - L_\tau}$ gauge model in light of the latest neutrino data, including neutrino oscillations, cosmological observations, direct mass measurements, and neutrinoless double-beta decay. Using the most conservative oscillation data, we find that normal ordering is excluded at approximately the 90% confidence level (CL). Incorporating cosmological constraints from Cosmic Microwave Background (CMB) observations strengthens this exclusion to about 95% CL, while further including Baryon Acoustic Oscillation (BAO) data increases it to nearly 99% CL. The inverted ordering is even more strongly disfavored. Our analysis is performed within a frequentist framework, minimizing sensitivity to prior assumptions inherent in Bayesian approaches. These results impose strong constraints on the viability of the minimal U(1)$_{L_\mu - L_\tau}$ gauge model.

***Stringent Constraints on Self-Interacting Dark Matter Using Milky-Way Satellite Galaxies Kinematics* [6]**

In collaboration with the members of U. Amsterdam, IPMU, Sendai Coll., and Tohoku U.

Self-interacting dark matter (SIDM) has been proposed to address small-scale challenges faced by the cold dark matter (CDM) paradigm, such as the diverse density profiles observed in dwarf galaxies. In this study, we analyze the kinematics of dwarf galaxies by incorporating the effects of gravothermal core collapse into SIDM models using a semi-analytical subhalo framework. Our analysis covers the stellar kinematics of both classical and ultrafaint dwarf galaxies. The results indicate a bimodal preference for small and large self-interaction cross sections in ultrafaint dwarf galaxies, while in classical dwarfs, larger cross sections progressively decrease the model's statistical support. The combined analysis decisively prefers CDM to SIDM when the self-interaction cross section per unit mass, σ/m, exceeds $\sim$0.2 cm^2/g, if a velocity-independent cross section is assumed. Our study significantly enhances our understanding of dark matter dynamics on small scales.

Bibliography

[1] T. Aoki, M. Ibe, S. Shirai and K. Watanabe, JHEP **07** (2024), 269 doi:10.1007/JHEP07(2024)269 [arXiv:2404.19342 [hep-ph]].

[2] M. Ibe, S. Shirai and K. Watanabe, JHEP **03** (2025), 044 doi:10.1007/JHEP03(2025)044 [arXiv:2411.05398 [hep-ph]].

[3] A. Chitose, M. Ibe, S. Neda and S. Shirai, JCAP **04** (2025), 010 doi:10.1088/1475-7516/2025/04/010 [arXiv:2411.13299 [hep-ph]].

[4] M. Ibe, S. Shirai and K. Watanabe, JHEP **03** (2025), 150 doi:10.1007/JHEP03(2025)150 [arXiv:2412.19484 [hep-ph]].

[5] M. Ibe, S. Shirai and K. Watanabe, [arXiv:2503.01399 [hep-ph]].

[6] S. Ando, K. Hayashi, S. Horigome, M. Ibe and S. Shirai, [arXiv:2503.13650 [astro-ph.CO]].

Particle Cosmology

[Spokesperson : Masahiro Kawasaki]
ICRR, The University of Tokyo, Kashiwa, Chiba 277-8582

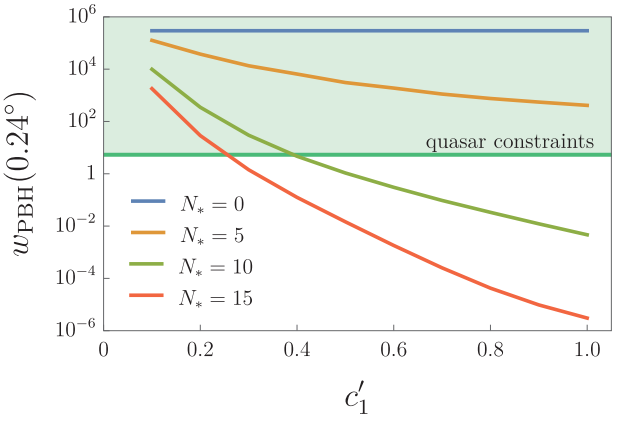


Fig. 9. Angular correlation for the different values of N_*. The green-shaded region shows the excluded region by the quasar observation. (Taken from Ref. [1])

***Supermassive black hole formation from Affleck-Dine mechanism with suppressed clustering on large scales* [1]**

In collaboration with the members of ICRR and Tohoku U.

We study a primordial black hole (PBH) formation model based on the framework of the inhomogeneous Affleck-Dine (AD) mechanism, which can explain the seeds of supermassive black holes (SMBHs). This model, however, predicts strong clustering of SMBHs that is inconsistent with the observation of angular correlation of quasars. In this paper, we propose a modified model that can significantly reduce the PBH clustering on large scales by considering a time-dependent Hubble-induced mass during inflation. The quasar angular correlation is suppressed by the large Hubble-induced mass in the early stage of inflation, while the small Hubble-induced mass in the late stage leads to the AD field fluctuations large enough for PBH formation, as in the original model. As a result, the modified scenario can successfully explain the seeds of SMBHs.

***Exactly solvable stochastic spectator* [2]**

In collaboration with the members of ICRR, RIKEN, and Kobe U.

The stochastic formalism of inflation allows us to describe the scalar-field dynamics in a non-perturbative way. The correspondence between the diffusion and Schrödinger equations makes it possible to exhaustively construct analytical solutions in stochastic inflation. Those exact statistical quantities, such as distribution and correlation functions, have one-to-one correspondence to the exactly solvable solutions in non-relativistic quantum mechanics in terms of classical orthogonal polynomials. A class of such solutions is presented by means of isospectral Hamiltonians with an underlying symmetry called shape invariance.

***Curvaton distribution from stochastic inflation* [3]**

The curvaton paradigm can realise a part of or all the observed curvature perturbation. Based on the stochastic formalism of inflation and closed-form exact distributions therein, the distribution of the curvature perturbation is presented in an analytical manner by identifying a test field with a curvaton. The parameter space consisting of the decay rate and the mass of the curvaton is studied to discuss the probability that the curvaton can contribute to the curvature perturbation in a non-negligible way.

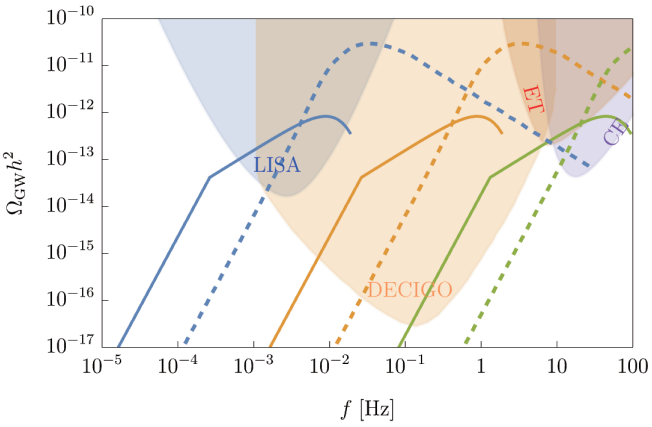


Fig. 10. GW signals expected from FOPTs with runaway bubbles that efficiently produce particles from bubble collisions. (Taken from Ref. [4])

***Gravitational Waves from Particles Produced from Bubble Collisions in First-Order Phase Transitions* [4]**

In collaboration with the members of ICRR, Johns Hopkins U., and DESY.

We discuss a new source of gravitational waves (GWs) from first-order phase transitions. The collisions of bubbles of the new phase can efficiently produce particles that couple to the background field undergoing the transition, thereby transferring a significant fraction of the released vacuum en-

ergy into a distribution of inhomogeneous and dynamic particle populations that persist long after the bubbles have disappeared. We study the GWs produced by such particle distributions, showing that GWs arise from the quadrupolar anisotropy in the radiation emitted from the bubble collisions, and present a semi-analytical calculation of the two-point correlation function for the associated energy distributions. We find that this new contribution can qualitatively modify the overall GW signal from such phase transitions, creating a distinct shift in the spectral slope at low frequencies that could be observed by future GW experiments. It is therefore important to take this new contribution into account for any transition where the background field has significant self-coupling or couplings to other fields that could lead to efficient particle production at bubble collision.

Bibliography

[1] K. Kasai, M. Kawasaki, K. Murai and S. Neda, Phys. Rev. D **111** (2025) no.8, 083513 doi:10.1103/PhysRevD.111.083513 [arXiv:2405.09790 [astro-ph.CO]].

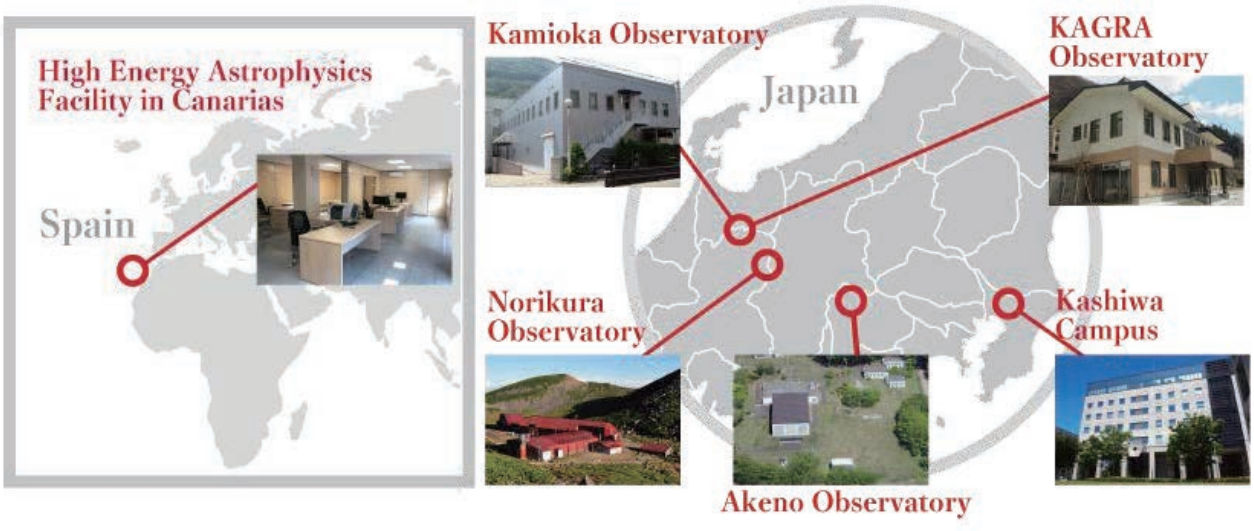
[2] M. Honda, R. Jinno, and K. Tokeshi, JCAP **12** (2024) 044 [arXiv:2409.16272 [astro-ph.CO]].

[3] K. Tokeshi, JCAP **06** (2025) 018 [arXiv:2411.15849 [astro-ph.CO]].

[4] K. Inomata, M. Kamionkowski, K. Kasai, and B. Shakya, [arXiv: 2412.17912 [astro-ph.CO]].

OBSERVATORIES and A RESEARCH CENTER

Location of the Institute and the Observatories



Norikura Observatory

Location:	Norikuradake, Nyukawa-cho, Takayama-shi, Gifu Prefecture 506-2100
Telephone (Fax):	+81-50-3730-3809
Telephone (satellite):	+81-90-7721-5674
Telephone (car):	+81-90-7408-6224

Akeno Observatory

Location:	5259 Asao, Akeno-machi, Hokuto-shi, Yamanashi Prefecture 408-0201
Telephone / Fax:	+81-551-25-2301 / +81-551-25-2303

Kamioka Observatory

Location:	456 Higashi-mozumi, Kamioka-cho, Hida-shi, Gifu Prefecture 506-1205
Telephone / Fax:	+81-578-85-2116 / +81-578-85-2121

KAGRA Observatory

Location:	238 Higashi-mozumi, Kamioka-cho, Hida-shi, Gifu Prefecture 506-1205
Telephone / Fax:	+81-578-85-2343 / +81-578-85-2346

Research Center for Cosmic Neutrinos

Location:	5-1-5 Kashiwanoha, Kashiwa, Chiba Prefecture 277-8582
Telephone / Fax:	+81-4-7136-3138 / +81-4-7136-3115

High Energy Astrophysics Facility in Canarias

Location:	C/Via Lactea, s/n E-38205 La Lagua - Tenerife Espana

NORIKURA OBSERVATORY

Introduction

Norikura Observatory (36.10°N and 137.55°E) was founded in 1953 and attached to ICRR in 1976. It is located at 2770 m above sea level, and is the highest altitude manned laboratory in Japan (Fig. 1). Experimental facilities of the laboratory are made available to all the qualified scientists in the field of cosmic ray research and associated subjects. The AC electric power is generated by the dynamo and supplied throughout the observatory. The observatory can be accessed easily by car and public bus in summer (July-September). The 70th anniversary of Norikura Observatory was celebrated in 2023. In 2024, a monument was built on the site of Asahi's hut, the first building of the observatory, which was demolished in 2018 (Fig. 2).



Fig. 1. Norikura Observatory



Fig. 2. Monument of the Asahi's hut

Norikura Observatory gave manned operation to the observations by the qualified scientists all year until the year 2003. However, the feasibility of the automatic operation of Norikura Observatory during the winter period has been tested since winter 2004, in order to study the possibilities to reduce maintenance and labor costs without causing serious inconveniences for the researchers. A long-distance (∼40km) wireless LAN system (11M bps) was set up in 2003. Two new easy-to-handle and easy-to-maintain dynamos of 115 KVA each, as shown in Fig. 3 were installed in 2004 as well. The unmanned operation of Norikura Observatory has been mostly successful in winter, during which the battery-backed-up solar panels and/or wind power generators kept supplying the electricity to the wireless LAN and ongoing cosmic-ray experiments.



Fig. 3. A dynamo of 115KV.

The present major scientific interests of the laboratory are focused on the modulation of high-energy cosmic rays in the interplanetary space associated with the solar activity, the generation of energetic particles by the solar flares, and the particle acceleration mechanism in thunderclouds, all of which require long-term observation. These studies have been carried out by the group of user universities, where ICRR provides them with a laboratory facility. A part of the facility has been open for the environmental study at high altitude, such as aerosol-related mechanism in the atmosphere, observation of total ozone and UV solar radiation, for botanical study in the high-altitude environment, etc..

Cosmic Ray Physics

Space weather observation using muon hodoscope

Mt. Norikura muon hodoscope has started its operation in May 1998, aiming to observe a precursory signature of the interplanetary shock approaching the Earth. The detector succeeded for the first time to observe a loss-cone signature, which is an intensity deficit within a narrow cone around the interplanetary magnetic field (IMF). The observation of the loss-cone precursor gives us unique information for the space weather forecast and for understanding the interplanetary disturbances in near-Earth space. Following this successful observation, we started monitoring the intensity of ∼50 GeV cosmic rays over the entire sky around Earth with the Global Muon Detector Network (GMDN). The GMDN consisted of

4 stations in Nagoya (Japan), Hobart (Australia), Sao Martinho (Brazil), and Kuwait City (Kuwait) and started operation in 2006. Muon detectors are complementary to neutron monitors, monitoring a lower energy range below ∼10 GeV, and the GMDN has a great advantage, particularly in the precise measurement of the cosmic ray anisotropy. Unfortunately, however, Mt. Norikura station became an unattended station for most of the year since 2004. Because the generator is also stopped, we created a self-sustaining system that uses solar power to generate all the electricity needed. However, the weather environment at Mt. Norikura in winter is extremely harsh, and it is necessary to overcome various obstacles such as low temperatures, snowfall, and strong winds. In order to achieve stable, continuous observation throughout the year, there are still many issues that need to be resolved. Meanwhile, in 2018, we installed another detector system at Syowa station in the Antarctic to expand the coverage area to monitor and for integrated analysis of muon detectors and neutron monitors. The experiences at Mt. Norikura station were quite a help to start observation under severe conditions in the Antarctic. The unique feature of the Syowa station is that it observes muon and neutron simultaneously, expecting a key role for integrated analysis. Taking advantage of this feature, local environmental effects, such as temperature effects, on cosmic ray count rate were studied. A few space weather events were analyzed with this new GMDN. We found an interesting variation suggesting adiabatic acceleration in the flux rope. We also reported the results of the first integrated analysis.

Recent progresses are reported in [1][2][3][4][5][6].



Fig. 4. Solar panels at Mt. Norikura (top) and PCTs installing at Syowa station in the Antarctic (bottom).

Observation of solar neutrons in solar cycle 24 and 25

We have studied the acceleration mechanism of solar energetic particles by observing neutrons (>100 MeV) produced by the interaction between high-energy ions and the solar atmosphere. These high-energy ions are accelerated in association with very gigantic solar flares. As neutrons are neutral particles, they are thought to keep the information of the acceleration at the solar surface rather than accelerated ions, which are reflected by the interplanetary magnetic field. Neutrons are attenuated by the Earth's atmosphere; therefore, a worldwide network of solar neutron observation has been operated since 2003. These stations are at high altitudes near the equator. The 64 m^2 solar neutron telescope at the Norikura observatory played the central role of the world-wide network. As the Norikura Observatory closes during the wintertime, which is much longer than the summertime, the electricity of the solar neutron telescope is maintained by batteries and solar cells.

Three achievements have been obtained by the observation of solar neutrons so far. The first is that the acceleration mechanism of solar energetic particles, which produce solar neutrons, is stochastic if it is assumed that neutrons are produced at the same time as the electromagnetic waves [7], [8]. The second is that there is at least one event neutrons are produced longer than hard X-rays [9]. The third is that the total energy which neutrons obtain during one solar flare does not exceed 0.1% of the energy of soft X-rays [10]. It is not clear whether the first achievement is obtained without assuming the production time of neutrons.

The observation of solar neutrons at Norikura has ceased in the summer of 2022. Several stations of the worldwide network of solar neutron observation have stopped observations recently. There are two stations that continue observing solar neutrons. One is at Sierra Negra (4,560 m) in Mexico. Another is at Chacaltaya (5,250 m) in Bolivia. The final puzzle of the acceleration mechanism of solar energetic particles is expected to be solved by the observation of these two stations. Recent progresses are reported in [11][12][13].

A new study for high precision measurement of muons

We are conducting research to repurpose the proportional counter section of the solar neutron telescope previously operated by Nagoya University at the Norikura Observatory into a hodoscope-type high-precision muon telescope. During the unmanned operation period of the observatory, providing power to the instruments has become a challenge. It has been found that the solar panel and lead-acid battery system received from Nagoya University has serious issues with the power transmission cables from the solar panels and the lead-acid batteries. To address the issues with the power lines, we conducted repairs as much as possible, and currently, 67% of the solar panels can supply power to the power controller. As there were almost no issues with the solar panels themselves, it was revealed that the arrangement of the power lines, considering snowfall during winter, is crucial. Additionally, we have replaced the lead-acid batteries with new $LiFePO_4$ batteries, which have higher energy density and better cost

performance per stored energy. Using this new system, we have been continuously operating a small-scale solar neutron telescope, a neutron monitor, and a Raspberry Pi-based environmental monitoring system since the summer of 2023. Unfortunately, the signal from the small-scale solar neutron telescope is lost just after the observatory became unmanned. However, the other instruments have been operating smoothly beyond the winter and into the 2024 spring.

Observational research on particle acceleration and cosmic-ray shower in thunderstorm electric fields via citizen science "Thundercloud Project"

Particle acceleration occurs in the strong electric field hidden by thunderclouds and lightning discharges, and various high-energy physics phenomena have been observed. This new interdisciplinary field covering cosmic ray physics, geophysics, and astronomy is collectively called "high-energy atmospheric physics" (Dwyer et al., Space Science Reviews, 2012). For example, in the electric field in thunderclouds, electrons are accelerated to 10 MeV or more and hit the atmosphere, producing bremsstrahlung, which is detected by ground and aircraft measurements (gamma-ray glow, Wada et al., Physical Review Research, 2018). Accelerated electrons in lightning discharges also produce bremsstrahlung. Such radiation events are detected outside the Earth's atmosphere by astronomical satellites and are called Terrestrial Gamma-ray Flash (TGF), and trigger photonuclear reactions (Enoto et al., Nature, 2017).

Our citizen science "Thundercloud Project" is a multi-site radiation monitoring of gamma rays from winter thunderclouds (gamma-ray glows) and high-energy radiation from lightning. For this project, we developed a portable radiation monitor called Compact Gamma-ray monitor (CoGaMo), which works only at the touch of a button, and installed it at about 70 locations around Kanazawa City with citizen supporters. The CoGaMo detectors have already succeeded in detecting several gamma-ray glows from thunderclouds. In particular, we reported a gamma-ray glow event coincided with a lightning discharge, suggesting a connection between the trigger of lightning and high-energy phenomena (e.g., electron acceleration) in the strong electric fields in thunderclouds [14] (Fig.5 (Top)). Mt. Norikura and other high mountains are other sites where we can detect gamma rays from thunderclouds. We are also planning to distribute CoGaMo detectors at Mt. Norikura. Furthermore, in this project, we newly developed a special board for radiation measurement called "PENGUIN," which can be used in combination with a Sony board-type computer "Spresense" (Fig.5 (Bottom)). With this board, a two-channel portable radiation monitor can be made and used for future observations.

Study of secondary cosmic rays from thundercloud

To study the relativistic electron acceleration mechanism by a thundercloud-derived electric field and the relation between thunder and cosmic-ray air showers, we started an experiment in 2015, mainly using gamma-ray detectors at Norikura Observatory. The experiment consists of gamma-ray detectors, a lightning sensor, an electric field meter, a weather

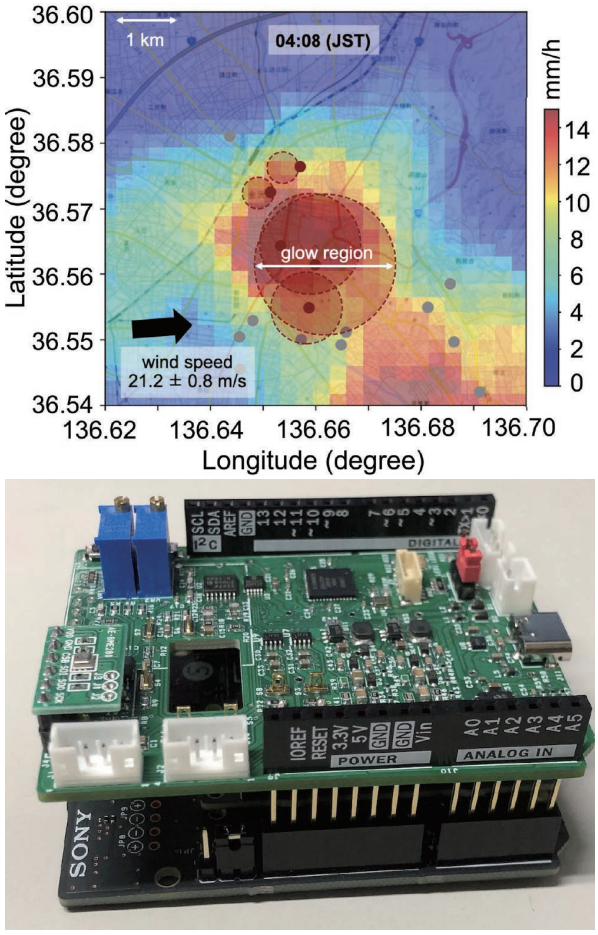


Fig. 5. (Top) Gamma-ray area irradiated from thunderclouds recorded by the Citizen Science "Thundercloud Project," overlaid on the map at Kanazawa, and rainfall area estimated by radar (Tsurumi et al., GRL, 2023). (Bottom) PENGUIN (Physics and Engineering Utility Introduction) board developed for use with the Arduino-compatible board computer Sony Spresense.

monitor, and an air shower array consisting of five scintillation detectors. Gamma-ray detectors using three crystals, NaI, CsI, and BGO, cover a total energy range of more than three orders of magnitude from 70 keV to 120 MeV.

Observation period: 47 days from August 2nd to September 17, 2018

There were no reports of lightning near the observatory, but fluctuations in electric field meters indicating the passage of thunderclouds were observed multiple times. In particular, during the passage of Typhoon No. 21, large electric field fluctuations exceeding 100 kV/m were observed, but no significant gamma-ray flux increase in synchronization with the fluctuations was observed.

Observation period: 62 days from July 17 to September 12, 2019

There were more sunny days than usual. There were no reports of lightning strikes in the vicinity during the observation period, but several thunderclouds were passing through. The largest electric field fluctuation was around 60 kV/m caused by Typhoon No. 20 on August 16th.

Observation period: 33 days from August 4 to September 5, 2020
The experiment was conducted on a reduced scale due to activity restrictions due by the coronavirus pandemic. A lightning gamma-ray detector was installed at the Norikura Observatory, and the small air shower observation device was discontinued. The maximum electric field strength fluctuation during observation was moderate at 40 kV/m.

Observation period: 41 days from August 2nd to September 11, 2022
The experiment was conducted on the same scale as in 2019, except that a small air shower array was not installed. On August 18, when there were reports of lightning strikes and intercloud discharge within a 1 to 3 km radius, electric field fluctuations exceeding 100 kV/m, the highest during the period, were observed. However, perhaps because the discharge site was far away, no significant gamma-ray flux exceedances synchronized with fluctuations were observed.

Observation period: 24 days from August 14 to September 6, 2023
During the observation period, there were many sunny and cloudy skies, there were no lightning events in the vicinity, and the electric field fluctuation was only observed to be around 45 kV/m at the maximum. We hope to continue observing electric field fluctuation events of 100 kV/m or more, where we can expect an increase in gamma rays due to the electric field.

Research on annual variations of ^{14}C concentration in *Pinus pumila*

Radiocarbon (^{14}C) is a cosmogenic nuclide that is mainly produced in the atmosphere by high-energy cosmic rays. The radiocarbon is collected from the atmospheric CO_2 and fixed in tree rings by photosynthesis. Solar activities and the extremely intense cosmic-ray events in the past have been investigated by measuring the ^{14}C concentration in the annual tree rings of old wood. However, since the amount of CO_2 in the atmosphere is affected by the global carbon cycle, the ^{14}C concentration in tree annual rings shows a delayed and attenuated response from the rate of production. Thus, it is important to investigate the dependence of ^{14}C concentration in the plant using modern samples for which the number of sunspots and the amount of secondary cosmic rays are accurately observed.

Since 2018, we have been continuously collecting cones and leaves of *Pinus pumila* that live in the alpine zone of Mt. Norikura (Fig.6 (Top)) and Mt. Zao, and measuring ^{14}C concentrations using a high-sensitivity accelerator mass spectrometer at Yamagata University. In addition, to compare the effects of fossil fuels, *Pinus densiflora* samples were collected from urban areas in Tokyo and Tendo city, Yamagata Prefecture, and their ^{14}C concentrations were also investigated. Figure 6 (bottom) shows the ^{14}C concentration (Δ^{14}C) in cone seeds for each sample collection year. The ^{14}C concentration in *P. pumila* samples collected from Mt. Norikura and Mt. Zao decreased from 2018 to 2023. The Δ^{14}C values in *P. densiflora* samples from Tendo city were lower of Δ^{14}C in all years than those from Mt. Norikura and Mt. Zao, and no dependence on collection year was observed. *P. densiflora* samples from Tokyo showed the lowest Δ^{14}C values in all years among the samples collected, which also showed a decreasing trend from 2019 onwards. We plan to continue collecting data.

Recent progresses are reported in [15][16][17][18][19].

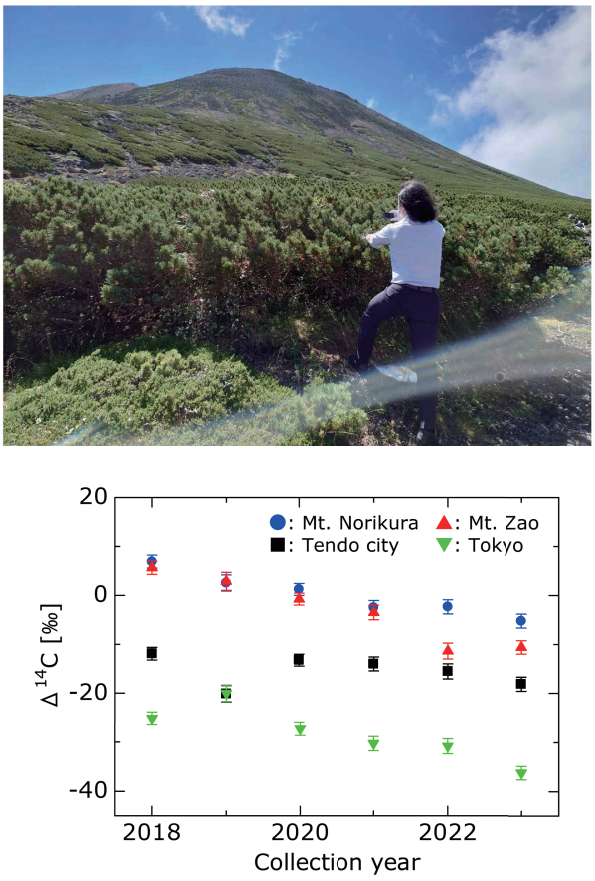


Fig. 6. (Top) Condition when collecting *Pinus pumila* at Mt. Norikura. (Bottom) Δ^{14}C values in cone seeds for each sample collection year.

Technical Development

Test experiment of the Fuel cell

The Norikura Observatory is currently unmanned from the end of October until July of the following year. During this period, even the diesel generator is offline, posing a substantial problem to continuous cosmic ray observation. Presently, a combination of solar panels and lead-acid batteries supplies power to detectors for this duration, but the output is naturally subject to weather conditions. Consequently, the motivation for research lies in utilizing environmentally friendly fuel cells to provide electricity more reliably for the period. Upon consultation with fuel cell system vendors and investigation of the operational performance of a small-scale fuel cell experimentally introduced by the observatory, which experienced failures within a few years, several issues related to the observatory's location have emerged, namely, its altitude of 2770 meters in a high mountainous area within a national park. Taking these factors into account, it has been concluded

that, for the time being, efforts should be directed towards enhancing the stability of the conventional solar panel and battery system, with fuel cells serving a supplementary role.

Environmental Study

Monitoring the cloud water quality for evaluation of the SO_2 in-cloud oxidation process

In East Asia (China), the rapid economic growth has increased fuel consumption, and the associated emissions from fossil fuels have risen since the 1980s [20]. The main substances are the primary aerosols, sulfur dioxide (SO_2), nitrogen oxides (NO_x), volatile organic compounds (VOC), and ammonia (NH_3). Of these, the atmospheric SO_2 emitted from thermal power plants and factories progressively increased since 1980 and turned to decline from 2006. This is because since the 11th Five-Year Plan (2006-2010), the Chinese government has set a restrictive target on SO_2 reduction and implemented a flue-gas desulfurization (FGD) system. Since 2011, the FGD penetration in thermal power plants has rapidly increased, leading to a decreasing trend until the present day.

It is well known that gaseous SO_2 is highly dissolved into cloud droplets and the subsequent oxidation brings formation of H_2SO_4, thereby generating acidic cloud and rain [21]. Such acidic substances are also thought to lead to severe problems in terrestrial ecosystems and the environment, such as forest decline, acidity of lakes and rivers, fish deaths, etc. In the 1960-1990s, clouds of strong acid (pH = 3 to 4) were observed near the summit of Mt. Norikura [22][23][24]. Therefore, we have monitored the cloud water quality in this site (Fig.7 (Top)) to assess in-cloud oxidation (acidification) of gaseous SO_2 during summertime in 1999-2000 and 2022-2023. As a result, the cloud pH increased from 4.0 to 4.7 during the past 20 years (Fig.7 (Bottom)), while the NO_3^- and SO_4^{2-} concentrations of cloud water reduced to less than one-fifth, suggesting that cloud water is neutralized and purified. However, the cloud water H_2O_2 and O_3, the most important oxidant for gaseous SO_2 oxidation, were approximately at the same level as 20 years ago.

Recent progresses are reported in [25][26][27][28].

Seasonal and diurnal variations in soil respiration rates at a treeline ecotone

This study examined the seasonal and diurnal variations in soil respiration rates (R_S) during a growing season at the treeline ecotone (2800 m) on a volcanic mountain in Japan, using an automated measurement equipment. The aboveground biomass, the total R_S during the growing season, and the R_S per day during the growing season were low at 2800 m. Seasonal R_S variations positively correlated with those of soil and air temperatures. The mean volumetric soil water content (W_S) during the growing season was much lower because of the scoria substrate. The monthly mean diel cycle of R_S was positively correlated with the soil temperature every month. The R_S decreased during the daytime, especially in August, despite no changes in the W_S. Seasonal and diurnal R_S variations could be reproduced from soil and air temperatures, and W_S. Estimating soil respiration rate from these variables will help understand the future carbon budget of forests due to global warming.



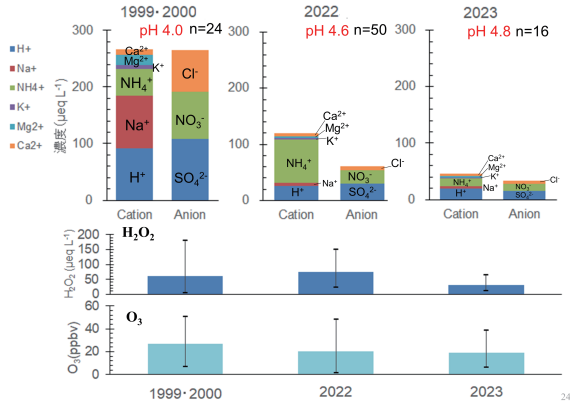


Fig. 7. (Top) Photograph showing gases, rainwater, cloud water, and aerosol sampling. (Bottom) Comparisons of cloud water and gas during 1999-2000, 2022, and 2023 at Mt. Norikura: (a) chemical compositions of cloud water; (b) H_2O_2 concentration of cloud water, and (c) O_3 gas concentration.

Recent progresses are reported in [29][30][31][32][33][34][35].

Bibliography

[1] R. Kataoka, T. Sato, C. Kato, A. Kadokura, M. Kozai, S. Miyake, K. Murase, L. Yoshida, Y. Tomikawa, and K. Munakata. Local environmental effects on cosmic ray observations at Syowa Station in the Antarctic: PARMA-based snow cover correction for neutrons and machine learning approach for neutrons and muons. Journal of Space Weather and Space Climate, 12:37, October 2022.

[2] K. Munakata, M. Kozai, C. Kato, Y. Hayashi, R. Kataoka, A. Kadokura, M. Tokumaru, R. R. S. Mendonça, E. Echer, A. Dal Lago, M. Rockenbach, N. J. Schuch, J. V. Bageston, C. R. Braga, H. K. Al Jassar, M. M. Sharma, M. L. Duldig, J. E. Humble, I. Sabbah, P. Evenson, P. S. Mangeard, T. Kuwabara, D. Ruffolo, A. Sáiz, W. Mitthumsiri, W. Nuntiyakul, and J. Kóta. Large-amplitude Bidirectional Anisotropy of Cosmic-Ray Intensity Observed with Worldwide Networks of

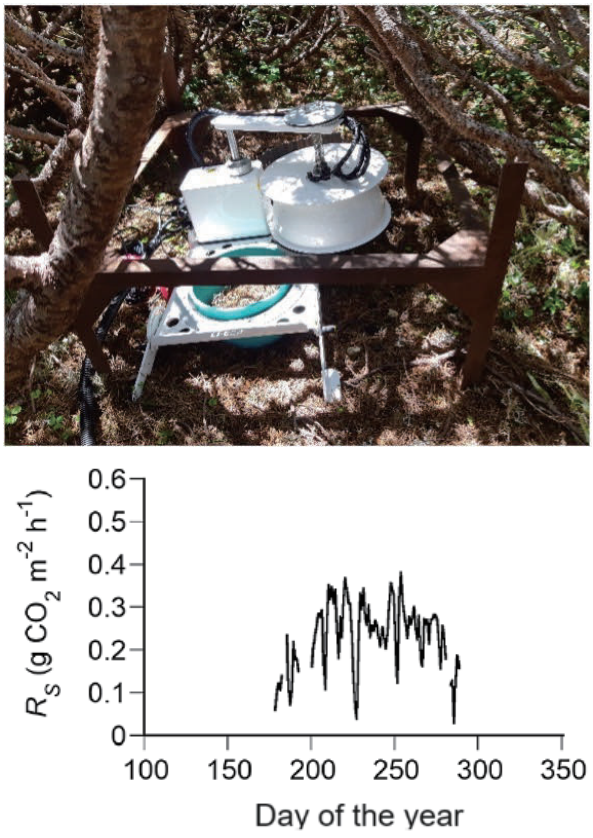


Fig. 8. (Top) Automated soil respiration measurement system in the *Pinus pumila* scrub. (Bottom) The seasonal change in daily mean soil respiration rates (R_S).

Ground-based Neutron Monitors and Muon Detectors in 2021 November. ApJ, 938(1):30, October 2022.

[3] W. Kihara, K. Munakata, C. Kato, R. Kataoka, A. Kadokura, S. Miyake, M. Kozai, T. Kuwabara, M. Tokumaru, R. R. S. Mendonça, E. Echer, A. Dal Lago, M. Rockenbach, N. J. Schuch, J. V. Bageston, C. R. Braga, H. K. Al Jassar, M. M. Sharma, M. L. Duldig, J. E. Humble, P. Evenson, I. Sabbah, and J. Kóta. A Peculiar ICME Event in August 2018 Observed With the Global Muon Detector Network. Space Weather, 19(3):e02531, March 2021.

[4] C. Kato, W. Kihara, Y. Ko, A. Kadokura, R. Kataoka, P. Evenson, S. Uchida, S. Kaimi, Y. Nakamura, H. A. Uchida, K. Murase, and K. Munakata. New cosmic ray observations at Syowa Station in the Antarctic for space weather study. Journal of Space Weather and Space Climate, 11:31, January 2021.

[5] R. R. S. Mendonça, C. Wang, C. R. Braga, E. Echer, A. Dal Lago, J. E. R. Costa, K. Munakata, H. Li, Z. Liu, J. P. Raulin, T. Kuwabara, M. Kozai, C. Kato, M. Rockenbach, N. J. Schuch, H. K. Al Jassar, M. M. Sharma, M. Tokumaru, M. L. Duldig, J. E. Humble, P. Evenson, and I. Sabbah. Analysis of Cosmic Rays' Atmospheric Effects and Their Relationships to Cutoff Rigidity and Zenith Angle Using Global Muon Detector Network Data. Journal of Geophysical Research (Space Physics), 124(12):9791–9813, December 2019.

[6] K. Munakata, T. Kuwabara, S. Yasue, C. Kato, S. Akahane, M. Koyama, Y. Ohashi, A. Okada, T. Aoki, H. Kojima and J. W. Bieber, "A "loss-cone" precursor of an approaching shock observed by a cosmic-ray muon hodoscope on October 28, 2003", Geophys. Res. Lett., 32, L03S04-1 4, doi:10.1029/2004GL021469, 2005 (January 11).

[7] Watanabe, K., et al., Astrophys. J., 592, 590-596, 2003

[8] Watanabe, K., et al., Astrophys. J., 636, 1135-1141, 2006.

[9] Sako, T., et al., Astrophys. J. Lett., 651, L69-L72, 2006.

[10] Lopez, D., et al., Astropart. Phys., 76, 19-28, 2016.

[11] Matsubara, Y., Gound level observation of solar neutrons (Japanese), RADIOISOTOPES, 68, 907-915, 2019.

[12] Muraki, Y., et al., Possible detection of solar gamma-rays by ground-level detectors in solar flares on 2011 March 7, Publ. Astron. Soc. Jpn, 72, 1-17, 2020.

[13] Newton-Bosch, J., et al., Atmospheric electric field effects on cosmic rays detected by the solar neutron telescope at Sierra Negra, J. Atmos. and S.-T. Phys., 253, 106156, 2023.

[14] Tsurumi, Enoto, Ikkatai, et al., "Citizen Science Observation of a Gamma-Ray Glow Associated With the Initiation of a Lightning Flash", Geophysical Research Letters, Volume 50, Issue 13, e2023GL103612 (2023).

[15] M. Takeyama, T. Moriya, H. Sakurai, H. Miyahara, F. Tokanai, Research of annual variations of ^{14}C concentrations in pinus pumila V, Extended Abstracts of the 84th JSAP Autumn Meeting, 20a-A310-3 (2023).

[16] M. Takeyama, T. Moriya, H. Sakurai, H. Miyahara, F. Tokanai, Research of annual variations of ^{14}C concentrations in pinus pumila IV, Extended Abstracts of the 83rd JSAP Autumn Meeting, 22a-C205-3 (2022).

[17] M. Takeyama, T. Moriya, H. Sakurai, H. Miyahara, F. Tokanai, Research of annual variations of ^{14}C concentrations in pinus pumila III, Extended Abstracts of the 82nd JSAP Autumn Meeting, 11a-N402-7 (2021).

[18] M. Takeyama, T. Moriya, H. Sakurai, H. Miyahara, F. Tokanai, Research of annual variations of ^{14}C concentrations in pinus pumila II, Extended Abstracts of the 81st JSAP Autumn Meeting, 8a-Z25-10 (2020).

[19] M. Takeyama, T. Moriya, H. Sakurai, H. Miyahara, F. Tokanai, Research of annual variations of ^{14}C concentrations in pinus pumila, Extended Abstracts of the 67th JSAP Spring Meeting, 14p-D209-4 (2020).

[20] Ohara,T. and Kurokawa, J. (2018) Long-term variation of emissions of air pollutants related to atmospheric aerosol in Asia, China and Japan. Earozoru Kenkyu 33: 95-101 (in Japanese).

[21] Seinfeld, J. H. and Pandis, S. N. (1998) Atmospheric chemistry and physics, John Wiley & Sons, New York, p. 1326, 1152.

[22] Okita, T.(1968). Concentration of sulfate and other inorganic metals in fog and cloud water and in aerosol. Journal of Meteorological Society Japan 46: 120-127.

[23] Minami Y. and Ishizaka Y. (1996). Evaluation of chemical composition in fog water near the summit of a high mountain in Japan. Atmospheric Environment 30: 3363-3376.

[24] Watanabe, K., Ishizaka, Y. and Takenaka, C. (1999). Chemical composition of Fog water near the summit of Mt. Norikura in Japan. Journal of Meteorological Society Japan 77: 997-1006.

[25] Kagawa, M., Katsuta, N. and Ishizaka, Y. (2021) Chemical characteristics of cloud water and the sulfate production under excess hydrogen peroxide in a high mountains region of central Japan. Water, Air, and Soil Pollution 237:177.

[26] Kagawa, M., Katsuta, N. and Ishizaka, Y. (2022) Selenite and selenate in clouds at a high-altitude mountain location in Central Japan. Atmospheric Research 276:106253.

[27] Kagawa, M., Katsuta, N., Naito, S., Masuki, Y., Yoshimizu, C., Chiba, H. and Tayasu, I. (2023) Sample pretreatment effects on isotopic compositions of oxygen and sulfur in $BaSO_4$ derived from atmospheric sulfate. Rapid Communications in Mass Spectrometry 37: e9659.

[28] Masako Kagawa (2023) Study of the dynamics of selenium in relation to the transport and oxidation of sulfur compounds in the atmosphere. The united graduate school of agricultural science, Gifu University. Doctor of Agriculture No.165.

[29] Takahashi, K., Otsubo, S. & Kobayashi, H. (2018) Comparison of photosynthetic traits of codominating subalpine conifers Abies veitchii and A. mariesii in central Japan. Landscape and Ecological Engineering 14: 91–97.

[30] Tateno, R., Tatsumi, C., Nakayama, M., Takahashi, K., Kerfahi, D. & Adams, J. (2019) Temperature effects on the first three years of soil ecosystem development on volcanic ash. Catena 172: 1–10.

[31] Takeda, S. & Takahashi, K. (2020) Elevational variation in abundance of coarse woody debris in subalpine forests, central Japan. Forest Ecology and Management 473: 118295.

[32] Takahashi, K. (2021) Productivity does not decrease at the climate extremes of tree ranges in the Japanese archipelago. Oecologia 197:259–269.

[33] Shimada, R. & Takahashi, K. (2022) Diurnal and seasonal variations in photosynthetic rates of dwarf pine Pinus pumila at the treeline in central Japan. Arctic, Antarctic, and Alpine Research 54:1–12.

[34] Takeda, S., Majima, R., Makita, N. & Takahashi, K. (2023) Five-year measurement data along a 1200 m elevational gradient reveals that global warming increases soil respiration. Frontiers in Forest and Global Change 6: 1145474.

[35] Takeda, S., Makita, N. & Takahashi, K. (2024) Seasonal and diurnal variations in soil respiration rates at a treeline ecotone and a lower distribution limit of subalpine forests. Journal of Plant Research.

AKENO OBSERVATORY

Introduction

The Akeno Observatory is situated in Akeno of Hokuto City, 20 km northwest of Kofu and 130 km west of metropolitan Tokyo. The location is at the longitude of 138.5°E and the latitude of 35.8°N. The altitude is ∼900 m above sea level. It was established in 1977 as a research center for air shower studies in the very high energy region, and it has been administered by the ICRR as a facility of joint-university-use.

The 40th anniversary of the Akeno Observatory was held in 2017.

Akeno Air Shower Experiments

The Akeno Air Shower Experiment started in 1979 with an array covering 1 km^2 area (the 1 km^2 array, see Fig.1). The array was enlarged to 20 km^2 in 1984 and was gradually expanded to the Akeno Giant Air Shower Array (AGASA) of approximately 100 km^2 area by 1990. The AGASA was built

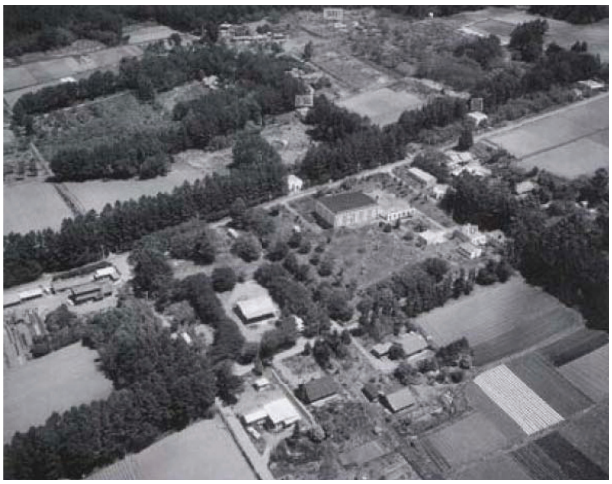


Fig. 1. Aerial View of Akeno Observatory and 1 km^2 Array Area

to detect Ultra-High Energy Cosmic Rays (UHECRs) in the energy range of 10^{20} eV.

One of the distinctive features of the Akeno experiments is that the measurements were made over five decades of energies well covering 10^{15} eV - 10^{20} eV by using both the surface detector for the electromagnetic component, and the shielded detector for muon component (Fig.2). The wide energy coverage was accomplished by the arrays of scintillation detectors of various inter-detector spacings from 3 m to 1 km and with different triggering conditions. This feature of the Akeno air shower measurement is well demonstrated in Fig.3, in which the spectra from Akeno 1 km^2 array for $10^{14.5}$ eV - $10^{18.8}$ eV [9] and AGASA for $10^{18.5}$ eV - $10^{20.3}$ eV [10] are plotted.

*[9] M. Nagano et al., J. Phys. **G10**, 1295 (1984); M. Nagano et al., J. Phys. **G18**, 423 (1992).

*[10] M. Takeda et al., Astropart. Phys. **19**, 447 (2003).



Fig. 2. One of the muon detector housings with concrete shielding.

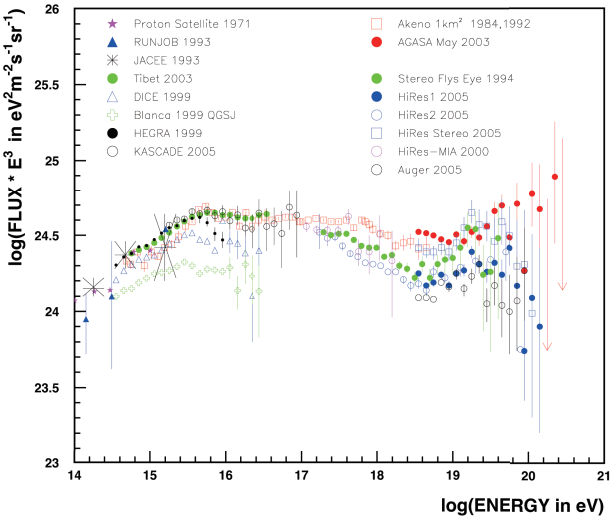


Fig. 3. Akeno energy spectrum measurements for 10^{15} eV - 10^{20} eV.

AGASA

The AGASA was composed of 111 surface detectors, each with a plastic scintillator of 2.2 m^2 area and 5 cm thickness. The counters were deployed with ∼1 km spacing covering the ground area of approximately 100 km^2 in the suburban area of Akeno, outside of the observatory campus. The AGASA served as the largest air shower array in the world since its commissioning in 1990 until it stopped data taking in January 2004, when the construction of the succeeding experiment, Telescope Array (TA), started in Utah. The AGASA was dismantled in 2007, together with other Akeno air shower arrays.

An exposure of 5.8 × 10^{16} m^2 s sr above 10^{19} eV was accumulated by AGASA in 13 years of operation. Extensive air showers with zenith angles smaller than 45° and with core

locations inside the array area were used for the analysis. The AGASA reported an extension of the energy spectrum beyond the predicted Greisen-Zatsepin-Kuzmin (GZK) cutoff in 1998 [11], and a total of eleven UHECR events were observed above 10^{20} eV by 2003.

Measurement of UHECRs

Since the AGASA measurement in 1998, the High Resolution Fly's Eye (HiRes) [12], the Pierre Auger Observatory (PAO) [13], and the Telescope Array (TA) [14] measured the energy spectra of UHECRs with higher statistics.

The HiRes observed the UHECR using the fluorescence telescope. The PAO and the TA measure the energy spectra using the surface array consisting of either water tanks (PAO) or plastic scintillators (TA), but the energy scale of the array is determined by the fluorescence telescope using a subset of events observed by the fluorescence telescope and surface array at the same time. The adoption of the energy scale by the fluorescence telescopes is based on its small dependence on the air shower simulation.

The energy spectra above 10^{18} eV by AGASA and other experiments are compiled and compared by the working group represented by UHECR experiments in the UHECR2012 symposium held in 2012 [15]. The result is plotted in Fig.4 with the energy scale of each experiment adjusted to a reference energy, which is set halfway between PAO and TA/HiRes.

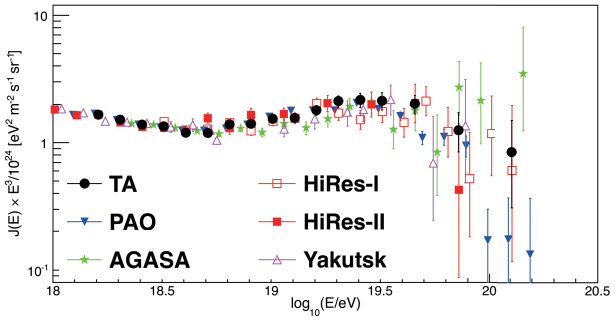


Fig. 4. Compilation of UHECR energy spectra (UHECR2012). The energy scales were adjusted as ×1.10 for PAO, ×0.91 for TA and HiRes, ×0.65 for AGASA and ×0.56 for Yakutsk.

The HiRes, PAO, and TA confirmed a flux suppression above approximately $10^{19.7}$ eV. Although the AGASA spectrum does not demonstrate the cutoff structure, the number of events above 10^{20} eV became only two after the energy rescaling, making the claim of the extended spectrum statistically insignificant. The estimate of systematic uncertainty of the energy measurement is approximately 20% for all the experiments, and rescalings for the TA/HiRes and PAO are within this limit. Rescaling of the surface array energy for AGASA and Yaktsuk indicates that there exist larger systematic uncertainties than originally estimated by running the air shower simulation. This difference in energy scale is obtained by the surface array and by the fluorescence telescope remains as a basic question in the understanding of the air shower phenomena.

Recent Research Activities

The study of UHECRs by AGASA in Akeno was succeeded by the TA experiment in Utah, USA, since 2008. After the cessation of AGASA, the Akeno Observatory has been used for small-scale cosmic ray experiments, astrophysical observations, and as a test and maintenance facility by the ICRR and university researchers. Fig.5 shows a recent photograph of the main site of the Akeno Observatory.

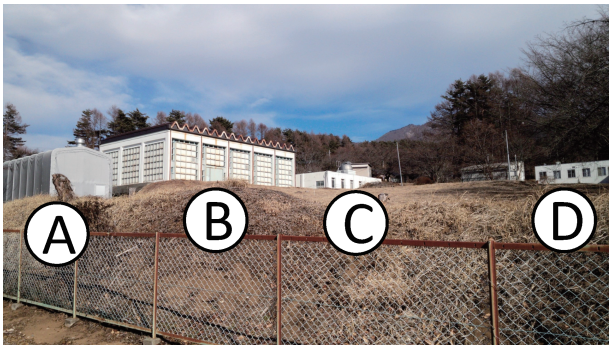


Fig. 5. The main site of the Akeno Observatory. There are the movable tent for a small atmospheric Cherenkov telescope (A), the large experimental hall (B), the research building (C), and the lodging facility (D) from the left.

In 2020, as countermeasures against COVID-19 infection, an air conditioner and a heat-exchange ventilator were installed in the large room of the research building, and a heat-exchange ventilator was installed in the dining room of the lodging facility, along with some other measures.

Observation by the multi-color imager for transients, survey and monstrous explosions (MITSuME) by N. Kawai (Tokyo Institute of Technology) et al.

One of the three MITSuME robotic telescopes was installed in the Akeno Observatory in 2003 (Fig. 6). The telescope has an aperture of 50 cm, an FOV of 28' × 28' and is equipped with a tricolor CCD camera capable of $g'R_CI_C$-bands photometry (g':400∼550 nm, Rc:570∼730 nm, Ic:730∼ 850 nm). It is operated remotely from the Tokyo Tech at the Ookayama Campus via a dedicated line. The operation of the telescope has continued in FY2021 as described below [16].

Upon receiving a GRB alert, it directs the telescope toward the GRB direction within two minutes, and makes a prompt observation of the GRB and its afterglow. The follow-up observation of GRBs was continued by the MITSuME telescope. Information about GRB events was reported to Gamma-Ray Burst (GRB) Coordinates Network Circular (GCNC).

In order to perform follow-up visible-light observations of gravitational wave objects, the MITSuME participated in

*11 M. Takeda et al., Phys. Rev. Lett. **81**, 1163 (1998).
*12 R.U. Abbasi et al., Phys. Rev. Lett. **100**, 101101 (2008).
*13 J. Abraham et al., Phys. Lett. **B685**, 239 (2010).
*14 T. Abu-Zayyad et al., Astrophys. J. **768**, L1 (2013).
*15 http://indico.cern.ch/conferenceDisplay.py?confId=152124
*16 N. Kawai et al., Research Result Presentations Meeting of the ICRR Inter-University Research Program 2021.

J-GEM (Japanese collaboration for Gravitational-wave ElectroMagnetic follow-up) and GROWTH(Global Relay of Observatories Watching Transients Happen) to establish a worldwide observation network focusing on the electromagnetic identification of gravitational wave sources as one of the scientific themes. In FY2021, the observation of gravitational waves by LIGO/Virgo was stopped. Therefore, the MITSuME participated in the follow-up observation of IceCube neutrino events that were derived from J-GEM.

The MITSuME team also conducted long-term monitoring observations of X-ray binary stars and blazars. The MITSuMe has also participated in OISTER (Optical and Infrared Synergetic Telescopes for Education and Research).



Fig. 6. The dome in which the MITSuME telescope was installed in Akeno.

Observation of galactic cosmic rays by large area muon telescope by A. Oshima (Chubu University) et al.

Telescopes consisting of four layers of proportional counter tubes, each covering an area of 25 square meters, have been operating in three muon houses at the Akeno Observatory, continuously measuring cosmic ray muons since 2003. Figure 2 shows one of the three muon houses, M8. The modal energy of the primary cosmic rays is approximately 2.5 GeV, corresponding to a 2-meter-thick concrete ceiling of the muon house at the latitude of the Akeno Observatory. The Akeno muon observation complements the muon observations conducted by the GRAPES-3 experiment in Ooty, India. Our muon observation aims to measure the modulation effects and anisotropies of galactic cosmic rays in the region of around 100 GeV and to detect transient phenomena of cosmic rays. This is expected to help us understand the flow of cosmic rays in the interplanetary magnetic field and provide clues to solve the mysteries of cosmic ray propagation. Additionally, we are challenging the establishment of a new space weather observation method through simultaneous multi-directional observations with high statistical precision. We have been updating the aging data acquisition system, and in 2018, the repair of the data acquisition system at M5 was completed. Since then, continuous observations have been conducted at M5, except during power outages and other interruptions. Currently, there are plans to upgrade the data acquisition system for the Akeno muon observation to an FPGA-based circuit. This upgrade will be implemented sequentially for M1, M8, and M5.

Research and development for a small atmospheric Cherenkov telescope at the Akeno Observatory by T. Yoshikoshi (ICRR) et al.

An alt-azimuth telescope with an aperture of three meters (Fig. 7) was set up in the Akeno Observatory for various prototype tests with atmospheric Cherenkov observations of gamma rays on the ground [17]. This telescope is the only telescope to observe atmospheric Cherenkov light emitted from air showers induced by TeV gamma rays in Japan.

In January 2021, the telescope was used to observe the Crab Pulsar in the visible light region for about ten hours. The collected data were analyzed in FY2021. The result was used to improve the signal-to-noise ratio of the Crab Pulsar observation and to study the removal of external noise.



Fig. 7. The Cherenkov telescope at the tour of the 40th anniversary of the Akeno Observatory in 2017.

Dark matter and Interstellar Meteoroid Study (DIMS) at the Akeno Observatory by F. Kajino (Konan University) et al.

The Dark Matter and Interstellar Meteoroid Study (DIMS) is a new experiment that aims at searching for macroscopic dark matter and interstellar meteoroids [18][19][20]. Nuclearites are nuggets of stable Strange Quark Matter (SQM), which are neutral in charge and hypothetical super-heavy macroscopic particles (macros), and may be important components of the dark matter in our universe. Nuclearites of galactic origins is expected to have a typical velocity of about 250 km/s in the galactic frame. The DIMS team studies the possibility of searching for such fast-moving particles using a very high-sensitivity CMOS camera with a wide field of view. In the first stage, the DIMS system consists of 4 high-sensitivity CMOS camera stations. and is going to be constructed at the Telescope Array cosmic-ray experimental site in Utah, USA. Due to the COVID-19 pandemic, the DIMS team did not transport the DIMS systems to Utah, and one of the systems was installed on the roof of the research building at the Akeno Observatory, as shown in Fig. 8. The observed Geminids Meteor

[*17] M. Ohishi et al., 33rd ICRC, (Rio deJaneiro), 587 (2013).
[*18] D. Barghini et al., PoS(ICRC2021)500.
[*19] D. Shinto et al., PoS(ICRC2021)502.
[*20] F. Kajino et al., PoS(ICRC2021)554

Shower taken by the DIMS camera at the Akeno Observatory is shown in Fig. 9. The preliminary results on limiting magnitudes of stars and the number of meteors as a function of magnitude were reported [21]. Three camera systems are installed at the Kiso Observatory, Shinshu University, and Akeno Observatory for stereoscopic observations.



Fig. 8. The DIMS camera installed on the roof of the research building at the Akeno Observatory in August 2021.

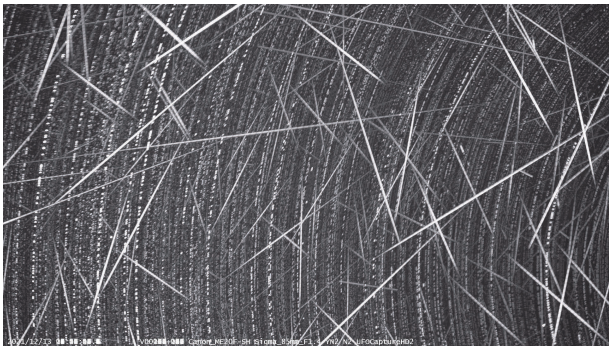


Fig. 9. Geminids Meteor Shower that was taken by DIMS camera at the Akeno Observatory on December 13th, 2021. Approximately 500 meteoroids are superimposed on the photograph.

Research and development for the Telescope Array observation in Utah by the TA collaboration and others

All the TA fluorescence imaging cameras and a part of the TA surface detectors were assembled in the Akeno Observatory by the TA collaboration team. All the unit mirrors of the TA fluorescence telescope were tested, and the atmospheric monitoring lidar of TA using a YAG laser was developed. In JFY 2015, the R&D of the surface detectors were performed for the TAx4 project that aims at quadrupling the TA surface detector array in Utah. In August 2016, 2017, and 2018, the TAx4 and TALE (TA Low Energy extension) scintillator counters were assembled.

The assembly of the surface detectors for the TALE-infill array [22] that is described in the TA section was scheduled at the Akeno Observatory in 2020, but due to the COVID-19 epidemic, the assembly had to be postponed. The 50 surface detectors for the TALE-infill array were assembled at the Akeno Observatory from the middle of October to early November in 2021. Figure 10 shows one of the surface detectors that was being assembled.



Fig. 10. A surface detector for the TALE-infill array that was being assembled at the Akeno Observatory. The student was aligning the ends of bundled fibers.

[21] F. Kajino et al., Research Result Presentation Meeting of the ICRR Inter-University Research Program 2021.

[22] S. Ogio et al., "The status of the TALE surface detector array and a TALE infill project", PoS(ICRC2021)255.

KAMIOKA OBSERVATORY

Located in Kamioka town, Hida city, Gifu Prefecture, about 200 km west of Tokyo, Kamioka Observatory was established in 1995 to operate the Super-Kamiokande experiment (SK). The laboratories are located 1000 m underground (2700 m water equivalent) in the Kamioka mine, accessible through a 1.7 km horizontal tunnel. Surface research buildings and dormitories are a 15-minute drive from the underground laboratories. In addition, the next-generation neutrino experiment project, Hyper-Kamiokande, began its construction in 2020 with the University of Tokyo and KEK as host organizations. The construction is currently underway underground in the Kamioka mine, with the aim of beginning observations in 2028.

The Super-Kamiokande experiment made groundbreaking discoveries regarding neutrino oscillations by observing atmospheric and solar neutrinos. The discovery of atmospheric neutrino oscillation was further confirmed by a long baseline neutrino oscillation experiment, K2K, which ran from 1999 to 2004 using an accelerator neutrino beam produced by the KEK proton synchrotron accelerator. The successor T2K experiment, which began in 2009, used a higher-intensity neutrino beam from the J-PARC proton accelerator. In 2011, T2K provided the first indication of the conversion of muon neutrinos into electron neutrinos. Since 2014, T2K has been using a muon anti-neutrino beam to investigate the differences between neutrino and anti-neutrino oscillations, aiming to understand why matter exists in the universe.

The underground site's low cosmic ray flux and low seismic noise environment make it ideal for various particle physics and astrophysics studies. A dark matter experiment conducted in Lab-C, called XMASS, started in 2010 using an 800-kg liquid xenon detector. The data collection ended in 2019, and the experiment yielded valuable low-background data for dark matter interactions and rare phenomena. A 100-m-long laser interferometer, a prototype for the 3-km gravitational wave antenna (KAGRA), was also located at the observatory. Additionally, the observatory accommodates experiments by external research institutions based on proposals. Notable projects include CANDLES in Lab-D and AXEL beside SK, double beta decay experiments using ^{48}Ca and ^{136}Xe, led by Osaka University and Tohoku University, respectively. NEWAGE in Lab-B is another dark matter experiment led by Kobe University aimed at detecting recoil nuclei directions.

The SK-Gd project aims to improve neutrino detection sensitivity by adding gadolinium to Super-Kamiokande, and the research has been conducted in Lab-E. A low-background Germanium detector and an inductively coupled plasma mass spectrometry system were installed in Lab-1 and Lab-A to measure extremely low-radioactivity backgrounds. The Lab-G area was excavated in 2015, and by 2016, SK-Gd equipment, including a Gd dissolving system, pre-treatment system, and Gd-water circulation system, was installed. In 2018, work was conducted to repair a water leak from the SK tank, and tests on the SK-Gd equipment were carried out in 2019. In 2020, soluble Gd salt was added to pure water to achieve a Gd concentration of 0.03% by 2022. This upgrade allows the identification of low-energy anti-neutrinos, enabling the world's first observation of relic supernova neutrinos via inverse beta decay. This upgrade also enhances the ability to study the ordering of the neutrino mass, matter–antimatter asymmetry, and proton decay.

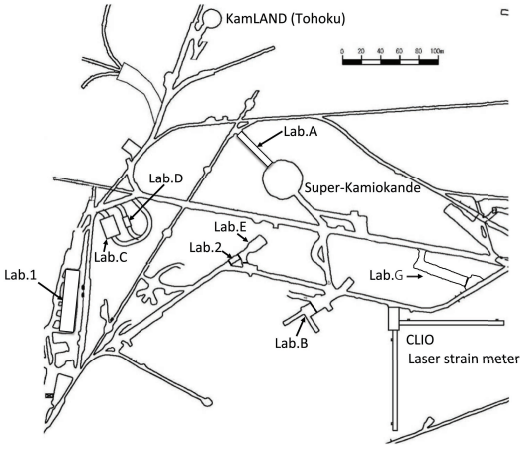


Fig. 1. Kamioka Underground Observatory.



Fig. 2. The surface buildings in Mozumi.

KAGRA OBSERVATORY

The KAGRA Observatory is located within Mt. Ikenoyama, on the border between Gifu and Toyama Prefectures in Japan, approximately 35 kilometers south of Toyama City. Established in 2016, the observatory was constructed to operate the Large-scale Cryogenic Gravitational Wave Telescope known as KAGRA. The facility features an L-shaped underground tunnel system located more than 200 meters beneath the mountain. The corner station of the tunnel is accessible via a 500-meter horizontal access tunnel from the Atotsu area.

In addition to its underground infrastructure, the observatory includes surface-level research buildings and utilizes rental space in the Hida City Community Center, located about 5 kilometers from the Atotsu entrance.

KAGRA is part of the global gravitational wave (GW) observatory network, which includes Advanced LIGO, Advanced Virgo, and the planned LIGO-India. Originally named LCGT, the KAGRA project received partial approval in 2010 under the Leading-edge Research Infrastructure Program. It has also been supported by the Program for Promoting Large-scale Science Projects, Facility Expense Subsidies, and Grants-in-Aid for Scientific Research provided by the Ministry of Education, Culture, Sports, Science and Technology (MEXT).

The Institute for Cosmic Ray Research serves as the lead institution for the KAGRA project, with the National Astronomical Observatory of Japan (NAOJ) and the High Energy Accelerator Research Organization (KEK) acting as co-host institutions. Currently, over 430 researchers from more than 90 institutions and universities worldwide are collaborating on the construction and data analysis efforts.

Tunnel excavation commenced in May 2012 and was completed in March 2014. The basic laboratory environment was established by September 2015. In March 2016, a 3-kilometer Michelson interferometer (iKAGRA) was successfully demonstrated, followed by the first operation through May 2016. By 2019, all interferometer components had been installed, completing the KAGRA Observatory. The system employs a power-recycled Fabry–Perot Michelson interferometer with resonant sideband extraction.

KAGRA began its first observing run on February 25, 2020. A two-week joint observation run, called O3GK, was conducted with GEO600 in April 2020. Subsequently, the O4 observing run commenced in May 2023 in collaboration with LIGO and Virgo. Efforts to enhance sensitivity and participate in the international observing run continue, contributing to the advancement of gravitational wave astronomy.



Fig. 1. Surface Research Building.



Fig. 2. Atotsu Entrance of KAGRA.

RESEARCH CENTER FOR COSMIC NEUTRINOS

The Research Center for Cosmic Neutrinos (RCCN) was established in 1999 with the aim of conducting research on neutrinos and related topics. Members of this center are participating in the Super-Kamiokande experiment, exploring the properties of neutrinos using data of atmospheric neutrinos and accelerator neutrinos, and searching for neutrino emissions from high-energy celestial objects in the universe. We have provided the occasion to discuss theoretical ideas and experimental results on neutrino physics. Additionally, we are involved in the project of the next-generation neutrino experiment, Hyper-Kamiokande, conducting research and development on the 50-cm diameter photomultiplier tube, and advancing preparations for the construction of the detector scheduled for 2026, with the ongoing goal of advancing neutrino research into the future.

The center also plays a role in the joint research program of ICRR. In addition to accepting research on neutrinos, as the facility utilization, in collaboration with the Computer Committee, the center manages a large-scale computer system used for joint research at this research institute by cosmic ray researchers nationwide (Fig 1). This computer system has a total of approximately 3,300 CPU cores, 9 petabytes of large-capacity disk, and data transfer performance of 18 gigabytes per second. It is capable of analyzing large amounts of data obtained from cosmic ray observation experiments and generating simulation data that requires high CPU capability. Since its update in the fiscal year 2020, it has been operated stably. Additionally, the center serves as the acceptance for a joint research program by the primary cosmic ray group, and operates the low-background experimental laboratory underground (see Fig 2). Furthermore, it accepts joint research solely for computer usage and research meetings related to future plans, among other activities.

The center also supports outreach activities for the general public regarding cosmic ray research. Since 2009, ICRR has jointly held public lecture events twice a year in spring and summer with the Kavli Institute for the Physics and Mathematics of the Universe (Kavli IPMU). Specifically, for the spring event, the center collaborates with the public relations office to plan and implement it. In the fiscal year 2024, on April 20th (Sat), a public lecture event titled ”Hyper-Kamiokande Experiment and Singularities” was held at the Kashiwa-no-ha Conference Center. The event featured Associate Professor Atsushi Takeda from our research institute and Professor Yukari Ito from Kavli IPMU as speakers. They discussed the related physics by the Hyper-Kamiokande experiment, and the singularities in shapes relate to the algebraic group. Additionally, a cross-talk session between the two speakers was conducted to address questions from the audience. Approximately 190 people attended the event in person, and the lecture was also streamed on YouTube, attracting about 950 viewers.



Fig. 1. Photo of the central computer facility in ICRR, upgraded in 2014.



Fig. 2. Photo of the low-background underground facility in ICRR.

HIGH ENERGY ASTROPHYSICS FACILITY IN CANARIAS

High Energy Astrophysics Facility in Canarias, established on April 1, 2019, in La Palma, Canary Islands, Spain is the actual base of international collaborations on the CTAO (Cherenkov Telescope Array Observatory) project co-hosted by the CTAO group of ICRR.

The Cherenkov Telescope Array Observatory (CTAO) is the next generation ground-based observatory for gamma-ray astronomy at very-high energies, participated by more than 1400 researchers from 25 countries. With more than 70 telescopes located in the northern and southern hemispheres, CTAO will be the world's largest and most sensitive high-energy gamma-ray observatory. The CTAO-Japan consortium is making a significant contribution to the construction of Large-sized Telescopes (LSTs), four telescopes of which are planned to be constructed at the northern hemisphere site in La Palma. The first LST was completed and made its first light at the end of December 2018.

Establishment of the local corporation assets was needed for daily activities such as local procurement and employment to manage and operate the site. High Energy Astrophysics Facility in Canarias was established as a room inside the building of CALP (The Centro de Astrofísica en La Palma), a branch of IAC (Instituto de Astrofisica de Canarias).



Fig. 1. High Energy Astrophysics Facility in Canarias.

APPENDICES

A. ICRR Workshops and Ceremonies

B. ICRR Seminars

C. List of Publications

(a) Papers Published in Journals

(b) Conference Papers (Proceedings)

D. Doctoral Theses

E. Public Relations

(a) ICRR News

(b) Public Lectures

(c) Visitors

F. Inter-University Research Activities

G. List of Committee Members

(a) Board of Councillors

(b) Advisory Committee

(c) Inter-University Research Advisory Committee

H. List of Personnel

A. ICRR Workshops and Ceremonies

Workshop “The Extreme Universe Viewed in Very-High-Energy Gamma Rays 2024”

Date: January 7-8, 2025
Place : Kashiwa Campus, The University of Tokyo, Japan

Outline: A workshop titled “The Extreme Universe Viewed in Very-High-Energy Gamma Rays 2024” was held on January 7–8, 2025. In October 2018, the first Large-Sized Telescope (LST) of the Cherenkov Telescope Array Observatory (CTAO) project was completed at the northern site in La Palma. After about a year of commissioning, it detected gamma rays from the Crab Nebula (November 2019) and the Crab Pulsar (early 2020). Since then, it has observed TeV gamma rays from various sources, including active galactic nuclei (such as FSRQs at redshift $\sim$1), the Galactic Center, the Geminga pulsar, and the recurrent nova RS Ophiuchi. The second to fourth LSTs are currently under construction, with completion expected by 2026, enabling stereoscopic observations.

Beginning this year, the workshop was co-hosted by the University of Tokyo’s Next-Generation Neutrino Science Multi-messenger Astronomy Organization (NNSO). In anticipation of the upcoming CTAO era, the workshop also served as a platform to strengthen coordination between CTAO and other multi-messenger observatories and to discuss strategies for multi-messenger astronomy involving CTAO.

There were 17 presentations (including one online), all delivered in English, with 50 participants each day from Japan, China, and Greece—45 attending on-site and 5 joining remotely. The workshop featured eight sessions covering a broad spectrum of topics: TeV–PeV gamma-ray astronomy, dark matter searches at accelerators, recent results from X-ray satellites (Einstein Probe, XRISM, IXPE), JWST’s “little red dots,” high-energy neutrinos from pulsar wind nebulae, gamma-ray emissions from pulsars, AGN jet studies using VLBI, and black hole magnetosphere physics. Additional subjects included AGN observations with CTAO’s LST-1, cosmic ray interactions with the intergalactic medium, and gamma-ray emissions from starburst galaxies. Researchers from various disciplines engaged in active discussions, and updates on current and future observation plans for the MAGIC and CTAO LST-1 telescopes were shared.

Participants: 50 participants



Fig. 1. Workshop “The Extreme Universe Viewed in Very-High-Energy Gamma Rays 2024”

Hyper-Kamiokande Collaboration Meeting

Date: October 21-26, 2024
Place : Wohlfahrt Toyama, Toyama, Japan

Outline: A Hyper-Kamiokande Collaboration Meeting was held over six days, from October 21 to 26, 2024, at the Wohlfahrt Toyama in Toyama City. These collaboration meetings are held three times annually, and this was the third meeting of 2024. A total of 201 participants from 16 countries attended the meeting, with 124 joining in person and 77 participating remotely.

The first two days and the morning of the third day were dedicated to pre-meetings within individual working groups. During these sessions, detailed reports and discussions were held concerning the activities of each group. From the afternoon of the third day until the morning of the final day, plenary sessions took place in the main hall. Numerous reports were presented on the status and plans for the construction of the experimental facility and the development and manufacturing of the detector components. Lively discussions were held on how to proceed with various challenges.

Following the plenary session, on the afternoon of the final day, participants traveled by four buses to the Hyper-K construction site in Hida City, Gifu Prefecture. They visited the huge underground cavern then under excavation and inspected the ongoing tests of the delivered 50cm PMTs.

Participants: 201 (124 onsite + 77 remote)



Fig. 2. Hyper-Kamiokande Collaboration Meeting at Wohlfahrt Toyama

B. ICRR Seminars

1. June,5,2024: Dr. Anna Pollmann (Chiba University), “Physics beyond the Standard Model.with IceCube”
2. June,24,2024: Dr. Manel Errando (Washington University in St. Louis), “Relativistic jets: what happens when black holes reveal their cosmic appetite?”
3. July,26,2024: Dr. Masaki Yamashita (Kavli IPMU) “First Measurement of Coherent Elastic Neutrino Nucleus Scattering of Solar 8B Neutrinos in XENONnT”
4. July,29,2024: Dr. Vivien Raymond (Cardiff University), “Gravitational Waves Observations by LIGO-Virgo-KAGRA: neutron stars, black holes and dark matter”
5. August,2,2024: Dr. Massimo Cappi (INAF/OAS-Bologna, Head of High Energy Division of INAF), “New opportunities in high energy astrophysics from space and from the ground”
6. October,11,2024: Dr. Mahmoud Alawashra (DEZY Zeuthen, Germany), “Marginal Role of the Electrostatic Instability in the GeV-scale Cascade Flux from 1ES 0229+200”
7. October,15,2024: Dr. Diego F. Torres (Institute of Space Sciences (ICE, CSIC), Barcelona, Spain), “Understanding and quantifying the similarity among gamma-ray pulsars”
8. Novenber,5,2024: Dr. Julian Sitarek (Universidad de Lodz, Poland), “Production and absorption of gamma rays with stars in neighbourhood of supermassive black holes.”
9. January,21,2025: Prof. Masayuki NAKAHATA (ICRR, UTokyo), “Commemorative Lecture for the Medal with Purple Ribbon & Final Lecture”
10. January,31, 2025: Dr. Akira Konaka (TRIUMF), “Water Cherenkov Test Experiment (WCTE) at CERN and its spin-off drinking water monitoring project”
11. February,17, 2025: Dr. Olaf Reimer (University of Innsbruck), “H.E.S.S. – status and selected results from the last 2 years”
12. March,14. 2025: Prof. Masataka Ohashi & Prof. Masato Takita (ICRR), “Final lectures of Professor Masataka Ohashi and Professor Masato Takita”

C. List of Publications

(a) Papers Published in Journals

1. ”Search for Gravitational-wave Transients Associated with Magnetar Bursts in Advanced LIGO and Advanced Virgo Data from the Third Observing Run”, Abbott R,Others (LIGO-Virgo-KAGRA collaboration), Astrophys. J. **966** 137, Apr.2024.
2. ”Observation of Gravitational Waves from the Coalescence of a 2.5–4.5 $M\odot$ Compact Object and a Neutron Star”, Abac AG,Others (LIGO-Virgo-KAGRA collaboration), Astrophys. J. Lett. **970** L34, Jul.2024.
3. ”Search for Gravitational-lensing Signatures in the Full Third Observing Run of the LIGO–Virgo Network”, Abbott R,Others (LIGO-Virgo-KAGRA collaboration), Astrophys. J. **970** 191, Jul.2024.
4. ”Evaluation of Microseismic Motion at the KAGRA Site Based on Ocean Wave Data”, S Hoshino , Y Fujikawa , M Ohkawa , T Washimi , T Yokozawa, Prog. Theor. Exp. Phys. **2024** 103F01 , Jul.2024.
5. ”Searching for gravitational-wave signals from precessing black hole binaries with the GstLAL pipeline”, Stefano SCHMIDT, Soichiro Morisaki, et al., Phys.Rev.D **110** (2024) 2, 023038, Jul.2024.
6. ”Ultralight vector dark matter search using data from the KAGRA O3GK run”, Abac AG,Others (LIGO-Virgo-KAGRA collaboration), Phys. Rev. D, **110**, 042001 , Aug.2024.

7. ”Search for Eccentric Black Hole Coalescences during the Third Observing Run of LIGO and Virgo”, Abac AG,Others (LIGO-Virgo-KAGRA collaboration), Astrophys. J. **973** 132, Sep.2024.

8. ”A Search Using GEO600 for Gravitational Waves Coincident with Fast Radio Bursts from SGR 1935+2154”, Abac AG,Others (LIGO-Virgo-KAGRA collaboration), Astrophys. J. **977** 255, Dec.2024.

9. ”Swift-BAT GUANO Follow-up of Gravitational-wave Triggers in the Third LIGO–Virgo–KAGRA Observing Run”, Raman G,Others (LIGO-Virgo-KAGRA collaboration), Astrophys. J. **980** 207, Feb.2025.

10. ”Extension of the characterization method for non-Gaussianity in gravitational wave detector with statistical hypothesis test”, Shunsei Yamamura, Hirotaka Yuzurihara, Takahiro Yamamoto, Takashi Uchiyama, Class. Quantum Grav.**41**, Sep.2024.

11. ”Measurement of J/ψ and $\psi(2S)$ production in p+p and p+d interactions at 120 GeV”, C.H. Leung et al., Physics Letters B **858**, Sep.2024.

12. ”Constraining kaon PDFs from Drell-Yan and J/ψ production”, Wen-Chen Chang et al., Physics Letters B **855**, Jun.2024.

13. ”Low-latency gravitational wave alert products and their performance at the time of the fourth LIGO-Virgo-KAGRA observing run”, Sushant Sharma Chaudhary et al., PNAS Vol.**121**, No. 18, Apr.2024.

14. ”On the Association of GW190425 with Its Potential Electromagnetic Counterpart FRB 20190425A”, Ignacio Magaña Hernandez, Virginia D’Emilio, Soichiro Morisaki, Mohit Bhardwaj, Antonella Palmese, ApJL **971** L5, Jul.2024.

15. ”Searching for Asymmetric and Heavily Precessing Binary Black Holes in the Gravitational Wave Data from the LIGO Third Observing Run”, Stefano Schmidt et al., Phys. Rev. Lett.**133**.201401, Nov.2024.

16. ”Challenges for Fast Radio Bursts as Multimessenger Sources from Binary Neutron Star Mergers”, Mohit Bhardwaj, Antonella Palmese, Ignacio Magaña Hernandez, Virginia D’Emilio, Soichiro Morisaki, 2024 ApJ **977** 122, Dec.2024.

17. ”The cold interstellar medium of a normal sub-L$\star$ galaxy at the end of reionization”, Valentino, F. et al., Astronomy & Astrophysics, Volume **685**, id.A138, 16 pp, May.2024.

18. ”Exploring Low-mass Black Holes through Tidal Disruption Events in the Early Universe: Perspectives in the Era of the JWST, Roman Space Telescope, and LSST Surveys”, Inayoshi, Kohei et al., 2024 ApJ **966** 164, May.2024.

19. ”EMPRESS. XIV. Strong High-ionization Lines of Young Galaxies at $z = 0-8$: Ionizing Spectra Consistent with the Intermediate-mass Black Holes with $M_{BH} \sim 10^3 - 10^6 M\odot$”,Hatano, Shun et al., 2024 ApJ **966** 170, May.2024.

20. ”$Ly\alpha$ Emission at z = 7-13: Clear Evolution of $Ly\alpha$ Equivalent Width Indicating a Late Cosmic Reionization History”, Nakane, Minami et al., 2024 ApJ **967** 28, May.2024.

21. ”Gateway to the Early Universe Unleashed by the James Webb Space Telescope”,Masami Ouchi, Kagaku(Published by Iwanami Shotenn), Volume**1102**,Jun,2024,

22. ”Galaxies and Black Holes in the Early Universe Surprise Astronomers”, Yuichi Harikane, Kagaku(Published by Iwanami Shotenn),Volume**1102**,Jun,2024,

23. ”Outshining in the spatially resolved analysis of a strongly lensed galaxy at z = 6.072 with JWST NIRCam”, Giménez-Arteaga, C et al., A&A, **686**, A63 (2024), May.2024.

24. ”JASMINE: Near-infrared astrometry and time-series photometry science”, Kawata, Daisuke et al., PASJ Volume **76**, Issue 3, pp.386-425, Apr.2024.

25. ”Statistics for Galaxy Outflows at z $\sim$ 6-9 with Imaging and Spectroscopic Signatures Identified with JWST/NIRCam and NIRSpec Data”, Zhang, Yechi et al. , 2024 ApJ **970** 19, Jul. 2024.

26. ”JWST Measurements of Neutral Hydrogen Fractions and Ionized Bubble Sizes at z = 7-12 Obtained with $Ly\alpha$ Damping Wing Absorptions in 27 Bright Continuum Galaxies”, Umeda, Hiroya et al., 2024 ApJ **971** 124, Aug. 2024.

27. ”SERENADE. II. An ALMA Multiband Dust Continuum Analysis of 28 Galaxies at 5 <z <8 and the Physical Origin of the Dust Temperature Evolution”, Mitsuhashi, Ikki et al., 2024 ApJ **971** 161, Aug. 2024.

28. ”$Ly\alpha$ Imaging around the Hyperluminous Dust-obscured Quasar W2246-0526 at z = 4.6”, Luo, Yibin et al., 2024 ApJ

972 51, Aug. 2024.

29. "Balmer Decrement Anomalies in Galaxies at $z \sim 6$ Found by JWST Observations: Density-bounded Nebulae or Excited H i Clouds?", Yanagisawa, Hiroto et al., 2024 ApJ **974** 180, Oct. 2024.

30. "Strong He i Emission Lines in High N/O Galaxies at $z \sim 6$ Identified in JWST Spectra: High He/H Abundance Ratios or High Electron Densities?", Yanagisawa, Hiroto et al, 2024 ApJ **974** 266, Oct. 2024.

31. "Low [O/Fe] Ratio in a Luminous Galaxy at the Early Cosmic Epoch (z>10): Signature of Short Delay Time or Bright Hypernovae/Pair-Instability Supernovae?", Minami Nakane et al., 2024 ApJ **976** 122, Nov. 2024.

32. "Dynamics of a Galaxy at z >10 Explored by JWST Integral Field Spectroscopy: Hints of Rotating Disk Suggesting Weak Feedback", Yi Xu et al., ApJ **976** 142, Nov. 2024.

33. "Probing the Origin of the Star Formation Excess Discovered by JWST through Gamma-Ray Bursts", Tatsuya Matsumoto et al. , 2024 ApJL **976** L16, Nov. 2024.

34. "JWST/NIRSpec spectroscopy of intermediate-mass quiescent galaxies at $z \sim 3-4$", Riku A. Sato et al., MNRAS Volume **534**, Issue 4, November 2024,, Oct. 2024.

35. "A Wide and Deep Exploration of Radio Galaxies with Subaru HSC (WERGS). X. The Massive and Passive Nature of Radio Galaxies at $z \sim 4$", Yuta Yamamoto et al , 2025 ApJ **978** 102, Dec. 2024.

36. "A Search for the Most Distant Galaxies Using the JWST", Yuichi Harikane, Astronomical Herald **2025.3**, pp144-157, Feb.2025.

37. "JWST, ALMA, and Keck Spectroscopic Constraints on the UV Luminosity Functions at $z \sim 7-14$: Clumpiness and Compactness of the Brightest Galaxies in the Early Universe", Y. Harikane et al., 2025 ApJ **980** 138, Feb. 2025.

38. "Monster Radio Jet (>66 kpc) Observed in Quasar at $z \sim 5$", A. Gloudemans et al., 2025 ApJL **980** L8, Feb. 2025.

39. "SILVERRUSH. XIV. *Ly*α Luminosity Functions and Angular Correlation Functions from 20,000 *Ly*α Emitters at $z \sim 2.2-7.3$ from up to 24 deg^2 HSC-SSP and CHORUS Surveys: Linking the Postreionization Epoch to the Heart of Reionization", Hiroya Umeda et al., 2025 ApJS **277** 37, Mar. 2025.

40. "Galaxy properties from the outskirts to the core of a protocluster at z = 3.70", Jun Toshikawa et al., MNRAS Volume **537**, Issue 4, March 2025, Feb. 2025.

41. "The Physical Origin of Extreme Emission Line Galaxies at High Redshifts: Strong [O III] Emission Lines Produced by Obscured Active Galactic Nuclei", Chenghao Zhu et al., 2025 ApJ **982** 27, Mar. 2025.

42. "Probing for chiral Z' gauge boson through scattering measurement experiments", Kento Asai, Arindam Das, Jinmian Li, Takaaki Nomura, Osamu Seto, Phys. Rev. D **109**, 075026, Apr. 2024.

43. "Contribution of Majoron to Hubble tension in gauged $U(1)_{L\mu-L}$ Model", Kento Asai, Tomoya Asano, Joe Sato, Masaki J. S. Yang, PTEP Volume **2024**, Issue 7, July 2024, 073E01, Jun. 2024.

44. "Primordial Origin of Supermassive Black Holes from Axion Bubbles", Kentaro Kasai, Masahiro Kawasaki, Naoya Kitajima, Kai Murai, Shunsuke Neda, Fuminobu Takahashi,, JCAP**05**(2024)092, May. 2024.

45. "Revisiting Metastable Cosmic String Breaking", Akifumi Chitose, Masahiro Ibe, Yuhei Nakayama, Satoshi Shirai, Keiichi Watanabe, J. High Energ. Phys. 2024, **68** (2024), Apr. 2024.

46. "New constraints on gauged $U(1)_{L\mu-L\gamma}$ models via Z - Z' mixing", Kento Asai, Coh Miyao, Shohei Okawa, Koji Tsumura, JHEP **12**, 2024, 018, Dec. 2024.

47. "Affleck-Dine leptogenesis scenario for resonant production of sterile neutrino dark matter", Kentaro Kasai, Masahiro Kawasaki, Kai Murai, JCAP **08** (2024) 008, Aug. 2024.

48. "MeV gamma rays from Q-ball decay", Shinta Kasuya, Masahiro Kawasaki, Naomi Tsuji, Phys. Rev. D **109**, 083039, Apr. 2024.

49. "Small Instanton Effects on Composite Axion Mass", Takafumi Aoki, Masahiro Ibe, Satoshi Shirai, Keiichi Watanabe, J. High Energ. Phys. 2024, **269** (2024), Jul. 2024.

50. ”Exactly solvable stochastic spectator”, Takeshi Araki, Kento Asai, Yohei Nakashima, Takashi Shimomura, JCAP**12**(2024)044, Dec. 2024.

51. ”Nucleon Decay as a Probe of Flavor Symmetry: The Case of Fake Unification”, Takeshi Araki, Kento Asai, Yohei Nakashima, Takashi Shimomura, JHEP**03** (2025) 044, Mar. 2025.

52. ”Comprehensive Bayesian Exploration of Froggatt-Nielsen Mechanism”, Takeshi Araki, Kento Asai, Yohei Nakashima, Takashi Shimomura, JHEP**03**(2025) 150, Mar. 2025.

53. ”Isotropy of Cosmic Rays beyond 10^{20}eV Favors Their Heavy Mass Composition”, R.U. Abbasi et al. (Telescope Array Collaboration), Physical Review Letters, **133**, 041001 (2024), Jul. 2024.

54. ”Mass composition of ultrahigh energy cosmic rays from distribution of their arrival directions with the Telescope Array”, R. U. Abbasi et al. (Telescope Array Collaboration), Physical Review D **110**, 022006 (2024), Jul. 2024.

55. ”GRANDlib: A simulation pipeline for the Giant Radio Array for Neutrino Detection (GRAND)””, R. Alves Batista et al. (GRAND Collaboration), Computer Physics Communications **308** (2025) 109461, Dec. 2024.

56. ”Intermediate Fluence Downward Terrestrial Gamma Ray Flashes as Observed by the Telescope Array Surface Detector”, R. U. Abbasi et al. (Telescope Array Collaboration), J. Geograph. Res.: Atmosphere, **129**, e2024JD041260 (2024), Dec. 2024.

57. ”First Time-Resolved Leader Spectra Associated With a Downward Terrestrial Gamma-Ray Flash Detected at the Telescope Array Surface Detector”, N. Kieu et al. (Telescope Array Collaboration), J. Geograph. Res.: Atmosphere, **129**, e2024JD041720 (2024), Dec. 2024.

58. ”MHD Simulation of the Inner Galaxy with Radiative Cooling and Heating”, Kensuke Kakiuchi, Takeru. K. Suzuki, Shu-ichiro Inutsuka, Tsuyoshi Inoue, and Jiro Shimoda, 2024 ApJ **966** 230, May. 2024.

59. ”The Dzhanibekov Effect as a Possible Source of Magnetar Activity”, Tomoki Wada, Jiro Shimoda, 2024 ApJ **972** 58, Aug. 2024.

60. ”Radiative Acceleration and X-ray Spectrum of Outflowing Pure Electron-Positron Pair Fireball in Magnetar Bursts”, Tomoki Wada, and Katsuaki Asano, PTEP Volume **2025**, Issue 3, March 2025, 033E01, Feb. 2025.

61. ”Fermi and eROSITA Bubbles as Persistent Structures of the Milky Way Galaxy”, Jiro Shimoda, and Katsuaki Asano, 2024 ApJ **973** 78, Sep. 2024.

62. ”Possible X-ray Cocoon Emission from GRB 050709”, Naoki Ogino et al., PASJ Volume **76**, Issue 3, June 2024, Pages 550–559, May. 2024.

63. ”Multiwavelength Modeling for the Shallow Decay Phase of Gamma-Ray Burst Afterglows”, Katsuaki Asano,, 2024 ApJ **970** 141, Jul. 2024.

64. ”Particle Acceleration and Magnetic Field Amplification by Relativistic Shocks in Inhomogeneous Media”, Kanji Morikawa, Yutaka Ohira, and Takumi Ohmura, 2024 ApJL **969** L1, Jun. 2024.

65. ”Radio Images inside Highly Magnetized Jet Funnels Based on Semi-Analytic GRMHD Models”, Taiki Ogihara, Tomohisa Kawashima, and Ken Ohsuga, 2024 ApJ **969** 22, Jun. 2024.

66. ”Radiation MHD Simulations of Soft X-ray Emitting Regions in Changing Look AGN”, Taichi Igarashi et al, ApJ **968**, 121(15pp) (2024), Jun. 2024.

67. ”Radiation and Outflow Properties of Super-Eddington Accretion Flows around Various Mass Classes of Black Holes: Dependence on the Accretion Rates”, Shogo Yoshioka, Shin Mineshige, Ken Ohsuga, Tomohisa Kawashima, and Takaaki Kitaki, PASJ 2024, **76**(5), 1015–1025, Aug. 2024.

68. ”Impacts of the $^{12}C(\alpha, \gamma)^{16}O$ Reaction Rate on ^{56}Ni Nucleosynthesis in Pair-Instability Supernovae”, Hiroki Kawashimo, Ryo Sawada, Yudai Suwa, Takashi J. Moriya, Ataru Tanikawa, Nozomu Tominaga, MNRAS, **531**, 2786-2801, May. 2024.

69. ”Progenitor Constraint-incorporating Shell Merger: The Case of Supernova Remnant G359.0-0.9”, Kai Matsunaga, Hiroyuki Uchida, Rei Enokiya, Toshiki Sato, Ryo Sawada, Hideyuki Umeda, Takuto Narita, Takeshi Go Tsuru,, ApJ, **970**, 4(8pp), Jul. 2024.

70. ”Ejecta Width and Magnetization Reflected in Gamma-Ray Burst Early Afterglows: Implication for Reverse Shock Component and Shallow Decay Phase”, Yo Kusafuka, Katsuaki Asano, MNRAS Volume **536**, Issue 2, January 2025, Dec. 2024.

71. ”Low Injection Rate of Cosmic-Ray Protons in the Turbulent Reacceleration Model of Radio Halos in Galaxy Clusters”, Kosuke Nishiwaki, and Katsuaki Asano, 2025 ApJ **978** 62, Dec. 2024.

72. ”Survey of Non-thermal Electron around Supermassive Black Holes through Polarization Flips”, Yuh Tsunetoe, Tomohisa Kawashima, Ken Ohsuga, Shin Mineshige, PASJ Volume **76**, Issue 6, December 2024, Sep. 2024.

73. ”Mapping the Distribution of the Magnetic Field Strength along the NGC 315 Jet”, Motoki Kino, Hyunwook Ro, Masaaki Takahashi, Tomohisa Kawashima, Jongho Park, Kazuhiro Hada, Yuzhu Cui, 2024 ApJ **973** 100, Sep. 2024.

74. ”Towards Multi Energy Neutrino Astronomy: Diagnosing Enhanced Circumstellar Material around Stripped-Envelope Supernovae”, Ryo Sawada, Yosuke Ashida, 2025 ApJ **982** 93, Mar. 2025.

75. ”A Multi-Frequency Study of Sub-Parsec Jets with the Event Horizon Telescope”, J. Röder, M. Wielgus, A. P. Lobanov, et al., A&A, **695**, A233 (2025), Mar. 2025.

76. ”First characterization of the emission behavior of Mrk 421 from radio to very high-energy gamma rays with simultaneous X-ray polarization measurements”, MAGIC Collaboration et al., Astronomy & Astrophysics, Volume **684**, id.A127, Apr. 2024.

77. ”Insights into the broadband emission of the TeV blazar Mrk 501 during the first X-ray polarization measurements”, MAGIC Collaboration, A&A, **685**, A117 (2024), May. 2024.

78. ”Constraints on Lorentz invariance violation from the extraordinary Mrk 421 flare of 2014 using a novel analysis method”, MAGIC Collaboration, JCAP**07**(2024)044, Jul. 2024.

79. ”Dark matter line searches with the Cherenkov Telescope Array”, CTA Collaboration, JCAP**07**(2024)047, Jul. 2024.

80. ”A detailed study of the very high-energy Crab pulsar emission with the LST-1”, CTA-LST Collaboration, Astronomy & Astrophysics, Volume **690**, id.A167, Oct. 2024.

81. ”Prospects for γ-ray observations of the Perseus galaxy cluster with the Cherenkov Telescope Array”, CTA Consortium, JCAP**10**(2024)004, Oct. 2024.

82. ”Standardised formats and open-source analysis tools for the MAGIC telescopes data”, MAGIC collaboration, Journal of High Energy Astrophysics, Volume **44**, pp. 266, Nov. 2024.

83. ”Constraints on VHE gamma-ray emission of flat spectrum radio quasars with the MAGIC telescopes”, MAGIC Collaboration et al., MNRAS Volume **535**, pp.1484-1506, Oct. 2024.

84. ”Broadband multi-wavelength properties of M87 during the 2018 EHT campaign including a very high energy flaring episode”, EHT, Fermi-LAT, H.E.S.S., MAGIC, VERITAS, EAVN Collaborations, A&A, **692**, A140 (2024), Dec. 2024.

85. ”Cosmic-ray acceleration and escape from supernova remnant W44 as probed by Fermi-LAT and MAGIC”, MAGIC Collaboration et al., A&A, **693**, A255 (2025), Jan. 2025.

86. ”Characterization of Markarian 421 during its most violent year: Multiwavelength variability and correlations”, MAGIC Collaboration et al., A&A, **694**, A195 (2025), Feb. 2025.

87. ”Detection of RS Oph with LST-1 and modelling of its HE/VHE gamma-ray emission”, CTAO-LST Collaboration, A&A, **695**, A152 (2025), Mar. 2025.

88. ”Insights from the first flaring activity of a high synchrotron peaked blazar with X-ray polarization and VHE gamma rays”, MAGIC Collaboration, A&A, **695**, A217 (2025), Mar. 2025.

89. ”Combined search in dwarf spheroidal galaxies for branon dark matter annihilation signatures with the MAGIC telescopes”, MAGIC collaboration, JCAP**03**(2025)020, Mar. 2025.

90. ”Galactic Center Observations with CTAO LST-1”, Abe, Shotaro; Abhishek; Doro, Michele; Inada, Tomohiro; Strzys,Marcel; Teshima, Masahiro; Vovk, Ievgen, EPJ Web of Conference, Volume **319** (2025) 05006, Mar. 2025.

91. ”Neural networks for separation of cosmic gamma rays and hadronic cosmic rays in air shower observation with a large

area surface detector array", S. Okukawa et al., Machine Learning: Science and Technology, **5**, 025016, (2024), Apr. 2024.

92. "Quantitative Constraint on the Contribution of Resolved Gamma-Ray Sources to the Sub-PeV Galactic Diffuse Gamma-Ray Flux Measured by the Tibet $AS\gamma$ Experiment", S. Kato et al., 2024 ApJL **977** L3, Nov. 2024.

93. "Detection response of the active components of the SciBar Cosmic Ray Telescope at Sierra Negra", F. Monterde-Andrade te al., Eur. Phys. J. C, (2024) **84**:981, Sep. 2024.

94. "Gamma/hadron discrimination by analysis of the muon lateral distribution and the ALPAQUITA array", M. Anzorena et al. (ALPACA Collaboration), Experimental Astronomy (2025) **59**:13, Feb.2025.

95. "Solar neutron event recorded by a muon telescope in Mexico City on November 4, 2003", E. Ortiz et al., Advances in Space Research, **73** (2024) 4853-4858, May.2024."

96. "Offline tagging of radon-induced backgrounds in XENON1T and applicability to other liquid xenon time projection chambers", E. Aprile et al., XENON Collaboration, Phys. Rev. D **110**, 012011, 2024, Jul. 2024.

97. "Effective field theory and inelastic dark matter results from XENON1T", E. Aprile et al., XENON Collaboration, Phys. Rev. D **109**, 112017, 2024, Jun. 2024.

98. "The XENONnT dark matter experiment", XENON Collaboration,, Eur. Phys. J. C **84**, 784 (2024), Aug. 2024.

99. "XENONnT Analysis: Signal Reconstruction, Calibration and Event Selection", E. Aprile et al., XENON Collaboration, Phys. Rev. D **111**, 062006, 2025, Mar. 2025.

100. "First Search for Light Dark Matter in the Neutrino Fog with XENONnT", E. Aprile et al., XENON Collaboration, Phys. Rev. Lett. **134**, 111802 (2025), Mar. 2025.

101. "Atmospheric neutrino oscillation analysis with neutron tagging and an expanded fiducial volume in Super-Kamiokande I-V", The Super-Kamiokande Collaboration, Phys. Rev. D **109**, 072014, Apr. 2024.

102. "Solar neutrino measurements using the full data period of Super-Kamiokande-IV", The Super-Kamiokande Collaboration, Phys. Rev. D **109**, 092001 (2024), May.2024.

103. "Second gadolinium loading to Super-Kamiokande", The Super-Kamiokande Collaboration, Nucl. Instrum. Methods. Phys. Res. A **1065** (2024) 169480, Aug. 2024.

104. "Search for Periodic Time Variations of the Solar ^8B Neutrino Flux between 1996 and 2018 in Super-Kamiokande", The Super-Kamiokande Collaboration, Phys. Rev. Lett. **132**, 241803, Jun. 2024.

105. "Performance of SK-Gd's Upgraded Real-time Supernova Monitoring System", Y. Kashiwagi et al. (The Super-Kamiokande Collaboration), APJ **970**, 93 (2024), Jul. 2024.

106. "New methods and simulations for cosmogenic induced spallation removal in Super-Kamiokande-IV", S. Locke et al. (The Super-Kamiokande Collaboration), Phys. Rev. D **110**, 032003, Aug. 2024.

107. "Combined Pre-supernova Alert System with KamLAND and Super-Kamiokande", The KamLAND Collaboration and The Super-Kamiokande Collaboration, 2024 ApJ **973** 140, Sep. 2024.

108. "Development of a data overflow protection system for Super-Kamiokande to maximize data from nearby supernovae", M. Mori et al. (The Super-Kamiokande Collaboration), PTEP Volume **2024**, Issue 10, October 2024, , Aug. 2024.

109. "Measurements of the charge ratio and polarization of cosmic-ray muons with the Super-Kamiokande detector", H. Kitagawa et al. (The Super-Kamiokande Collaboration), Phys. Rev. D **110**, 082008 (2024), Oct. 2024.

110. "First Indication of Solar ^8B Neutrinos via Coherent Elastic Neutrino-Nucleus Scattering with XENONnT", E. Aprile et al., XENON Collaboration, Phys. Rev. Lett. **133**, 191002, Nov. 2024.

111. "Search for proton decay via $\rho \to e^+\eta$ and $\rho \to \mu^+\eta$ with a 0.37 Mton-year exposure of Super-Kamiokande", N.Taniuchi et al. (The Super-Kamiokande Collaboration), Phys. Rev. D **110**, 112011 (2024), Dec. 2024.

112. "First Joint Oscillation Analysis of Super-Kamiokande Atmospheric and T2K Accelerator Neutrino Data", Super-Kamiokande Collaboration and T2K Collaboration, Phys. Rev. Lett. **134**, 011801 (2025), Jan. 2025.

113. ”Modification on Thermal Motion in Geant4 for Neutron Capture Simulation in Gadolinium Loaded Water”, Y. Hino et al., Prog. Theor. Exp. Phys. **2025**, 013C01, Dec. 2024.

114. ”Implementation and investigation of electron-nucleus scattering in NEUT neutrino event generator”, S. Abe, Phys. Rev. D **111**, 033006 (2025), Feb. 2025.

(b) Conference Papers (Proceedings)

1. ”Detector characterization of KAGRA for the fourth observing run”, Yuzurihara, H. et al.(KAGRA Collaboration), 38th International Cosmic Ray Conference (ICRC2023), JUL. 26 - AUG. 3, 2023.

2. ”Calibration of the gravitational wave telescope KAGRA”, Chen, D. et al.(KAGRA Collaboration), ICRC2023, JUL. 26 - AUG. 3, 2023.

3. ”Calibration of the integrating sphere for O4 in KAGRA gravitational wave telescope.”, Fujii, S. et al.(KAGRA Collaboration), ICRC2023, JUL. 26 - AUG. 3, 2023.

4. ”A study on the effect of working fluid filling ratio and inclination for cryogenic heat pipes”, Wanison, R.; Kimura, N.; Murakami, M.; Nakai, H. et al., THE 12TH INTERNATIONAL CONFERENCE ON MECHANICAL ENGINEERING (TSME - ICoME 2022), 14–16, DEC. 2022.

5. ”Control noise reduction of cryogenic suspension in KAGRA”, Tamaki, M. et al.(KAGRA Collaboration), ICRC2023, JUL. 26 - AUG. 3, 2023.

6. ”Evaluation of the global magnetic noise for the stochastic gravitational wave background search”, Washimi, T. et al., ICRC2023, JUL. 26 - AUG. 3, 2023.

7. ”Comparison of training methods for Convolutional Neural Network model for Gravitational - Wave detection from Neutron Star - Black Hole Binaries”, Garg, S. et al., ICRC2023, JUL. 26 - AUG. 3, 2023.

8. ”Coating thermal noise investigation for KAGRA”, Mori, Y. ; Nakayama, Y. ; Ushiba, T. ; Yamamoto, K., ICRC2023, JUL. 26 - AUG. 3, 2023.

9. ”Investigation of the environmental noise at KAGRA detector”, Yokozawa, T. et al.(KAGRA Collaboration), ICRC2023, JUL. 26 - AUG. 3, 2023.

10. ”Quantum noise enhancement for gravitational wave detectors: Status of squeezed vacuum research at TAMA and KAGRA”, Page, M.A. ; Eisenmann, M.; Zhao, Y. ; Aritomi, N. ; Capocasa, E.; Guo, Y. et al., ICRC2023, JUL 26 - AUG. 3, 2023

11. ”The first joint observation by KAGRA with GEO 600”, Uchikata, N. et al.(LIGO Collaboration, Virgo Collaboration, KAGRA Collaboration), ICRC2023, JUL. 26 - AUG. 3, 2023.

12. ”Status of KAGRA”, Itoh, Y. et al.(KAGRA Collaboration), ICRC2023, JUL. 26 - AUG. 3, 2023.

13. ”Development of Gravity Field Calibrator for KAGRA”, Bajpai, R. et al.(KAGRA Collaboration), ICRC2023, JUL. 26 - AUG. 3, 2023.

14. ”Compensation of defective pixels by mechanical shift of an NIR array detector used in the NINJA echelle spectrograph”, Yanagisawa, K. et al., Conference on Ground - Based and Airborne Instrumentation for Astronomy X, JUN. 16 - 21, 2024.

15. ”Overview of the LAPYUTA mission (Life - environmentology, Astronomy, and PlanetarY Ultraviolet Telescope Assembly)”, Tsuchiya, F. et al., Conference on Space Telescopes and Instrumentation - Ultraviolet to Gamma Ray, JUN. 16 - 21, 2024.

16. ”FINER: Far - Infrared Nebular Emission Receiver for the Large Millimeter Telescope”, Tamura, Y. et al., Conference on Millimeter, Submillimeter, and Far - Infrared Detectors and Instrumentation for Astronomy XII, JUN. 18 - 22, 2024.

17. ”Concept study of GREX - PLUS: Galaxy Reionization EXplorer and PLanetary Universe Spectrometer”, Inoue, AK. et al., Conference on Space Telescopes and Instrumentation - Optical, Infrared, and Millimeter Wave, JUN. 16 - 22, 2024.

18. ”TAx4 surface detectors data analysis”, Fujisue, K (Telescope Array Collaboration), 6th international symposium on Ultra High Energy Cosmic Rays (UHECR), OCT. 03 - 07, 2022.

19. ”Updates on the Hotspot and the Perseus - Pisces supercluster Excess Observed by the Telescope Array Experiment”, Kim, J ; Ivanov, D ; Kawata, K. et al., (Telescope Array Collaboration), 6th international symposium on Ultra High Energy Cosmic Rays (UHECR), OCT. 03 - 07, 2022.

20. ”Search for the large - scale cosmic - ray anisotropies using the TA and TALE surface detector arrays”, Kimura, Y ; Fujii, T ; Ogio, S ; Tsunesada, Y (Telescope Array Collaboration), 6th international symposium on Ultra High Energy Cosmic Rays (UHECR), OCT. 03 - 07, 2022.

21. ”The energy spectrum of ultra - high energy cosmic rays measured at the Pierre Auger Observatory and the Telescope Array”, Bergman, DR et al., (Pierre Auger Collaborations ; Telescope Array Collaborations), 6th international symposium on Ultra High Energy Cosmic Rays (UHECR), OCT. 03 - 07, 2022.

22. ”Overview and First Results of EUSO - SPB2”, Eser, J. et al., (JEM-EUSO Collaboration), ICRC2023, JUL. 26 - AUG. 3, 2023.

23. ”The EUSO - SPB2 Cherenkov Telescope - Flight Performance and Preliminary Results”, Gazda, E. et al., (JEM-EUSO Collaboration), ICRC2023, JUL. 26 - AUG. 3, 2023.

24. ”Study of multiple ring ELVES with the Mini - EUSO telescope on - board the International Space Station”, Romoli, G. et al.(JEM-EUSO Collaboration), ICRC2023, JUL. 26 - AUG. 3, 2023.

25. ”The Targets of Opportunity Source Catalog for the EUSO - SPB2 Mission”, Wistrand, H. et al., ICRC2023, JUL. 26 - AUG. 3, 2023.

26. ”Overview of the EUSO - SPB2 Target of Opportunity program using the Cherenkov Telescope”, Heibges, T. et al.(JEM-EUSO Collaboration), ICRC2023, JUL. 26 - AUG. 3, 2023.

27. ”Depth of maximum of air - shower profiles: testing the compatibility of the measurements at the Pierre Auger Observatory and the Telescope Array”, Yushkov, A. et al.(Pierre Auger Collaboration), ICRC2023, JUL. 26 - AUG. 3, 2023.

28. ”EUSO - SPB2 Fluorescence Telescope Calibration and Field Tests”, Kungel, V. et al.(JEM-EUSO Collaboration), ICRC2023, JUL. 26 - AUG. 3, 2023.

29. ”EUSO - SPB2 Fluorescence Telescope in - flight performance and preliminary results”, Filippatos, G. et al.(JEM-EUSO Collaboration), ICRC2023, JUL. 26 - AUG. 3, 2023.

30. ”Highlights from the Telescope Array Experiment”, Kim, J. et al.(Telescope Array Collaboration), ICRC2023, JUL. 26 - AUG. 3, 2023.

31. ”Study of the upgraded EUSO - TA performance via simulations”, Bisconti, F. et al.(JEM-EUSO Collaboration), ICRC2023, JUL. 26 - AUG. 3, 2023.

32. ”Search for Strange Quark Matter from the International Space Station with the Mini - EUSO experiment”, Casolino, M. et al.(JEM-EUSO Collaboration), ICRC2023, JUL. 26 - AUG. 3, 2023.

33. ”Neutrino Target of Opportunity Sky Coverage and Scheduler for EUSO - SPB2”, Posligua, J. et al.(JEM-EUSO Collaboration), ICRC2023, JUL. 26 - AUG. 3, 2023.

34. ”The EUSO - TA ground - based detector: results and perspectives”, Plebaniak, Z. et al.(JEM-EUSO Collaboration), ICRC2023, JUL. 26 - AUG. 3, 2023.

35. ”Possible interpretations of the joint observations of UHECR arrival directions using data recorded at the Telescope Array and the Pierre Auger Observatory”, Kuznetsov, M. et al.(Pierre Auger Collaboration), ICRC2023, JUL. 26 - AUG. 3, 2023.

36. ”Implications of Mini - EUSO measurements for a space - based observation of UHECRs”, Bertaina, M. et al.(JEM-EUSO Collaboration), ICRC2023, JUL. 26 - AUG. 3, 2023.

37. ”High - speed Video Camera Observations Associated with a Terrestrial Gamma - ray Flash at the Telescope Array Detector.”, Abbasi, R. et al.(Telescope Array and Lightning Collaboration), ICRC2023, JUL. 26 - AUG. 3, 2023.

38. ”Auger@TA: An Auger - like surface detector micro - array embedded within the Telescope Array Project”, Mayotte, S. et al.(Pierre Auger and Telescope Array Collaborations), ICRC2023, JUL. 26 - AUG. 3, 2023.

39. ”Search for EeV photon–induced events at the Telescope Array”, Kharuk, I. et al.(Telescope Array Collaboration), ICRC2023, JUL. 26 - AUG. 3, 2023.

40. ”POEMMA (Probe of Extreme Multi - Messenger Astrophysics) Roadmap Update”, Olinto, A.V. et al.(POEMMA and JEM-EUSO Collaboration), ICRC2023, JUL. 26 - AUG. 3, 2023.

41. ”A search for Elves in Mini - EUSO data using CNN - based one - class classifier”, Piotrowski, L.W. et al.(JEM-EUSO Collaboration), ICRC2023, JUL. 26 - AUG. 3, 2023.

42. ”Commissioning, Calibration, and Performance of the Cherenkov Telescope on EUSO - SPB2”, Matamala, O.F.R. et al.(JEM-EUSO Collaboration), ICRC2023, JUL. 26 - AUG. 3, 2023.

43. ”Overview of the JEM - EUSO program for the study of ultra - high - energy cosmic - rays from space”, Casolino, M. et al.(JEM-EUSO Collaboration), ICRC2023, JUL. 26 - AUG. 3, 2023.

44. ”Cosmic Ray Energy Spectrum and Mass Composition measured by the TALE Fluorescence Detector”, AbuZayyad, T. et al.(Telescope Array Collaboration), ICRC2023, JUL. 26 - AUG. 3, 2023.

45. ”Measurement of the cosmic ray energy spectrum with the TA×4 SD array”, Fujisue, K. et al.(Telescope Array Collaboration), ICRC2023, JUL. 26 - AUG. 3, 2023.

46. ”Analysis of EAS - like events detected by the Mini - EUSO telescope”, Battisti, M. et al.(JEM-EUSO Collaboration), ICRC2023, JUL. 26 - AUG. 3, 2023.

47. ”Measurement of the cosmic ray energy spectrum in the 2nd knee region with the TALE - SD array”, Komae, I. et al.(Telescope Array Collaboration), ICRC2023, JUL. 26 - AUG. 3, 2023.

48. ”Updates of the surface detector array of the TAx4 experiment”, Kido, E.(for the Telescope Array Collaboration), ICRC2023, JUL. 26 - AUG. 3, 2023.

49. ”Influence of Galactic magnetic fields on UHECR energy spectrum and mass composition on the Earth”, Higuchi, R. ; Fujii, T. ; Kawata, K. ; Kido, E. ; Nagataki, S.; Sako, T., ICRC2023, JUL. 26 - AUG. 3, 2023.

50. ”Update on the searches for anisotropies in UHECR arrival directions with the Pierre Auger Observatory and the Telescope Array”, Caccianiga, L. et al.(Pierre Auger Collaboration), ICRC2023, JUL. 26 - AUG. 3, 2023.

51. ”Overcoming Challenges in Finding Ultra - High - Energy Cosmic Ray Sources with a Bayesian Hierarchical Framework: Impact of the Galactic magnetic field and mass composition”, Watanabe, K. ; Fedynitch, A. ; Capel, F. ; Sagawa, H., ICRC2023, JUL. 26 - AUG. 3, 2023.

52. ”Systematic uncertainty in the analysis of the TA fluorescence detector from fluorescence yield models”, Komori, K. et al.(Telescope Array Collaboration), ICRC2023, JUL. 26 - AUG. 3, 2023.

53. ”Status of the DIMS project for macroscopic dark matter search using ultra - high sensitivity CMOS cameras at the Telescope Array UHECR observatory”, Shinozaki, K. et al.(DIMS Collaboration), ICRC2023, JUL. 26 - AUG. 3, 2023.

54. ”Hadronic interaction model dependence in cosmic Gamma - ray flux estimation using a surface air shower array with an underground muon detector”, Okukawa, S. et al.(ALPACA Collaboration), ICRC2023, JUL. 26 - AUG. 3, 2023.

55. ”Infrared Cloud Monitoring with UCIRC2”, Diesing, R. et al.(JEM-EUSO Collaboration), ICRC2023, JUL. 26 - AUG. 3, 2023.

56. ”Machine Learning for Mini - EUSO Telescope Data Analysis”, Bertaina, M. et al.(JEM-EUSO Collaboration), ICRC2023, JUL. 26 - AUG. 3, 2023.

57. ”Trigger - Less Muon Data Acquisition (TM - DAQ) System for the GRAPES - 3 Muon Telescope”, Sureshkumar, R. et al, XXV DAE - BRNS High Energy Physics (HEP) Symposium, 12 - 16, DEC., 2022.

58. ”Monocular and Hybrid Analysis for TA×4 Fluorescence Detectors”, Kusumori, Y. et al.(Telescope Array Collaboration), ICRC2023, JUL. 26 - AUG. 3, 2023.

59. ”Summer Thunderstorm - Induced Muon Events (TIMEs) at GRAPES - 3 Experiment: A Detailed Investigation”, Nayak, P.K. et al., XXV DAE - BRNS High Energy Physics (HEP) Symposium, 12 - 16, DEC., 2022.

60. ”Angular Resolution and Pointing Accuracy of the GRAPES - 3 Experiment Obtained by Moon Shadow Observation”, Pattanaik, D. et al., XXV DAE - BRNS High Energy Physics (HEP) Symposium, 12 - 16, DEC., 2022.

61. ”The Data Processor of the SPB2 Fluorescence Telescope: in flight performance”, Scotti, V. et al.(JEM-EUSO Collaboration), ICRC2023, JUL. 26 - AUG. 3, 2023.

62. ”Diffuse Gamma - Rays at 10 - 300 TeV with the GRAPES - 3 Experiment”, Pant, B.P. et al., XXV DAE - BRNS High Energy Physics (HEP) Symposium, 12 - 16, DEC., 2022.

63. ”Tests and characterisation of the KI trigger for fast events on the EUSO - SPB2 Fluorescence Telescope”, Miyamoto, H. et al.(JEM-EUSO Collaboration), ICRC2023, JUL. 26 - AUG. 3, 2023.

64. ”Effects of Tonga Volcano Eruption Observed by the GRAPES - 3 Detectors”, Hariharan, B. et al., XXV DAE - BRNS High Energy Physics (HEP) Symposium, DEC. 12 - 16, 2022.

65. ”Development and Installation of Proportional Counter for Large Area Muon Telescope at GRAPES - 3”, Jain, A. et al., XXV DAE - BRNS High Energy Physics (HEP) Symposium, DEC. 12 - 16, 2022.

66. ”Monitoring the Upper Atmosphere and Interplanetary Magnetic Field Using Atmospheric Muons at GRAPES - 3”, Paul, S. et al., XXV DAE - BRNS High Energy Physics (HEP) Symposium, DEC. 12 - 16, 2022.

67. ”DIMS Experiment for Macroscopic Dark Matter and Interstellar Meteoroid Study”, Kajino, F. et al.(DIMS Collaboration), ICRC2023, JUL. 26 - AUG. 3, 2023.

68. ”Effects of atmospheric transparency on Telescope Array air shower analysis”, Mizuno, K. ; Tomida, T. ; Yamazaki, K. et al.(Telescope Array Collaboration), ICRC2023, JUL. 26 - AUG. 3, 2023.

69. ”Analysis of above - the - limb cosmic rays for EUSO - SPB2”, Cummings, A. et al.(JEM-EUSO Collaboration), ICRC2023, JUL. 26 - AUG. 3, 2023.

70. ”Simulating Geomagnetic Effects on Muons in Extensive Air Showers for the EUSO - SPB2 Mission”, Fuehne, D. ; Heibges, T. et al.(JEM-EUSO Collaboration), ICRC2023, JUL. 26 - AUG. 3, 2023.

71. ”Machine Learning for the EUSO - SPB2 Fluorescence Telescope Data Analysis”, Filippatos, G. ; Zotov, M. et al.(JEM-EUSO Collaboration), ICRC2023, JUL. 26 - AUG. 3, 2023.

72. ”Anisotropies in the Arrival Direction Distribution of Ultra - High Energy Cosmic Rays Measured by the Telescope Array Surface Detector”, Kim, J. ; Ivanov, D. ; Kawata, K. ; Sagawa, H. ; Thomson, G. et al.(Telescope Array Collaboration), ICRC2023, JUL. 26 - AUG. 3, 2023.

73. ”Small - Scale Anisotropy in Cosmic Ray Flux Observed by GRAPES - 3 at TeV Energies”, Chakraborty, M. et al., XXV DAE - BRNS High Energy Physics (HEP) Symposium, 12 - 16, DEC., 2022.

74. ”Science with the Global Cosmic - ray Observatory (GCOS)”, Batista, R.A. et al., ICRC2023, JUL. 26 - AUG. 3, 2023.

75. ”Results and performance of the Mini - EUSO telescope on board the ISS”, Marcelli, L. et al.(JEM-EUSO Collaboration), ICRC2023, JUL. 26 - AUG. 3, 2023.

76. ”FPGA Based Time Calibration Trigger System for the GRAPES - 3 Experiment”, Jain, A. et al., XXV DAE - BRNS High Energy Physics (HEP) Symposium, 12 - 16, DEC., 2022.

77. ”A New Method to Determine Muon Multiplicity at the GRAPES - 3 Experiment”, Scaria, R. et al., XXV DAE - BRNS High Energy Physics (HEP) Symposium, 12 - 16, DEC., 2022.

78. ”Cosmic Ray Diurnal Variation over Two Decades Measured by the GRAPES - 3 Muon Telescope”, Zuberi, M. et al., XXV DAE - BRNS High Energy Physics (HEP) Symposium, 12 - 16, DEC., 2022.

79. ”Offline simulation and reconstruction software framework for the JEM - EUSO missions”, Paul, T. et al.(JEM-EUSO Collaboration), ICRC2023, JUL. 26 - AUG. 3, 2023.

80. ”Calibration and testing of the JEM–EUSO detectors using stars observed in the UV band”, Plebaniak, Z. ; Przybylak, M. et al.(JEM-EUSO Collaboration), ICRC2023, JUL. 26 - AUG. 3, 2023.

81. ”Power supply system construction and power monitoring analysis for the dark matter search experiment DIMS.”, Mori, M. ; Tameda, Y. ; Shinto, D. et al.(DIMS Collaboration), ICRC2023, JUL. 26 - AUG. 3, 2023.

82. ”An end - to - end calibration of the Mini - EUSO detector in space”, Miyamoto, H. et al.(JEM-EUSO Collaboration), ICRC2023, JUL. 26 - AUG. 3, 2023.

83. ”Black Hole Spacetime and Properties of Accretion Flows and Jets Probed by Black Hole Explorer - Science Cases Proposed by BHEX Japan Team - ”, Kawashima, T et al., Conference on Space Telescopes and Instrumentation - Optical, Infrared, and Millimeter Wave, JUN. 16 - 22, 2024.

84. ”The Japanese Vision for the Black Hole Explorer Mission”, Akiyama, K et al., Conference on Space Telescopes and Instrumentation - Optical, Infrared, and Millimeter Wave, JUN. 16 - 22, 2024.

85. ”High - z gamma - ray bursts unraveling the dark ages and extreme space - time mission - HiZ - GUNDAM”, Yonetoku, D et al.(Wide Field X-ray Monitor Collaboration; Near Infrared Telescope Collaboration; Satellite Syst Collaboration; Sci Collaboration; Follow-Up Collaboration), Conference on Space Telescopes and Instrumentation - Ultraviolet to Gamma Ray, JUN. 16 - 21, 2024.

86. ”The cosmic - ray electron and positron spectrum measured with CALET on the International Space Station”, Akaike, Y. ; Torii, S. et al.(CALET Collaboration), ICRC2023, JUL. 26 - AUG. 3, 2023.

87. ”Highlights from the CALET observations for 7.5 years on the International Space Station”, Torii, S. et al.(CALET Collaboration), ICRC2023, JUL. 26 - AUG. 3, 2023.

88. ”Boron flux in cosmic rays and its flux ratio to primary species measured with CALET on the International Space Station”, Maestro, P. ; Akaike, Y. et al.(CALET Collaboration), ICRC2023, JUL. 26 - AUG. 3, 2023.

89. ”Interpretation of the CALET Electron+Positron Spectrum by Astrophysical Sources”, Motz, H. et al.(CALET Collaboration), ICRC2023, JUL. 26 - AUG. 3, 2023.

90. ”Early Gamma - Ray Afterglow from Gamma - Ray Bursts”, Asano, K., ICRC2023, JUL. 26 - AUG. 3, 2023.

91. ”Results from Calorimetric Electron Telescope (CALET) Observations of Gamma - rays on the International Space Station”, Mori, M. ; Cannady, N. et al.(CALET Collaboration), ICRC2023, JUL. 26 - AUG. 3, 2023.

92. ”Refinement of the High - Energy Gamma - ray Selection for CALET on the International Space Station”, Cannady, N. et al.(CALET Collaboration), ICRC2023, JUL. 26 - AUG. 3, 2023.

93. ”Feasibility study on an analysis of CR helium flux with the CALET detector based on an extended acceptance”, Mattiazzi, M. ; Brogi, P. et al.(CALET Collaboration), ICRC2023, JUL. 26 - AUG. 3, 2023.

94. ”Observational Challenges on the ISS: A Case Study with CALET”, Cannady, N. ; Kawakubo, Y. et al.(CALET Collaboration), ICRC2023, JUL. 26 - AUG. 3, 2023.

95. ”Measurement of iron cosmic - ray primaries below 10GeV/n by use of the geomagnetic effect with CALET”, Ichimura, M. ; Kasahara, K. et al.(CALET Collaboration), ICRC2023, JUL. 26 - AUG. 3, 2023.

96. ”Results of the Ultra - Heavy Cosmic - Ray Analysis with CALET on the International Space Station”, Zober, W.V. ; Rauch, B.F. et al.(CALET Collaboration), ICRC2023, JUL. 26 - AUG. 3, 2023.

97. ”Latest results on cosmic rays light elements with the Calorimetric Electron Telescope (CALET) on the International Space Station”, Stolzi, F. et al.(CALET Collaboration), Multifrequency Behaviour of High Energy Cosmic Sources XIV (MULTIF2023), JUN. 12 - 17, 2023.

98. ”Resuts of the Heavy Cosmic - Ray Analysis with CALET on the International Space Station”, Checchia, C. et al.(CALET Collaboration), Multifrequency Behaviour of High Energy Cosmic Sources XIV (MULTIF2023), JUN. 12 - 17, 2023.

99. ”High Energy Neutrino Emission from Global Accretion Flows around Supermassive Black Holes”, Kawashima, T. ; Asano, K. et al.(CALET Collaboration), ICRC2023, JUL. 26 - AUG. 3, 2023.

100. ”Status of the operations of CALET for 7.5 years on the International Space Station”, Tamura, T. ; Akaike, Y. ; Kobayashi, K. rt al.(CALET Collaboration), ICRC2023, JUL. 26 - AUG. 3, 2023.

101. ”Iron and Nickel fluxes measured by CALET on the International Space Station”, Stolzi, F. ; Checchia, C. ; Bigongiari, G. ; Akaike, Y. et al.(CALET Collaboration), ICRC2023, JUL. 26 - AUG. 3, 2023.

102. ”Optimizing Selection Criteria for the CALET Ultra - Heavy Cosmic Ray Analysis”, Zober, W.V. ; Rauch, B.F. ; Ficklin, A.W. ; Cannady, N. et al.(CALET Collaboration), ICRC2023, JUL. 26 - AUG. 3, 2023.

103. ”Statistical analysis into the drivers behind relativistic electron precipitation events observed by CALET on the International Space Station”, Ficklin, A.W. et al.(CALET Collaboration), ICRC2023, JUL. 26 - AUG. 3, 2023.

104. ”Observation of spectral structures in the flux of cosmic ray protons with CALET on the International Space Station”, Kobayashi, K. ; Marrocchesi, P.S. et al.(CALET Collaboration), ICRC2023, JUL. 26 - AUG. 3, 2023.

105. ”CALET Search for electromagnetic counterparts of gravitational waves in O4”, Kawakubo, Y. et al.(CALET Collaboration), ICRC2023, JUL. 26 - AUG. 3, 2023.

106. ”Dark Matter Limits from the CALET Electron+Positron Spectrum with Individual Astrophysical Source Background”, Motz, H. et al.(CALET Collaboration), ICRC2023, JUL. 26 - AUG. 3, 2023.

107. ”Magnetic Energy Dissipation through Multiple Collisions of Jets and Winds”, Kusafuka, Y. ; Asano, K. ; Ohmura, T. ; Kawashima, T., ICRC2023, JUL. 26 - AUG. 3, 2023.

108. ”Helium flux and its ratio to proton flux in cosmic rays measured with CALET on the International Space Station”, Brogi, P. et al.(CALET Collaboration), ICRC2023, JUL. 26 - AUG. 3, 2023.

109. ”Multi - messenger Constraints on Particle Acceleration in the Formation History of Galaxy Clusters”, Nishiwaki, K. ; Asano, K. ; Murase, K., ICRC2023, JUL. 26 - AUG. 3, 2023.

110. ”Cosmic - Ray Modulation during Solar Cycles 24 - 25 Transition Observed with CALET on the International Space Station”, Miyake, S. et al.(CALET Collaboration), ICRC2023, JUL. 26 - AUG. 3, 2023.

111. ”Event - by - Event Analysis for TeV Electron Candidates with CALET on the International Space Station”, Cannady, N. et al.(CALET Collaboration), ICRC2023, JUL. 26 - AUG. 3, 2023.

112. ”Flux ratios of primary elements measured by CALET on the International Space Station”, Checchia, C. et al.(CALET Collaboration), ICRC2023, JUL. 26 - AUG. 3, 2023.

113. ”Imager of MPPC - based Optical photon counter from Yamagata”, Hashiyama, K et al., Conference on X - Ray, Optical, and Infrared Detectors for Astronomy XI, JUN. 16 - 20, 2024.

114. ”Theoretical implications on the very high energy emission from GRB 190114C”, Miceli, D et al.(MAGIC Collaboration), 16th Marcel Grossmann Meeting, JUL. 05 - 10, 2021.

115. ”The next generation cameras for the Large - Sized Telescopes of the Cherenkov Telescope Array Observatory”, Heller, M. et al.(MAGIC Collaboration), ICRC2023, JUL. 26 - AUG. 3, 2023.

116. ”Performance of joint gamma - ray observations with MAGIC and LST - 1 telescopes”, Di Pierro, F. et al.(CTA-LST project and MAGIC Collaboration), ICRC2023, JUL. 26 - AUG. 3, 2023.

117. ”ctapipe - Prototype Open Event Reconstruction Pipeline for the Cherenkov Telescope Array”, Linhoff, M. et al.(CTA Collaboration), ICRC2023, JUL. 26 - AUG. 3, 2023.

118. ”First Science Results from CTA LST - 1 Telescope and status of LST - 2 - 4”, Mazin, D. et al.(CTA LST project), ICRC2023, JUL. 26 - AUG. 3, 2023.

119. ”Bright blazar flares with CTA”, Cerruti, M. et al., ICRC2023, JUL. 26 - AUG. 3, 2023.

120. ”New constraints on Lorentz invariance violation using the extraordinary flare of Mrk 421 in 2014”, D’Amico, G. et al.(MAGIC Collaboration), ICRC2023, JUL. 26 - AUG. 3, 2023.

121. ”Detecting and characterizing pulsar halos with the Cherenkov Telescope Array Observatory”, Eckner, C. et al., ICRC2023, JUL. 26 - AUG. 3, 2023.

122. ”Multi - wavelength analysis of the galactic PeVatron candidate LHAASO J2108+5157”, Pirola, G. et al.(CTA-LST project), ICRC2023, JUL. 26 - AUG. 3, 2023.

123. ”Evidence of hadronic origin of the gamma - ray emission from the nova RS Oph by the MAGIC telescopes”, Green, D.M. et al.(MAGIC Collaboration), ICRC2023, JUL. 26 - AUG. 3, 2023.

124. ”The Real Time Analysis framework of the Cherenkov Telescope Array’s Large - Sized Telescope”, Caroff, S. et al.(CTA-LST project), ICRC2023, JUL. 26 - AUG. 3, 2023.

125. ”Search for pair echo signatures in the gamma - ray light curve of GRB190114C”, Vovk, I., ICRC2023, JUL. 26 - AUG. 3, 2023.

126. ”Highlights of Galactic Science with the MAGIC telescopes”, Strzys, M.C. et al.(MAGIC Collaboration), ICRC2023, JUL. 26 - AUG. 3, 2023.

127. ”Exploring the Universe’s Extreme Events: Galactic Transients at High and Very High Energies”, Hadasch, D., ICRC2023, JUL. 26 - AUG. 3, 2023.

128. ”Interpolation of Instrument Response Functions for the Cherenkov Telescope Array in the Context of pyirf”, Dominik, R.M. et al.(CTA Collaboration), ICRC2023, JUL. 26 - AUG. 3, 2023.

129. ”Performance of the Large - Sized Telescope prototype of the Cherenkov Telescope Array”, Morcuende, D. et al.(CTA-LST project), ICRC2023, JUL. 26 - AUG. 3, 2023.

130. ”Detection of the 2021 Outburst of RS Ophiuchi with the LST - 1”, Kobayashi, Y. et al.(CTA-LST project), ICRC2023, JUL. 26 - AUG. 3, 2023.

131. ”Measurement of the primary cosmic - ray proton spectrum between 40 TeV and a few hundred TeV with the Tibet hybrid experiment (Tibet - III + MD)”, Katayose, Y. et al.(Tibet ASγ Collaboration), ICRC2023, JUL. 26 - AUG. 3, 2023.

132. ”Low energy performance boost through a hardware stereoscopic trigger between CTA LST - 1 and MAGIC”, Baxter, J. et al.(CTA-LST project and MAGIC Collaboration), ICRC2023, JUL. 26 - AUG. 3, 2023.

133. ”Multiwavelength characterization of two flaring blazars: insight into the emission region of intermediate - synchrotron - peaked BL Lacs”, Loporchio, S. et al.(Fermi-LAT and MAGIC Collaboration), ICRC2023, JUL. 26 - AUG. 3, 2023.

134. ”Joint Observation of the Galactic Center with MAGIC and CTA - LST - 1”, Abe, S. et al.(MAGIC Collaboration and the CTA-LST Project), ICRC2023, JUL. 26 - AUG. 3, 2023.

135. ”MAGIC observation of BL Lacertae flaring period in 2020”, Imazawa, R. et al.(MAGIC Collaboration), ICRC2023, JUL. 26 - AUG. 3, 2023.

136. ”Performance of the MAGIC stellar intensity interferometer and expansion to MAGIC + CTAO - LST1 stellar intensity interferometer”, Cifuentes, A. et al., SPIE Astronomical Telescopes + Instrumentation, JUN. 16 - 21,2024.

137. ”Long - term study of the intermittent extreme behaviour of 1ES 2344+514”, Arbet - Engels, A. et.al., ICRC2023, JUL. 26 - AUG. 3, 2023.

138. ”A survey to evaluate diversity, equity and inclusion in large Collaborations”, van Scherpenberg, J. et al.(MAGIC Collaboration), ICRC2023, JUL. 26 - AUG. 3, 2023.

139. ”Characterization of SiPM and development of test bench modules for the next - generation cameras for Large - Sized Telescopes for Cherenkov Telescope Array”, Saito, T. ; Hashiyama, K. ; Iwasaki, H. ; Kubo, H. ; Mizote, M. ; Okumura, A. ; Tajima, H. ; Yamamoto, T. (CTA-LST project), ICRC2023, JUL. 26 - AUG. 3, 2023.

140. ”Cosmic Rays origin studies in the W44 region with Fermi - LAT and MAGIC observations”, Di Tria, R. et al.(MAGIC Collaboration), 7th Heidelberg International Symposium on High - Energy Gamma - Ray Astronomy (Gamma2022), JUL. 4 - 8, 2022.

141. ”Expected exclusion limits to TeV dark matter from the Perseus Cluster with the Cherenkov Telescope Array”, Hernández - Cadena, S. et al.(CTA Collaboration), ICRC2023, JUL. 26 - AUG. 3, 2023.

142. ”Constraints on axion - like particles with the Perseus Galaxy Cluster with MAGIC”, D’Amico, G. et al.(MAGIC Collaboration), ICRC2023, JUL. 26 - AUG. 3, 2023.

143. ”Long term study of the blazar S5 0716+714: investigating a turbulent jet at all wavelengths”, Podobnik, F. et al.(MAGIC Collaboration), ICRC2023, JUL. 26 - AUG. 3, 2023.

144. ”Gamma - ray Spectral Line emission search from Dark Matter Annihilation up to 100 TeV towards the Galactic Centre

with MAGIC", Inada, T. et al.(MAGIC Collaboration), ICRC2023, JUL. 26 - AUG. 3, 2023.

145. "MAGIC observations of the putative PeVatron SNR G106.3+2.7 in the proximity of the Boomerang PWN", Saito, T. ; Oka, T. ; Kubo, M.S.H. (MAGIC Collaboration), 7th Heidelberg International Symposium on High - Energy Gamma - Ray Astronomy (Gamma2022), JUL. 4 - 8, 2022.

146. "Improvement of the follow - up observations of IceCube neutrinos by CTA LST", Noda, K. et al.(CTA-LST project), ICRC2023, JUL. 26 - AUG. 3, 2023.

147. "Event reconstruction using pattern spectra and convolutional neural networks for the Cherenkov Telescope Array", Aschersleben, J. ; Vecchi, M.; Wilkinson, M.H.F. ; Peletier, R.F. et al.(CTA Consortium), 7th Heidelberg International Symposium on High - Energy Gamma - Ray Astronomy (Gamma2022), JUL. 4 - 8, 2022.

148. "The broadband 3 - year monitoring of the blazar 1ES 1959+650: a SED analysis of the low state", Nanci, C. et al.(MAGIC, OVRO and TELAMON Collaboration), ICRC2023, JUL. 26 - AUG. 3, 2023.

149. "Multiwavelength study of GRB 201216C using the sub - TeV emission detected by MAGIC", Fukami, S. et al.(MAGIC Collaboration), ICRC2023, JUL. 26 - AUG. 3, 2023.

150. "GRB 221009A observations with LST - 1 at VHE gamma rays", Aguasca - Cabot, A. et al.(CTA LST project), High Energy Phenomena in Relativistic Outflows VIII (HEPROVIII), OCT.23 - 26, 2023.

151. "Galactic Center Studies with CTA - LST - 1", Abe, S. ; Ohtani, Y. ; Strzys, M. ; Teshima, M. ; Vovk, I. et al.(CTA-LST project), ICRC2023, JUL. 26 - AUG. 3, 2023.

152. "Imaging Atmospheric Cherenkov Telescopes pointing determination using the trajectories of the stars in the field of view.", Dalchenko, M. ; Heller, M. et al.(CTA-LST project), ICRC2023, JUL. 26 - AUG. 3, 2023.

153. "Update on the performance of the MAGIC Intensity Interferometer", Martínez, I.J. et al.(MAGIC Collaboration), ICRC2023, JUL. 26 - AUG. 3, 2023.

154. "Sensitivity of the Cherenkov Telescope Array to the gamma - ray emission from neutrino sources detected by IceCube", Sergijenko, O. et al.(CTA Consortium and FIRESONG Team), ICRC2023, JUL. 26 - AUG. 3, 2023.

155. "Defining the data legacy of the MAGIC telescopes: adopting a standardised data format and open - source analysis tools", Nigro, C. et al.(Telescope Array Collaboration), ICRC2023, JUL. 26 - AUG. 3, 2023.

156. "Potential of the Cherenkov Telescope Array for studying the young nearby supernova remnants", Prokhorov, D.A. et al.(CTA Consortium), ICRC2023, JUL. 26 - AUG. 3, 2023.

157. "First results of pulsar observations with the LST - 1", Mas - Aguilar, Á. Et al.(CTA LST project), ICRC2023, JUL. 26 - AUG. 3, 2023.

158. "LST - 1 observations of an enormous flare of BL Lacertae in 2021", Nozaki, S. ; Asano, K. ; Escudero, J. ; Emery, G. ; Priyadarshi, C. et al.(CTA-LST project), ICRC2023, JUL. 26 - AUG. 3, 2023.

159. "Dark matter searches in dwarf spheroidal galaxies with the Cherenkov Telescope Array", Saturni, F.G. ; Doro, M. ; Morselli, A. ; Rodríguez - Fernández, G. et al., (CTA Collaboration), ICRC2023, JUL. 26 - AUG. 3, 2023.

160. "The Cosmic - ray Electron and Positron Spectrum Measured with MAGIC", Chai, Y. et al.(MAGIC Collaboration), ICRC2023, JUL. 26 - AUG. 3, 2023.

161. "Pybkgmodel - a background modelling toolbox for the CTA", Strzys, M.C. ; Abe, S. ; de Bony de Lavergne, M. ; Hütten, M. ; Mender, S. ; Vovk, I. et al.(CTA Collaboration), ICRC2023, JUL. 26 - AUG. 3, 2023.

162. "Basic simulation study on the discrimination between primary electrons and gamma rays for the next generation IACTs", Shina, K. ; Kimura, T. ; Gunji, S. ; Goto, R. ; Kikuta, R. ; Ohishi, M. ; Sako, T. ; Yoshikoshi, T., ICRC2023, JUL. 26 - AUG. 3, 2023.

163. "Performance update of an event - type based analysis for the Cherenkov Telescope Array", Bernete, J. et al.(CTA Collaboration), ICRC2023, JUL. 26 - AUG. 3, 2023.

164. "MAGIC Upper Limits on the VHE emission from Flat Spectrum Radio Quasars", Mondal, H.A. et al.(MAGIC Collaboration and the Fermi-LAT collaboration), ICRC2023, JUL. 26 - AUG. 3, 2023.

165. ”Joint searches by FACT, H.E.S.S., MAGIC and VERITAS for VHE gamma - ray emission associated with neutrinos detected by IceCube”, Schüssler, F. et al.(FACT, Fermi-LAT, H.E.S.S., IceCube, MAGIC and VERITAS collaborations), ICRC2023, JUL. 26 - AUG. 3, 2023.

166. ”Chasing Gravitational Waves with the Cherenkov Telescope Array”, Green, J.G. et al.(CTA Consortium), ICRC2023, JUL. 26 - AUG. 3, 2023.

167. ”Observation of Active Galactic Nuclei with the Large - Sized Telescope prototype of the Cherenkov Telescope Array”, Takeishi, R. et al.(CTA-LST project), ICRC2023, JUL. 26 - AUG. 3, 2023.

168. ”Galactic Center Observations with CTA - LST - 1”, Shotaro Abe (CTA-LST project), 58th Rencontres de Moriond 2024, Very High Energy Phenomena in the Universe, MAR. 24 - 31, 2024.

169. ”Highlights from the Tibet ASγ experiment”, Takita, M. et al.(Tibet ASγ Collaboration), ICRC2023, JUL. 26 - AUG. 3, 2023.

170. ”Modeling of TeV Galactic Cosmic - ray Anisotropy based on Intensity Mapping in an MHD Model Heliosphere”, Amenomori, M. et al., 15th International Conference on Numerical Modeling of Space Plasma Flows (ASTRONUM), JUN. 26 - 30, 2023.

171. ”Unveiling the molecular environment of the enigmatic PeVatron candidate LHAASO J2108+5157”, Toledano–Juárez, I. et al., ICRC2023, JUL. 26 - AUG. 3, 2023.

172. ”Neural Networks for Gamma Ray/Cosmic Ray Separation in Air Shower Observation with a Large Area Surface Scintillation Detector Array”, Okukawa, S. et al., ICRC2023, JUL. 26 - AUG. 3, 2023.

173. ”Observation of gamma rays from the northern celestial sky up to the sub - PeV range with the Tibet air shower array and its underground muon detector array”, Kato, S. et al., ICRC2023, JUL. 26 - AUG. 3, 2023.

174. ”Nobeyama Cygnus - X Survey: Physical Properties of $C^{18}O$ clumps in DR - 6(W), DR - 9 and DR - 13S regions”, de la Fuente, E. et al., ICRC2023, JUL. 26 - AUG. 3, 2023.

175. ”Solar neutron event recorded by a muon telescope in Mexico City on November 4, 2003”, Ortiz, E. et al., ICRC2023, JUL. 26 - AUG. 3, 2023.

176. ”Observation of multi - ten TeV to sub - PeV gamma rays from the HESS J1843 - 033 region with the Tibet air shower array”, Kato,S. et al.(Tibet ASγ Collaboration), The 27th European Cosmic Ray Symposium, JUL. 25 - 29, 2022.

177. ”Effect of optical properties of FDs on reconstruction analysis”, Sato, D. et al.(Telescope Array Collaboration), ICRC2023, JUL. 26 - AUG. 3, 2023.

178. ”Overview status of the ALPACA experiment”, Subieta Vasquez, M.A. et al.(ALPACA Collaboration), ICRC2023, JUL. 26 - AUG. 3, 2023.

179. ”Extending the dynamic range of the 2 - inch - diameter PMT for the ALPACA experiment”, Kawashima, T. et al.(ALPACA Collaboration), ICRC2023, JUL. 26 - AUG. 3, 2023.

180. ”Performance studies of the ALPACA experiment”, Yokoe, Y. et al.(ALPACA Collaboration), ICRC2023, JUL. 26 - AUG. 3, 2023.

181. ”Sub - PeV to PeV Photon Observations Using the New Air Shower Array in Bolivia”, T.Sako et al.(ALPACA COllaboration), Beyond Standard Model: From Theory to Experiment (BSM - 2023), 6 - 9 NOV, 2023.

182. ”PICOLON dark matter search project by large - volume NaI(Tl) scintillator”, Fushimi, K. ; Chernyak, D. ; Ejiri, H. ; Hata, K. et al., ICRC2023, JUL. 26 - AUG. 3, 2023.

183. ”Low energy atmospheric neutrino flux calculation with accelerator - data - driven tuning”, Sato, K., ICRC2023, JUL. 26 - AUG. 3, 2023.

184. ”Screening ultra - low alpha emissivity from the material surface based on a gaseous TPC with PMTs”, Ito, H. ; Ichimura, K. ; Hosokawa, K. ; Nakamura, K.D. ; Minamino, A. ; Miuchi, K., ICRC2023, JUL. 26 - AUG. 3, 2023.

185. ”T2KSK Joint ν Oscillation Sensitivity”, Barrow, D ; Berns, L ; Blanchet, A. et al.(T2K Collaborations ; Super - Kamiokande Collaborations), 11th Neutrino Oscillation Workshop (NOW), SEP. 04 - 11, 2022.

186. ”Search for Boosted Dark Matter in Super - Kamiokande with low - energy electrons”, Iovine, N. et al.(Super-Kamiokande Collaboration), ICRC2023, JUL. 26 - AUG. 3, 2023.

187. ”Measurement of the charge ratio and polarization of cosmic - ray muon using the tagged Decay - e events in Super - Kamiokande”, Nakano, Y. ; Tada, T. ; Kitagawa, H. ; Koshio, Y. et al.(Super-Kamiokande Collaboration), ICRC2023, JUL. 26 - AUG. 3, 2023.

188. ”Evaluation of neutron tagging efficiency on 0.03% Gd mass concentration in SK - Gd experiment”, Nakanishi, F. et al.(Super-Kamiokande Collaboration), ICRC2023, JUL. 26 - AUG. 3, 2023.

189. ”Time - dependent and Time - independent Directional Search for High - Energy Astrophysical Neutrino Point Sources in Super - Kamiokande”, Wang, X. et al.(Super-Kamiokande Collaboration), ICRC2023, JUL. 26 - AUG. 3, 2023.

190. ”First result of a search for Diffuse Supernova Neutrino Background in SK - Gd experiment”, Harada, M. et al.(Super-Kamiokande Collaboration), ICRC2023, JUL. 26 - AUG. 3, 2023.

191. ”Measurement of cosmogenic ^{9}Li in Super - Kamiokande with gadolinium loaded water”, Shinoki, M. et al.(Super-Kamiokande Collaboration), ICRC2023, JUL. 26 - AUG. 3, 2023.

192. ”Measurement of the kaon to pion production ratio with the Super - Kamiokande”, Tada, T. ; Nakano, Y. ; Koshio, Y. et al.(Super-Kamiokande Collaboration), ICRC2023, JUL. 26 - AUG. 3, 2023.

193. ”Study of the neutrino - oxygen neutral - current quasielastic cross section using atmospheric neutrinos in the SK - Gd experiment”, Sakai, S. et al.(Super-Kamiokande Collaboration), ICRC2023, JUL. 26 - AUG. 3, 2023.

194. ”Status and Prospect of SK - Gd Project”, Hino, Y. et al.(Super-Kamiokande Collaboration), ICRC2023, JUL. 26 - AUG. 3, 2023.

D. Doctoral Theses

1. TeV Gamma-Ray Emission across the Galactic Center Ridge with the First CTA Large-Sized Telescope,
   ABE, Shotaro,
   Ph.D Thesis, Mar. 2025

2. Origins of Gravitational-wave Sources with Hierarchical Bayesian Analysis,
   IWAYA, Masaki,
   Ph.D Thesis, Mar. 2025

3. Study of Pulsed Emission of the Crab Pulsar with a High Time Resolution Optical Photon Counting Imager,
   HASHIYAMA, Kazuaki,
   Ph.D Thesis, Mar. 2025

4. Neutrino mass ordering determination using atmospheric neutrinos with neutron detection in Super-Kamiokande,
   MIKI, Shintaro,
   Ph.D Thesis, Mar. 2025

5. Origin of the matter structure and nucleon decay,
   WATANABE, Keiichi,
   Ph.D Thesis, Mar. 2025

6. Demographics of the High-z Galaxy Dynamics Probed with ALMA,
   Dongsheng, Sun,
   Ph.D Thesis, Mar. 2025

E. Public Relations

(a) ICRR News

ICRR News is a quarterly publication written in Japanese about scientific and educational activities at ICRR.

Below lists the main topics in the issues published in FY 2024:

No.118 (2024 Winter-Spring)

- Features : Plenty Outcomes Produced from Precise Observations of James Webb Space Telescope, Observational Cosmology Group
- Features : Press Release 2023.12.4, The James Webb Space Telescope Discovered Numerous Supermassive Black Holes in the Distant Universe
- Features : Press Release 2023.12.11, The James Webb Space Telescope Identifies Galaxies with Extremely Low C/N and Low O/N
- Features : Press Release 2023.12.22, The Cosmic Dawn was Brighter Than Expected
- Features : Press Release 2024.1.17 T2K Experiment Enters a New Phase with Significantly Improved Sensitivity for its World Leading Neutrino Oscillation Research
- Features : Press Release 2023.12.26 LST-1 finds the oldest AGN in Very High Energy Field
- Features : Press Release 2024.1.18 M87* One Year Later: Proof of a Persistent Black Hole Shadow
- Reports : 2024 Spring School Held in ICRR, UTokyo Kashiwa Campus, Participated by 30 Undergraduate Students
- Reports : Associate Prof.Osamu Miyakawa Talks at ICRR-IPMU Joint Public Lecture in UTokyo Hongo Campus, ”Gravitational Waves Detction by Underground KAGRA Site in Kamioka, Japan”
- Awards : Assistant Prof. Yuichi Harikane (Observational Cosmology Group) Wins The ASJ Young Astronomer Award
- Awards : Graduate Student (D2), Kaoru Takahashi (Telescope Array Group) Wins Best Poster Award in WINGS-QSTEP Colloquium
- Awards : Three Graduate Students (Theory Group and Dark Matter Direct Detection Group) Win Exellent Presentation Award in Young Researchers Conference
- Awards : Graduate Student (D2), Yoshino Kaminaga (Dark Matter Direct Detection Group) Wins Best Poster Award in SMART2023
- Topics : Prof. Shoichi Ogio (Telescope Array Group) inaugurated as ICRR Director on April.1, 2024
- Topics : Prof. Takaaki Kajita Delivers Last Lecture ”Looking Back Research Activities in ICRR” for 400 People
- Topics : Hyper-Kamiokande 4th Meeting Held in KEK Tokai Campus
- Topics : Research Results Presentation Meeting of the FY2023 Inter-University Research Program Held in Hybrid Style
- Topics : FY2023 ICRR Master and Doctor Workshop Held in Hybrid Style
- Topics : KAGRA Dameges Caused by 2024.1.1 Earthquake in Noto Peninshula
- Topics : ICRR-IPMU Joint Public Lecture to be Held in Spring
- Information : Staff Reassignment
- Information : ICRR Seminar

No.119 (2024 Summer)

- Features : Ultra-high-energy Cosmic Rays Above 100EeV Look Like Heavy Atomic Nucleus : Telescope Array Group
- Features : Press Release 2024.6.28, Isotropy of Cosmic Rays Beyond 10^{20} eV Favors their Heavy Mass Composition
- Features : Press Release 2024.5.30, Why Does Inflation Look Single Field to Us?
- Features : Press Release 2024.7.11, First Measurement of a Nuclear Recoil Signal from Solar Neutrinos with XENONnT
- Reports : ICRR-IPMU Joint Public Lecture in 2024 Spring Held in Kashiwa, 950 People Participating Online and Onsite

- Reports : Mockup Test for Hyper-Kamiokande Starts in Kashiwa Campus
- Awards : Graduate Student (M2), Hiroki Kawachi (Dark Matter Direct Detection Group) Wins Poster Award in Workshop on Low BG Technologies 2024
- Awards : ICRR Former Director, Masayuki Nakahata Wins Distinguished Service Award of Gifu Prefecture
- Topics : Stone Monument of "Asahi Hut" Installed in Mt. Norikura
- Topics : Open Discussion for KAGRA Project Held in Tokyo
- Topics : Honor of UTokyo Professor Emeritus Given to Dr. Takaaki Kajita
- Topics : Donation from Kamioka Civic Group Given to ICRR
- Topics : ICRR Catalogue 2024 Published Online
- Information : Staff Reassignment
- Information : ICRR Seminar

No.120 (2024 Autumn and Winter)

- Features : ICRR Former Director, Masayuki Nakahata Wins Medal with Purple Ribbon
- Features : Conglatulatory Words from Dr. Takaaki Kajita
- Features : Press Release 2024.12.13, M87's Powerful Jet Unleashes Rare Gamma-Ray Outburst
- Reports : Kashiwa Campus Open Day 2024, The Total Number of 2010 People Enjoys ICRR Events
- Reports : Super-Kamiokande Open Day, 300 People Enjoy Visiting
- Reports : Female Student's Event "Yappari Butsuri ga Suki" Held in Kashiwa Campus : Ms.Yuki Iwamura of Nikon Co.Ltd. Delivers a Lecture
- Awards : Postdoctoral Fellow, Sei Kato (Tibet Experiment, ALPACA Experiment Group) Wins Young Scientist Award of the Physical Society of Japan
- Awards : Former ICRR Graduate Student, Han Seungho (Current Position: Pstdoctoral Fellow of Kyoto Univ.) Wins 26th High Energy Physics Young Researcher's Award
- Awards : Postdoctoral Fellow, Masayuki Harada (Super-Kamiokande Experiment Group) Wins Young Scientist Award of the Physical Society of Japan
- Awards : Four Graduate Students Win Student Presentation Award of the Physical Society of Japan in 2024 Conference
- Awards : Graduate Student (D2), Yo Kusafuka Wins Poster Grand Prize in 2nd Conference of Creation of Multi-messenger Astrophysics
- Awards : Graduate Student (M2), Chisato Koyama (Telescope Array Group) Wins Poster Award in UHECR 2024
- Topics : IN2P3, KEK and UTokyo Sign MoU to Promote Hyper-Kamiokande Project
- Topics : University of Victoria (Canada), KEK and UTokyo Sign MoU to Promote Hyper-Kamiokande Project
- Topics : Prof. Masayuki Nakahata and Prof. Masatake Ohashi Win Distiguished Service Award of Hida City
- Topics : Status of KAGRA Damaged by Earthquake Revealed
- Topics :Minister of Education, Culture, Sports, Science and Technology, Masahito Moriyama Visits Super-Kamiokande, KAGRA and ICRR HQ in Kashiwa Campus
- Topics : ICRR Calendar 2025 Published and on Sale
- Topics : ICRR Annual Report 2023 Published Online

- Topics : Open Call for Spring School 2025
- Information : Staff Reassignment
- Information : ICRR Seminar

(b) Public Lectures

- ”The Saturday Lecture of Taki Junior and Senior High School”, April 17, 2024, Home & nico Hall Konan Civic Cultural Center, Konan-City, Aichi, Takaaki Kajita (ICRR, The University of Tokyo)
- ”ICRR & IPMU Joint Lecture in Spring”, April 20, 2024, Kashiwa-no-ha Conference Cente, Kashiwa-City, Chiba, Atsushi Takeda (ICRR, The University of Tokyo)
- ”Public Lecture for the 50th Anniversary of Nagase-Landauer, LTD.”, May 24, 2024, Hotel Nikko Tsukuba, Tsukuba-City, Ibaraki, Takaaki Kajita (ICRR, The University of Tokyo)
- ”Public Lecture for Students of the National Defence Academy”, June 6, 2024, National Defence Academy, Yokosuka-City, Kanagawa, Takaaki Kajita (ICRR, The University of Tokyo)
- ”Public Lecture at the Heisei-Kotoku Juku organized by Kitanippon Newspaper Campany”, June 8, 2024, Ecchuuza, Toyama-City, Toyama, Takaaki Kajita (ICRR, The University of Tokyo)
- ”The Novel Lauriates Forum by Yomiuri Newspaper Campany”, July 15, 2024, Yasuda Auditorium, Bunkyo-Ward, Tokyo, Takaaki Kajita (ICRR, The University of Tokyo)
- ”Public Lecture for Workshop by Net-journalist Association”, July 31, 2024, Hongo Campus of UTokyo, Bunkyo-Ward, Tokyo, Takaaki Kajita (ICRR, The University of Tokyo)
- ”Interferometer Workshop for Kagoshima La-Salle High School”, July 22, 2024, ICRR, UTokyo, Kashiwa-City, Chiba, Soichiro Morisaki (ICRR, The University of Tokyo)
- ”Public Lecture for Strategic Professional Development Program for Young Researchers (MEXT)”, August 2, 2024, Online from Tokyo Midtown Hibiya, Chiyoda-Ward, Tokyo, Takaaki Kajita (ICRR, The University of Tokyo)
- ”Public Lecture for Motomachi Highe School students from Hiroshima-City”, October 1, 2024, ICRR, Utokyo, Kashiwa-City, Chiba, Yasuhiro Murakami (ICRR, The University of Tokyo)
- ”Handmade Spectrometer Workshop for Elementary School Students with their Parents”, August 6, 2024, Tokatsu Techno Plaza, Kashiwa-City, Chiba, Masami Ouchi (ICRR, The University of Tokyo)
- ”Memorial Lecture for the Renewal of Chunichi Culture Center in Sakae”, September 7, 2024, Chunichi Culture Center in Sakae,Nagoya-City, Aichi,Takaaki Kajita (ICRR, The University of Tokyo)
- ”Public Lecture for the Open University of Japan”, September 23, 2024, Brain Research Institute, Niigata University, Niigata-City, Niigata, Takaaki Kajita (ICRR, The University of Tokyo)
- ”Public Lecture for the UTokyo Fair in LaLaport Kashiwanoha”, September 29, 2024, LaLaport Kashiwanoha, Kashiwa-City, Chiba, Shoichi Ogio (ICRR, The University of Tokyo)
- ”Dialogue between Young Leaders and Nobel Laureates organized by STS Forum”, October 5, 2024, The Prince Kyoto Takaragaike, Kyoto-City, Kyoto, Takaaki Kajita (ICRR, The University of Tokyo)
- ”Mini Lecture for Matsue-minami high school students”, October 9, 2024, ICRR, UTokyo Kashiwa Campus, Kashiwa-City, Chiba, Kazumasa Kawata (ICRR, The University of Tokyo)
- ”Public Lecture for Alliance Forum Foundation”, October 15, 2024, Nihonbashi Life Science Hub, Chuo-Ward, Tokyo, Takaaki Kajita (ICRR, The University of Tokyo)
- ”Public Lecture for the Kashiwa Campus Open Day”, October 26, 2024, ICRR, UTokyo Kashiwa Campus, Kashiwa-City, Chiba, Shoichi Ogio (ICRR, The University of Tokyo)
- ”Science Cafe for the Kashiwa Campus Open Day”, October 26, 2024, ICRR, UTokyo Kashiwa Campus, Kashiwa-City, Chiba, Ryo Sawada (ICRR, The University of Tokyo)

- ”Science Cafe for the Kashiwa Campus Open Day”, October 26, 2024, ICRR, UTokyo Kashiwa Campus, Kashiwa-City, Chiba, Keitaro Fujita (ICRR, The University of Tokyo)
- ”Public Lecture at the annual conference of Oriental Astronomical Association”, November 2, 2024, Tokyo Future University, Adachi-Ward, Tokyo, Takaaki Kajita (ICRR, The University of Tokyo)
- ”Public Lecture for the Itabashi Trade Fair”, November 16, 2024, Uemura Memorial Kaga Sports Center, Itabashi-Ward, Tokyo, Masato Takita (ICRR, The University of Tokyo)
- ”Official event of Ig Novel Prize ’Ig Nobel Face-to-Face 2024 in Japan’”, November 17, 2024, Miraikan, Koto-Ward, Tokyo, Takaaki Kajita (ICRR, The University of Tokyo)
- ”ICRR & IPMU Joint Lecture in Fall”, December 8, 2024, Yasuda Auditorium, UTokyo Hongo Campus, Bunkyo-Ward, Tokyo, Kazumasa Kawata (ICRR, The University of Tokyo)
- ”Public Lecture for the program ”Dream with Science” by Higashimatsuyama City”, December 19, 2024, Higashimatsuyama Citizen’s Cultural Center, Higashimatsuyama-City, Saitama, Takaaki Kajita (ICRR, The University of Tokyo)
- ”Public Lecture for New Years Party of the Saitama Ladies Management Club”, February 5, 2025, Hotel Brillante Musashino, Saitama-City, Saitama, Takaaki Kajita (ICRR, The University of Tokyo)
- ”Joint Science Cafe with Tamarokuto Science Center”, March 2, 2025, Tamarokuto Science Cente, Nishitokyo-City, Tokyo, Masayuki Nakahata (ICRR, The University of Tokyo)
- ”Public Lecture for annual conference of the Institute of Electronics, Information and Communication Engineers”, March 26, 2024, Tokyo City University, Setagaya-Ward, Tokyo, Takaaki Kajita (ICRR, The University of Tokyo)
- ”Lecture for Toyama High School Students”, July 4, 2024, Toyama High School , Toyama-City, Toyama, Takashi Uchiyama (ICRR, The University of Tokyo)
- ”Public Lecture for Researchers’ Talk in Kamiokalab”, July 7, 2024, Hida Space Science Museum Kamiokalab, Hida-City, Gifu, Hideyuki Tagoshi (ICRR, The University of Tokyo)
- ”Science Seminar of Geo Space Adventure”, July 13, 2024, Kamioka Community Center, Hida-City, Gifu, Kenta Tanaka (ICRR, The University of Tokyo)
- ”Science Seminar of Geo Space Adventure”, July 14, 2024, Kamioka Community Center, Hida-City, Gifu, Kentaro Munemiya (The Institute for Science Tokyo)
- ”Lecture for Kibogaoka High School Students”, August 2, 2024, Kibogaoka High School , Yokohama-City, Kanagawa, Kazuhiro Yamamoto (Toyama University)
- ”Lecture for Keio Shonan Fujisawa Junior&Senior High School Students”, August 9, 2024, Keio Shonan Fujisawa Junior&Senior High School , Fujisawa-City, Kanagawa, Shinji MIyoki (ICRR, The University of Tokyo)
- ”Open Discussion for KAGRA project”, August 24, 2024, Tokyo City University, Setagaya-Ward, Tokyo, Takaaki Kajita, Masatake Ohashi (ICRR, The University of Tokyo)
- ”Lecture for Open College in Hida”, September 7, 2024, Hida Earth Wisdom Center, Takayama-City, Gifu, Masatake Ohashi (ICRR, The University of Tokyo)
- ”Public Lecture for School of Mountain, Cosmos and Hope”, October 13, 2024, Kamioka Library, Hida-City, Gifu, Masatake Ohashi (ICRR, The University of Tokyo)
- ”Public Lecture for people in Hida-City ”, November 9, 2024, Hida Kamioka High School, Hida-City, Gifu, Masatake Ohashi (ICRR, The University of Tokyo)
- ”Public Lecture for Researchers’ Talk in Kamiokalab”, November 10, 2024, Hida Space Science Museum Kamiokalab, Hida-City, Gifu, Akimitsu Takamori (Earthquake Research Institute, The University of Tokyo)
- ”Lecture for Hida Kamioka High School Students”, January 17, 2025, KAGRA Site, Hida-City, Gifu, Osamu Miyakawa (ICRR, The University of Tokyo)
- ”Public Lecture for Researchers’ Talk in Kamiokalab”, June 9, 2024, Hida Space Science Museum Kamiokalab, Hida-City, Gifu, Masashi Yoshida (ICRR, The University of Tokyo)

- ”Lecture for Toyama High School Students”, July 4, 2024, Toyama High School , Hida-City, Gifu, Ko Abe (ICRR, The University of Tokyo)
- ”Lecture for Yoshiki High School Students”, July 5, 2024, ICRR Kamioka Laboratory, Hida-City, Gifu, Takatomi Yano (ICRR, The University of Tokyo)
- ”Public Lecture for Kamioka Geo Space Adventure”, July 13, 2024, ICRR Kamioka Laboratory, Hida-City, Gifu, Yosuke Kataoka, Masayuki Harada, Masayuki Nakahata, Masato Shiozawa, Shintaro Miki, Yuki Kanemura, Yumiko Takenaga (ICRR, The University of Tokyo)
- ”Lecture for Senior High Schhol Attached to Kyoto University of Education”, July 19, 2024, ICRR Kamioka Laboratory, Hida-City, Gifu, Yoshinari Hayato (ICRR, The University of Tokyo)
- ”Lecture for Kibogaoka High School Students”, August 1, 2024, ICRR Kamioka Laboratory, Hida-City, Gifu, Yoichi Asaoka (ICRR, The University of Tokyo)
- ”Online Lecture at UTokyo Open Day for High School Students”, August 6, 2024, ICRR Kamioka Observatory, Hida-City, Gifu, Katsuki Hiraide (ICRR, The University of Tokyo)
- ”Public Lecture for People in Takayama-City”, August 8, 2024, Takayama City Culturel Hall, Takayama-City, Gifu, Masato Shiozawa (ICRR, The University of Tokyo)
- ”Lecture for Keio Shonan Fujisawa Junior&Senior High School Students”, August 9, 2024, ICRR Kamioka Laboratory, Hida-City, Gifu, Yasuhiro Takemoto (ICRR, The University of Tokyo)
- ”Lecture for Nanao High School Students”, August 23, 2024, ICRR Kamioka Laboratory, Hida-City, Gifu, Makoto Miura (ICRR, The University of Tokyo)
- ”Lecture for Princess Chulabhorn Science High Schools Students”, September 6, 2024, ICRR Kamioka Laboratory (Online), Hida-City, Gifu, Shunichi Mine (ICRR, The University of Tokyo)
- ”Public Lecture for Researchers’ Talk in Kamiokalab”, October 13, 2024, Hida Space Science Museum Kamiokalab, Hida-City, Gifu, Yohei Noguchi (ICRR, The University of Tokyo)
- ”Public Lecture for Kamioka Open Day”, November 2, 2024, ICRR Kamioka Laboratory, Hida-City, Gifu, Kei Ieki, Jun Kameda, Hiroyuki Sekiya, Shoei Nakayama (ICRR, The University of Tokyo)
- ”Public Lecture for Kamioka Open Day”, November 2, 2024, Kamioka Community Center, Hida-City, Gifu, Masayuki Nakahata (ICRR, The University of Tokyo)
- ”Lecture for Keizaikai Club Members”, November 29, 2024, ICRR Kamioka Laboratory, Hida-City, Gifu, Katsuki Hiraide (ICRR, The University of Tokyo)
- ”Open Lecture for Asahi Culture Center”, November 30, 2024, Yokohama branch of Asahi Culture Center, Yokohama-City, Kanagawa, Hiroyuki Sekiya (ICRR, The University of Tokyo)
- ”Lecture for Doshisha Junior High School Students”, December 20, 2024, ICRR Kamioka Laboratory, Hida-City, Gifu, Hidekazu Tanaka (ICRR, The University of Tokyo)
- ”Public Lecture for People in Hida-City”, March 15, 2025, Kamioka Community Center, Hida-City, Gifu, Masayuki Nakahata (ICRR, The University of Tokyo)
- ”Lecture for Academic Conference of Medical Screening in Gifu Prefecture”, March 16, 2025, Hida Earth Wisdom Center, Takayama-City, Gifu, Masato Shiozawa (ICRR, The University of Tokyo)
- ”Public Lecture for People in Imizu-City”, March 23, 2025, Shinminato Museum, Imuzu-City, Toyama, Atsushi Takeda (ICRR, The University of Tokyo)
- ”Let’s look at UTokyo Lab!”, March 27, 2025, ICRR Kamioka Laboratory (Online), Hida-City, Gifu, Atsushi Takeda (ICRR, The University of Tokyo)
- ”Lecture for Planetarium Staff”, April 16, 2024, ICRR (Online), Kashiwa-City, Chiba, Yuichi Harikane (ICRR, The University of Tokyo)
- ”Public Lecture Organized by JPS”, May 18, 2024, ICRR (Online), Kashiwa-City, Chiba, Yuichi Harikane (ICRR, The

University of Tokyo)

- ”Public Lecture Organized by Hakubi Center, Kyoto Univ.”, May 30, 2024, Kyoto University, Kyoto-City, Kyoto, Yuichi Harikane (ICRR, The University of Tokyo)
- ”UTokyo Open Lecture”, June 15, 2024, Yasuda Auditorium, Bunkyo-Ward, Tokyo, Masami Ouchi (ICRR, The University of Tokyo)
- ”Public Lecture Organized by NPO Group ’Suuri no Tsubasa’ ”, August 4-5, 2024, Iwatesan Youth House, Takizawa-City, Iwate, Yuichi Harikane (ICRR, The University of Tokyo)
- ”Public Lecture ’Salon de Sora’ Organized by Yomiuri Culture”, September 8, 2024, Yokohama Center of Yomiuri Culture, Yokohama-City, Kanagawa, Masami Ouchi (ICRR, The University of Tokyo)
- ”Lecture for Oita Maizuru High School Students”, September 19, 2024, ICRR (Online), Kashiwa-City, Chiba, Yoshiaki Ono (ICRR, The University of Tokyo)
- ”Lecture for Musashi High School Students”, November 20, 2024, Musashi High School and Junior High School, Nerima-Ward, Tokyo, Yuichi Harikane (ICRR, The University of Tokyo)
- ”Lecture for High School Teachers”, November 26, 2024, Industrial Promotion Center, Kariya-City, Aichi, Yuichi Harikane (ICRR, The University of Tokyo)
- ”Public Lecture Organized by Young Astronauts Club, Japan”, December 22, 2024, Public Hall ’SanSan’, Mitaka-City, Tokyo, Yuichi Harikane (ICRR, The University of Tokyo)

(c) Visitors

Kashiwa Campus (Total: 24 groups, 2732 people)

- Junior High and High schools: 11 groups
- Universities and Graduate schools: 2 groups
- Researchers: 6 groups
- Inspections: 0 group
- Press: 4 groups
- Others: 1 group

KAMIOKA Observatory (Total: 87 groups, 2091 people)

- Junior High and High schools: 14 groups
- Universities and Graduate schools: 17 groups
- Researchers: 12 groups
- Inspections: 19 groups
- Press: 6 groups
- Others: 19 groups

KAGRA Observatory (Total: 46 groups, 390 people)

- Junior High and High schools: 0 groups
- Universities and Graduate schools: 8 groups
- Researchers: 10 groups
- Inspections: 17 groups
- Press: 2 groups
- Others: 9 groups

F. Inter-University Research Activities

Numbers of Researchers

		Number of Applications	Number of Adoptions	Number of Researchers
Results of Application (by Facility)				
Kamioka Observatory	Domestic	39	39	1,962
	International	6	6	44
Akeno Observatory	Domestic	6	6	103
Norikura Observatory	Domestic	8	8	92
Primary Cosmic rays, Kashiwa underground facility	Domestic	6	6	29
KAGRA Observatory	Domestic	24	24	637
	International	7	7	35
High Energy Astrophysics Facility in Canarias	Domestic	13	13	299
	International	1	1	13
Laboratorial Facilities in Kashiwa	Domestic	1	1	11
Large-Scale Computer System in Kashiwa	Domestic	12	12	190
	International	3	3	27
Conference Facilities in Kashiwa	Domestic	9	9	239
Overseas Facilities (Utah, Tibet and Bolivia)	Domestic	16	16	286
	International	6	6	39
Annual Sums	Domestic	134	134	3,848
	International	23	23	158

Results of Application (by Research Division)				
Neutrino and Astroparticle Division	Domestic	40	40	1,968
	International	6	6	44
High Energy Cosmic Ray Division	Domestic	58	58	1,093
	International	8	8	64
Astrophysics and Gravity Division	Domestic	26	26	704
	International	7	7	35
Research Center for Cosmic neutrinos	Domestic	10	10	83
	International	2	2	15
Annual Sums	Domestic	134	134	3,848
	International	23	23	158

Research Project Titles

1. Astroparticle physics using the Super-Kamiokande detector
2. Study of atmospheric neutrino flux and neutrino oscillations
3. Study of simulation for atmospheric neutrino
4. Study of flavor identification of atmospheric and beam neutrinos
5. Study of solar neutrino energy spectrum
6. Precise measurement of Day/Night effect for B8 solar neutrinos
7. Study for Supernova monitor
8. Study of Supernova Relic Neutrinos
9. Search for proton decay via $e^+\pi^0$ mode
10. Study of proton decay $p \to \nu K^+$

11. Study in upward-going muons and high energy neutrinos
12. Sidereal daily variation of $\sim$10TeV galactic cosmic ray intensity observed by the Super-Kamiokande
13. Neutrino search associated with astronominal transient events
14. Study of cosmic ray muon intensity modulations using underground particle experiments
15. Tokai to Kamioka Long Baseline Experiment T2K
16. Neutrino interaction study using accelerator data
17. Study for improvement of neutrino oscillation measurement in T2K expriment
18. Energy calibration for Super-Kamiokande
19. Research and development of computer simulation of Super-Kamiokande detector
20. Development of low concentration radon detection system
21. Hyper-Kamiokande project
22. Development of the Large Aperture Photodetector for a next-generation neutrino detector
23. Development of software for the next generation neutrino detector
24. New Photogrammetry Calibration for Super-Kamiokande and Hyper-Kamiokande
25. Novel Probes of Fundamental Physics with Nucleon Decays in Neutrino Experiments
26. Measurement of radon underground laboratories and evaluation of effects from radon to experiments
27. Study for lowering backgrounds of radioisotopes in large volume detectors
28. Development of a radioactivity assay system for underground experiments
29. Measurement of neutron flux at the Kamioka underground laboratory
30. RI measurement for SK-Gd project with HPGe detector
31. Generation three direct dark matter search experiment
32. Detector structure study for future direct dark matter search experiment
33. Research and Development for XENONnT and future Dark Matter Searches
34. Direction-sensitive dark matter search
35. A study on the near-infrared emission of liquid xenon
36. Study of double beta decay of ^{48}Ca
37. Studies on the background evaluation using laser spectroscopy analysis
38. Searches for neutrinoless double beta decay with high-pressure Xenon gas detector
39. Strain, tilt, seismic measurement in Kamioka-mine
40. Observation of two neutrinos emisson double beta decay using Zr-96 nuclei
41. R&D for a Small Atmospheric Cherenkov Telescope in Akeno Observatory
42. Observation of the Galactic Cosmic Ray Intensities using the Large Area Muon Telescopes
43. Multi-Color Imager for Transients, Survey and Monstrous Explosions
44. Research on geoid measurement technology using astronomical plumb deviation measurement

45. Space weather observation using muon hodoscope at Mt. Norikura
46. Observation of cosmogenic nuclides concentrations at Mt. Norikura
47. Study of secondary cosmic rays from Thundercloud at Mt. Norikura
48. Investigation of alpine plants on Mt.Norikura
49. Atmospheric mercury speciation dynamics and mercury wet deposition monitoring at the high-altitude
50. Evaluation of atmospheric SO_2 to cloud acidification at free troposhere through atmospheric observation at Mt. Norikura
51. A new study for high precision measurement of muons at Mt.Norikura
52. Citizen Science "Thundercloud Project" to elucidate the particle acceleration and interaction between cosmic rays and thunderclouds
53. Very-High-Energy Gamma-ray Observatory CTA Project
54. Development of Focal Plane Instruments for the CTA Large Sized Telescopes
55. Development of the readout system for the CTA large sized telescopes
56. Engineering runs of the first Large Size Telescope of CTA and construction of LST2-4 in La Palma Canary Islands, Spain
57. Commissioning and upgrade of the onsite data center for CTA North in La Palma, Spain
58. Development of SiPM modules for CTA-LST(4)
59. Development of the CTA/LST telescope control system
60. Maintenance and operation of the optical and power systems in CTA LST
61. Development of analysis method and initial observation with CTA Large-Sized Telescope
62. Development of camera for CTA small-sized telescopes
63. CTA Monte Carlo Simulation
64. Search for neutrino sources with the Large-Aperture Atmospheric Cherenkov Telescope
65. The extreme Universe viewed in very-high-energy gamma rays 2024
66. Study of High Energy Gamma-ray Objects with the MAGIC telescope
67. Development of a background reconstruction toolbox for the LST1 prototype and the upcoming CTA
68. Study of Extremely-high Energy Cosmic Rays by Telescope Array
69. R&D of the measurement of atmospheric transparency at the Telescope Array site
70. Study of very high energy cosmic rays around 10^{17} eV with the TALE hybrid experiment
71. Evaluation of optical characteristics of atmospheric fluorescence telescope by standard light source mounted on drone
72. Development and analysis of night-cloud observation by CCD camera for automatic observation of air fluorescence detector
73. Observing ultrahigh-energy cosmic rays with new fluorescence detectors at Telescope Array site
74. Research and development of a Fresnel lens air fluorescence telescope for next-generation UHECR observation
75. Experimental Study of High-energy Cosmic Rays in the Tibet ASγ experiment
76. Sidereal daily variation of $\sim$10TeV galactic cosmic ray intensity observed by the Tibet Air Shower Array
77. Study of the composition of cosmic rays at the Knee

78. A study on variation of interplanetary magnetic field with the cosmic-ray shadow by the sun.
79. Air shower observation for high-energy gamma-ray and cosmic ray detections at the Chacaltaya Cosmic Ray Observatory
80. Study of High Energetic Radiation from Thundercloud in the Altiplano
81. Study of solar magnetic fields using the cosmic-ray Sun's shadow observed at the southern hemishpere
82. Study of high-energy cosmic-ray anisotropy at the Chacaltaya Cosmic Ray Observatory
83. Development of an advanced Compton camera using SOI pixel semiconductor
84. Design study of a Compton camera for the study of cosmic rays
85. Study of High-Energy Cosmic-Ray Sources by Observations in Space with CALET
86. Comprehensive study of high-energy astrophysical phenomena
87. Development of a new code for cosmic-ray air shower simulation
88. Cosmic ray interactions in the knee and the highest energy regions
89. Development of improvements and test observations for the elucidation of very-high-energy particle-emitting objects by NTA
90. Clear identification of very high energy particle sources by NTA
91. Project for make "Cosmic Ray" to a common word (Application of Virtual Reality technology)
92. Development of the data acquisition system for the extension of the TAx4 surface detectors
93. Search for UHECR sources considering the galactic magnetic field and the mass composition
94. Preliminary research for developing the open data system
95. Development of the detector calibration system for the next-generation high-energy neutrino experiments
96. Development of a novel pulse generator system for the prototyping and testing of new trigger electronics for the ALPACA experiment
97. Potential acceleration of PeV cosmic rays by stellar-mass black hole binaries probed with the ALPACA and ALPAQUITA experiments
98. Workshop for study of cosmic-ray sources using air-shower observations
99. Research of a Large-Scale Gravitational Wave Telescope(XIV)
100. Study of Gravitational-wave by cryogenic laser interferometer CLIO in KAMIOKA Mine(VIII)
101. Development of Monitor and Interlock System for KAGRA
102. Research on cryogenic payload for KAGRA
103. R&D for the intensity stabilization of the laser system in KAGRA
104. Development of scattered light measurement technique and noise reduction for improving sensitivity in KAGRA V
105. Development of optical cavity for ultranarrow stable lasers
106. Study of Environmental Noise Reduction in KAGRA
107. Study of the environmental noise of KAGRA detector by environmental injection
108. Noise characteristics analysis using machine learning and deep learning and its application to interferometer diagnosis (IV)
109. Development of glitch data analysis system for improving gravitational detection

110. Reduction of Non-Stationary Noise in KAGRA (II)
111. Development of a noise source identification tool for improving the sensitivity of KAGRA telescope
112. Numerical Simulation of Electro-Magnetic Wave Propagation in Gravitational wave Detector XII
113. Development of a high performance sapphire mirror suspension
114. Control and automatic operation for KAGRA
115. Construction of KAGRA data transfer and storage system (10)
116. Promotion of collaborative research to incorporate KAGRA data into the low latency
117. International gravitational wave search network (4)
118. Construction of a diagnostic system for the gravitational wave detector
119. Precise geophysical observation at the Kamioka underground site and modeling of crustal activities
120. Gravitational Wave Data Analysis
121. Investigating the relationship between sapphire's impurities, absorption and birefringence for KAGRA upgrade
122. Improvement of gravitational wave telescope calibration with a new global network calibration scheme.
123. Development of new control method and high sensitive cryogenic sensor for KAGRA cryogenic mirror suspension system
124. Exploring the Early Universe and the Galaxy/Black-Hole Formation by a Combination of Large Observational Facilities and Collaboration
125. Evolution of the universe and particle physics
126. Detection of time variations for cosmogenic nucleid Be-7
127. Time profile of radioactive Cs concentration and its aerosol size distribution in local area
128. Development of new analysis techniques for supernova neutrino observation by Super-Kamiokande
129. Behavior of radionuclides in the marine environment
130. Measurement of the intrinsic radioisotopes in electron-tracking Compton telescopes for studying the radiation mechanism of extragalactic diffuse gamma-rays
131. Water Purification System R&D for Precision Neutrino Detectors
132. Frontier of the planetary material science
133. Precise calculation of the atmospheric neutrino flux
134. CRC workshop for future plans in cosmic ray research
135. The 9th YMAP symposium
136. Water Transparency Measurement in Super-Kamiokande
137. Study of supernova neutrinos in Super-Kamiokande
138. Data Taking, Calibrations, Measurements and Analysis with Super-Kamiokande I - VII
139. Installation of Super-Kamiokande outer detector laser system
140. Towards a multiphysics liquid Xe TPC with scintillation and charge multiplication readouts
141. An auto-flashing system in Hyper-Kamiokande for monitoring the detector evolution with time
142. Research and Development of the high-performance segment mirrors and the camera entrance windows for the CTA

Large Size Telescopes

143. Ultra-high-energy cosmic-ray origin studies with the Telescope Array and TAx4 surface detector
144. Study of the Hot-spot in Ultra High Energy Cosmic Rays with a New Large Telescope Array
145. Study of high-energy cosmic rays at a high altitude in Tibet, China
146. Study for Galactic CR origin using the ALPACA air shower array in Bolivia
147. Constraining the nature of the emission in PeVatrons observed by Alpaca.
148. Bayesian analysis on the origin of ultra-high energy cosmic ray events collected by the TA experiment
149. Study of the signals and reconstruction of cosmic ray events via surface detectors from the Telescope Array and the Pierre Auger cosmic ray detectors
150. Filter cavity experiments for the frequency dependent squeezed light for KAGRA
151. Self interacting dark matter and gravitational waves
152. Position control system for silicon monolithic suspension in cryogenic gravitational waves detectors.
153. Implementing Sophisticated Data Analysis Methods on KAGRA Data
154. Applications of machine learning technique on gravitational wave detection
155. Test Run Analysis of KAGRA O4 Data for Stochastic Gravitational-Wave Background Search
156. Implementing parameter estimation for CBC sources using particle swarm optimization
157. High-energy neutrino measurement at Super-Kamiokande
158. Constraining systematics at T2K and Super-Kamiokande oscillation analyses using neutrino-nucleus interaction models

G. List of Committee Members

(a) Board of Councillors

OGIO, Shoichi	ICRR, UTokyo
MORIYAMA, Shigetaka	ICRR, UTokyo
KUBO, Hidetoshi	ICRR, UTokyo
TAGOSHI, Hideyuki	ICRR, UTokyo
OKOSHI, Shinichi	Graduate School of Science, UTokyo
SAITO, Nobuhito	UTokyo
SAITO, Naohito	Institute of Particle and Nuclear Studies, KEK
AOKI, Shinya	Yukawa Institute for Theoretical Physics, Kyoto Univ.
DOI, Mamoru	National Astronomical Observatory of Japan
KAJINO, Fumiyoshi	Faculty of Science and Engineering, Konan Univ.
NISHIJIMA, Kyoshi	School of Science, Tokai University
YOKOYAMA, Junichi	Kavli Institute for the Physics and Mathematics of the Universe, UTokyo
YAMADA, Toru	Institute of Space and Astronautical Science
ISHINO, Masaya	International Center for Elementary Particle Physics, UTokyo
SHIOKAWA, Kazuo	Institute for Space-Earth Environmental Research, Nagoya Univ.

(b) Advisory Committee

OGIO, Shoichi	ICRR, UTokyo
TAKAHASHI, Fuminobu	Graduage School of Science, Tohoku Univ.
TOMA, Kenji	Frontier Research Institute for Interdisciplinary Sciences, Tohoku Univ.
MINAMINO, Akihiro	College of Engineering Science, Yokohama National Univ.
TAMII, Atsushi	Research Center for Nuclear Physics, Osaka Univ.
NAKAJIMA, Yasuhiro	Graduate School of Science, UTokyo
DOTANI, Tadayasu	Institute of Space and Astronautical Science, JAXA
YAMAMOTO, Tokonatsu	Faculty of Science and Engineering, Konan Univ.
ITOW, Yoshitaka	Institute for Space-Earth Environmental Research, Nagoya Univ.
KANDA, Nobuyuki	Graduate School of Science, Osaka Metropolitan Univ.
HIBINO, Kinya	Faculty of Engineering, Kanagawa Univ.
MORIYAMA, Shigetaka	ICRR, UTokyo
KUBO, Hidetoshi	ICRR, UTokyo
TAGOSHI, Hideyuki	ICRR, UTokyo
SHIOZAWA, Masato	ICRR, UTokyo
MIYOKI, Shinji	ICRR, UTokyo
KAWASAKI, Masahiro	ICRR, UTokyo
ASANO, Katsuaki	ICRR, UTokyo

(c) Inter-University Research Advisory Committee

HIBINO, Kinya (Chairperson)	Faculty of Engineering, Kanagawa Univ.
YAMAMOTO, Tokonatsu	Faculty of Science and Engineering, Konan Univ.
KUSHIDA, Junko	School of Science, Tokai Univ.
ITOW, Yoshitaka	Institute for Space-Earth Environmental Research, Nagoya Univ.
NISHIMURA, Yasuhiro	Faculty of Science and Engineering, Keio Univ.
TSUNESADA, Yoshiki	Graduate School of Science, Osaka Metropolitan Univ.
INOUE, Yoshiyuki	Graduate School of Science, Osaka Univ.
ISHIHARA, Aya	Institute for Advanced Academic Research, Chiba Univ.
ASO, Yoichi	National Astronomical Observatory of Japan
MORIYAMA, Shigetaka	ICRR, UTokyo
USHIBA, Takafumi	ICRR, UTokyo
OKUMURA, Kimihiro	ICRR, UTokyo
HAYATO, Yoshinari	ICRR, UTokyo
SAKO, Takashi	ICRR, UTokyo
SAITO, Takayuki (Organizer)	ICRR, UTokyo
OGIO, Shoichi (Observer)	ICRR, UTokyo

H. List of Personnel

Director OGIO,Shoichi,

Vice-Director MORIYAMA, Shigetaka

ICRR HQ in Kashiwa Campus

- High Energy Cosmic Ray Division

Scientific Staff	ASANO, Katsuaki,	HADASCH, Daniela,	KAWATA, Kazumasa,
	KIDO, Eiji,	KUBO, Hidetoshi,	MAZIN, Daniel,
	NODA, Koji,	NONAKA, Toshiyuki,	NOZAKI, Seiya,
	OGIO,Shoichi,	OHISHI, Michiko,	OHNISHI, Munehiro,
	SAITO, Takayuki,	SAKO, Takashi,	SASAKI, Makoto,
	SHIMODA, Jiro,	SITAREK, Julian,	STRZYS, Marcel,
	TAJIMA, Hiroyasu,	TAKEDA, Masahiro,	TAKITA, Masato,
	VOVK, Ievgen,	YAMAMOTO, Tokonatsu,	YOSHIDA, Tatsuo,
	YOSHIKOSHI, Takanori,		
Technical Staff	AOKI, Toshifumi,	KHANGULYAN, Dmitry,	KOIZUMI, Chikako,
	OHOKA, Hideyuki,	SEKINO, Koichi,	TAMURA, Akiko,
Research Fellow	ANZORENA, Marcos,	CHAI, Yating,	FUJISUE, Kozo,
	FUJITA, Keitaro,	Garcia Ginez Rocio,	KATO, Sei,
	KAWASHIMA, Tomohisa,	NISHIWAKI, Kousuke,	OHMURA, Takumi,
	OSHIMA, Hitoshi,	SAGAWA, Hiroyuki,	SAWADA, Ryo,
	TAKEISHI, Ryuji,	YEUNG, Kin Hang,	
Secretary	IDOMURA, Takako,	SHIRAGA, Ryoko,	SUGAHARA, Midori,
	TAKAGI, Akiko,		

- Astrophysics and Gravity Division

Scientific Staff	HARIKANE, Yuichi,	IBE, Masahiro,	KAWASAKI, Masahiro,
	ONO, Yoshiaki,	OUCHI, Masami,	
Research Fellow	ASAI, Kento,	LIANG, Yongming,	TOKESHI, Koki,
	ZHANG, Yechi,		

Kamioka Observatory

Director	SHIOZAWA, Masato,		
Scientific Staff	ABE, Ko,	ASAOKA, Yoichi,	BRONNER, Christophe,
	GONIN, Michel,	HAYATO, Yoshinari,	HIRAIDE, Katsuki,
	HOSOKAWA, Keishi,	IEKI, Kei,	IKEDA, Motoyasu,
	KAMEDA, Jun,	KATAOKA, Yosuke,	KATORI, Teppei,
	LOPEZ Gejo Francisco,	MIURA, Makoto,	MORIYAMA, Shigetaka,
	NAKAHATA, Masayuki,	NAKAYA, Tsuyoshi,	NAKAYAMA, Shoei,
	NISHIMURA, Yasuhiro,	PRONOST, Guillaume,	SATO, Kazufumi,
	SEKIYA, Hiroyuki,	TAKEDA, Atsushi,	TAKEMOTO, Yasuhiro,
	TANAKA, Hidekazu,	YANO, Takatomi,	WENDELL, Roger
	DI LODOVICO, Francesca Romana,		
Administrative Staff	KITANO, Ayano,		
Technical Staff	HAMA, Satoshi,	HIGASHI, Tetsuji,	ISHITA, Katsumi,
	MINE, Shunichi,	ONO, Junji,	ONOUE, Tatsuya,
Public Relations Staff	TAKENAGA, Yumiko,		
Research Fellow	ABE, Seisho,	HARADA, Masayuki,	NOGUCHI, Yohei,
	YOSHIDA, Masashi		
Secretary	DOI, Kyoko,	MAEDA, Yukari,	NISHIDA, Hiromi,
	OGAWA, Chitose,		

KAGRA Observatory

Director	MIYOKI,Shinji,		
Scientific Staff	KAJITA, Takaaki,	MIO, Norikatsu,	MIYAKAWA, Osamu,
	MORISAKI, Soichiro,	NARIKAWA,Tatsuya,	OHASHI,Masatake,
	OSHINO, Shoichi,	SAWADA,Takahiro,	TAGOSHI, Hideyuki,
	TAKAHASHI, Hiroki,	UCHIYAMA, Takashi,	USHIBA, Takafumi,
	YAMAMOTO, Takahiro,	YOKOZAWA, Takaaki,	YUZURIHARA, Hirotaka,
Administrative Staff	KATO, Daichi,	OKINAKA, Mihoko,	
Technical Staff	AOUMI, Masakazu,	KAMIIZUMI, Masahiro,	KIMURA, Nobuhiro,
	MORIWAKI, Shigenori,	NAKAGAKI, Koji,	NODE, Ayako,
	OMAE, Akio,	SAKAI, Akiko,	SAKAMOTO, Eri,
	SAWADA, Hiroyasu,	SHIMODE, Katsuhiko,	TAKAHASHI, Masahiro,
	TAKASE, Takashi,	YAMAGUCHI, Hirokazu,	YOSHIMURA, Mitsuharu,
Research Fellow	GHOSH, Tathagata,	PENA ARELLANO, Fabian,	TANAKA, Kenta,
	TUYENBAHEV, Darkhan,	UCHIKATA, Nami,	
Secretary	KIKUCHI, Rie,	KUDO, Naomi,	NOJIRI, Midori,

High Energy Astrophysics Facility in Canarias

Director	KUBO, Hidetoshi,

Research Center for Cosmic Neutrinos

Director	ITOW, Yoshitaka,		
Scientific Staff	OKUMURA, Kimihiro,	TASHIRO, Takuya,	TOKANAI, Fuyuki,
Technical Staff	AOYAMA, Shohei,		
Research Fellow	HAN,Seungho,		
Secretary	KITSUGI, Atsuko,	MASHIMA, Chieko,	

Norikura Observatory

Director	SAKO, Takashi,		
Technical Staff	AWAI, Kyosuke,	HAYAKAWA, Hideaki,	INOME, Yusuke,
	OKAZAKI, Nao,	SHIMODAIRA, Hideaki,	TOMURA, Tomonobu,
	YASUI, Hiromi,		

Akeno Observatory

Director	OGIO, Shoichi,
Technical Staff	EBISAWA, Yutaka,

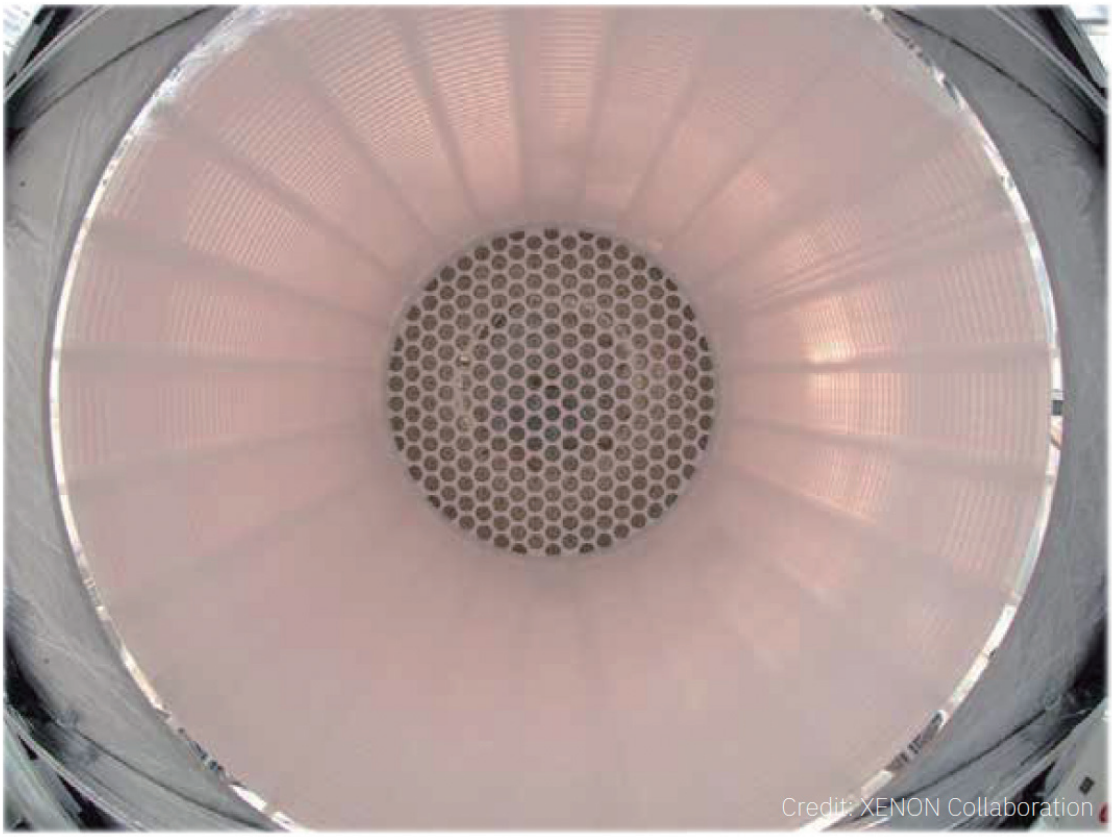
Graduate Students

Doctor	ABE, Shotaro,	BAXTER, Joshua Ryo,	CHITOSE, Akifumi,
	GOTO, Ryota,	HASHIYAMA, Kazuaki,	HIDO, Shingo,
	IWAYA,Masaki,	KAMINAGA, Yoshino,	KANEMURA, Yuki,
	KASAI, Kentaro,	KATO,Takashi,	KAWASHIMA, Teruyoshi,
	KUSAFUKA, Yo,	MATSUMOTO, Akinori,	MIKI, Shintaro,
	MURAKAMI, Yasuhiro,	NEDA, Shunsuke,	SHIMIZU, Kotaro,
	SUN, Dongsheng,	TAKAHASHI, Kaoru,	TAMAKI, Masahide
	TOMIYA, Takuya,	UMEDA, Hiroya,	WANG, Xubin,
	WATANABE, Keiichi,	XU, Yi,	YOKOE, Yoshichika,
	ZHU Chenghao,		

Master	AOKI, Takafumi,	BUN, Aken,	CHEN, Shuoyu,
	FUKUMOTO, Yusaku,	HIROOKA, Kou,	ICHINOSE, Yuto,
	IMAIZUMI, Ginga,	INAMOTO, Ryohei,	ITOKAWA, Takumi,
	KAGEURA, Yuta,	KOBAYASHI, Kazuya,	KOYAMA, Chisato,
	MIZUNO, Atsushi,	NAKANE, Minami,	NIHIJIMA, Ryotaro,
	OTSUZUKI, Kotaro,	SHINODA, Ryotaro,	SUGIMOTO, Futatsu,
	SUZUKI, Motoki,	TAKADA, Kazuki,	TSUCHIDA, Shunsuke,
	YANAGISAWA, Hiroto,		

Administrative Division

Administrative Staff	AKIYAMA, Makiko,	FUKUHARA, Nana,	HIDESHIMA, Saori,
	KOURO, Hideyoshi,	MARUMORI, Yasuko,	MATSUMOTO, Takehiko,
	NAKAYA, Yukiko,	NAMAI, Hiroki,	OKANO, Yuka,
	ONOGUCHI, Yukio,	SAITO, Akiko,	WATANABE, Taishi,
	YAMAGISHI, Yukinao,	YAMAGUCHI, Akiko,	YAZAKI, Keiichi,
Research Administrator	KAMO, Miwako,	KURACHI, Masafumi,	OTA, Ritsuko,
	SATO, Ritsuko,		
Public Relations Staff	ITO, Yoriko,	NAKAMURA, Makio,	YAMAGUCHI, Kyohei,
Archive Room	NAKAMURA, Kenzo,		



INSTITUTE FOR COSMIC RAY RESEARCH
THE UNIVERSITY OF TOKYO

Address 5-1-5, Kashiwanoha, Kashiwa-shi, Chiba, 277-8582 Japan
TEL +81-4-7136-3102
FAX +81-4-7136-3115
URL www.icrr.u-tokyo.ac.jp

ICRR
Institute for Cosmic Ray Research
University of Tokyo